



HAL
open science

Study and Optimisation of the Lithium Metal Anode of Rechargeable Batteries. Coupling Modeling and Characterization

Alex Cipolla

► **To cite this version:**

Alex Cipolla. Study and Optimisation of the Lithium Metal Anode of Rechargeable Batteries. Coupling Modeling and Characterization. Material chemistry. Université Grenoble Alpes [2020-..], 2022. English. NNT: 2022GRALI031 . tel-03689299

HAL Id: tel-03689299

<https://theses.hal.science/tel-03689299>

Submitted on 7 Jun 2022

HAL is a multi-disciplinary open access archive for the deposit and dissemination of scientific research documents, whether they are published or not. The documents may come from teaching and research institutions in France or abroad, or from public or private research centers.

L'archive ouverte pluridisciplinaire **HAL**, est destinée au dépôt et à la diffusion de documents scientifiques de niveau recherche, publiés ou non, émanant des établissements d'enseignement et de recherche français ou étrangers, des laboratoires publics ou privés.

THÈSE

Pour obtenir le grade de

DOCTEUR DE L'UNIVERSITÉ GRENOBLE ALPES

Spécialité : 2MGE : Matériaux, Mécanique, Génie civil, Electrochimie

Arrêté ministériel : 25 mai 2016

Présentée par

Alex CIPOLLA

Thèse dirigée par **Sébastien MARTINET**, Ingénieur HDR, CEA
et co-encadrée par **Benoit MATHIEU** et **Céline BARCHASZ**, Ingénieur -
Chercheur, CEA

préparée au sein du **Laboratoire des Matériaux du CEA-LITEN**
dans l'**École Doctorale I-MEP2 - Ingénierie - Matériaux,**
Mécanique, Environnement, Energétique, Procédés,
Production

Etude et Amélioration d'Accumulateurs à Anode de Lithium Métal en Couplant Modélisation et Caractérisation.

Study and Optimisation of the Lithium Metal Anode of Rechargeable Batteries. Coupling Modeling and Characterization.

Thèse soutenue publiquement le **3 mars 2022**,
devant le jury composé de :

Monsieur Yann BULTEL

PROFESSEUR DES UNIVERSITES, Grenoble INP, Président du jury

Monsieur Alejandro A. FRANCO

PROFESSEUR DES UNIVERSITES, Université de Picardie Jules Verne,
Rapporteur

Monsieur Sylvain FRANGER

PROFESSEUR DES UNIVERSITES, ICCMO, Université de Paris-Sud,
Rapporteur

Monsieur Birger HORSTMANN

DOCTEUR EN SCIENCES, Deutsches Zentrum für Luft – und Raumfahrt
(DLR), Examinateur

Monsieur Sébastien MARTINET

INGENIEUR HDR, CEA, Directeur de thèse

et des membres invités :

Monsieur Marc DESCHAMPS, responsable électrochimie et tests, Blue
Solutions

Madame Céline BARCHASZ, ingénieur-chercheur, CEA

Monsieur Benoit MATHIEU, ingénieur-chercheur, CEA

Monsieur Benoit CHAVILLON, ingénieur-chercheur, CEA



Résumé

Le lithium métal représente le candidat optimal comme électrode négative dans les batteries au lithium, de par sa capacité théorique élevée (3860 mAh.g⁻¹) et son faible potentiel (-3,04 V ESH). En revanche, l'inconvénient majeur de cette technologie est la formation de dendrites qui peut provoquer des emballements thermiques et des courts-circuits internes. Ces dernières sont également responsables de la durée de vie limitée des cellules lithium métal. La maîtrise de l'électrodépôt du lithium est nécessaire pour le développement de cette technologie haute densité d'énergie et demande une compréhension approfondie de ces phénomènes dendritiques.

L'objectif de ce travail est de corréler données expérimentales et modèle afin de comprendre la formation et la croissance des dendrites. Le modèle permet de théoriser les conditions dans lesquelles la croissance des dendrites est facilitée ou évitée, et comment les propriétés des composants de la cellule et la nature de la surface d'électrode peuvent l'affecter, pour suggérer des solutions permettant de réduire les dendrites. D'autre part, la partie expérimentale a pour but de définir un cadre de techniques permettant de déterminer des paramètres fiables à utiliser dans le modèle, et de valider ses tendances.

Le modèle continu proposé montre que l'interphase électrode/électrolyte ('SEI' pour Solid Electrolyte Interphase) est fondamentale pour évaluer la formation de dendrites et leur croissance, tandis que la définition d'une densité de courant limite n'est pas une condition suffisante pour éviter les dendrites. Cette prise en compte de la SEI dans le modèle permet d'étudier l'influence de ses propriétés mécaniques et électrochimiques sur la croissance dendritique. A partir de la géométrie de surface initiale et des propriétés électrochimiques et mécaniques des composants, le modèle est capable de prédire les conditions qui favorisent la croissance dendritique et de distinguer différentes morphologies de surface. Des dendrites arborescentes (tree-like), moussues (mossy-like) et whiskers sont obtenues selon la densité de courant appliquée. De plus, l'ajout de la mécanique de la SEI permet au modèle de faire la distinction entre la croissance induite par la pointe (tip-induced) et celle induite par la racine (root-induced). À partir des résultats du modèle, une SEI avec une faible résistivité, un coefficient de diffusion élevé et une vitesse de réaction rapide réduit la croissance des dendrites, tandis que la résistance mécanique de la SEI est une arme à double tranchant puisqu'une résistance élevée peut à la fois limiter l'expansion

incontrôlée de l'électrode de lithium, mais également stimuler la croissance en cas de fractures.

Enfin, les propriétés électrochimiques et mécaniques de la SEI formée dans un électrolyte liquide sont déterminées par spectroscopie d'impédance électrochimique (SIE) et microscopie à force atomique (AFM). L'évolution des spectres d'impédance en fonction du temps permet de caractériser l'évolution de la SEI et de déterminer ses propriétés (épaisseur, coefficient de diffusion et résistivité). D'autre part, l'AFM est utilisée dans le mode spectroscopie de force, à partir duquel il est possible de déterminer des valeurs locales du module de Young de la SEI. La spectrométrie photoélectronique X (XPS), capable d'identifier les composants chimiques à la surface des électrodes, permet de valider les résultats de l'AFM. Enfin, les tendances prédites par le modèle sont validées grâce à la mise au point d'une nouvelle configuration de cellule lithium métal, adaptée à une étude operando de l'électrodépôt du lithium métal par microscopie optique.

Ce travail représente une étude complète de la formation et croissance des dendrites dans les accumulateurs au lithium métal. Tandis que seuls les électrolytes liquides sont considérés ici, la méthodologie pourrait tout à fait être étendue aux électrolytes solides et aux revêtements artificiels à la suite de ce travail.

Abstract

Lithium metal represents the optimal candidate for the negative electrode in lithium batteries, due to its high theoretical capacity (3860 mAh.g⁻¹) and low potential (-3.04 V SHE). On the other hand, the major drawback of this technology is the formation of dendrites, which can cause thermal runaway and internal short-circuits, and are responsible for the limited lifetime of the cells. A dendrite-free lithium deposition is needed to improve this high energy density technology, thus, a deeper understanding of the phenomena and parameters that influence dendrite growth and formation is necessary.

The goal of this work is the correlation between experiments and modelling, to understand the formation and the growth of dendrites. The output of the model allows one to theorize in which conditions dendrites growth is boosted or avoided, and how the properties of the cell components and the design of the electrode surface can affect it, to suggest solutions to reduce dendrites. On the other hand, the experimental work has the purpose to define a framework of techniques to find reliable parameters to be used in the model, and to validate the trends of the model.

The proposed continuum model shows that the Solid Electrolyte Interphase (SEI) is fundamental to assess dendrites formation and growth, while the definition of a limiting current density is not a sufficient condition to avoid dendrites. Thanks to the introduction of the SEI concept and properties, the proposed model studies the influence of its mechanical and electrochemical properties on the dendritic growth. Starting from the initial surface geometry and the electrochemical and mechanical properties of the cell components, the model is able to predict the conditions that favours dendritic growth and to distinguish different surface morphologies. Tree-like, mossy-like and whisker dendrites are obtained, depending on the applied current density. Moreover, the addition of the mechanics of the SEI allows the model to distinguish between tip-induced growth and root-induced growth. From the model results, it can be concluded that a SEI with low resistivity, high diffusion coefficient and fast reaction rate can reduce dendrite growth, while the mechanical resistance of the SEI is a double-edge sword because it can limit the uncontrolled expansion of the lithium electrode but also boost the root-growth in case of fractures.

Electrochemical impedance spectroscopy (EIS) and atomic force microscopy (AFM) techniques are used to find electrochemical and mechanical properties of the SEI formed in liquid electrolytes. By following electrochemical impedance response over time, it is possible to observe SEI evolution and determine mean values for its thickness, its diffusion coefficient and its conductivity. On the other hand, the AFM technique is used in the force spectroscopy mode, from which it is possible to determine local values of the SEI Young's modulus. X-ray photoelectron spectroscopy (XPS) technique, which is able to identify the chemical components on the electrode surface, helps to validate the results of AFM. Finally, the trends predicted by the model are validated with a novel cell configuration suitable for an operando optical microscopy study of lithium metal stripping/plating.

This work represents a comprehensive study on dendrites formation and growth in lithium metal batteries. While it considers only liquid electrolytes so far, as a perspective, it could easily be expanded to solid electrolytes and artificial coatings.

Résumé Étendu

Le lithium métal représente le candidat optimal comme électrode négative dans les batteries au lithium, de par sa capacité théorique élevée (3860 mAh.g^{-1}) et son faible potentiel ($-3,04 \text{ V ESH}$). Afin de faire de l'électrode négative au lithium métal une technologie viable, de formidables défis doivent être surmontés, dont les plus grands sont la sécurité et la cyclabilité. Ses problèmes reposent sur des phénomènes d'interface entre l'électrode et l'électrolyte où se produisent le dépôt et le stripping inhomogènes du lithium. Alors que des hétérogénéités sont également présentes dans les batteries lithium-ion commerciales, ici leurs effets sont amplifiés par le changement de volume élevé de l'électrode au lithium.

Comme le montre la figure 0.1, l'expansion élevée de l'électrode de lithium métallique représente un problème pour l'interphase d'électrolyte solide (SEI), qui est une couche de passivation qui se forme spontanément à la surface de l'électrode de lithium vierge et agit comme une barrière au dépôt de lithium. La SEI n'est pas suffisamment stable mécaniquement pour s'adapter aux changements de volume de l'électrode de lithium. Par conséquent, des fissures se forment dans la SEI fragile, ce qui expose le lithium frais en dessous et favorise le dépôt de lithium dans ces zones. Ainsi, le dépôt inhomogène forme des structures filiformes à partir des fissures, communément appelées dendrites. Ces structures peuvent provoquer des courts-circuits internes si elles se développent suffisamment pour atteindre l'électrode opposée, entraînant potentiellement des risques d'emballement thermique et d'explosion. Lors du stripping du lithium, le « lithium mort » reste isolé électriquement dans l'électrolyte. Cela entraîne une diminution du lithium cyclable; donc une durée de vie limitée de la cellule. De plus, après un cyclage continu, l'électrode de lithium devient poreuse, tandis que la SEI s'épaissit, et la quantité de lithium mort augmente, ce qui réduit encore les performances de la cellule.

La maîtrise de l'électrodépôt du lithium est nécessaire pour le développement de cette technologie haute densité d'énergie et demande une compréhension approfondie de ces phénomènes dendritiques.

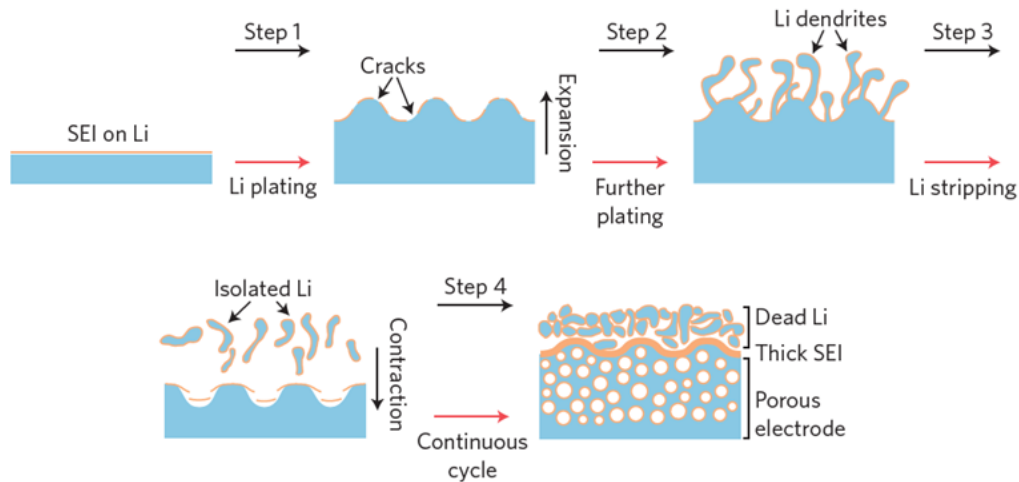


Figure 0.1: Illustration théorique des phénomènes de formation, de croissance et de vieillissement des dendrites dans les batteries au lithium métal.

Le mot « dendrite » dérive du mot grec « dendron » qui signifie « arbre ». En effet, ils sont souvent décrits comme des structures arborescentes. Néanmoins, les structures arborescentes ramifiées ne sont qu'un sous-ensemble des morphologies qui peuvent être formées par l'électrodépôt de lithium. Souvent, le lithium se dépose dans des structures qui ressemblent davantage à des particules ou à des filaments. Des dendrites arborescentes (tree-like dendrites) se forment à des densités de courant élevées, où l'épuisement du lithium à l'interface déclenche une croissance rapide de la dendrite à partir de sa pointe (croissance induite par la pointe ou tip-induced). À l'inverse, aux faibles densités de courant, des whiskers se forment. À de faibles densités de courant, une SEI robuste se forme à la surface du lithium métal, ce qui provoque une augmentation de la pression sur l'électrode sous-jacente pendant le dépôt de lithium. À un certain seuil, la pression est relâchée dans un ou plusieurs trous, où les whiskers sont libres de croître. Les whiskers poussent à partir de la racine, comme les cheveux humains, dans un mécanisme appelé croissance induite par la racine (root-induced). À des densités de courant intermédiaires, la croissance induite par les pointes et la croissance induite par les racines sont théorisées pour arriver. Ce mode de croissance hybride conduit à des dendrites moussues (mossy-like dendrites).

Pour mieux comprendre les dendrites divers modèles ont été proposés pour simuler l'électrodépôt de lithium au cours des dernières décennies. Malgré les nombreuses tentatives, un modèle unificateur qui étudie les effets mécaniques et électrochimiques de la SEI sur la croissance des dendrites n'est pas présent dans la littérature, en particulier pour la croissance induite par les racines des dendrites.

L'objectif de ce travail est de corréler modèle et données expérimentales afin de comprendre la formation et la croissance des dendrites. Le modèle permet de théoriser les conditions dans lesquelles la croissance des dendrites est facilitée ou évitée, et comment les propriétés des composants de la cellule et la nature de la surface d'électrode peuvent l'affecter, pour suggérer des solutions permettant de réduire les dendrites. D'autre part, la partie expérimentale a pour but de définir un cadre de techniques permettant de déterminer des paramètres fiables à utiliser dans le modèle, et de valider ses tendances.

Le modèle proposé est continu et 2D, avec l'ajout de l'épaisseur de la SEI, définie comme une propriété de l'interface lithium/électrolyte, qui donne une dimension supplémentaire où il est possible d'étudier les phénomènes de transport qui se produisent au sein de la SEI. En plus de la SEI, les phénomènes de transport dans l'électrolyte liquide et dans l'électrode sont simulés. La densité de courant du dépôt de lithium sur l'électrode est modélisée avec une cinétique de Butler-Volmer, qui produit un changement dans la géométrie de la surface du lithium, qui à son tour provoque une déformation de la SEI. La SEI déformé exerce une pression sur la surface du lithium métal, ce qui contribue à déformer l'électrode de lithium, en modifiant davantage la géométrie de sa surface. Par ce couplage de l'électrochimie et de la mécanique du modèle, le changement morphologique de la surface du lithium et de l'épaisseur SEI au cours l'électrodéposition de lithium est étudiée.

Afin de montrer l'effet de chaque phénomène sur l'évolution des dendrites, trois séries de résultats sont présentées. Les trois modèles à partir desquels les résultats sont obtenus sont les suivants :

- Un modèle de base qui ne considère que les phénomènes de transport dans l'électrode et l'électrolyte, en négligeant le SEI
- Un modèle amélioré qui ajoute les phénomènes de transport à l'intérieur de la SEI actif, qui change son épaisseur au cours de la simulation
- Le modèle complet, qui ajoute les effets de la mécanique de la SEI au modèle amélioré

En comparant les résultats du modèle de base et du modèle amélioré, il est montré que la SEI est fondamentale à considérer pour évaluer la formation et la croissance des dendrites. Grâce à l'introduction de la SEI, différentes morphologies de surface d'électrode ont été produites par les simulations et les résultats sont cohérents avec la littérature. En utilisant les paramètres de la littérature, des dendrites arborescentes,

moussues et whisker ont été identifiés, respectivement à des densités de courant appliquées de 10 mA.cm^{-2} , 1 mA.cm^{-2} et $0,1 \text{ mA.cm}^{-2}$, tandis que un dépôt quasi homogène a été trouvé à $0,01 \text{ mA.cm}^{-2}$ (figure 0.2).

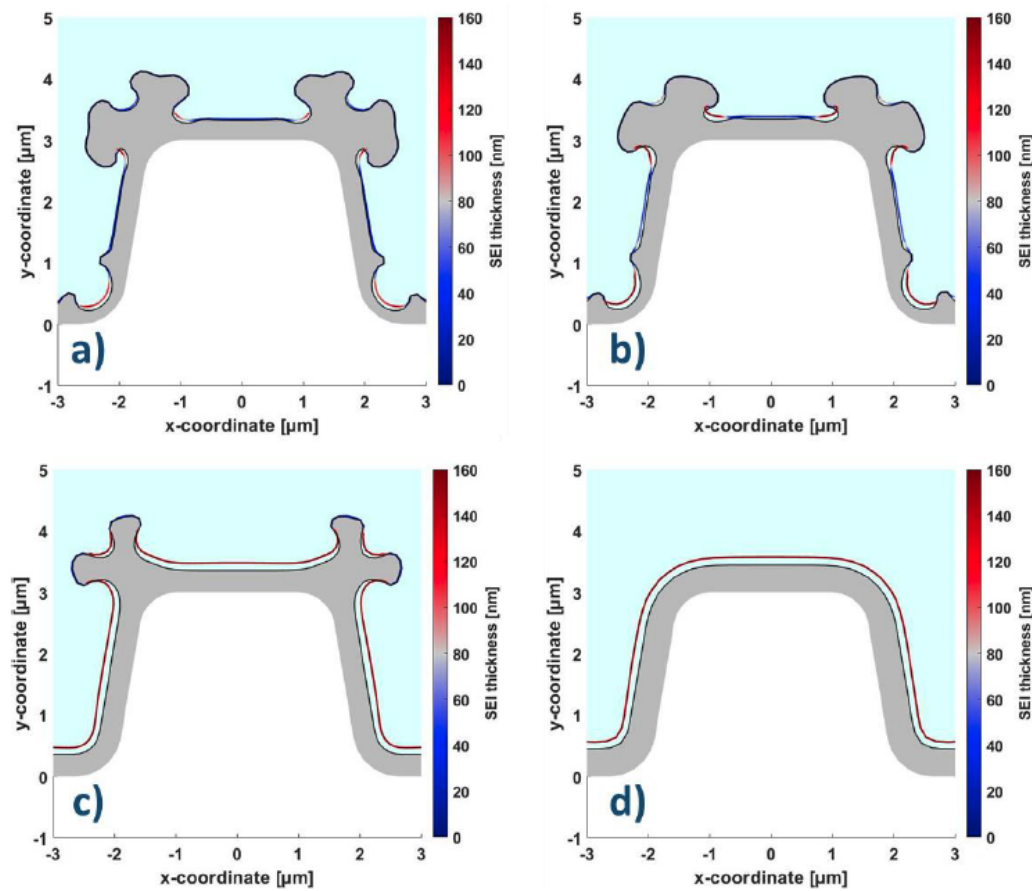


Figure 0.2: Épaisseur de la SEI en fin de simulation en couleur [nm]. Lithium déposé lors de la simulation en gris. a) Simulation après 40 s avec une densité de courant appliquée de 10 mA.cm^{-2} . b) Simulation après 400 s avec une densité de courant appliquée de 1 mA.cm^{-2} . c) Simulation après 4 000 s avec une densité de courant appliquée de $0,1 \text{ mA.cm}^{-2}$. d) Simulation après 40 000 s avec une densité de courant appliquée de $0,01 \text{ mA.cm}^{-2}$.

À partir de l'analyse de sensibilité sur les propriétés électrochimiques de la SEI, on peut conclure qu'une SEI avec une faible résistivité, un coefficient de diffusion élevé et une vitesse de réaction rapide peut réduire la croissance des dendrites.

Le modèle complet confirme l'importance de considérer à la fois les effets électrochimiques et mécaniques de la SEI pour avoir une description complète des différents mécanismes de croissance qui ont été observés expérimentalement. En effet, l'ajout de la mécanique de la SEI a permis de distinguer les croissances induites par la pointe et par la racine, ces dernières étant présentes à plus faible densité

de courant appliqué, conformément à la littérature. La résistance mécanique de la SEI est une arme à double tranchant puisqu'une résistance élevée peut à la fois limiter l'expansion incontrôlée de l'électrode de lithium, mais également stimuler la croissance en cas de fractures.

Puisque les résultats de la simulation montrent l'importance du SEI sur l'évolution des dendrites, un cadre des expériences pour déterminer les propriétés électrochimiques et mécaniques de la SEI formée dans un électrolyte liquide est proposé. Avec la spectroscopie d'impédance électrochimique (SIE), l'évolution des spectres d'impédance en fonction du temps permet de caractériser l'évolution de la SEI et de déterminer ses propriétés moyennes (épaisseur, coefficient de diffusion et résistivité). D'autre part, la microscopie à force atomique (AFM) est utilisée dans le mode spectroscopie de force, à partir duquel il est possible de déterminer des valeurs locales du module de Young de la SEI. La spectrométrie photoélectronique X (XPS), capable d'identifier les composants chimiques à la surface des électrodes, permet de valider les résultats de l'AFM.

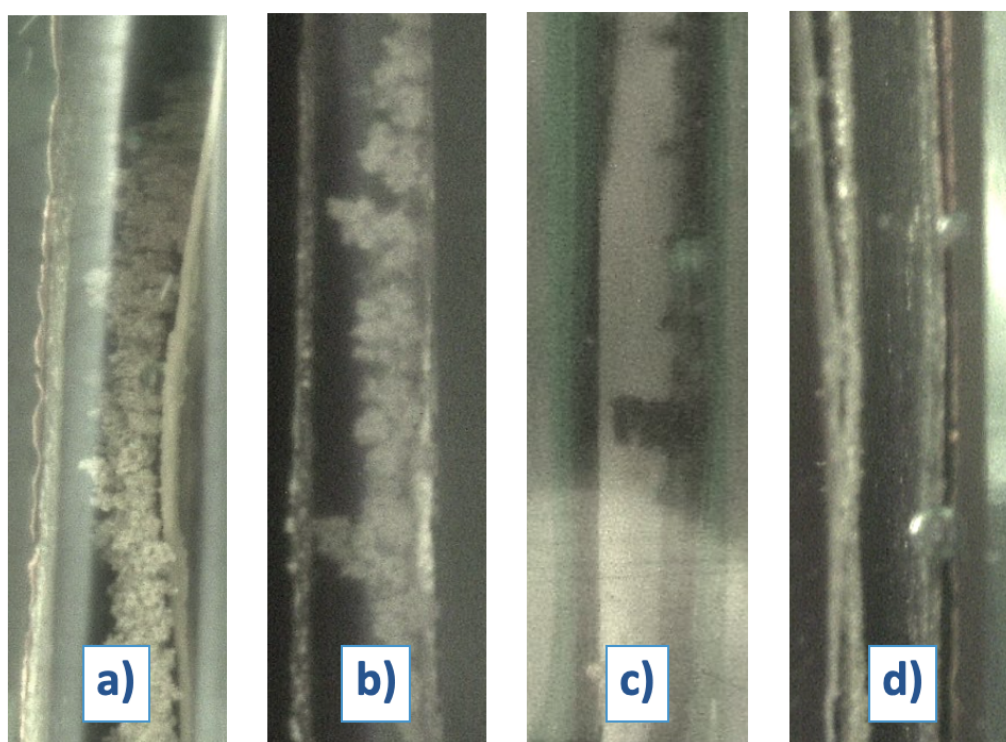


Figure 0.3: Images de dendrites obtenues par microscopie optique *operando*. a) Dendrites arborescentes avec une densité de courant appliquée de $10 \text{ mA}\cdot\text{cm}^{-2}$. b) Dendrites moussues avec une densité de courant appliquée de $1 \text{ mA}\cdot\text{cm}^{-2}$. c) Whiskers avec une densité de courant appliquée de $0,1 \text{ mA}\cdot\text{cm}^{-2}$. d) Dépôt homogène avec une densité de courant appliquée de $0,01 \text{ mA}\cdot\text{cm}^{-2}$.

Enfin, les tendances prédites par le modèle sont validées grâce à la mise au point d'une nouvelle configuration de cellule lithium métal, adaptée à une étude *operando* de l'électrodépôt du lithium métal par microscopie optique. Les images du microscope optique valident qualitativement les résultats du modèle, avec des dendrites arborescentes, moussues et whisker obtenu, respectivement à des densités de courant appliquées de 10 mA.cm^{-2} , 1 mA.cm^{-2} et $0,1 \text{ mA.cm}^{-2}$, tandis que un dépôt homogène a été trouvé à $0,01 \text{ mA.cm}^{-2}$ (figure 0.3).

Ce travail représente une étude complète de la formation et croissance des dendrites dans les accumulateurs au lithium métal. Tandis que seuls les électrolytes liquides sont considérés ici, la méthodologie pourrait tout à fait être étendue aux électrolytes solides et aux revêtements artificiels à la suite de ce travail.

Contents

1	Introduction	17
1.1	Battery Energy Storage and Challenges	17
1.2	Lithium Batteries and Lithium Metal Electrode	18
1.2.1	Brief History of Lithium Batteries	18
1.2.2	Lithium Metal Electrode	19
1.2.3	Lithium Metal Challenges	20
1.2.4	Dendrites Morphology and Nomenclature	22
1.2.5	Solid Electrolyte Interphase (SEI)	24
1.2.6	Electrolyte Compositions for Rechargeable Lithium Metal Batteries	26
2	Literature Review	29
2.1	Modeling Lithium Metal	29
2.1.1	Discrete Models	29
2.1.2	Phase-Field Continuum Models	33
2.1.3	Multi-Domain Continuum Models	38
2.1.4	Conclusion on Models in the Literature	45
2.2	Characterization of Lithium Metal and SEI	47
2.2.1	Optical Microscopy	48
2.2.2	Scanning Electron Microscopy and Transmission Electron Microscopy	51
2.2.3	Atomic Force Microscopy	55
2.2.4	Electrochemical Impedance Spectroscopy	62
2.2.5	X-ray Photoelectron Spectroscopy	66
2.2.6	Conclusion on Experiments in the Literature	68
2.3	Aims and Methodology of the Work	68
3	Model Presentation	71
3.1	Model Framework	71
3.2	Equations	74
3.2.1	Transport Phenomena in the Electrolyte and Electrode	74

3.2.2	Active SEI Model	78
3.2.3	Mass Transport in the SEI	81
3.2.4	SEI Mechanics	84
3.2.5	Lithium Electrode Mechanics	87
3.2.6	Modified Butler-Volmer	90
3.2.7	Moving geometry	97
3.3	Overview of the Model and Comsol [®] Environment	98
4	Model Results	101
4.1	Basic Model: no SEI	103
4.2	Improved Model: SEI Addition, no Mechanics	109
4.2.1	Effect of SEI Formation Kinetics	120
4.2.2	Effect of SEI Resistivity	123
4.2.3	Effect of SEI Diffusion Coefficient	126
4.2.4	Effect of the Geometry of the Defect	130
4.3	Full Model	132
4.4	Lithium Stripping and Pores Creation	138
4.4.1	Lithium Stripping	138
4.4.2	Pores Creation	140
4.5	Conclusion on Model Results	142
5	Experiments	145
5.1	Model Parameters	145
5.2	Time-Difference Impedance Spectroscopy	147
5.2.1	Experimental Methodology	147
5.2.2	Data Analysis Methodology	150
5.2.3	Results with Ethers-based Cells	154
5.2.4	Results with Comparison with Alternative Methods	158
5.2.5	Results with Carbonates-based Cells	159
5.3	<i>Post-mortem</i> Analysis: XPS and AFM	161
5.3.1	X-ray Photoelectron Spectroscopy	163
5.3.2	AFM Methodology	165
5.3.3	AFM Results	169
5.4	<i>Operando</i> Optical Microscopy	172
5.4.1	Methodology	172
5.4.2	Results	175
5.5	Conclusions on the Performed Experiments	184
6	Final Conclusions and Future Developments	187

List of Figures	193
List of Tables	203
List of Acronyms	205
List of Main Symbols	207
Bibliography	209

Introduction

In this introductory chapter, a brief description of the current energy storage scenario and its challenge is made. Then, the history of lithium batteries is summarized, discovering the role that lithium metal electrodes had in the past. Later, advantages and challenges of lithium metal are discussed, with particular attention to dendrites and their different morphologies. Finally, components that influence dendrites formation and growth such as electrolyte and solid electrolyte interphase (SEI) are presented.

1.1 Battery Energy Storage and Challenges

Battery energy storage is one of the key components of the energy sector, both for stationary applications, enabling a deeper penetration of renewable energies in the electric grid and ensuring more flexibility and reliability to the power supply, and for automotive applications, promoted by an increased interest in electric mobility, driven by a consensus in reducing pollution.

The total installed capacity of stationary battery storage reached 34 GWh at the end of 2020, with 5 GW of new storage power added in 2020, while the market for electric vehicles batteries is already ten times larger than the stationary one [1]. As a matter of fact, electric car sales reached a record 3 million in 2020, up 40% from 2019, and according to the IEA's Net Zero Emissions by 2050 Scenario, 300 million electric cars will be on the road by 2030 [2]. Automotive battery production increased in parallel with the demand, reaching 160 GWh in 2020 (up 33% from 2019) while the average cost of batteries decreased by 13%, arriving at a global average price of 137 USD.kWh⁻¹.

In order to reach the targets for a more sustainable future, different challenges related to batteries have to be overcome and several improvements have to be made, both technological and economical. Among them, further reducing the cost of battery packs, increasing the sustainability of the batteries value chain, incrementing

the lifetime and the safety of the batteries and increasing their energy density are major challenges to be addressed.

1.2 Lithium Batteries and Lithium Metal Electrode

Lithium batteries are the most widely used battery storage technology, due to their high energy density and relatively long lifetime. In this section, the history of lithium batteries is explored and the importance of lithium metal batteries, together with the correlated challenges, is analyzed.

1.2.1 Brief History of Lithium Batteries

The history of lithium batteries is fascinating, with many contributions from all over the world and many ideas and solutions that quickly gained popularity and just as quickly felt into oblivion. Some solutions stayed relevant for more than 30 years and other managed to make an unexpected comeback, like lithium metal electrode.

In the initial stage of the technology, lithium batteries were of the primary type (non rechargeable), their success led to the interest for developing a secondary, rechargeable type. The first commercial rechargeable lithium batteries were pioneered by Stanley Whittingham in the late 1970s at Exxon, and they were based on titanium disulfide (TiS_2) or molybdenum disulfide (MoS_2) positive electrodes, while lithium metal was used as the negative electrode, and a liquid organic solution was used as electrolytes [3]. This device was commercialized for the first time in the late 1980s by Moli Energy and sold in millions of units. The technology could already be cycled hundreds of times; however, frequent faults and accidents, caused by the dendrites formation, slowed down and ultimately halted its development [4].

Parallel to the problems of the lithium metal electrode, the research on the insertion or intercalation electrodes was giving extraordinary results. The groundbreaking approach consisted of the combination of two insertion electrodes, both of which being able to insert and deintercalate lithium ions reversibly, depending on the charging or discharging process. This kind of battery was called "lithium rocking chair battery", because lithium ions "rock" between the two electrodes [4]. The fundamental discovery of lithium cobalt oxide (LiCoO_2) as a positive electrode material in 1980 by Goodenough [5] laid the foundation for success of the rocking chair technology. However, more than 10 years passed before the technology could

reach a practical application. In 1991, Sony Corporation® released the lithium ion rechargeable battery on the market, based on the rocking chair battery concept, renamed by the Japanese engineers lithium ion rechargeable battery. The electrode materials were graphite in the negative electrode and lithium cobalt oxide in the positive.

Despite the outstanding success of lithium ion batteries, they are slowly approaching their limits in terms of energy density and power. New challenges, opened by electric mobility and renewable energy sources, demand significantly higher energy density, which is unlikely to be met with lithium ion chemistries. Therefore, investigating new materials to overcome these limits is fundamental. Among them, reviving the lithium metal negative electrode is becoming popular, and in the next section the reasons behind this shift are explained.

1.2.2 Lithium Metal Electrode

Lithium metal represents the optimal choice for the negative electrode material, due to the high theoretical capacity (3860 mAh.g^{-1}) and the lowest electrochemical potential (-3.04 V compared to the standard hydrogen electrode, SHE), which earned it the definition of “Holy Grail of batteries” [6]. In Fig. 1.1, the volumetric energy density (simply called energy density in [7]) and gravimetric energy density (or specific energy) of the cells that use a lithium metal electrode, thus Li-LMO (Lithium - Lithium Transition-Metal Oxide), Li-S (Lithium-Sulfur) and Li-air, are compared to more traditional lithium ion battery technology and to gasoline.

In 2017, according to Lin *et al.* [7], the state-of-the-art lithium ion cells could reach a specific energy around 250 Wh.kg^{-1} in 2020, and in 2021, this forecast remains valid since all the major producers have commercial cells in this range of energy density (*e.g.* 263 Wh.kg^{-1} for LG INR21700-M50, 261 Wh.kg^{-1} for SAMSUNG INR21700-50E, 267 Wh.kg^{-1} for SONY 21700-52EM [8]). On the other hand, lithium metal batteries-based can reach a higher specific energy, respectively 440 Wh.kg^{-1} for Li-LMO, 650 Wh.kg^{-1} for Li-S and 950 Wh.kg^{-1} for Li-air, as shown in Fig. 1.1. Moreover, the estimated volumetric energy density of the Li-air battery is comparable to the one of petrol, being greater than 1100 Wh.l^{-1} . It is worth highlighting that the previous energy densities are estimated at the cell level, and they naturally decrease at the pack level.

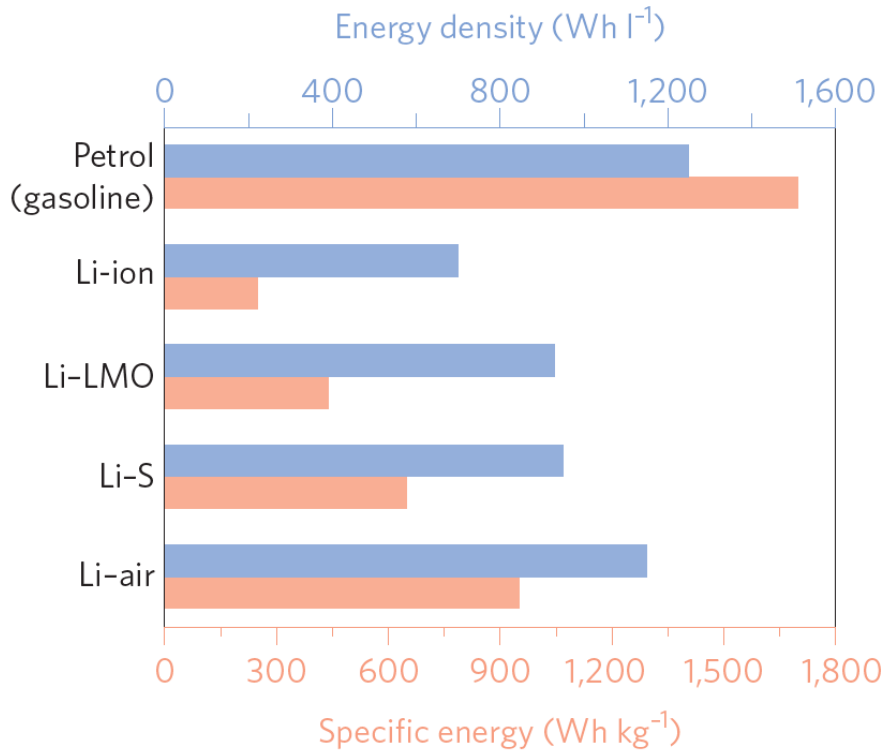


Figure 1.1: Specific energy [Wh.kg⁻¹] and energy density [Wh.l⁻¹] of different lithium cell technologies compared to gasoline [7].

1.2.3 Lithium Metal Challenges

In order to make lithium metal negative electrodes a viable technology, formidable challenges have to be overcome, the greatest of which are safety and cyclability. Its problems rely on interfacial phenomena between the electrode and the electrolyte where the inhomogeneous deposition and stripping of lithium happens as well as the formation of the solid electrolyte interphase.

The solid electrolyte interphase (SEI) is a passivation layer that is formed spontaneously on the surface of the pristine lithium electrode, due to the decomposition of electrolyte components at the low potential lithium surface. The formation of the SEI adds a further degree of heterogeneity in the system, which favors inhomogeneous nucleation and growth of the lithium metal electrode [9].

While heterogeneities are also present in the commercial lithium ion batteries, here their effects are amplified by the high volume change of the lithium electrode. It is worth to note that all electrode materials undergo volume change during operation, from the 10% that can be reached by commercial intercalation electrodes to 400% for alloy-type negative electrodes (like silicon-based negative electrodes) [7]. On the other hand, the volume change of a lithium metal electrode is virtually infinite, due to its hostless nature.

Fig. 1.2 presents a theoretical illustration for lithium plating and stripping on a lithium metal electrode. It can be noticed that the inhomogeneous deposition of lithium metal represents a problem for safety due to the formation of lithium dendrites, which are metallic structures that form on the negative electrode during plating. These structures can cause internal short-circuits if they grow enough to reach the opposite electrode, potentially leading to thermal runaway and explosion hazards, which are the problems that have blocked this technology in the 1980s. Inhomogeneous deposition is also an issue for the solid electrolyte interphase (SEI), which is not mechanically stable enough to accommodate the volume changes of the lithium electrode [6]. Therefore, cracks are formed in the fragile SEI, which exposes the fresh lithium underneath.

The SEI acts like a barrier to lithium deposition, thus, deposition is favored in the zones where the fresh lithium is exposed. Therefore, the formation of cracks and heterogeneous composition within the SEI layer further promote the inhomogeneous deposition of lithium dendrites.

During lithium stripping, "dead lithium" can also remain electrically isolated in the electrolyte, since the narrow roots of the dendrites can easily physically detach from the bulk electrode [10]. This causes a reduction of cyclable lithium, thus a limited lifetime of the cell. Moreover, after continuous cycling, the lithium electrode becomes porous, while the SEI becomes thicker, and the amount of dead lithium increases, further reducing the performance of the cell. Therefore, dendrite-free lithium deposition is necessary to improve this technology, and a deep understanding of interfacial phenomena during lithium deposition and stripping is needed. Before concluding this introductory chapter, a review on dendrites morphology and their nomenclature is detailed in the next section.

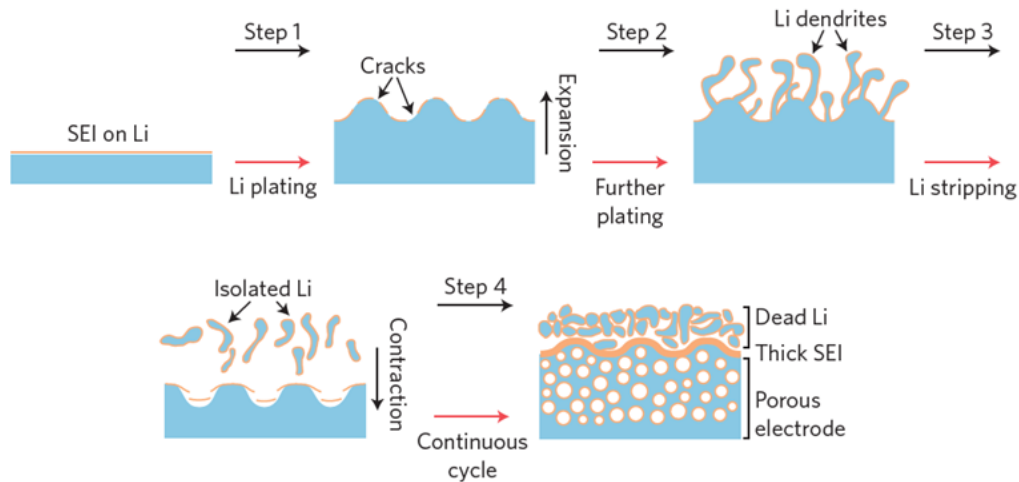


Figure 1.2: Theoretical illustration of dendrites formation, growth and aging phenomena in lithium metal batteries [7].

1.2.4 Dendrites Morphology and Nomenclature

The word "dendrite" derives from the Greek word "*dendron*" which literally means "tree". Indeed, they are often described as tree-like structures. In metallurgy, this word is related to the type of structures that are common during molten metal solidification and metal electrodeposition. However, Zhang *et al.* [9] argued that there is an ambiguity in calling dendrites the structure that lithium can form during its electrodeposition. Indeed, branched, tree-like structures are just a subset of the morphologies that can be formed by lithium electrodeposition. Often, lithium deposits in structures that are more particle-like or needle-like. Despite these differences, the term dendrites is ubiquitous in the literature and refers to all the structures that lithium forms during its deposition.

To sort out the ambiguity around dendrite definitions and the nomenclature of its different shapes, in this work, the nomenclature from the work of Bai *et al.* [11] is used in the literature review (chapter 2) and to describe the results obtained with the proposed model (chapters 3 and 4).

Fig. 1.3 shows the three growth modes suggested by Bai *et al.* [11]. In their work they combined optical *operando* techniques and *post-mortem* analyses to find and theorized the reason behind the different growth modes, which are:

- Pure dendrites or tree-like dendrites
- Mossy-like dendrites
- Whiskers or needle-like dendrites

Tree-like dendrites form at high current densities. The third row of Fig. 1.3 shows the mechanism that is theorized to lead to this kind of morphology. Above a limiting current density, salt depletion occurs at the lithium/electrolyte interface at a time, called Sand's time, causing instabilities at the interface, thus dendrite nucleation. Lithium depletion at the interface triggers a fast growth of the dendrite from its tip (tip-induced growth). Further details on limiting current density and Sand's times are discussed in the literature review of the models, section 2.1.3.

On the opposite, at low current densities, whiskers are formed. According to Bai *et al.*, at low current densities, a robust SEI is formed on the surface of the lithium metal, which causes an increase of pressure on the underneath electrode during lithium deposition. At a certain threshold, the pressure is released in one or more holes, where whisker protrusions are free to grow. Whiskers grow from their root, like human hair, in a mechanism called root-induced growth (first row of Fig. 1.3).

According to Bai *et al.* [11], the most interesting scenario occurs at intermediate current densities, under which the rate of lithium deposition becomes comparable with the rate of SEI formation. At intermediate current densities, both tip-induced growth and root-induced growth are theorized to happen (surface growth [11]). This hybrid growth mode leads to the globular shape of the mossy-like dendrites, shown in the central row of Fig. 1.3.

Before presenting the theoretical and experimental literature that led to the detection and explanation of the different dendrites morphologies, two components of the cell that influence these structures are presented, the SEI and the electrolyte.

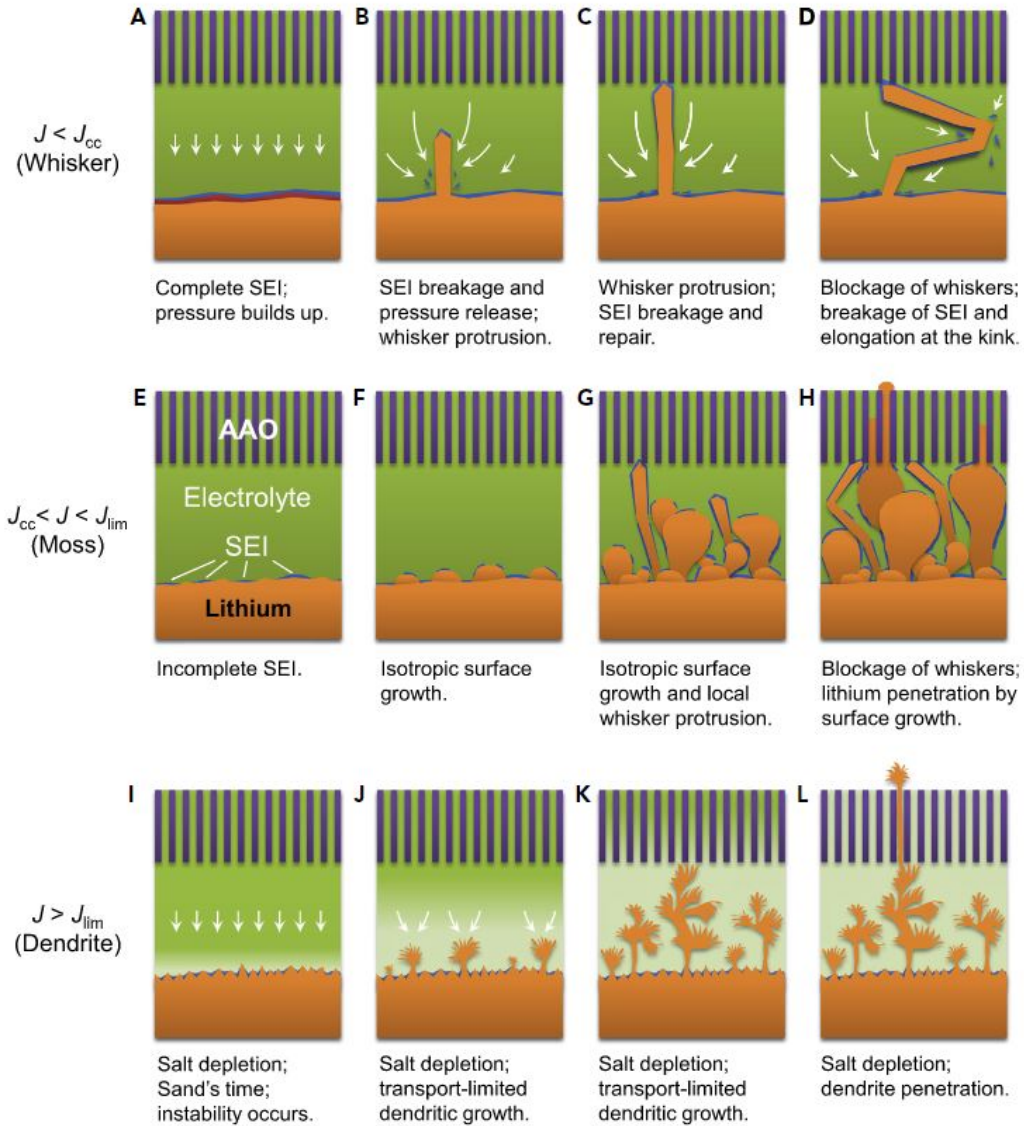


Figure 1.3: Illustration of different dendrite morphologies that can grow on a lithium metal electrode [11].

1.2.5 Solid Electrolyte Interphase (SEI)

Since it is a fundamental component for dendrite formation and growth, and it is of central importance for the model and the experiments that are presented in this work, it is necessary to detail further the concept of the SEI.

The Solid Electrolyte Interphase (SEI) is a general concept that describes a passivation layer [12] formed on the negative electrode surface from the decomposition

of electrolyte components, which electronically isolates the electrode from continuously reacting with the electrolyte but still allows lithium ion transport. It is generally formed during the early stages of the cell assembly and its initial charging cycles, nevertheless, its chemistry and properties change and evolve during the lifetime of the cell [13]. For low potential negative electrodes (such as graphite or lithium metal-based ones), it usually consists of by-products from electrolyte components (salts, solvents, additives) electrochemical reduction [14]. The complexity of the mechanisms involved in its formation makes the SEI a multi-layered and heterogeneous structure. It is generally of nanometer scale (10-200 nm) [15] [16], depending on the electronic properties of the SEI components and temperature [17]. In most of the organic-based electrolytes, it is generally described as a bi-layered component, composed of an inner inorganic layer and an outer organic one [18].

The inner layer, which is in contact with the electrode surface, is usually described as a dense and inorganic film, mainly composed of lithium carbonate (Li_2CO_3), lithium fluoride (LiF) and lithium oxide (Li_2O) [18]. It permits lithium ion transport, which is carried by crystallographic point defects in the SEI lattice, like vacancies or interstitials. The diffusion is theorized to happen through knock-off diffusion, in which a lithium ion replaces another lithium ion in the SEI lattice position, rather than moving itself via a direct hopping mechanism [18].

On the other hand, the outer layer, near the SEI/electrolyte interface, is described as a porous and mostly organic film, made of lithium alkyl carbonates (*e.g.* ROLi, ROCO_2Li). Here, the lithium ion transport mechanism is assumed to be the pore diffusion according to the Fick's law [18].

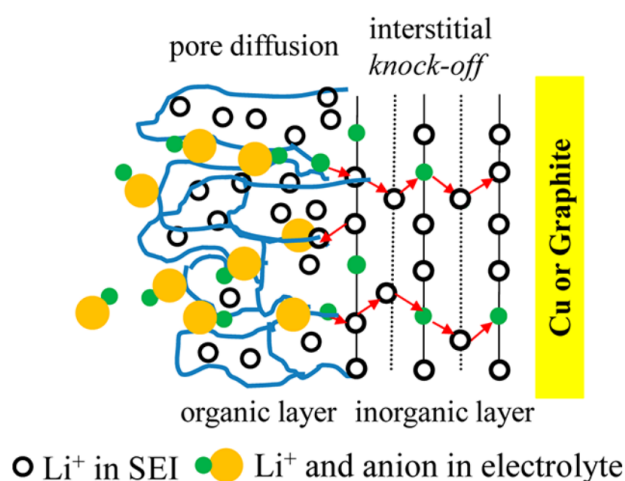


Figure 1.4: Ion diffusion mechanisms in the SEI [18].

1.2.6 Electrolyte Compositions for Rechargeable Lithium Metal Batteries

SEI properties and composition, thus dendrite morphology, are influenced by the electrolyte composition used in the lithium metal battery. Therefore, before reviewing models and experiments to simulate and characterize dendrites, the most common electrolytes for lithium metal batteries are presented. Most of the electrolyte compositions are based on a nonaqueous solution of two or more solvents mixed with one or more lithium salts [19].

Liquid Electrolytes

Carbonates-based solvents are classically used in commercial lithium ion batteries [7], and attracted the main research attention throughout the history of lithium batteries [19]. They were adopted firstly for their capacity to dissolve lithium salts, as well as for their electrochemical stability window. The first candidate was propylene carbonate (PC), due to its high dielectric constant and stability. Nevertheless, it causes capacity fading and poor cyclability (Coulombic efficiency $<85\%$ [19]) due to a continuous reactivity with lithium metal, which sparked the research on alternative solvents. Ethylene carbonate (EC) rapidly established as an electrolyte co-solvent thanks to its comparable viscosity, higher dielectric constant and its ability to form a stabler SEI layer on the graphite electrode [19]. Other co-solvents like dimethyl carbonate (DMC), diethyl carbonate (DEC) and ethyl methyl carbonate (EMC) are usually employed for their low viscosity and melting point. Thus, electrolytes based on a mixture of EC and other carbonates became the most diffused electrolyte solvents in commercial lithium ion batteries, but they are not ideal for lithium metal cells [7], due to the inadequate properties of the SEI that they formed. The SEI that is formed with this category of solvents are mainly composed of lithium alkyl carbonates (ROCO_2Li) in the outer layer and Li_2CO_3 and Li_2O in the inner layer [7]. To improve the properties of the SEI, additives like vinylene carbonate (VC) and fluoroethylene carbonate (FEC) are usually used [20] [21], since they are able to form a more compact and stable SEI with the formation of LiF domains.

Alternatively to the carbonates-based solvents, ethers were studied since the 80s [19]. They were preferred for the improved reversibility of lithium electrodes (Coulombic efficiency $>98\%$ [7]) compared to carbonates electrolytes. This has been attributed to the formation of oligomers of polydioxolane in the SEI, which provide good flexibility and strong binding affinity to the lithium metal surface [22].

Nevertheless they were ruled out for lithium ion commercial application due to their low anodic decomposition voltage (<4 V vs lithium) and high flammability [19]. These electrolyte compositions came back into the spotlight with the development of lithium-sulfur batteries, with the low potential sulfur cathode being less restrictive in terms of anodic stability [7] [9].

Concerning the lithium salt, the most used salt in carbonates-based electrolytes is lithium hexafluorophosphate (LiPF_6) for its good ionic conductivity and large electrochemical stability window, while lithium bis(trifluoromethanesulfonyl)imide (LiTFSI) is often used in ethers-based electrolytes such as in lithium-sulfur cells [19].

Solid State Electrolytes

Solid state electrolytes (SSE) are becoming an important alternative to mechanically prevent dendrite growth. Solid electrolytes mainly fall into two categories: inorganic ceramic electrolytes and solid polymer electrolytes. In addition to the ideal properties of all electrolytes, an ideal solid electrolyte should have high mechanical resistance to prevent dendrites penetration and good contact with electrodes surface.

The first attempts to include solid state electrolytes in batteries were in the 60s, when β -alumina was used in the development of high temperature sodium-sulfur batteries [23]. The discovery of new inorganic ceramic electrolytes continued in the 60s and 70s [24], while the discovery in 1973 of ionic transport in a solid polymer material based on poly(ethylene oxide) (PEO) [25], opened the possibility of using solid polymer electrolytes in lithium batteries, as demonstrated by Armand in 1978 [4].

In the first phase of their development, SSEs were limited to high temperature applications, nevertheless, concerns over the safety of lithium ion batteries motivated the research to use them at ambient temperature [24]. Their use in lithium batteries started in the late 80s, with the discovery of lithium ion conduction in a PEO-based system [24]. In the 90s, inorganic solid state electrolytes have been also used in the lithium ion batteries research, like lithium phosphorus oxynitride (LiPON) [26]. Since the 2000s, solid electrolytes have been used in emerging lithium batteries chemistries, involving lithium metal electrodes, such as lithium-air batteries, lithium-sulfur batteries and lithium-bromine batteries [24]; and PEO-based electrolytes raised the attention of the battery community. Indeed, many papers

cited in the next chapter, Literature Review, involve studies on PEO-based solid electrolytes.

Finally, solid state batteries containing lithium metal as negative electrode, PEO-based electrolyte operating at 60-80°C and LiFePO_4 as positive electrode have been successfully launched onto the market as lithium metal polymer (LMP[®]) batteries by the Bolloré Group and its subsidiary Blue Solutions over the past decade, and there were successfully implemented in automotive applications in 2011 thanks to the car sharing project called Bluecar [27].

Literature Review

In this chapter, literature about modeling and characterization of lithium metal negative electrodes is presented. Different categories of models are presented to understand their strengths and weaknesses and to see how the proposed model is established compared to literature. The experiments that are presented in this chapter either discovered useful insights on dendrites and SEI, or are the foundation for the experiments performed in this work (chapter 5).

2.1 Modeling Lithium Metal

Various models have been proposed to simulate lithium plating during the past decades. They can be divided into two main families: discrete models and continuum ones. The second family can be further divided into multi-domain continuum models and phase-field continuum models. In multi-domain continuum models, interfaces between domains (usually composed of a lithium metal electrode and an electrolyte) are considered to be infinitely sharp [28], therefore, properties are discontinuous at the interface, and the multi-domain structure is described by the position of the interfacial boundaries. Thus, for each domain, a set of differential equations is solved along with their boundary conditions. On the other hand, phase-field continuum models adopt a diffuse-interface approach, in which the interface evolution is described by means of a set of phase-field variables that are continuous in time and across the neighbor of the diffuse interface, as shown in Fig. 2.1.

2.1.1 Discrete Models

Discrete models study plating and stripping of lithium by using a system composed by lattice cells, where the single cell does not correspond to a single atom of lithium but to a number of atoms. Kinetic Monte Carlo (KMC) is a statistical technique, often used in this family of models [29] [30], which is useful to study the change in morphology during deposition or dissolution. In 1993, Trigueros *et al.* [31] studied diffusion-controlled electrodeposition of zinc by using Monte Carlo simulation, from

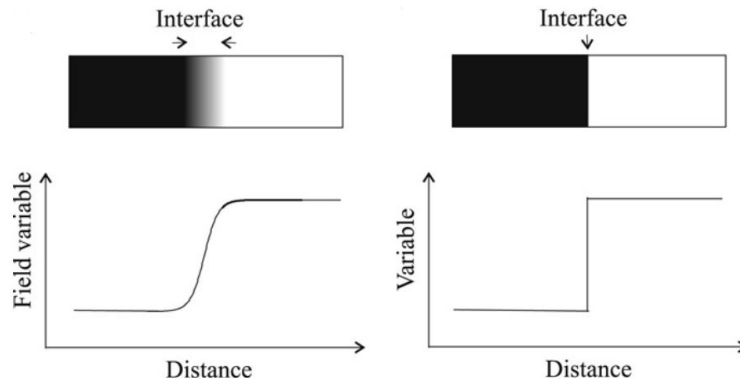


Figure 2.1: Difference between diffuse and sharp interfaces. On the left: diffuse interface, where properties evolve continuously between their equilibrium values in the neighbor of the interface. On the right: sharp interface, where properties are discontinuous at the interface [28].

which they obtained fractal patterns that represent the growth of zinc dendrites. In a theoretical paper from 2005, Guo *et al.* [32] linked electrodeposition and structures' morphology by specifying the relative probability of attachment of the metal on the substrate or on the metal itself.

Later on, in 2019, Tewari and Mukherjee [29] used a two dimensional lattice Kinetic Monte Carlo model to simulate plating and stripping of lithium ions on a lithium metal electrode surface during the charging and discharging process. In order to do so, they defined all the possible events that can occur during the charging and the discharging process, such as:

- Diffusion of the metal ion in the liquid electrolyte
- Electrochemical reduction (resp. oxidation) of the metal ion at the interface between the electrode and the electrolyte while discharging (resp. charging)
- Diffusion of the metal atom at the surface

Different probabilities were associated with each of the considered events, which were used as inputs for the Kinetic Monte Carlo model. By changing the probabilities of each event, different morphologies were obtained during charging (Fig. 2.2) and during discharging (Fig. 2.3), thus, highlighting the dependence of the morphology on the reaction rate (probability of reduction or oxidation), ion diffusion (probability of diffusion in the electrolyte) and surface diffusion (probability of surface diffusion).

During charging (Fig. 2.2), a uniform deposition is obtained when the ion diffusion in the electrolyte is high and the reaction rate is low. Going down on the vertical side of the triangle, reaction rate remains low (reaction limited region), but the diffusion in the electrolyte decreases while the surface diffusion increases leading to non-uniform deposition (whiskers type heterogeneities). On the contrary, the diffusion limited region is defined on the horizontal side of the triangle, where the ion diffusion is low. Here, whiskers or needle-like dendrites are formed, depending on the ratio between the probability of reduction and the probability of surface diffusion. It has to be noticed that throughout the literature, whiskers and needle-like dendrites are synonyms [33], while in this work a slight distinction is made. On the diagonal lines (mixed controlled region), where each of the three probabilities is not negligible, mossy-like and tree-like dendrites (called simply dendrite in the figure) are formed.

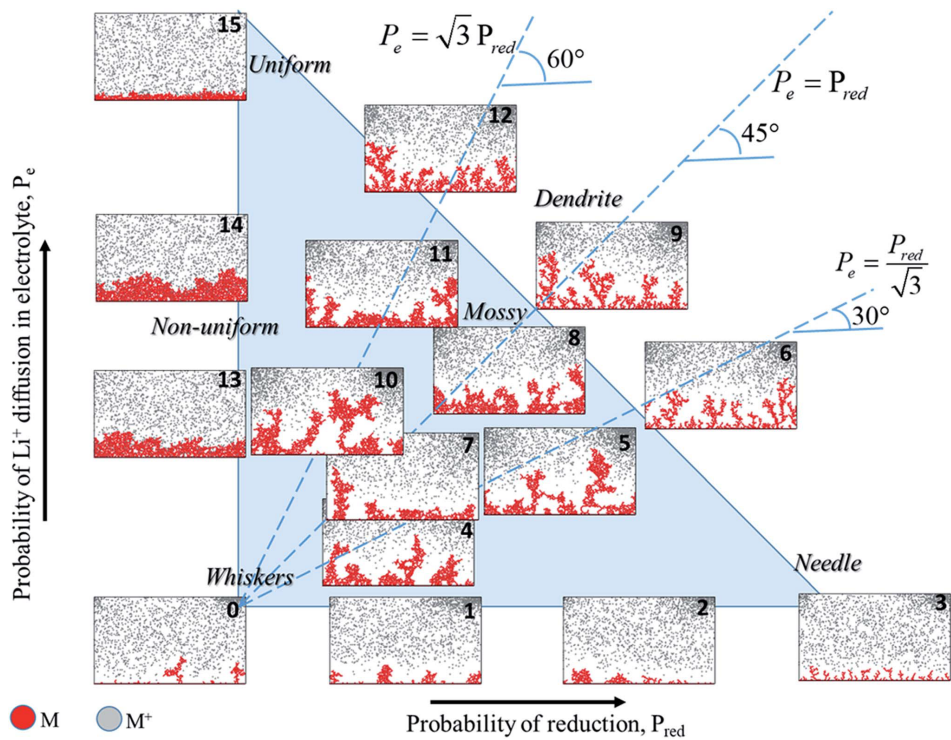


Figure 2.2: Deposition morphologies during charging, obtained through Tewari and Mukherjee's model [29].

While discharging (Fig. 2.3), it is possible to spot the conditions in which dead lithium (in blue) is formed by changing the three probabilities. They concluded that the surface diffusion is a key parameter in reducing the amount of dead lithium formed.

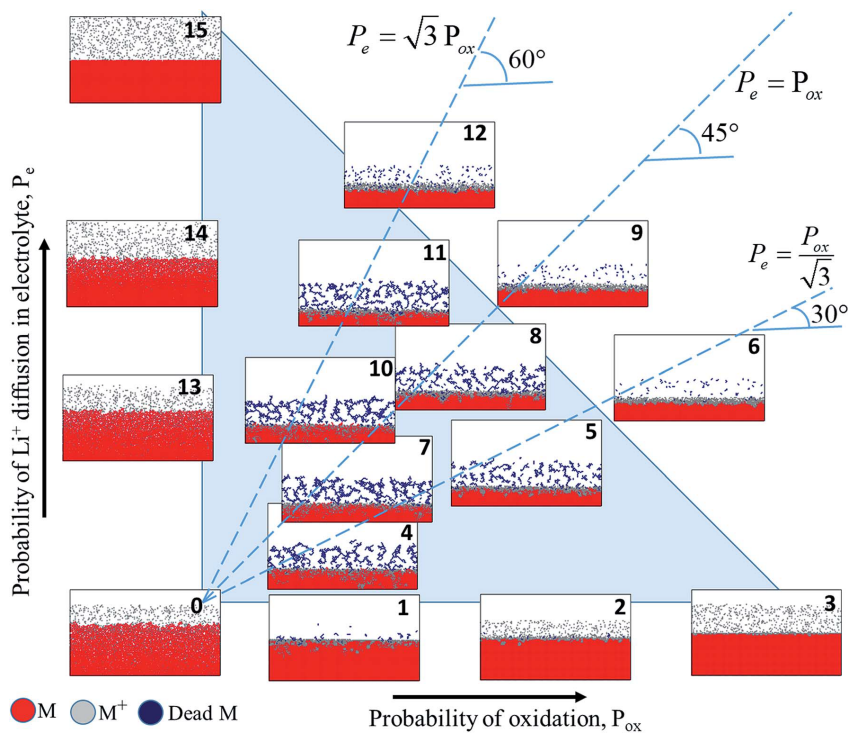


Figure 2.3: Deposition morphologies during discharging, obtained through Tewari and Mukherjee’s model [29].

Hao *et al.* [30] expanded the use of the kinetic Monte Carlo algorithm to explore and compare electrodeposition across different metallic electrodes, in particular, lithium, sodium, magnesium and aluminum, while, Aryanfar *et al.* [34] used the Monte Carlo calculation to find strategies to inhibit dendrite growth.

To conclude, the main benefits of using discrete models is the possibility to simulate complex morphologies with low computing power and without encountering boundary-related problems that are further explored in the multi-domain continuum models section. On the contrary, the biggest difficulty is to link the probabilities used for the KMC model, to parameters that can be found via experiments. Moreover, the presence of the SEI has always been neglected in the discrete models that simulate lithium deposition on a lithium metal electrode.

As pointed out in the work of Tewari *et al.* [29], KMC can only resolve small length and time scales in the case of electrochemical plating and stripping modeling. Thus, to bypass these limitations multi paradigm studies should be carried out by coupling KMC and continuum scale transport. Indeed, a continuum model could

constitute an important bridge between the experiments and the discrete model, in order to have a stronger physical connection between the probabilities of the KMC and the experimental parameters.

2.1.2 Phase-Field Continuum Models

Phase-field models have been applied to a wide array of phenomena, from solidification to recrystallization and grain growth. Phase-field modeling, which is based on the theory of irreversible thermodynamics, is well suited for simulating time-dependent evolving morphologies, which are harder to be modeled with multi-domain continuum models (sharp-interface model).

In the simplest phase-field model, two phases are defined. The first step to implement a phase-field model is to define a field variable between 0 and 1. The field variable corresponds to one of the two phases at the two extremes, and it is between 0 and 1 at the interface. Then, a total free energy of the system is computed by integrating over the volume of the domain a function of the gradient of the phase-field variable, which is non-zero only in the interfacial region, and the free energy density, which is the function of the field variable. The free energy density has two local minima corresponding to the two phases and an energy barrier to be crossed during the reactions. In order to describe the interface of a system, the total free energy is minimized.

The first attempt to use the phase-field method to model the kinetics of electrodeposition was made by Guyer *et al.* [35] in their 1D model. Later, Okajima *et al.* [20] simulated a 2D electrodeposition of copper by combining a Cahn-Hilliard equation and a Butler-Volmer kinetics. In 2014, Ely *et al.* [36] demonstrated that starting from heterogeneous nuclei of lithium, the rate of electrodeposition at the tip of the nuclei was higher than the rate related to the average overpotential, thus favoring needle-like dendrites. Later, Chen *et al.* [37], argued that the previous models, by assuming a linear reaction kinetics, lost thermodynamic consistency under high charging voltage. Thus, they proposed a phase-field model that evolves non-linearly with the variation of the electrochemical overpotential. Therefore, they managed to correlate the dendrites morphology with the applied voltage and the initial surface morphology.

In 2018, Yurkiv *et al.* [33] extended the previous works by adding the effect of SEI, of the elastic deformation of the solid electrode during lithium deposition,

and of anisotropic diffusion of lithium ions in the electrolyte. Yurkiv's model [33] was based on a 2D representation of the cell. The two phases were composed of a solid lithium electrode and the electrolyte, in which lithium ions diffuse, while the total free energy of the system was computed as follows:

$$F(\xi, c, \phi, u) = \int_V \left[f_{ch}(\xi, c) + \frac{1}{2} \kappa_\xi (\nabla \xi)^2 + f_{elch}(\xi, c, \phi) + f_{els}(\xi, u) + f_{ns}(c) \right] dV \quad (2.1)$$

In this model, the total free energy depends on the phase-field variable ξ , on the mole fraction of the lithium ion, c , the electric potential, ϕ and the displacement field, u . Inside the integral, the first term represents the chemical free energy density, f_{ch} , and the second is the gradient of the phase-field variable, $(\nabla \xi)^2$, multiplied by the surface energy, κ_ξ . The other terms are the electrochemical energy density, f_{elch} , which is computed from the local charge density, the elastic energy density, f_{els} , which arises from the solid phase deformation during the electrodeposition, and the noise term applied in the vicinity of the solid/liquid interface, f_{ns} , which tries to mimic the random, according to Yurkiv *et al.*, diffusion of lithium ions through the SEI layer.

Mass and charge transports were modeled with a system of governing equations, which is usually called the Nernst-Planck-Poisson model, often used in multi-domain continuum models as well. The main difference between the two families of the continuum model was the phase transport equation, which was assumed to be a non-conserved quantity and described by the Allen-Cahn equation in this paper.

In Fig. 2.4, Yurkiv *et al.* [33] compared their results to the one of Chen *et al.* [37], by using the same assumptions in terms of parameters and geometry. Phase-field variable (first row), lithium ion concentration (second row) and electric potential (third row) distributions are shown. According to this model, the number of branches that grow from the initial nucleus are solely due to the crystallographic orientation of lithium (body centered cubic). Indeed, four equal branches are expected to form during electrodeposition, but in this case only three of them form due to the boundary conditions. On the other hand, the number of branches that grow from the main three branches is a function of the applied overpotential, with fiber-like pattern (needle-like) at low applied overpotential and fully dendritic behavior at high overpotential.

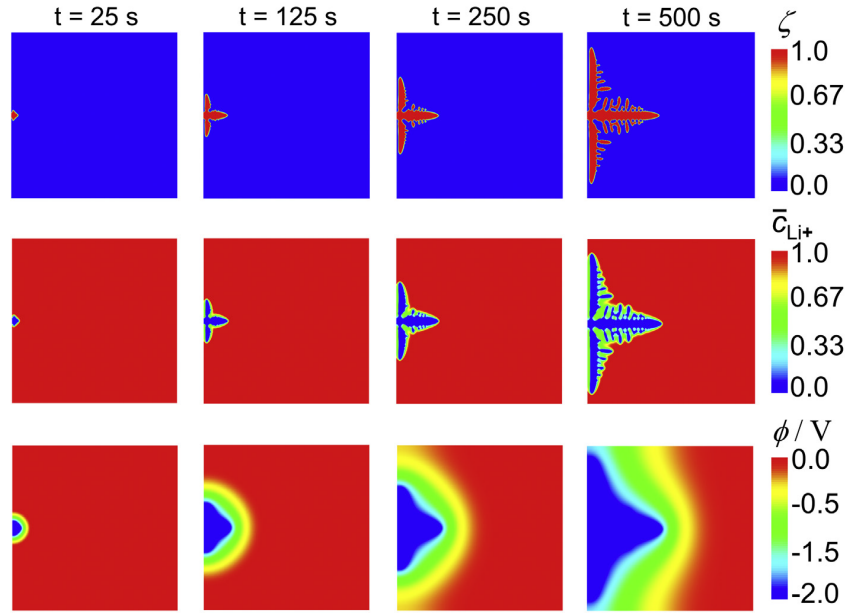
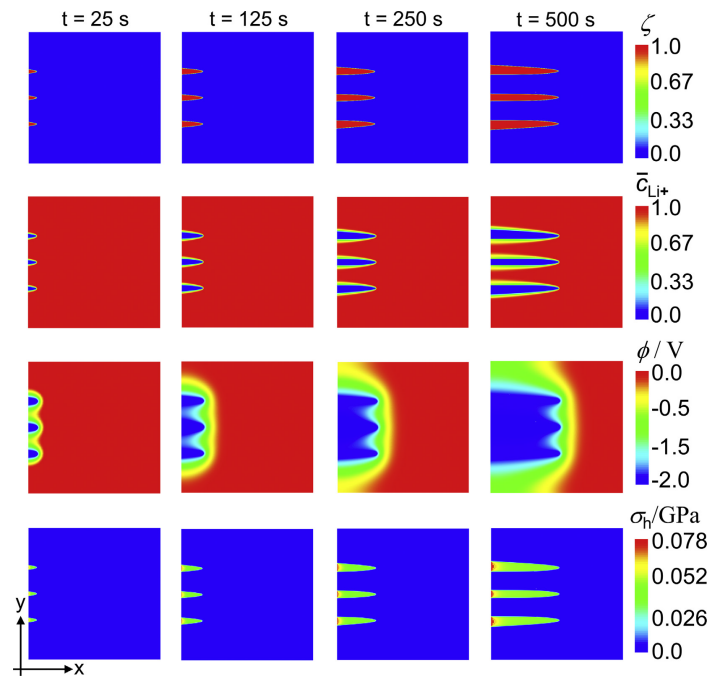
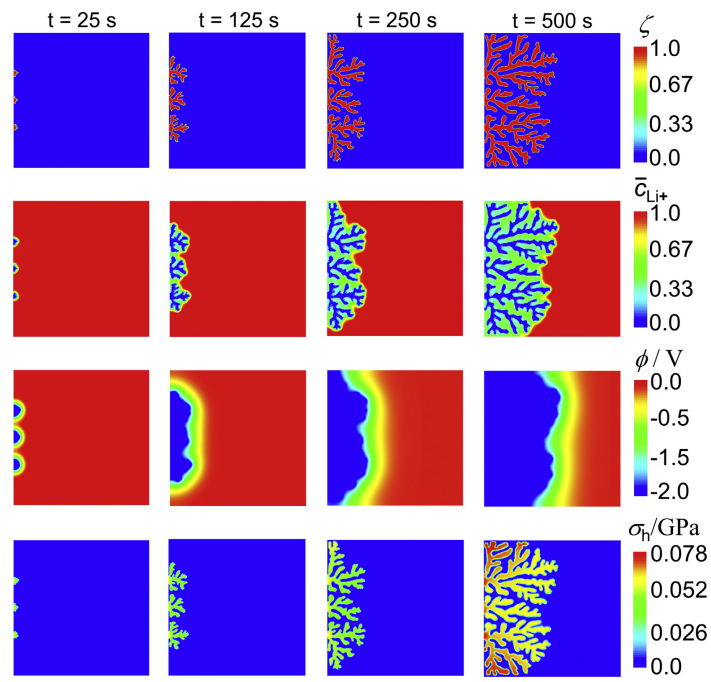


Figure 2.4: Results of phase-field model: Phase field (first row), lithium ion concentration (second row) and electric potential (third row) [33].

On the other hand, Yurkiv *et al.* [33] were able to obtain lithium filament structures and then tree-like structures (called bush-like in the paper) by applying the same overpotential. Filament structure, presented in Fig. 2.5a, were explained by assuming an anisotropic electrolyte solution, which is an addition with respect to the isotropic electrolyte used in the work of Chen *et al.* [37]. Thus, the consequent anisotropic diffusion of the lithium ions in the electrolyte led to a main direction of growth, therefore to the filament or fiber-like structures. By adding the term that takes into account the contribution of the elastic energy density in Eq. 2.1, Yurkiv *et al.* were able to analyze the hydrostatic stress evolution during the growth of the filaments, as shown in the last row of Fig. 2.5a. The highest stress values were found in the root of the filaments, which was theorized by Kushima *et al.* [38]. Furthermore, the lithium concentration profile suggested that electrodeposition occurs on the sides of the filaments with enhancement at the root, which is again consistent with the root growth theory of Kushima *et al.*. Fig. 2.5b shows a tree-like morphology, which was the result of random diffusion of lithium ions through the anisotropic SEI grain boundaries according to Yurkiv *et al.*. This phenomenon was modeled with a term that was added in Eq. 2.1 as a noise, f_{ns} .



(a)



(b)

Figure 2.5: Results of phase-field model: Phase field (first row), lithium ion concentration (second row), electric potential (third row) and hydrostatic stress (fourth row). a) Filament growth. b) Bush-like morphology [33].

To conclude, phase-field models have the remarkable advantage, compared to multi-domain models, to be capable of simulating complex morphologies, as shown in Fig. 2.4 and 2.5. Such complexity is impossible to be achieved with the models that are presented in the next section. Therefore, they are closer to the morphologies that are experimentally observed during lithium deposition.

The same feature that constitutes the phase-field models strength, the phase-field variable, makes them also further from reality, since in real cells the interface between the electrolyte and the electrode is sharp and not diffuse. Furthermore, the geometry of the simulation strongly depends on theoretical parameters, like the mode of the anisotropy, which is assumed to be equal to 4, due to the lithium metal crystallography; and the function (usually with a double-well shape), which is used to describe the phase-field variable and consequently its barrier height. These parameters were assumed arbitrarily in the work of Chen *et al.* [37] and Yurkiv *et al.* [33]. The strong dependency on theoretical parameters can constitute a problem while aiming at validating the model with experimental parameters. For example, phase-field models typically require thermodynamic quantities inside the interfaces that are often impossible to obtain experimentally. On the contrary, physically measurable quantities like surface energy are only indirectly related to the input parameters of the model.

Moreover, all the phase-field simulations were made by applying a voltage difference on the geometry and not an applied current, like in many experiments. The profile of lithium concentration across the electrolyte is not consistent with the one found in the multi-domain models. In the case of phase-field models, the concentration is uniform for most of the electrolyte domain and drops sharply close to the interface (second row in Fig. 2.4 and 2.5) while in the multi-domains model the concentration gradient is distributed across the whole electrolyte domain, with a higher slope close to the interface [39] [40].

Finally, the biggest weakness of these models is the complexity of adding the SEI to the simulation, which is assumed to be crucial for dendrites formation and growth. The best attempt to introduce the SEI in a phase-field model was made by Yurkiv *et al.* [33], but still in a simplified way by adding a noise to the total free energy of the system, which is far from modeling the effect of the electrochemical and mechanical properties of the SEI on the dendrites morphology. As an alternative to these models, multi-domain continuum models are described in the next section.

2.1.3 Multi-Domain Continuum Models

Multi-domain continuum models represent the largest category of models of dendrite evolution in the literature. Barton and Bockris [41] proposed the first comprehensive model to study dendrites growth in 1962. Their work about dendritic deposition on a silver metal substrate assumed that the dendrites growth occurs because the plating on its tip is governed by spherical diffusion which is higher than the linear diffusion that happens anywhere else on the electrode surface. The effect of surface energy was incorporated to prevent the infinite thinning of the dendrites. The mechanism of growth proposed by Barton and Bockris was called surface-tension mitigated growth [41]. Diggle *et al.* (1969) [42] expanded the previous theory, by using a Butler-Volmer kinetic expression, which allowed for higher overpotentials to be described by the model.

Chazalviel Group

A different approach was used by Chazalviel *et al.* [39] [43] in their electromigration-limited model. According to this theory, at high currents and/or potentials, the lack of electroneutrality close to the electrode affects the morphology of deposited lithium, promoting the dendrites growth. Therefore, dendrites growth depends on the concentration gradient across the electrolyte, which was defined as follows:

$$\frac{\partial c}{\partial x} = \frac{Jt_a}{eD} \quad (2.2)$$

where c [mol.m⁻³] is the ionic concentration, x [m] the direction perpendicular to the two electrode surfaces, J [A.m⁻²] the current density, D [m².s⁻¹] the diffusion coefficient of lithium in the electrolyte, e [C] the electronic charge and t_a [-] the anionic transport number.

According to Chazalviel, for a symmetrical cell, if the above-defined concentration gradient is smaller than the ratio between the initial concentration and the semi-distance between the two electrodes, after a transient regime, the voltage profile tends to a stationary value and no dendritic behavior is expected. On the other hand, if the concentration gradient is higher than the above mentioned ratio, the lithium ion concentration drops to zero at the electrode surface (lithium depletion) after a time called Sand's time, τ , defined as follows:

$$\tau = \pi D \left(\frac{c_0 e}{2Jt_a} \right)^2 \quad (2.3)$$

At the Sand's time, the potential of the cell diverges, and the electroneutrality in the electrolyte is locally not observed anymore at the electrode interface, leading to an excess of negative charges at the negative electrode. This situation creates instabilities, like dendrites, which grow to compensate for the increase of the space charge. The model predicted that dendrites would form only at current densities higher than the limiting current density J^* , which was defined as follows:

$$J^* = \frac{2ec_0D}{t_aL} \quad (2.4)$$

The assumption that dendrites form only above the limiting current density, has been widely refuted by the experiments [11] [44], which were also performed by Chazalviel's group [45]. Therefore, they extended the model to low currents by adding inhomogeneity in the salt concentration around the surface, which is responsible for an inhomogeneous lithium flux, and ultimately for dendrites growth. Nevertheless, the extended model was able to predict only tip-induced nucleation, while the experiments suggested that at lower current density, root-induced and multidirectional-induced nucleation mechanisms are present, as shown in the work of Bai *et al.* [11].

Newman Group

Between 2003 and 2005, Monroe and Newman studied how the surface morphology and the mechanical properties of the electrode and the electrolyte impact dendrites growth [40] [46] [47]. In this section, a quick description of their work is presented, while a detailed analysis of their theory is presented in section 3.2.6.

In 2003, they used the method developed by Barton and Bockris [41], to study the growth of one needle-like dendrite in a binary electrolyte. Like in the work of Barton and Bockris, the surface energy and the tip radius influences the overpotential at the lithium/electrolyte interface. Like Diggle *et al.* [42], they derived a Butler-Volmer equation that takes into account the effect of the surface curvature on the reaction rate. From the simulations, they concluded that, differently from Chazalviel, the cell could fail already if run above 75% of the limiting current density defined by Chazalviel (Eq. 2.4), thus placing a much more conservative limit on the charge rate, with respect to Chazalviel.

In their following work [46], they extended the previous models [40] [41], in which surface tension was the only factor that opposes the instability of the surface, and consequently dendrite formation. On the contrary, in this work, the kinetic model, thus the overpotential at the interface, was modified to take into account the effects of the elastic deformation, the viscous stress and the external pressure.

In 2005 [47], Monroe and Newman applied their extended kinetic model to perform a linear stability analysis of a small sinusoidal protrusion on the lithium/electrolyte interface, representing a dendrite nucleation site, to determine whether the amplitude of the perturbation would grow. In order to quantify the effects of the mechanical forces on the kinetics, the impact of stress distribution in the system was required. In this paper, both the lithium electrode and the solid electrolyte (PEO-based) were considered as isotropic linear-elastic materials, which could be described by their shear moduli and Poisson's ratios. From the stability analysis, Monroe and Newman found that an electrolyte with a shear module 1.8 times the one of the lithium metal could theoretically prevent the protrusion from growing. On the other hand, surface forces, which were central in Barton and Bockris work [41], have a negligible impact on the dendrite propagation.

However, later on, experiments showed that lithium dendrites could penetrate in the solid electrolyte [48], even if it has a larger shear stress than the one predicted by Monroe and Newman. The work of Foroozan *et al.* [48] highlighted that other parameters like defects, grain boundaries and heterogeneities were important for dendrites growth but neglected in the Monroe and Newman theory. Moreover, the mechanical strength of the lithium dendrite was shown to be much higher than the one of the bulk lithium, due to the bigger effect of the SEI layer on the small cross section, leading to an easier penetration through a stiff solid electrolyte [49].

In 2012, Ferrese and Newman built a 2D model of a full lithium metal cell including a LiCoO_2 positive composite electrode in order to study the change in morphology of the negative lithium metal electrode during cycling [50]. In 2014, the model was expanded to include the effect of a stiff separator on the negative electrode deformation [51], starting from Monroe and Newman theory developed ten years earlier [46], with the geometry reported in Fig. 2.6.

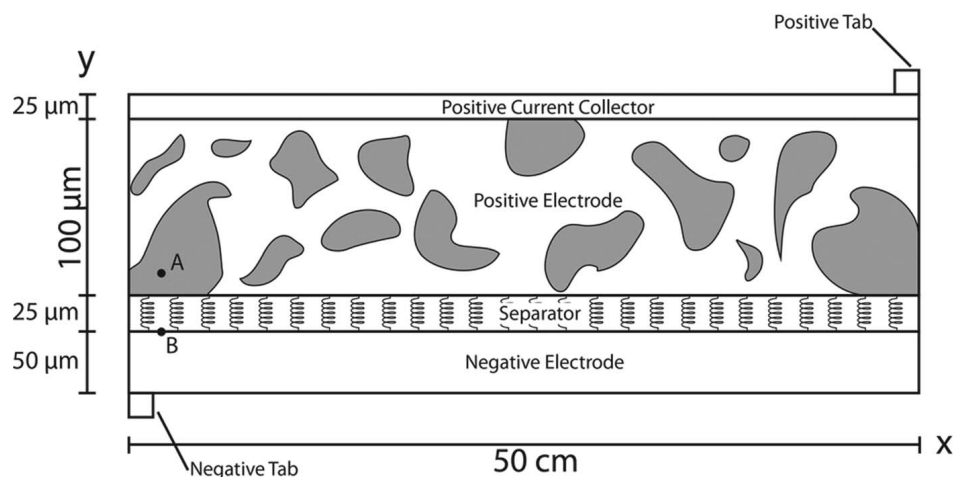


Figure 2.6: 2D geometry used by Ferrese and Newman, consisting of a negative current collector, a lithium metal negative electrode, a polymer separator, a composite positive electrode, and an aluminum positive current collector [51].

Among the factors that influence the lithium metal electrode deformation, the cell geometry, the slope of the open circuit potential of the positive electrode, the applied current density and the mechanical properties of the separator were discussed. It was found that a stiff separator could cause elastic and plastic deformation of the lithium negative electrode, which could flatten the electrode surface. The lithium metal electrode was considered to be an elastic solid, following Hooke's law, which behaves plastically if the stress passes a certain threshold (von Mises yield criterion). On the other hand, the separator was modeled as an array of ideal springs in parallel (Fig. 2.6), which can only deform elastically with a null Poisson's ratio.

Ferrese and Newman were able to separate the mechanical effect of the separator by modifying the reaction kinetics (according to Newman and Monroe theory [46]) and the mechanical effect of the separator that produces plastic deformation in the electrode. When comparing the magnitude of the two effects on flattening the negative electrode, the plastic deformation was found to have a much larger role, as reported in Fig. 2.7, where three different simulations are reported. In all the simulations, the cell underwent the same current density and depth of discharge. The 'Pliable Separator Butler-Volmer Kinetics' line took into account a liquid electrolyte with no mechanical effect on the lithium electrode and a classic Butler-Volmer description of the kinetics. The 'Butler-Volmer Kinetics' and 'Pressure-Modified Kinetics' lines included elastic and plastic deformations due to the stiff separator. The difference among them were due to the fact that the 'Pressure-Modified Kinetics' had a modified kinetics according to Newman and Monroe theory [46], thus confirming that the biggest factor to flatten the lithium metal surface, at the cell level, was due to the

plastic deformation of the lithium metal itself and not due to the effect that the mechanics has on the kinetics.

These models have established the foundation for the simulation of dendrites nucleation and growth, nevertheless, contribution of the SEI was still missing.

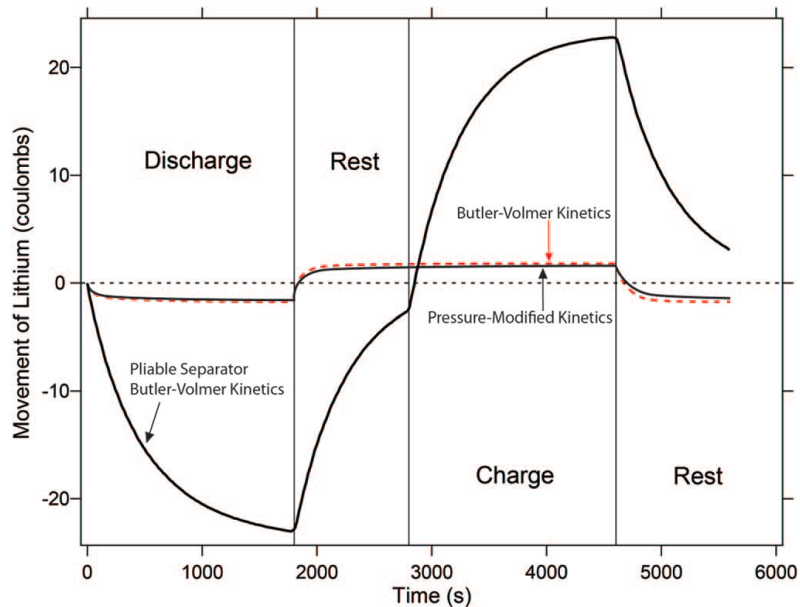


Figure 2.7: Movement of lithium along the lithium/separator interface during one cycle at a rate of C/5, with different mechanical phenomena considered [51].

Yoon group

More recently, in 2018, Yoon *et al.* [16] studied lithium deposition and stripping in a transient simulation, in which they added a non-reactive SEI layer on the lithium metal electrode, without including any mechanical effect of the SEI on the lithium deposition. To model charge and mass transport in the electrolyte, they used a Nernst-Planck equation with the assumption of electroneutrality. The kinetics was modeled by using the Butler-Volmer equation. Like phase-field models, they applied a voltage difference and not a current density as input for the simulation, thus preventing the comparison with the limiting current density theorized by Chazalviel.

Despite this, Fig. 2.8 shows that starting from the same geometrical defect on the lithium electrode surface, the concentration of lithium drops to zero at the interface (lithium depletion) in the simulation with higher applied voltage (0.7 V). Thus the limit theorized by Chazalviel is passed, and deposition of lithium happens more vertically, with the formation of lithium branches and tree-like dendrites. According

to Chazalviel [39], electroneutrality is violated in these conditions, but in the work of Yoon *et al.* this aspect is not mentioned at all. On the contrary, the concentration of lithium is higher than zero at the interface for the lower applied voltage (0.4 V), and the deposition of lithium forms mossy-like dendrites. In the simulations presented in Fig. 2.8, the SEI was not considered.

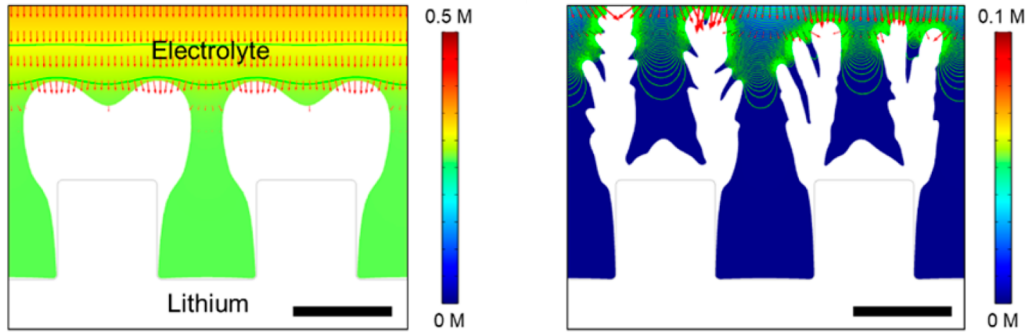


Figure 2.8: Evolution of lithium deposition at different deposition rates, with lithium concentration in color [M]. Left: slow deposition rate (at 0.4 V). Right: fast deposition rate (at 0.7 V) [16].

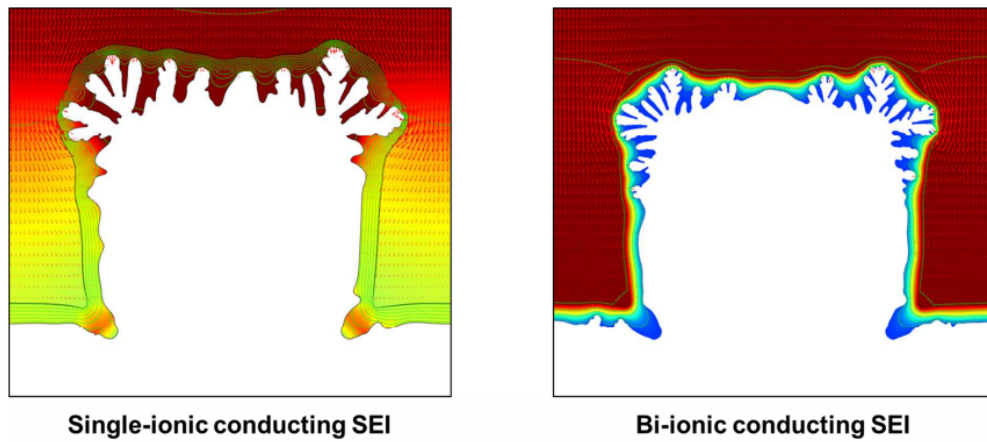


Figure 2.9: Evolution of lithium deposition with the addition of the SEI. Left: single-ionic conducting SEI. Right: bi-ionic conducting SEI [16].

On the other hand, the results with the addition of the SEI are presented in Fig. 2.9. On the right, the SEI was introduced as an additional layer with a thickness of 200 nm and a lithium ion diffusion coefficient 100 times lower than the one assumed for the electrolyte (bi-ionic conducting SEI). No side reaction that could lead to SEI formation was considered in this study. According to Yoon *et al.*,

lithium deposition was much more dendritic with the addition of the SEI, due to the lower diffusion coefficient. On the left, the SEI was assumed to be a single-ionic conductor, thus no lithium ion concentration gradient was present within the SEI. Nevertheless, the branching growth was still observed, due to the additional ohmic drop introduced by the SEI.

Liu and Lu

Differently from the work of Yoon *et al.*, Liu and Lu [15] included in their transient simulation the process of SEI growth and stretching due to the dendrites growth beneath. They modified the Butler-Volmer equation to include the SEI resistance but not its mechanical effect on the deposition kinetics, while the effect of the surface energy was considered too small to affect the kinetics at the geometrical scale of the simulations reported in the paper. No lithium concentration drop was considered within the SEI.

The SEI was modeled with the concept of SEI coverage density, which is explained in detail in section 3.2.2. Like in the work of Yoon *et al.* [16], transport phenomena in the electrolyte were governed by the Nernst-Planck equation under the hypothesis of electroneutrality.

In Fig. 2.10, the results from the simulation are reported. As in the work of Yoon *et al.* [16], the same geometric defect at the electrode surface was selected. But differently from Yoon *et al.*, they applied a current density and not a potential difference on the cell. This allowed them to better highlight the quantity of deposited lithium on the metal electrode. Indeed, in both simulations, a quantity of lithium corresponding to $0.014 \text{ mAh.cm}^{-2}$ was deposited, leading to a more meaningful difference of morphology at the end of the simulation.

Through the simulations, it was noted that the SEI around the defect tip becomes thinner and thinner, allowing a higher lithium deposition rate at the tip. On the contrary, the negative curvature at the base of the defect led to a larger SEI thickness in that area. The authors reported that at higher current densities, the defect grows very quickly into a sharp needle shape. They concluded by saying that a flat initial lithium surface and a uniform SEI layer with low resistance are important to reduce dendrites formation and growth.

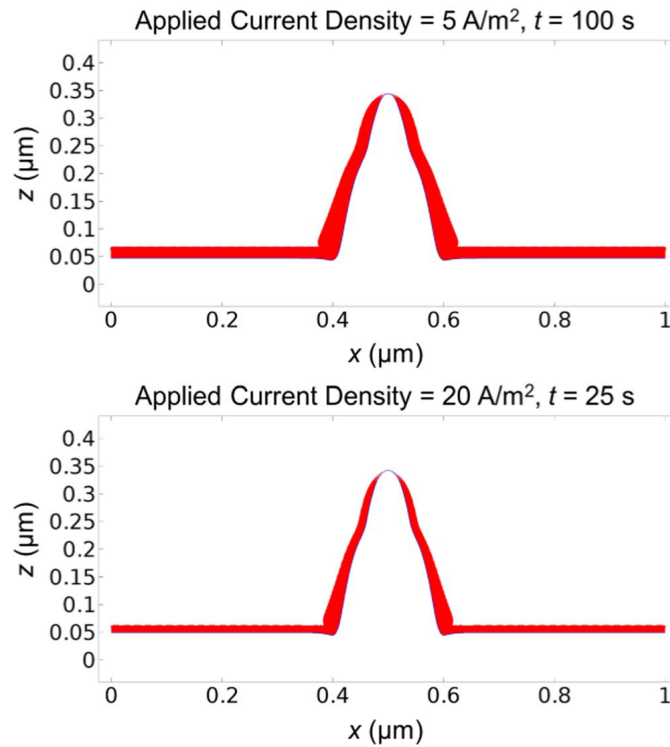


Figure 2.10: Defect evolution due to lithium deposition at different applied current densities (5 A.m⁻² top figure and 20 A.m⁻² bottom), according to Liu and Lu's model [15].

2.1.4 Conclusion on Models in the Literature

To conclude on this literature review, multi-domain continuum models seem to offer more flexibility to simulate the complex phenomena that happen at the lithium electrode surface. Most importantly, they are suitable to introduce the effect of SEI, which is highly regarded as a key component to influence dendrite formation and growth, and to study the effects of its properties on dendrite evolution.

On the other hand, two or more domains, with the relative boundaries and boundary conditions, are needed to be defined. This leads to a reduction of the complexity of the morphology that can be simulated, and the simulations have to be stopped before one of the following phenomena occur:

- Lithium metal is exposed to the electrolyte after cracks in the SEI are formed. If the SEI is modeled as a 2D domain, like in the work of Yoon *et al.* [16], this phenomenon leads to the division of the SEI domain in more domains and new boundaries and boundary conditions have to be defined. On the contrary, Liu

and Lu introduced the concept of SEI coverage density [15], which allowed this phenomenon to be simulated in multi-domain continuum models.

- Dead lithium in the electrolyte. During lithium stripping, lithium can remain electrically or physically isolated in the electrolyte from the bulk electrode. In their work [16], Yoon *et al.* simulated lithium stripping after lithium deposition on an initial geometric defect of the surface. They were able to report a thinning of the necking region (see Fig. 2.11) that eventually leads to isolated lithium in the electrolyte, but they were not able to simulate the detachment of the lithium piece. Indeed, this implies the creation of a new domain, specifically for the single piece of isolated lithium, with its own new boundary conditions.
- Merge of nearby dendrites and pores generation. Yoon *et al.* [16] simulated plating on nearby geometric defects on the lithium surface. Nevertheless, Fig. 2.12, in which the merge of nearby dendrites and the consequent creation of pores is represented, shows an expected shape after continuous deposition and not the results from the model simulation. Indeed, the merge of nearby dendrites implies the same topological problems of dead lithium and cracks in the SEI.

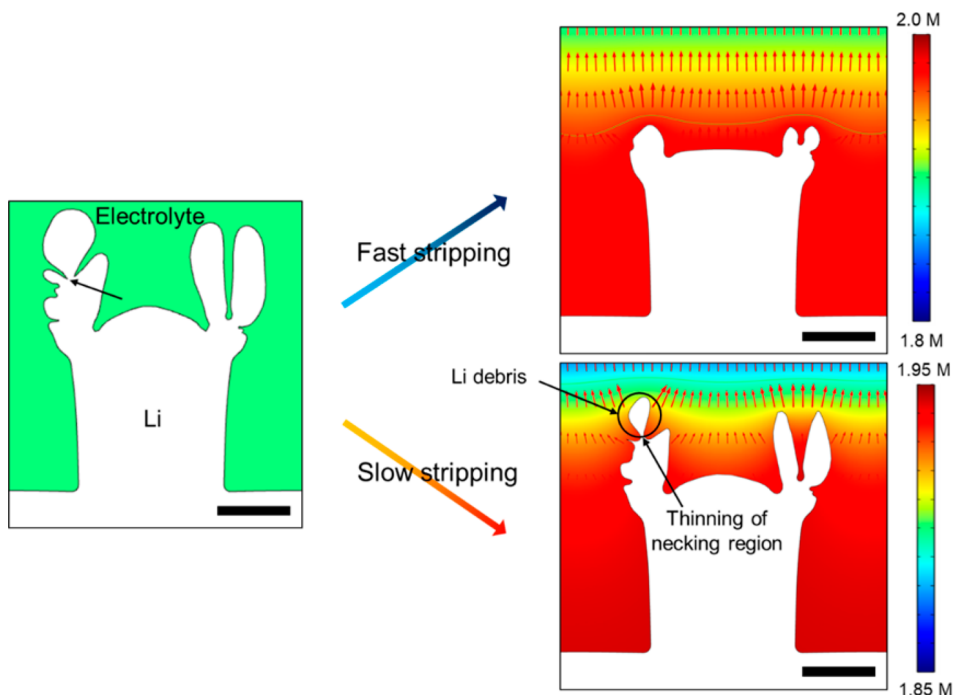


Figure 2.11: Lithium stripping simulations at fast and slow rates from Yoon's model [16].

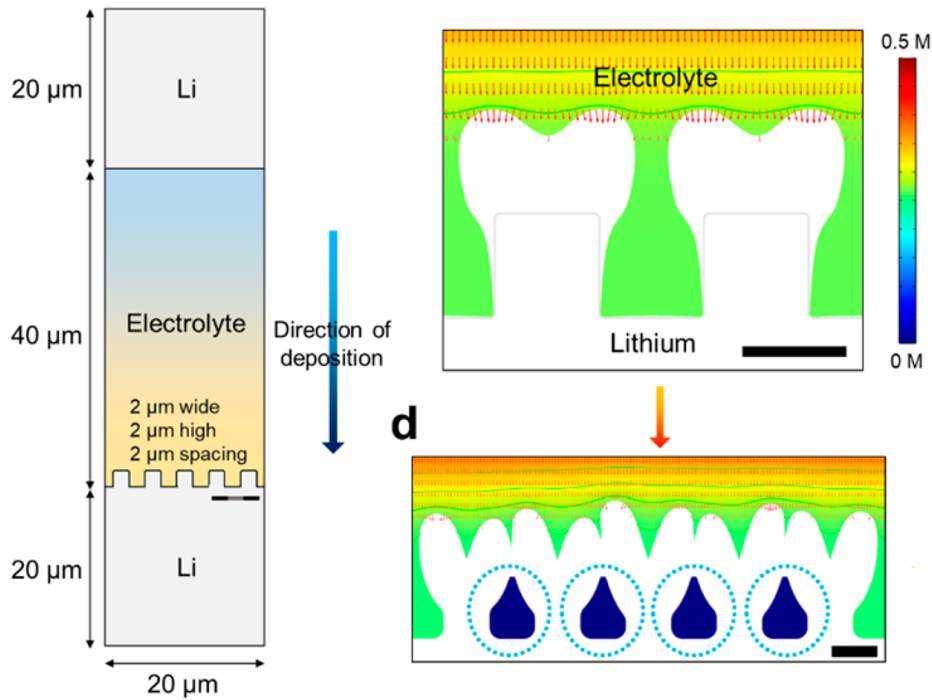


Figure 2.12: Merge of nearby dendrites based on Yoon's model prediction [16].

Despite the numerous attempts, a unifying model that studies the electrochemical and the mechanical (fundamental for root-induced growth [11]) effects of the SEI on the dendrites growth was not present in the literature.

The model that has been developed during this thesis work belongs to the two-domain continuum model category, because this family of models is the most suitable to be integrated with the planned set of experiments, and through literature it has proven itself to be able to better integrate SEI phenomena. It tries to study the dendrites growth under the presence of a reactive SEI [15], whose mechanical and electrochemical properties modify the kinetics of reaction at the lithium metal interface, in a transient simulation.

2.2 Characterization of Lithium Metal and SEI

This section presents a literature review related to the methods that allows the characterization of the lithium metal surface, of dendrites formation and SEI properties. Since used in this thesis work, a particular attention is given to optical microscopy, electrochemical impedance spectroscopy (EIS), X-ray photoelectron spectroscopy (XPS) and atomic force microscopy (AFM), while scanning electron microscopy

(SEM) and transmission electron microscopy (TEM) works are discussed for their contribution to the overall lithium metal research and the insights they provided on dendrites evolution and characterization.

Other techniques, that are not discussed in this work, but that are useful to characterize lithium metal and are often used in the literature, are: nuclear magnetic resonance (NMR) [52] [53], magnetic resonance imaging (MRI) [54], X-ray microscopy/tomography [55] [56] [57] and, Fourier-transform infrared spectroscopy (FTIR) [58].

The section starts with imaging techniques and continues with AFM, which can be used as an imaging technique or to determine surface properties, and ends with experiments to characterize SEI properties.

2.2.1 Optical Microscopy

Optical microscopy has been widely used to characterize lithium metal due to its accessibility and simplicity. It has a lower spatial resolution than SEM and TEM, nevertheless it is capable of capturing electrode surface change and dendrite growth [48]. Different from SEM and TEM, there is not the risk of creating artifacts that influence the results of the experiments, due to the interaction between the electron beam and the sample [48]. With optical microscopy, it is easier to record *in-situ* and *operando* dendrites growth, under operating conditions close to the real cell application, because components and designs do not have to be drastically modified to fulfill the requirements imposed by SEM or TEM. Nevertheless, special cell designs have been invented in order to perform these experiments, and different examples are found in the literature.

The first attempt to use this technique was made at the end of the last century. Among them, in 1998, Brissot *et al.* [44], in the group of Chazalviel, performed *in-situ* optical observation of dendrite growth in a lithium metal symmetric cell using a LiTFSI/PEO polymer electrolyte, *i.e.* the same polymer used in the work of Newman and Monroe [47]. To observe the dendrite evolution, they designed a parallelepipedic, quasi-bidimensional cell, with the dendrites growing on the thin cross-section of the electrodes, which is very far from the geometry used in practical batteries, orders of magnitude lower than the reaction area of real cells. In their experiments, they were able to observe whiskers, mossy-like dendrites and tree-like

dendrites, by changing the magnitude of the current applied to the cell (0.2, 0.7 and 1.3 mA.cm⁻²), shown in Fig. 2.13.

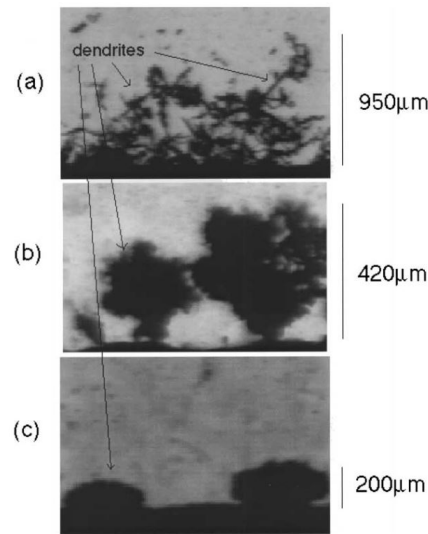


Figure 2.13: Dendrites obtained with optical microscopy by applying different current densities: a) Needle-like dendrites. b) Tree-like dendrites c) Bush-like dendrites [44].

Brissot *et al.* setup was more recently reused by Kong *et al.* [59], which is shown in Fig. 2.14. In their work, they used a lithium metal symmetric cell with LiPF₆/EC:DMC electrolyte, sandwiched between two transparent quartz windows. The distance between the two electrodes was in the order of millimeters, thus the produced dendrites were bigger than the dendrites found via SEM or TEM. Moreover, the absence of a separator impacted dendrite formation compared to the real case scenario.

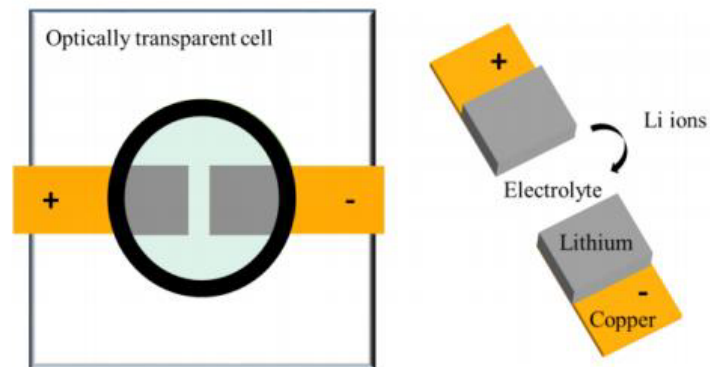


Figure 2.14: Cell design used by Kong *et al.* for *operando* optical microscopy [59].

In 2016, Bai *et al.* [60] showed morphology transition of dendrite growth in a lithium metal symmetric capillary cell, with a thinner middle part, filled with $\text{LiPF}_6/\text{EC}:\text{DMC}$ electrolyte. The geometry of the cell is shown in Fig. 2.15a. By applying a constant current, they found that mossy-like dendrites start to form ((Fig. 2.15c-d), while the salt concentration near the lithium surface starts to decrease, as reported by the increase in the voltage profile (2.15b). After 40 minutes, the voltage diverged, signaling the salt depletion at the electrode surface in agreement with the theory of Chazalviel *et al.* [43], when tree-like dendrites start to form (Fig. 2.15e-g).

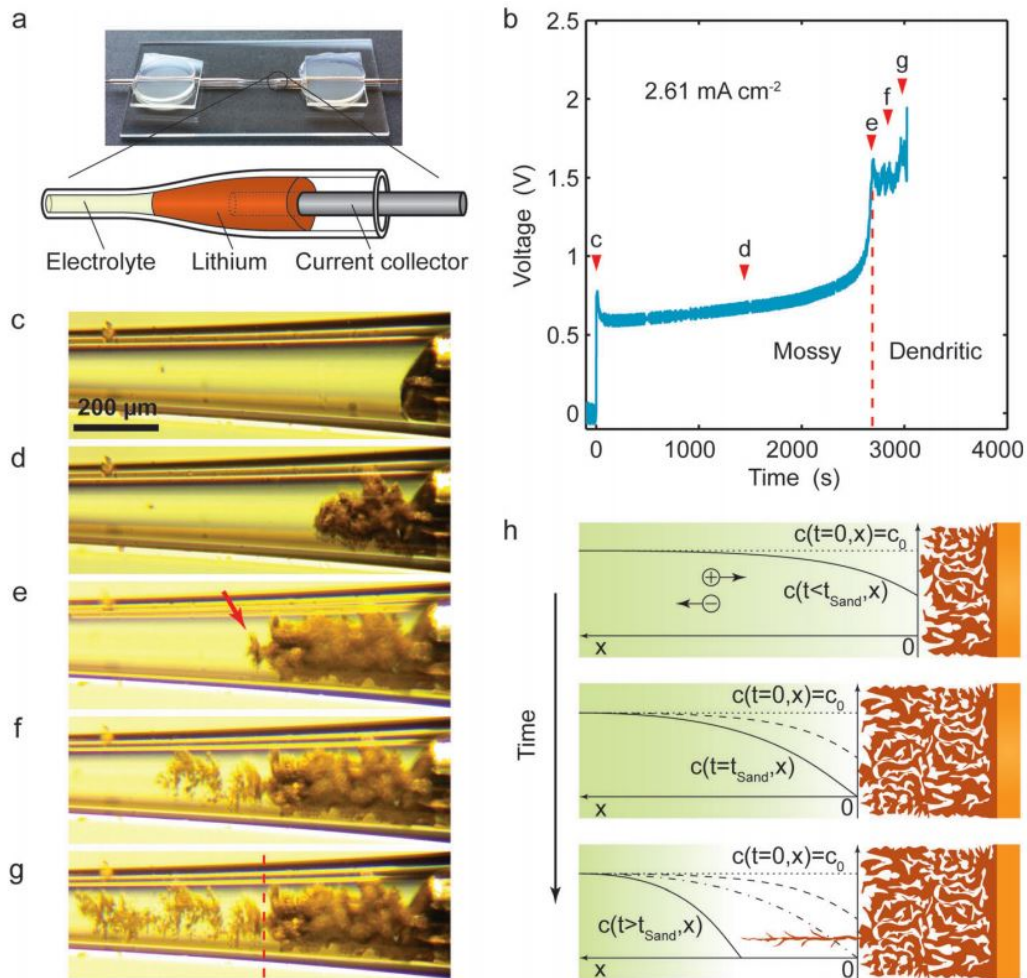


Figure 2.15: *In-situ operando* observations of lithium electrodeposition in a glass capillary. a) Design of the cell. (b) Voltage profiles under current. c–g) *Operando* optical photos of the growth of lithium during the electrodeposition. (h) Theoretical interpretation of the growth mechanisms [60].

By increasing the applied current density, Bai *et al.* found that the transition from mossy to tree-like dendrites happens faster, in accordance with the Sand's time

theory. Thus, the tree-like part of the dendrites is more prominent at high current densities, as shown in Fig. 2.16.

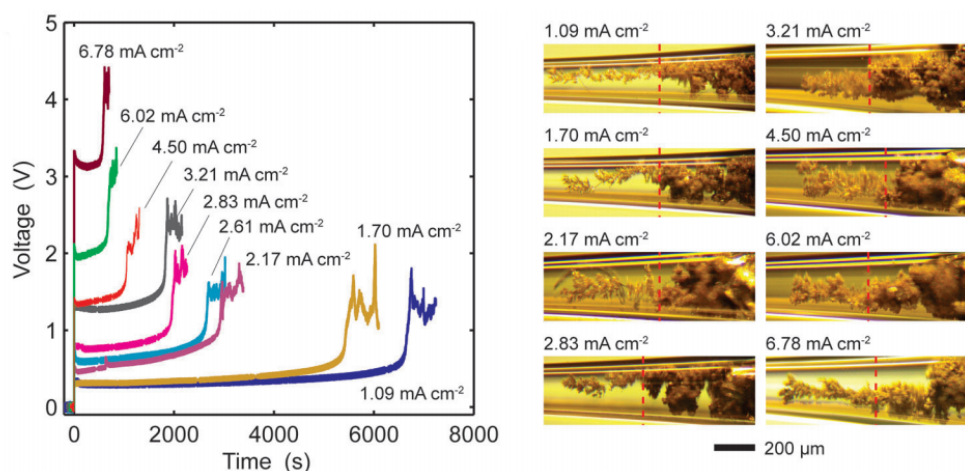


Figure 2.16: Morphology of deposition from optical microscopy at different applied current densities [60].

2.2.2 Scanning Electron Microscopy and Transmission Electron Microscopy

Scanning electron microscopy (SEM) is the most common technique to examine lithium electrode surface topography [9]. It uses a focused beam of electrons to scan the surface of the sample. By interacting with the atoms of the sample, the electrons produce various signals that contain information about the surface morphology and composition of the sample. Since the 70s, this method has been used for lithium batteries both *ex-situ* and *in-situ*. This technique has a very high spatial resolution compared to optical systems, but the penetration depth of the rays is lower than transmission electron microscopy, thus, this technique is able to capture information concerning the sample surface and composition.

Transmission electron microscopy (TEM) is a microscopy technique that relies on a higher voltage electron beam. The main difference between this technique and SEM is based on the way the electrons interact with the sample. In SEM, the images are made by detecting electrons that are reflected from the sample. On the contrary, TEM images are created by using electrons that pass through the sample. Thus, TEM is able to provide information related to the crystalline structure and particle morphology of the sample with respect to SEM [48].

TEM has been used to provide not only information about the morphology of the lithium surface, but also phase contrast images to study the crystalline structure and chemical composition of the sample. *In-situ* TEM allowed the direct observation of lithium dendrites nucleation and growth, achieved for the first time in 2011 by Ghassemi *et al.* [61]. Nevertheless, Foroozan *et al.* [48] argued that the utilization of an open cell required for TEM observations leads to a large deviation from real cell conditions, which can invalidate conclusions. In most of the setups, *in-situ* TEM requires high vacuum during the experiments, thus ionic liquid electrolytes (IL) or solid state electrolytes (SSE) have to be used in most of the experiments, while the high vapor pressure of practical liquid electrolytes makes them incompatible with this technique.

In-situ TEM can be used to study the SEI formation on the lithium metal electrode, however, Zhang *et al* [9] argued that the SEI formed with IL or SSE is very different from the one which is formed with conventional electrolytes. Thus, the creation of a setup (liquid cell) that allows the study of a liquid electrolyte under TEM was needed, even at the cost of sacrificing the resolution of the images with respect to the open cell in vacuum conditions.

In 2014, Sacci *et al.* [62] were able to study the initial SEI formation on lithium metal in a LiPF₆/EC:DMC commercial electrolyte. They demonstrate that the SEI forms prior to lithium deposition and it remains on the surface after lithium stripping. In 2015, Mehdi *et al.* [63] used STEM (Scanning transmission electron microscopy) to study SEI formation and dendrites evolution under lithium deposition and stripping, with a LiPF₆/PC electrolyte.

Thanks to TEM, and specifically *in-situ* ETEM (environmental transmission electron microscopy), in 2017, the root-induced growth mechanism (section 1.2.4) was observed by Kushima *et al.* [38]. They observed that after small lithium nuclei appear on the surface of the gold electrode, they evolve into long whiskers, whose tip shape and width remain constant during the growth, differently from mossy-dendrites in Fig. 2.17, which is a sign of root-growth (Fig. 2.18a). The kinks that are formed during the whiskers growth (A1, A2) were attributed to the new SEI that is formed on the side of the whisker, which redirects the direction of growth. They also observed that root-grown dendrites are less stable during stripping, as shown in Fig. 2.18b, due to the thinner SEI layer at the root, which causes an easy formation of dead lithium.

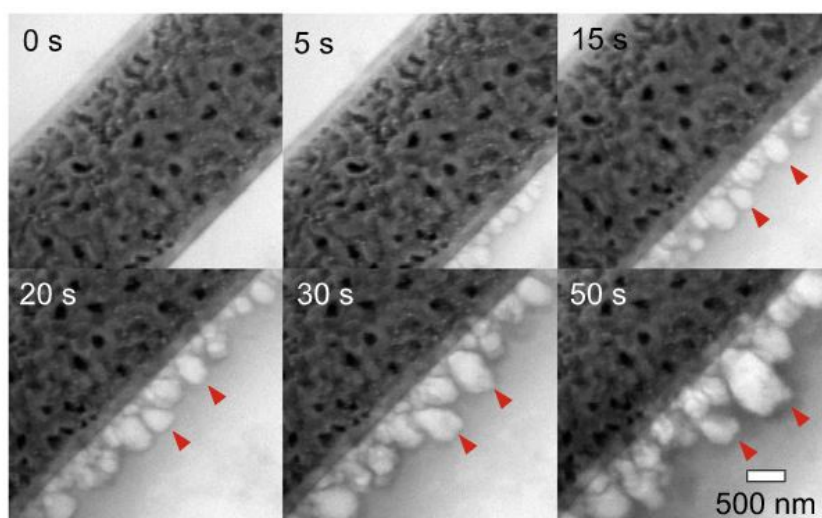


Figure 2.17: TEM images of mossy lithium growth on the gold electrode at -4.0 V vs lithium cobalt oxide. The morphology of the surface changed, indicating a tip-induced growth [38].

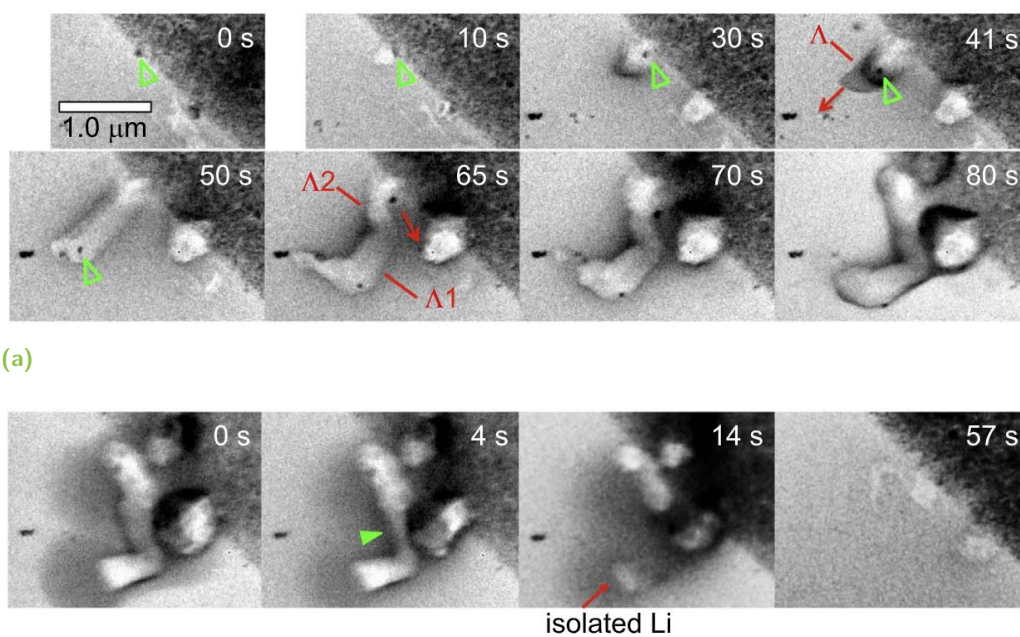


Figure 2.18: TEM images of a whisker during lithium deposition at -6.0 V vs lithium cobalt oxide (a) and dissolution at 0.0 V vs LCO (b). The morphology suggests a root-based mechanism [38].

In 2018, Zachman *et al.* [64] used cryo-TEM, which is a solution to reduce the radiation damage, to identify different dendrite morphologies. They rapidly froze (vitrification) the liquid electrolyte (LiPF₆/EC:DMC) of a symmetric lithium metal coin cell, in order to preserve the structures at the electrolyte/electrode interface, thus enabling structural and chemical mapping of the lithium metal surface with *ex-situ* cryo-TEM (Fig. 2.19).

Two different types of dendrites were found to coexist on the surface of the electrode after 24 h cycling at a constant current density of 1 mA.cm⁻². They concluded that Type I dendrites, which are similar to the mossy-like dendrites defined in section 1.2.4, are bigger (few μm) with low curvature and a thicker SEI film, while the Type II dendrites, which are similar to the tree-like dendrites defined in section 1.2.4, are smaller (hundreds of nm) and tortuous.

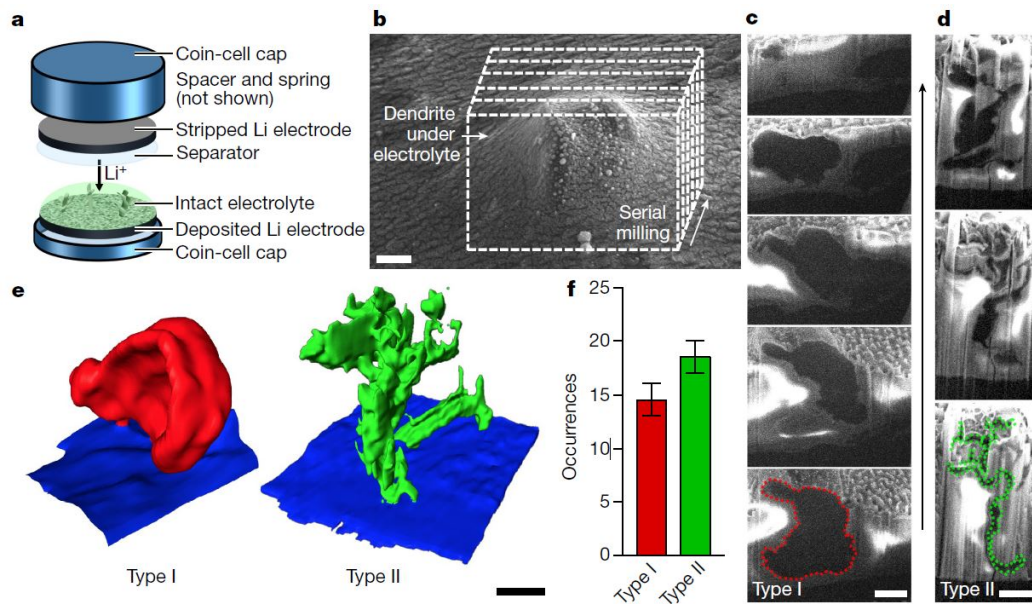


Figure 2.19: Morphology of deposition found by Zachman *et al.* using cryo-TEM. a) Structure of the coin cell. b-d) Images of the electrode surface and dendrites cross-sections. e) Reconstruction of dendrite morphologies. f) Occurrence of the different types of dendrites [64].

2.2.3 Atomic Force Microscopy

Atomic force microscopy (AFM) can be used to study lithium electrode topography, SEI morphology and their mechanical properties. Regarding its spatial resolution, it is lower than SEM and TEM, but much higher than optical microscopy. On the other hand, differently from SEM and TEM, it can give 3D topography images of the sample, thanks to its probe tip that raster scans the sample. During the scanning, the relative position between the tip and the sample is recorded, thus, the height of the sample is inferred. Moreover, AFM can perform force spectroscopy to measure the mechanical properties of the sample, like Young's modulus.

AFM for Surface Morphology Investigation

A seminal study on the application of AFM to study lithium deposition was made in 1996 by Aurbach and Cohen [65], in which they performed *in-situ* AFM on deposited lithium over a copper substrate in a liquid electrolyte. They demonstrated the feasibility and non-destructiveness of atomic force microscopy applied on a lithium surface. In 1998, Morigaki and Otha [58] proved with *in-situ* AFM that the structure of the lithium surface, thus of the SEI, consists of grain boundaries, ridge-lines and flat areas. A result, which, according to Zhang *et al.* [9], could not be proven by SEM nor optical microscopy.

The following study of Aurbach and Cohen [66] (2000) used *in-situ* AFM to show the influence of the electrolyte composition and applied current density on the morphology of the lithium electrode. Different morphologies were found depending on the different types of SEI formed, and the breakdown and repair of the SEI during lithium deposition and dissolution was observed for the first time.

Kitta and Sano [67] studied the nucleation of dendrites during a galvanostatic lithium deposition on a flat lithium metal surface with a LiPF₆/PC electrolyte. In their work, they used the peak force tapping (PFT) mode of AFM, arguing that the conventional AFM (*e.g.* contact mode used by Aurbach and Cohen [66]) has a relatively slow imaging rate (around 10 minutes per image), which is too slow to record the dendrites nucleation and growth for high current densities. During the PFT scanning mode, a collection of force curves from all the scanned pixels of the AFM image provided a faster acquisition of surface morphology without damaging the sample. Together with the topographic height images, PFT allowed to record adhesion mapping images, by examining the attraction between the atoms of a

surface and the AFM probe, thus their adhesion force. They observed that the heterogeneous nucleation of lithium was linked to the intensity of the adhesion force, and that there was a strong correlation between adhesion force and dendrite growth rate. They theorized that the increase in adhesion force was due to a thicker SEI, since a weak adhesion force on a dendrite nucleation site causes a preferential growth for lithium dendrites.

Fig. 2.20 shows topographic height images (top row) and adhesion mapping images (bottom row) from Kitta and Sano paper [67]. They claimed that the protrusions labeled with blue arrows grow noticeably larger than the ones indicated with purple arrows, and have a noticeably lower adhesion force, thus a thinner SEI. Fig. 2.21 represents the mechanism theorized by Kitta and Sano for protrusion growth. In the top row, during lithium deposition, protrusions with a thick SEI grow more slowly than for thinner SEI surface film. At open circuit (bottom row), the SEI has time to grow, leading to a uniform SEI coverage, which results in uniform adhesion forces and a more uniform deposition.

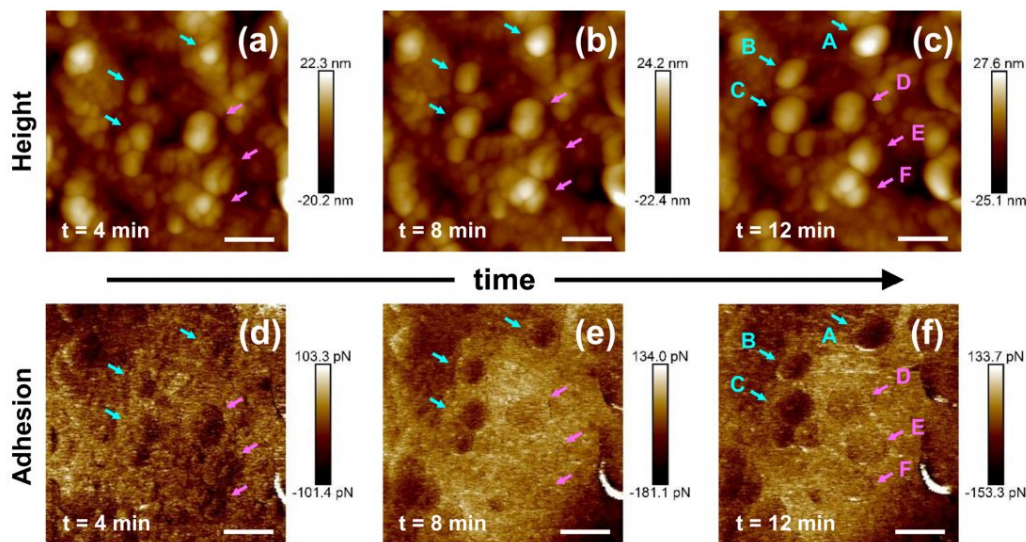


Figure 2.20: AFM images of lithium metal surface during electrodeposition. White scale bars indicated a length of 100 nm. a-c) Topographic height. d-f) Adhesion mapping [67].

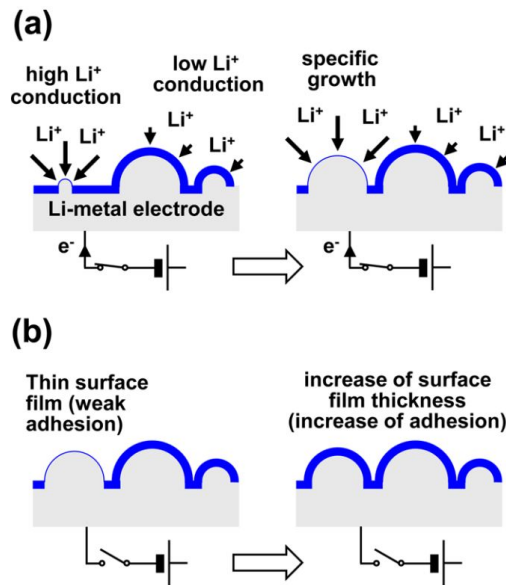


Figure 2.21: Theoretical interpretation of protrusion growth and SEI formation during lithium deposition in (a) and open circuit conditions in (b) [67].

In 2020, Zhang *et al.* [49] coupled AFM with an open-cell set-up for environmental transmission electron microscopy (AFM-ETEM), as shown in Fig. 2.22. Thanks to this setup, they were able to study lithium whisker growth from a lithium electrode covered with a Li₂CO₃ layer. A negative potential was applied between the AFM silicon tip and the lithium electrode, which led to lithium plating in the form of lithium whisker, facilitated by an arc-discharged multiwall carbon nanotube attached to the AFM tip. In this experiment, the lithium metal substrate and the whisker effectively acted as two opposite electrodes of a symmetric lithium cell, with the SEI behaving as a solid electrolyte between the two electrodes. The growth of the whisker could be observed with the ETEM. As in the work of Kushima *et al.* [38], the morphology of the geometrically unchanged tip of the whiskers, shown in Fig. 2.22, suggested a root-growth mechanism.

Moreover, the AFM tip can generate an axial compression on the whisker, simulating the effect of a separator or a solid electrolyte pressure on lithium dendrites, which can lead to the collapse of the whisker (bottom-right image from Fig. 2.22). In this study they found that the yield strength of whiskers decreases with the increase of the whisker diameter, while it can reach up to 244 MPa, which is three orders of magnitude higher than bulk lithium (0.655 MPa [68]).

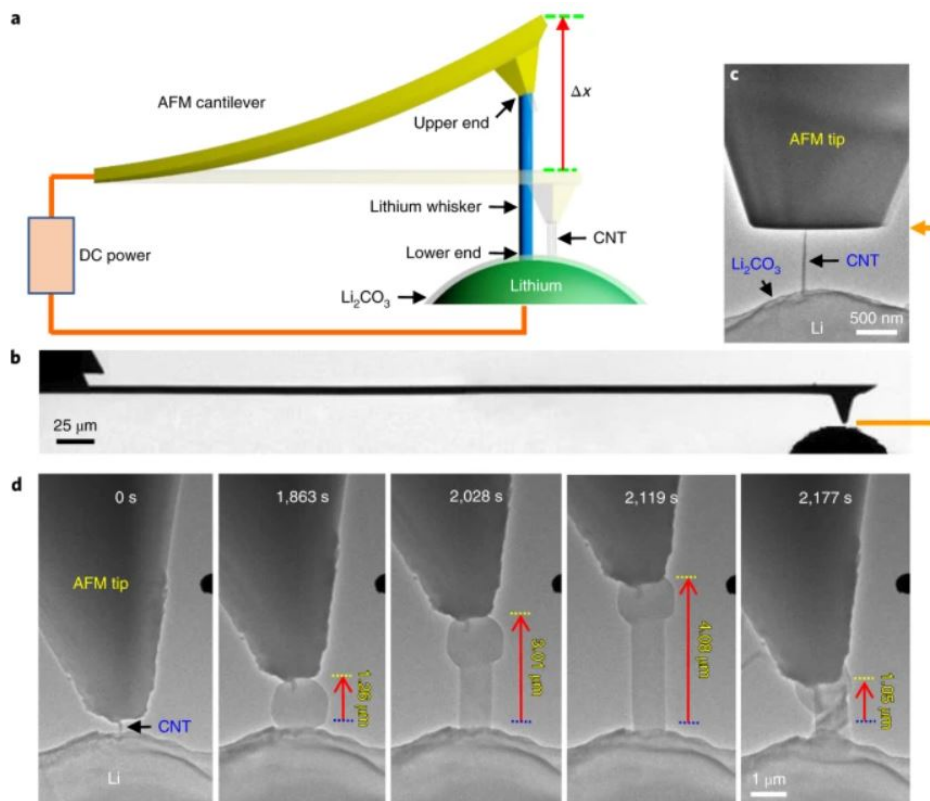


Figure 2.22: a) Setup of the AFM machine with the lithium sample. b-c) TEM images of the AFM cantilever and tip. d) TEM images of whisker growth and collapse [49].

AFM for SEI Mechanical Properties Detection

As previously mentioned, AFM can also be useful to find the mechanical properties of the SEI film. Concerning this point, a very explanatory paper was written in 2013 by Weadock *et al.* [69]. In their work, they used AFM with a colloidal probe, to study the mechanical properties of the SEI layer in a sodium ion battery. They used a Cu/Si substrate working electrode, a sodium metal counter electrode, and NaPF₆/EC:DEC electrolyte. After cycling the cell, force curves of the samples were obtained in the force spectroscopy mode of the AFM, from which the local Young's moduli of the SEI were derived. Their results indicated that the SEI forms an inhomogeneous and bi-layered structure (previously explained in section 1.2.5). Indeed, they found a difference of two orders of magnitude between the highest and lowest Young's modulus of the SEI recorded, due to the different range of interaction across the different points. Lower moduli have a higher range of interaction, which, according to Weadock *et al.*, proves the existence of a less dense layer (usually referred as outer organic layer) on top of a denser layer (usually referred as inner inorganic layer) of

SEI. The less dense layer is thicker, which explains the longer range of interaction that was observed in the force curves.

In 2019, Zhang *et al.* [70] coupled *in-situ* AFM and *ex-situ* X-ray photoelectron spectroscopy (XPS) to study the structure and chemical composition of SEI on a highly oriented pyrolytic graphite (HOPG) surface, with LiTFSI aqueous concentrated electrolyte. Like Weadock *et al.* [69], they determined the Young's modulus of the sample by force-distance curves between the sample and the probe, obtained with AFM peak-force tapping mode. Their measured value of elastic modulus was similar to the theoretical values of LiF and Li₂CO₃, computed, for instance, with density functional theory (DFT) in the work of Shin *et al.* [71] and shown in Fig. 2.23. Like in the study of Weadock *et al.* [69], lower Young's modulus areas were found to have a higher range of interaction.

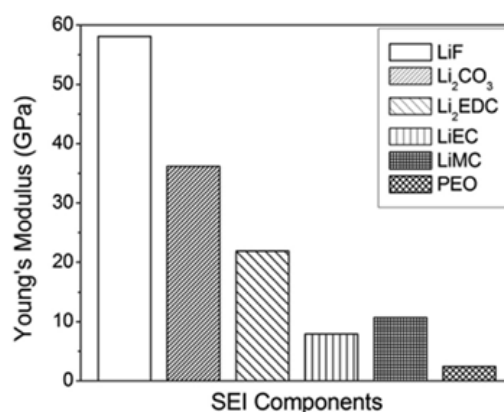


Figure 2.23: Theoretical Young's modulus value of the most common components of the SEI [71].

In order to further investigate the dual-layer structure of the SEI, Kranz *et al.* [72] proposed to combine SEM and SEI scratching experiments using an AFM tip and a force of 40 nN (resp. 140 nN) to remove the outer (resp. inner) layer of the SEI. Then, they studied the thickness and the ionic conductivity of the two layers, but unfortunately, not the mechanical properties, which could have validated the work of Weadock [69] and Zhang [70].

Last but not least, in 2020, Yoon *et al.* [73] used a novel experimental technique to characterize the mechanical properties of the SEI that were not only limited to the elastic behavior of the SEI, but also able to find other relevant properties such as the yield strength and the inelastic response. The sample was composed of a free-standing narrow membrane, shown in Fig. 2.24, laying on a rigid substrate at its edges in such a manner that the results of AFM were not influenced by the

substrate. The membrane was subjected to a lateral pressure which determined a deflection. Under elastic deformation, the pressure-deflection relationship is cubic and it deviates from the cubic trend when inelastic deformation is present in the membrane. From the pressure-deflection relationship, the stress-strain relation along the circumferential direction (hoop) could be derived.

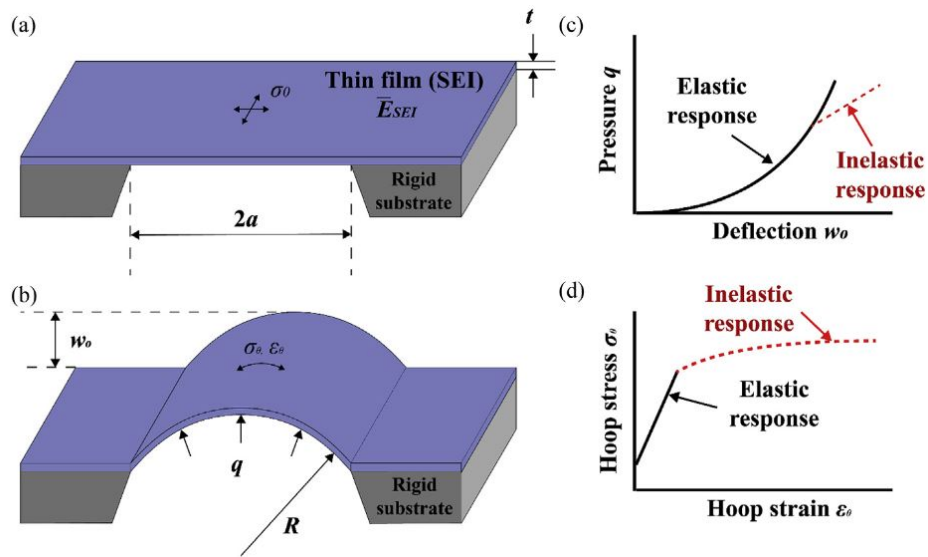


Figure 2.24: a-b) SEI free-standing narrow membrane on a rigid substrate. c) Pressure response to membrane deflection. d) Hoop stress response to hoop strain [73].

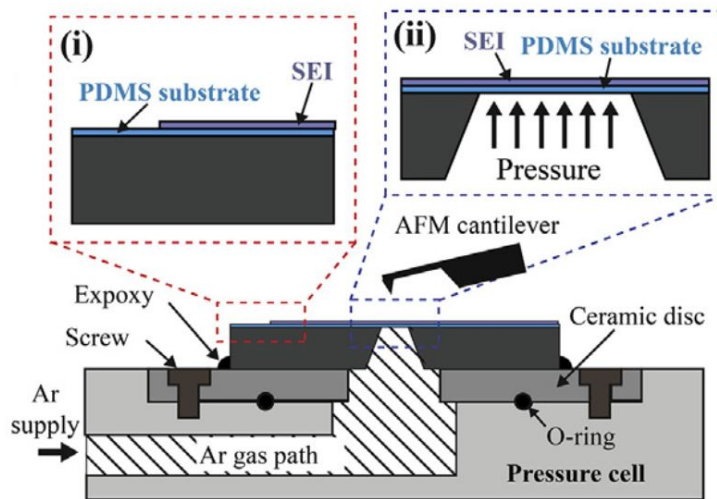


Figure 2.25: Custom cell design that enabled controlled pressure to be applied on the final SEI sample [73].

Fig. 2.25 shows the AFM set-up, where lithium was deposited on the substrate, reacted with the electrolyte film, and was entirely converted by a SEI film. The membrane was assembled in the custom-designed machine, which enabled the control of the lateral pressure applied on the sample, while the AFM allowed measuring SEI thickness, deflection and surface topography evolution. The response of the substrate was subtracted to have a more accurate result.

The results of Yoon *et al.* [73] work are reported in Fig. 2.26. Two different carbonates-based electrolytes were used in their work: LiPF_6 in ethylene carbonate (EC) and LiPF_6 in a mixture of EC and fluoroethylene carbonate (FEC). FEC is an additive, which is broadly known for improving the cycling performance of lithium metal electrodes. Indeed, the results of Fig. 2.26 shows that the addition of FEC (8:2 by weight with respect to EC) increases by 80% the elastic modulus and by 20% the elastic limit of the SEI. Moreover, the results show that the stress-strain response of the SEI can be approximately characterized as an elastic–perfectly plastic behavior.

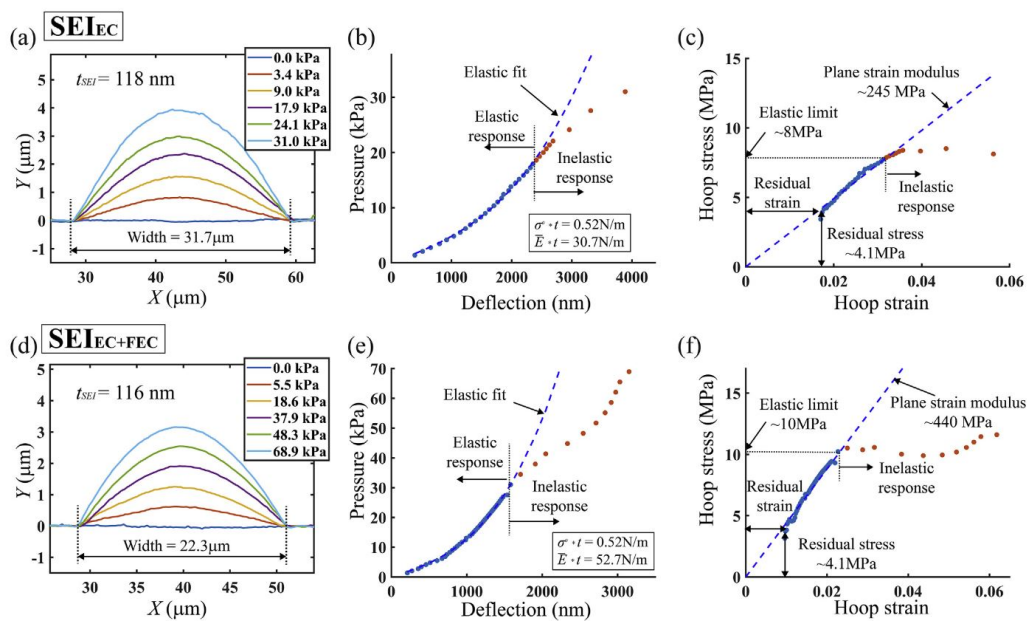


Figure 2.26: Pressure-deflection response, and hoop stress vs strain curves measured with AFM during the deformation of the SEI membrane. [73]

2.2.4 Electrochemical Impedance Spectroscopy

Electrochemical impedance spectroscopy (EIS) is widely used to characterize electrochemical devices. It consists of the application of a sinusoidal voltage or current perturbation on a system over a wide range of frequencies. This approach relies on the hypothesis that the device under investigation has a linear response. Processes inside an electrochemical device are usually strongly nonlinear. Therefore, the EIS measurements must be made in such a manner that the system approaches a pseudo-linear condition. This is achieved by imposing a perturbation amplitude small enough that the system response can be considered linear. Since the physical phenomena inside an electrochemical device, like a battery, have different characteristic times, it is possible to identify which phenomenon is dominant by looking at the EIS response at different frequencies.

In order to go a step further, time-difference impedance spectroscopy (DIS) can be used to characterize electrodes covered by a passivating layer, like the SEI, that grows in time.

Vorotyntsev *et al.* proposed the time-difference impedance spectroscopy in 2001 [74]. In their work, they used the DIS to study the evolution of the SEI on lithium metal electrodes in an $\text{LiAsF}_6/\text{EC}:\text{DMC}$ electrolyte composition. DIS consists in measuring electrochemical impedance spectra at different times, separated by resting periods for the cell. Under open-voltage conditions, according to Vorotyntsev *et al.* the changes in the EIS spectra over time are solely due to the change in morphology and/or composition of the SEI. Thus, the difference between two impedance spectra, measured at different times, can provide very useful information on the nature of the growing SEI.

According to Vorotyntsev *et al.*, the phenomena that lead to a change in the SEI can be classified in two main categories: film growth, thus increase in thickness, and film aging, thus change in time of its local properties. Depending on the magnitude of the different phenomena, three different shapes can be obtained from time-difference impedance spectra:

- a complicated shape with loops in both the first and fourth quadrants of the complex plane, which can be interpreted as a rapid evolution of local characteristics of the film *e.g.* disappearance of a certain part of the film and replacement by a new film (Fig. 2.27 upper-right)

- a regular shape with a flattened semicircle, which can mean that the film is growing but the new-formed layer is heterogeneous (Fig. 2.27 bottom-left)
- a regular semicircle, which can be interpreted as the film is growing without any change in the layer homogeneity (Fig. 2.27 bottom-right)

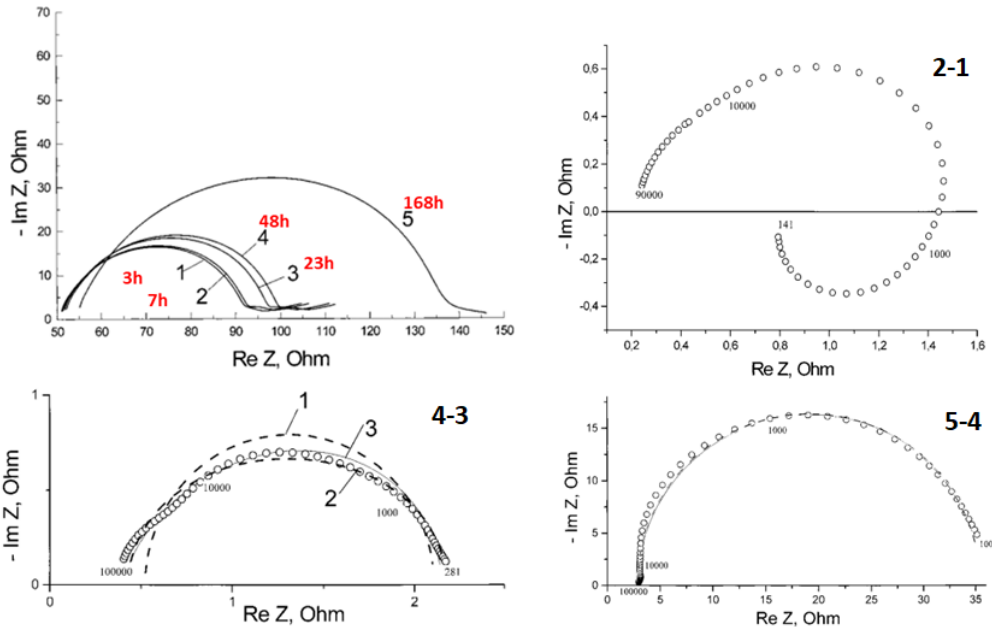


Figure 2.27: Impedance spectra from the work of Vorotyntsev *et al.* (top-left plot). Impedance spectra differences between the second and the first spectrum (2-1), the fourth and the third (4-3) and the fifth and the fourth (5-4) [74].

Fig. 2.27 shows the results from the work of Vorotyntsev *et al.* [74]. Impedance spectra of lithium metal electrodes were measured in a three-electrode cell, with electrodes surface of 0.785 cm^2 . The voltage amplitude used for the EIS was 5 mV and the range of frequencies extended from 100 kHz to 10 mHz, while the duration of each impedance spectrum measurement was around 20 minutes. The upper-right graph in Fig. 2.27 shows the impedance spectra obtained at 3, 7, 23, 48 and 168 h after the cell assembly. On the other hand, the other three graphs show the impedance difference between the measured spectra. The difference between the spectrum recorded after 7 hours and the one after 3 hours (upper-right), indicates that the SEI is evolving drastically in the first phase of the experiment (2-1). In the bottom row, a flattened and a regular semicircle are represented, thus the SEI tends to evolve in a more regular and uniform manner as time passes.

A different approach was used by Bouchet *et al.* in their work [75], in which they studied a lithium symmetric cell with a surface area of 3 cm^2 and a LiTFSI/PEO polymer electrolyte. The impedance spectra were recorded in the range from 1 MHz to 100 mHz, with a voltage amplitude of 3 mV. Differently from Vorotyntsev *et al.*, they did not compute the difference between spectra taken at different times, but they directly associated an equivalent circuit to the performed spectra.

Both the obtained impedance spectrum and the associated equivalent circuit are presented in Fig. 2.28, from which it is possible to distinguish the different phenomena happening in the lithium symmetric cell. At very high frequencies, the cell response was attributed to the inductance and resistance of electrical connections. At high frequencies, a parallel resistance capacitance element was used to describe the electrolyte response, while at medium frequency a component with a resistance in parallel with a constant phase element (CPE) was used to describe the passive layer response. On the other hand, the second bigger semicircle is described by another resistance in parallel with a constant phase element and a Warburg element.

In their work, they observed that already at the initial time, a semicircle corresponding to the passive layer was present, which was assumed to be the native layer of the SEI and was fitted with one R//CPE element. Then, the semicircles of following spectra were fitted by two R//CPE elements in series, one with the values of the native layer, and the other one assumed to represent a second layer formed during the cell aging.

Morales-Ugarte *et al.* [76] [77] continued the work of Bouchet *et al.* [75], by using time-difference impedance spectroscopy to study the properties of the SEI formed on lithium metal electrodes in contact with different ionic liquids. Differently from Vorotyntsev *et al.* [74], they used a symmetric lithium CR2032-type coin cell to perform the experiments, in which the electrodes had a surface of 2 cm^2 . The EIS measurements were performed by applying a voltage amplitude of 20 mV in a range of frequencies between 1 MHz and 10 mHz. The impedance spectra obtained by performing the EIS on coin cells with different ionic liquids are shown in Fig. 2.29, and differently from Vorotyntsev *et al.* [55], the first spectrum was recorded on the freshly assembled coin cell, and the last one after 60 h.

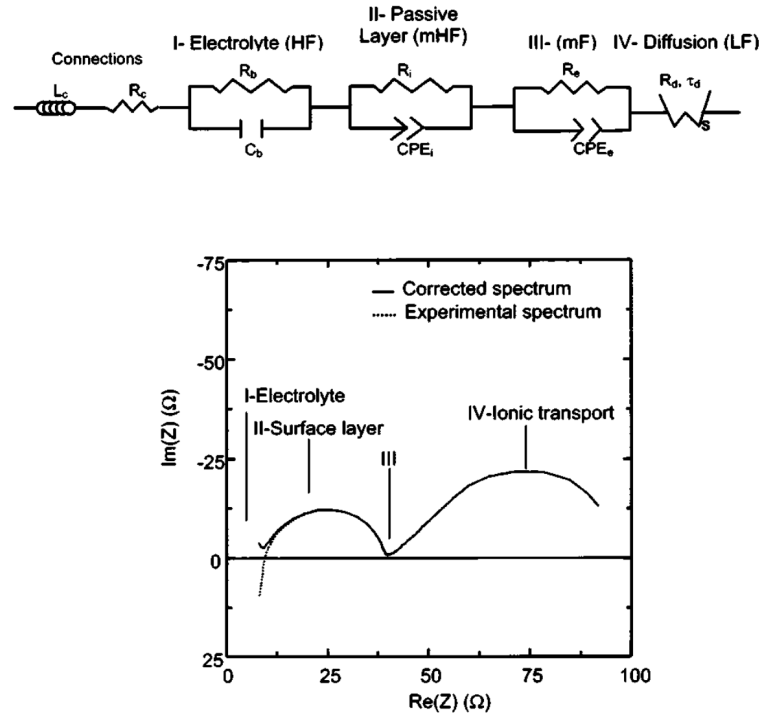


Figure 2.28: Equivalent electric circuit and impedance spectrum relative to a lithium symmetric cell, from the work of Bouchet *et al.* [75].

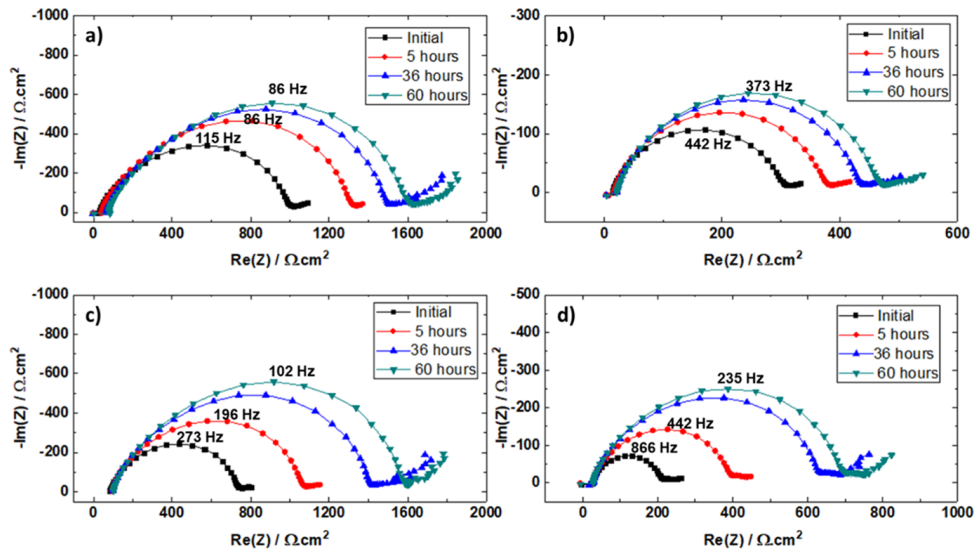


Figure 2.29: Evolution of the impedance response containing (a) $C_1C_6ImTFSI$, (b) C_1C_6ImFSI , (c) $C_1C_6ImTFSI/LiTFSI$, and (d) $C_1C_6ImFSI/LiTFSI$ electrolytes [76].

Fig. 2.30 shows the differences in impedance from Morales-Ugarte *et al.* experiments. While Vorotyntsev *et al.* computed the differences between two consequent spectra, here the initial spectrum is subtracted to the following ones. The semicircles thus obtained are more regular than the ones obtained by Vorotyntsev, also due to the different electrolytes that were used in this more recent study. The regular semicircles were associated with a simple Randles circuit, from which it was possible to obtain the SEI and electrolyte properties (more details in chapter 5). Like Bouchet *et al.* [75], they concluded that the SEI shows a bi-layer nature, with a native layer and a second layer that increases continuously during cell aging.

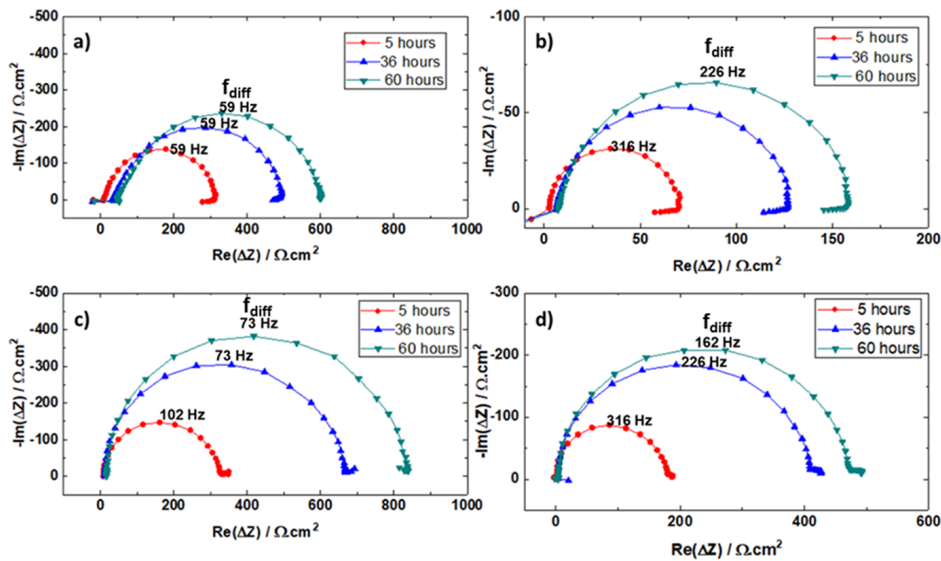


Figure 2.30: Evolution of the impedance spectra difference containing (a) $C_1C_6ImTFSI$, (b) C_1C_6ImFSI , (c) $C_1C_6ImTFSI/LiTFSI$, and (d) $C_1C_6ImFSI/LiTFSI$ electrolytes [76].

2.2.5 X-ray Photoelectron Spectroscopy

X-ray Photoelectron Spectroscopy (XPS) is a technique that analyses the electrons emitted by a sample subject to X-rays. By measuring the kinetic energy of the emitted electrons, it is possible to determine their binding energies. Then, it is possible to obtain a XPS spectrum, which is a plot of the number of electrons detected at a specific binding energy. By studying the peaks on the XPS spectrum it is possible to identify the chemical element within the sampling volume, since XPS is a surface technique with an analysis depth around 10 nm.

XPS technique has been used to characterize the surface of lithium metal electrodes and to obtain information about the chemistry of the components that are

present on it. For instance, for the first time in 1987 by using XPS, Aurbach *et al.* [78] were able to find the major species at the lithium surface, including Li_2O , LiF , Li_2CO_3 and RCO_2Li . Later on, different studies used the XPS to study the effect of electrolyte solvents, lithium salts or additives on the composition of the SEI. For instance, Ismail *et al.* [79] used XPS to study the surface composition of lithium metal electrodes in contact with polymer electrolytes, while the above mentioned work of Morales-Ugarte *et al.* [76] studied the surface composition of the electrode in contact with ionic liquids, as shown in Fig. 2.31.

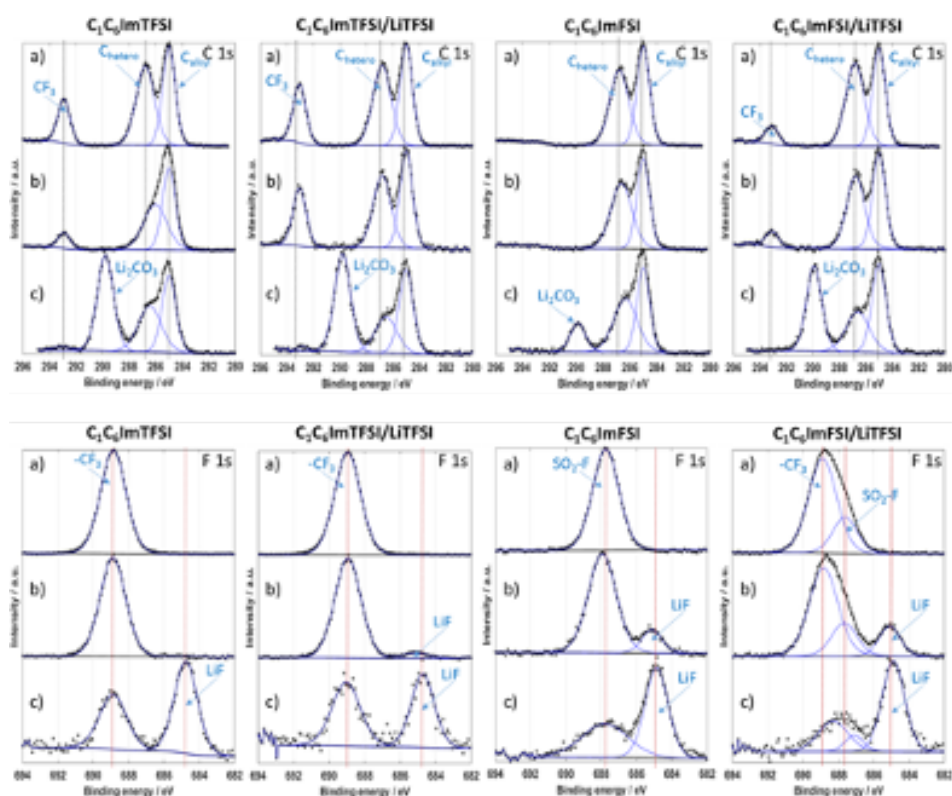


Figure 2.31: XPS spectra of carbon C 1s core level (first row) and F 1s core level (second row), with different IL-based electrolytes, registered at the surface of a) neat IL-based electrolyte, b) separator, c) lithium electrode [76].

2.2.6 Conclusion on Experiments in the Literature

Experiments are demonstrated to be a valuable resource to characterize the morphology of lithium metal electrodes and the properties of the SEI film. In the last 50 years, each experimental technique has been refined in the direction of performing *in-situ* and *operando* experiments, with tailored cell designs. Nevertheless, many experiments are still performed far from the real case scenario, in particular with optical microscopy [63] [64] [44], giving results that are hard to be generalized.

Moreover, experiments like EIS return mean values of properties, which miss the complex, inhomogeneous nature of the lithium metal surface and the electrolyte. At the other hand of the spectrum, experiments like AFM give back information that are too detailed and linked to the local heterogeneity, thus difficult to generalize.

Finally, underlying mechanisms behind lithium deposition and dendrites formation are not fully understood and cannot be just theorized by looking at the results of the experiments, thus, a stronger coupling between the experiments and the model is necessary and is discussed in the next section.

2.3 Aims and Methodology of the Work

This PhD work started at the end of 2018, as a collaboration between two laboratories within DEHT department of CEA Liten in Grenoble, with complementary expertise in experimental projects involving lithium metal electrodes and in modeling lithium ion batteries and fuel cells. The collaboration was motivated by the strong belief that a strict correlation between experiments and model is necessary to understand the formation and the growth of dendrites, in order to make lithium metal batteries safer and commercially widespread.

This work had the goal to produce the first model specifically for lithium metal electrodes within the DEHT research department. Therefore, a foundation work was required to explore the different modeling alternatives in the literature. The first goal of the model was to define which phenomena have a bigger impact on dendrite growth during lithium plating on a lithium metal electrode. The multi-domain continuum model was the typology of model identified to better fit this task, for its ability to incorporate electrochemical and mechanical phenomena and the proven effectiveness in adding the SEI. Once these phenomena were found, the most

important goal of the model was to theorize in which conditions dendrite growth is boosted and in which it is avoided, and how the properties of the cell components and the design of the electrode surface can affect it, to suggest solutions to reduce dendrites.

Besides the modeling work, the goals of the experimental part were to define a framework of techniques to find reliable parameters to be used in the model, as well as to validate the outputs of the model. The choice of model type, thus the definition of its parameters, helped to identify these experiments. Moreover the confirmed importance of the SEI layer, based on literature review, experiments at CEA and simulations performed in this work, has redirected the attention of the experiments towards the study of this crucial component. The attention towards the SEI was also amplified by the uncertainty found in the literature in its description and by the strong hypotheses made to identify its properties, which are critically discussed in chapter 5. All the experiments were designed to be as close as possible to the real case scenario and their results were critically reviewed to point out strengths and limits of each technique. Relying on the laboratory experiences and equipment, EIS was found to be the ideal technique to study SEI evolution in coin cells, while AFM, which was made available only towards the end of this work, was identified as the most used (if not the only) technique to identify SEI mechanical properties. XPS was later used to validate the important findings of EIS and AFM, by identifying the chemical components present on the lithium electrode surface in contact with the electrolyte. Finally, optical microscopy was used to validate the trends of the model thanks to its relatively simplicity to perform *operando* experiments on lithium metal cells using experimental conditions close to the real cases.

To outline this work in a logical manner, the manuscript continues with the presentation of the model (chapter 3) and its results (chapter 4), while in chapter 5, the performed experiments and their results are discussed.

Model Presentation

In this chapter the model, which is proposed in this work, is presented in detail. The structure of the chapter is listed below.

- Introduction of the model and the subunits that compose it.
- Detailed presentation of the equations that are used in the model and the hypotheses behind them.
- Comparison of the model with other relevant models in the literature and description of its implementation in Comsol[®] Multiphysics.

The model described in this chapter contains all the phenomena studied in this thesis work and it is called "full model" in the next chapter. In order to highlight the contributions of the different phenomena, chapter 4 presents also simplified models, which are just simplifications of the model presented in this chapter. Simplifying assumptions are each time presented and discussed.

3.1 Model Framework

The model relied on the solid theoretical basis provided by Newman and Monroe [46] regarding the influence of mechanics on the reaction kinetics on the electrode surface, and therefore its influence on dendrite growth, with the addition of a reactive SEI [15]. Different from Newman and Monroe and from Barai *et al.* [80], the effect of a solid electrolyte that acts as a barrier for dendrite growth was not considered and no external compressive stress was applied. Thus, in order to highlight the mechanical effect of the SEI, a liquid electrolyte was chosen for the simulations [50]. Therefore, the only pressure on the lithium surface was applied by the SEI.

The geometry that was used by the model for most of the simulation is shown in Fig. 3.1. It was a 2D geometry, like nearly all the models found in the literature [29] [33] [51] [16], with the addition of the SEI thickness, defined as a property of the lithium/electrolyte interface, which gave an extra dimension where it was possible to study the transport phenomena that happened within the SEI. Since at

this stage, the SEI and the electrolyte properties were uniform, like in the work of Yoon *et al.* [16] and Liu *et al.* [15], an initial artificial geometric defect on the lithium surface was needed in order to observe a heterogeneous lithium deposition, thus, to study dendrites evolution with different components properties and different operating conditions. On the contrary, a perfect lithium/electrolyte interface would yield to uniform deposition. The dimensions of the defect were arbitrarily chosen to avoid geometry problems (already discussed in section 2.1.4) in the very first phases of the simulation. Thus, the defect had a rounded rectangle shape with size $3 \times 4 \mu\text{m}$ and radius of curvature of $0.6 \mu\text{m}$.

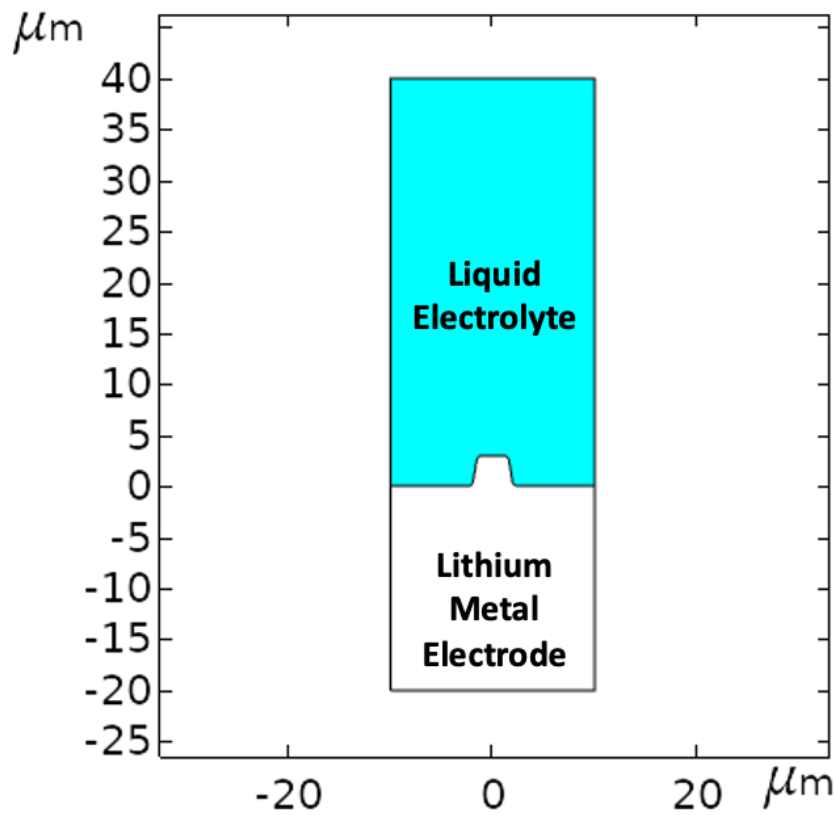


Figure 3.1: Geometry of the model, electrolyte (light blue), lithium negative electrode (white).

Two components were defining the 2D geometry, the liquid electrolyte with a binary salt and the lithium metal negative electrode. The dimensions for the electrode ($20 \times 20 \mu\text{m}$) and the electrolyte ($20 \times 40 \mu\text{m}$) were derived from the lithium deposition transient model of Yoon *et al.* [16]. The counter electrode, which was assumed to be a lithium metal electrode, was not modeled, following the hypothesis that it was

far enough not to influence the phenomena that happen on the studied electrode surface, at the initial stage of the dendrite formation. Therefore, the top side was assumed as an infinite and rigid source of lithium ions. The lithium/electrolyte interface was modeled using a moving boundary. The electrode and electrolyte domains were periodically remeshed to preserve numerical accuracy as the interface deforms and smaller features were created.

The SEI was modeled using the concept of SEI coverage density [15], thus its thickness was a dimensional property of the lithium metal boundary. This choice was motivated by the small thickness of the SEI (few nm) compared to other characteristic dimensions of the system (μm) and it allowed an easy and accurate implementation of the chosen model for SEI evolution. Initially, the electrode/electrolyte interface is stress-free, different from Newman and Monroe [47].

Fig. 3.2 presents the framework of the model and it shows the logical connections among the subunits. These connections do not represent a temporal order among the different units, since all the equations were solved at the same time by a fully coupled solver in Comsol[®] Multiphysics. The model can be divided in four subunits (in orange): the electrochemical model, the moving geometry, the mechanical model of the SEI and the mechanical model of the Li metal electrode.

The electrochemical model subunit considered mass and charge transport in the electrolyte and in the SEI, while in the electrode only charge transport was studied. The main output of this part was the current density of lithium deposition on the electrode, which was modeled with a modified Butler-Volmer kinetics (more details in section 3.2.6).

The lithium deposition caused a change in the geometry of the model, which was studied within the moving geometry subunit. From this unit, it was possible to obtain the displacement of the SEI, which was used as input for the mechanical model of the SEI unit. Thus, the deformed SEI exercised a pressure on the lithium metal interface, and the consequent stress of the lithium was studied in the related mechanical subunit. Its stress, together with the SEI stress, contributed to modify the Butler-Volmer kinetics, while the eventual deformation of the lithium electrode added its contribution to the moving geometry subunit. Through this coupling of the electrochemical and mechanical models, the morphological changes of the lithium surface and of the SEI thickness during lithium electrodeposition were studied.

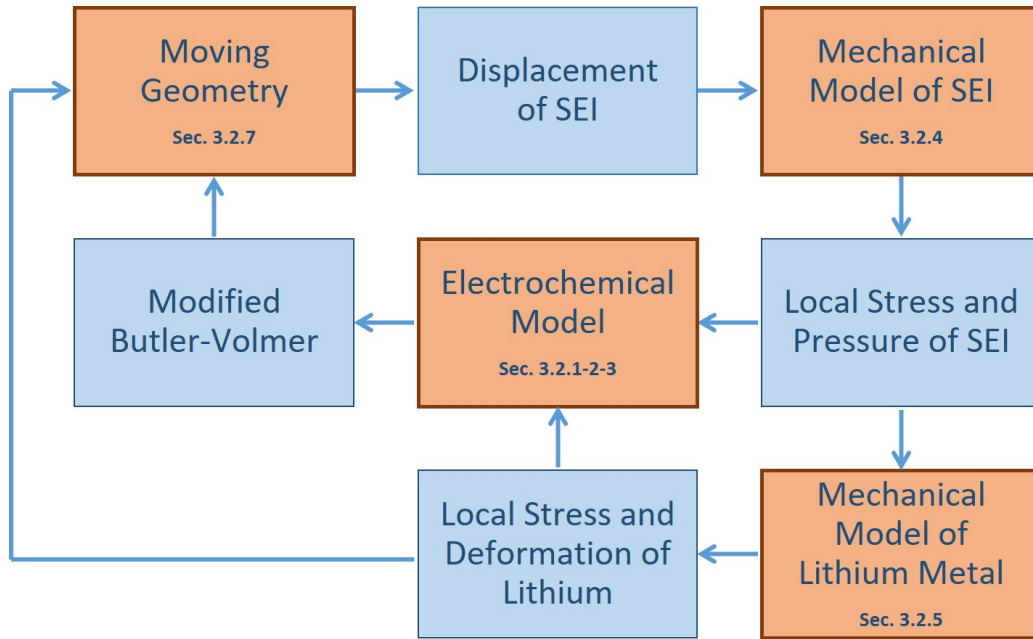


Figure 3.2: Framework of the model. Subunits in the orange boxes. Input/output in the blue boxes.

3.2 Equations

In this section, the equations that constitute the model are presented, together with their boundary and initial conditions, and the hypotheses behind them.

3.2.1 Transport Phenomena in the Electrolyte and Electrode

Lithium ions entered the electrolyte from the top boundary, which was assumed as an infinite and rigid source of lithium ions, while a current collector was assumed at the bottom boundary of the electrode domain. Zero flux boundary conditions were used at the left and the right boundaries (Fig. 3.1). In the electrolyte, mass and charge transport phenomena were studied, involving both diffusion and migration effects, while in the electrode, only charge transport was modeled.

Mass Transport in the Electrolyte

The electrolyte was assumed to be a binary solution, and mass transport within it followed the concentrated solution theory. Thus, the conductivity, the transference

number, and the diffusion coefficient of the lithium salt characterized the transport phenomena in the electrolyte [81]. Therefore, the concentration profile in electrolyte was estimated as follows:

$$\frac{\partial c_e}{\partial t} = \frac{\partial}{\partial x_i} \left[D_e \left(1 - \frac{d \ln c_{sol}}{d \ln c_e} \right) \frac{\partial c_e}{\partial x_i} \right] \quad (3.1)$$

where c_e [mol.m⁻³] is the concentration of the salt, D_e [m².s⁻¹] its diffusion coefficient in the electrolyte and c_{sol} [mol.m⁻³] the concentration of the solvent. Like in the work of Ferrese *et al.* [50] and Barai *et al.* [82], the solvent concentration depended weakly on the electrolyte concentration, therefore the ratio $d \ln c_{sol} / d \ln c_e$ was negligible. Moreover, like the above mentioned works, the diffusion coefficient was considered constant, uniform and independent from lithium ion concentration, thus it could be taken out from the partial derivative. Additionally, under the assumption of zero bulk velocity of the electrolyte, and a constant value of the transference number of the lithium ion, t_+ [-], Eq. 3.1 could be rewritten according to the following Fick's second law, which was used in the model:

$$\frac{\partial c_e}{\partial t} = D_e \frac{\partial^2 c_e}{\partial x_i^2} \quad (3.2)$$

The boundary conditions, relative to the mass transport in the electrolyte, are shown in 3.3. At the top boundary, a Neumann boundary conditions was specified, and the gradient of the salt concentration was proportional to the applied current density, i_{app} [A.m⁻²], which was the main input of the model. At the left and right boundaries, a no-flux boundary condition was defined. At the bottom boundary, in this case lithium/electrolyte interface, the gradient of the salt concentration was proportional to the Butler-Volmer current density, i_{BV} [A.m⁻²], which is defined in detail in section 3.2.6. Since the Butler-Volmer current density was a function of the concentration, at the lithium/electrolyte interface a mixed boundary condition was applied.

$$\left\{ \begin{array}{ll} D_e \frac{\partial c_e}{\partial n} = -\frac{1-t_+}{F} i_{app}, & \text{Top Boundary} \\ \frac{\partial c_e}{\partial n} = 0, & \text{Left and Right Boundary} \\ D_e \frac{\partial c_e}{\partial n} = -\frac{1-t_+}{F} i_{BV}, & \text{Lithium/Electrolyte Interface} \end{array} \right. \quad (3.3)$$

The initial concentration of lithium salt was set to be equal to an arbitrary value, c_0 , and uniform within the whole electrolyte domain.

Charge Transport in the Electrolyte

Charge transfer in the electrolyte was driven both by the ohmic current (first term of Eq. 3.4) and the diffusion-induced current (second term of Eq. 3.4), while convective transport was neglected. Thus, based on the principle of electroneutrality and charge conservation, and under the assumption that the activity coefficient was constant, the charge transport was modeled according the following extended Ohm's law:

$$\frac{\partial}{\partial x_i} \left(\kappa \frac{\partial \phi_e}{\partial x_i} + \frac{2RT\kappa(1-t_+)}{F} \frac{\partial \ln(c_e)}{\partial x_i} \right) = 0 \quad (3.4)$$

where ϕ_e [V] is the potential of the electrolyte, κ [S.m⁻¹] its conductivity, R [J.(mol.K)⁻¹] the universal gas constant, T [K] the temperature, and F [C.mol⁻¹] the Faraday's constant.

Boundary conditions for charge transport in the electrolyte are presented in 3.5, and responded to the same logic of the boundary conditions for mass transport in the electrolyte. Thus, a Neumann boundary condition that depends on the applied current density at the top boundary, zero-flux boundary conditions at the left and right boundaries, and a mixed boundary condition that depends on the Butler-Volmer current density at the lithium/electrolyte interface.

$$\left\{ \begin{array}{l} \left(\kappa \frac{\partial \phi_e}{\partial n} + \frac{2RT\kappa(1-t_+)}{F} \frac{\partial \ln(c_e)}{\partial n} \right) = -i_{app}, \quad \text{Top Boundary} \\ \left(\kappa \frac{\partial \phi_e}{\partial n} + \frac{2RT\kappa(1-t_+)}{F} \frac{\partial \ln(c_e)}{\partial n} \right) = 0, \quad \text{Left and Right Boundary} \\ \left(\kappa \frac{\partial \phi_e}{\partial n} + \frac{2RT\kappa(1-t_+)}{F} \frac{\partial \ln(c_e)}{\partial n} \right) = -i_{BV}, \quad \text{Lithium/Electrolyte Interface} \end{array} \right. \quad (3.5)$$

The potential in the electrolyte was arbitrarily set to zero as the initial condition, due to the symmetrical nature of the considered cell, and the initial potential of the lithium electrode, which was as well set to zero.

Charge Transport in the Electrode

No accumulation of charge was assumed in the electrode, therefore, the charge transport equation was the following Laplace's equation, defined in the lithium metal domain:

$$\sigma_s \frac{\partial^2 \phi_s}{\partial x_i^2} = 0 \quad (3.6)$$

where ϕ_s [V] is the potential of the electrode and σ_s [S.m⁻¹] its conductivity. Since the conductivity of lithium was several orders of magnitude larger than the one of the electrolyte, variations in potential within the lithium metal were negligible.

Boundary conditions for charge transport in the electrode included a mix boundary condition at the top boundary or lithium/electrolyte interface, where the gradient of the potential was proportional to the Butler-Volmer current. A zero-flux boundary condition was set at the left and right boundaries; while a Dirichlet boundary condition at the bottom boundary, where the potential was arbitrarily set to zero.

$$\left\{ \begin{array}{ll} \sigma_s \frac{\partial \phi_s}{\partial n} = -i_{BV}, & \text{Lithium/Electrolyte Interface} \\ \frac{\partial \phi_s}{\partial n} = 0, & \text{Left and Right Boundary} \\ \phi_s = 0, & \text{Bottom Boundary} \end{array} \right. \quad (3.7)$$

As in the case of the electrolyte, the initial condition for the electrode potential was set to zero within the whole electrode domain.

3.2.2 Active SEI Model

The first attempt to introduce the SEI in our model was made by following the steps of Yoon *et al.* [16], thus by adding an additional 2D domain to the model. It has to be pointed out that the SEI thickness considered by Yoon in his model was of 200 nm, while other papers report a lower SEI thickness. For example, Liu and Lu [15] assumed a uniform initial thickness of 10 nm, which is the initial thickness that was used as well in this thesis work, being also consistent with the experimental values found in chapter 5.

Fig. 3.3 shows the size of a SEI of 100 nm of thickness (red line) on the top of the lithium surface (black line), compared to a zoom of the geometry of the model, which as reported in Fig. 3.1, is 60 x 20 μm . Even with a SEI thickness ten times higher than the initial one assumed in the model, the difference in size between the cell geometry and the SEI thickness is evident. On top of that, the SEI thickness was assumed to change due to SEI formation and change in morphology of the electrode underneath. Thus, differently from Yoon *et al.* [16], the option of modeling the SEI in a 2D fashion was discarded. Indeed, the 2D modeling would have increased the chance to encounter the errors reported in section 2.1.4, such as undefined new boundaries and singularities in the mesh.

From Liu and Lu work [15], the concept of SEI coverage density was introduced, and it allowed one to study the phenomena in the SEI without adding an additional 2D domain to the model. SEI coverage density is conceptually similar to SEI thickness but broader, since it was defined by Liu and Lu as the volume of SEI on a unit area of the substrate surface, and it was assumed to be a spatial dependent variable of the lithium metal surface. Despite the above-mentioned difference, for sake of simplicity, the concepts of SEI coverage density and SEI thickness are used interchangeably in this work.

In their work, Liu and Lu assumed the SEI to be a homogeneous medium, and the newly formed SEI is homogeneous as well. Following this assumption, it was possible to write the following mass conservation equation:

$$(l + dl)(h_{SEI} + dh_{SEI}) - lh_{SEI} = q_{SEI}l dt \quad (3.8)$$

The previous equation considered a small element of SEI of initial length, l , and thickness, h_{SEI} . After a time interval, dt , the final length of the element was $l + dl$,

while its thickness becomes $h_{SEI} + dh_{SEI}$. The final volume was given by the product of the final length and the final thickness, which was equal to the initial length multiplied by the time interval and the increase of SEI thickness due to its formation reaction, q_{SEI} .

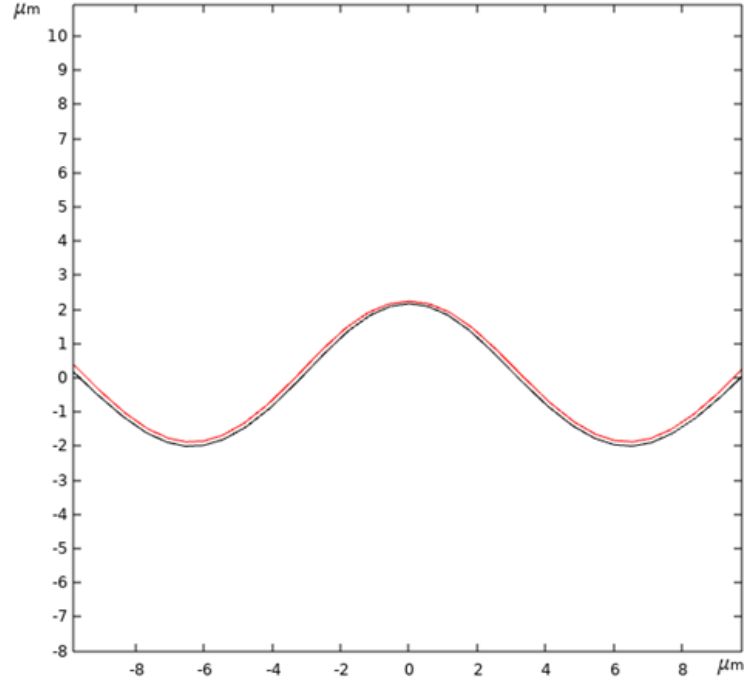


Figure 3.3: Thickness of the SEI (100 nm - red line) compared to a zoom of the 2D geometry used in our model.

Equation 3.8 can be rewritten by defining the strain rate of the substrate surface, $\dot{\epsilon}$, equal to $dl/(l dt)$. Thus, leading to the following growth equation [15], which was used in this work:

$$\frac{\partial h_{SEI}}{\partial t} = q_{SEI} - \dot{\epsilon} h_{SEI} \quad (3.9)$$

The first term on the right side of the equation is the growth rate of SEI due to its rate of reaction. The second term is the rate of coverage density reduction due to stretching of the substrate surface area. According to Liu and Lu [15], the stretching referred to the decrease of SEI coverage density associated with the increase of the substrate surface area. The stretch could be due to a physical stretch (e.g. like a rubber) or due to a change in porosity of the SEI.

The rate of reaction was proportional to the specific molar volume of the SEI, \bar{V}_{SEI} [$\text{m}^3 \cdot \text{mol}^{-1}$], multiplied by its formation current density, i_{SEI} [$\text{A} \cdot \text{m}^{-2}$], and it

was computed as follows:

$$q_{SEI} = -\frac{\bar{V}_{SEI}}{2F} i_{SEI} \quad (3.10)$$

On the other hand, the strain rate of the substrate surface was proportional to the surface curvature, κ_c [m^{-1}], and to the normal velocity of deformation of the substrate surface, v_n [$\text{m}\cdot\text{s}^{-1}$], which is explained in detail in Sec. 3.2.7. Thus, the strain rate of the substrate surface was computed as follows:

$$\dot{\epsilon} = v_n \kappa_c \quad (3.11)$$

The SEI formation current density was computed according to the Tafel-type kinetics used by Lin *et al.* [83]. In their work, they modeled the SEI formation reaction between the lithiated graphite negative electrode and the electrolyte solvent. This model can be extended to lithium metal electrodes, since, as experimentally shown by Aurbach *et al.* in 1994 [84], the electrolyte reduction reactions occurring on the graphite surface are very similar to the ones on the lithium metal. In Lin *et al.* study, lithium ethylene dicarbonate $(\text{CH}_2\text{OCO}_2\text{Li})_2$ was considered to be the main component of the SEI layer, formed from the reaction process of ethylene carbonate (EC) with metallic lithium.

When the SEI becomes thicker, its formation reaction is slowed down because the electrolyte diffusion through the SEI is limited. This can be modeled by adding a further mass transport equation for EC, like in the work of Safari *et al.* [85]. Alternatively, which was the approach adopted in this thesis work, the decaying growth rate with respect to the thickness of the SEI film can be approximated by an exponential decay function, which was added to the following equation dictating the current associated with SEI formation:

$$i_{SEI} = -e^{-\lambda h_{SEI}} F k_{SEI} c_{sol} \exp\left(\frac{\alpha_{SEI} F \Phi}{RT}\right) \quad (3.12)$$

where λ [m^{-1}] is a scale factor of the SEI formation current with respect to the SEI thickness, k_{SEI} [$\text{m}\cdot\text{s}^{-1}$] the SEI reaction rate constant, c_{sol} [$\text{mol}\cdot\text{m}^{-3}$] the solvent concentration, and α_{SEI} [-] the charge transfer coefficient of SEI formation reaction.

Fig. 3.4 shows a representation of the different current densities used in the model. An applied current density, i_{app} was placed at the top boundary of the elec-

trolyte domain; while a total lithium current density, i_{tot} arrived at the SEI interface. The total current density was the sum of the SEI formation current density, i_{SEI} and the lithium reaction current density, i_{BV} , described by a Butler–Volmer equation.

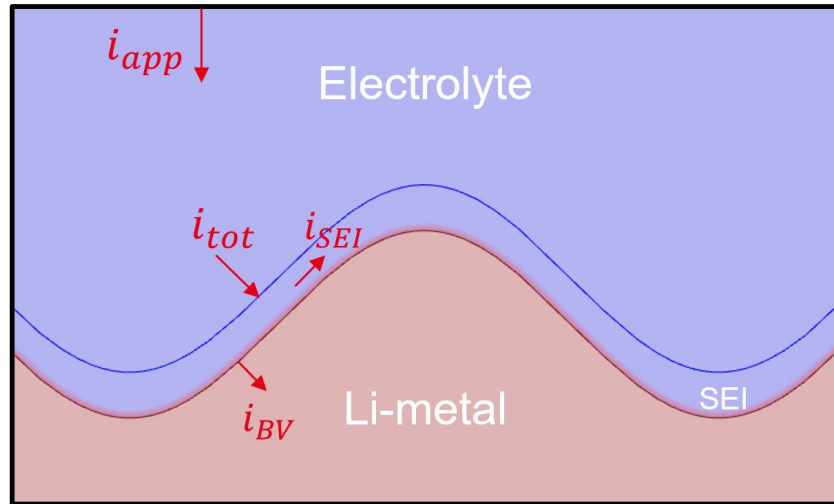


Figure 3.4: Graphical representation of the different current densities used in the model.

3.2.3 Mass Transport in the SEI

In the literature, the division of the SEI in outer and inner layers is often presented [18] [69] [49]. As described in the previous chapter, the outer layer is a porous layer composed of organic materials mostly coming from the decomposition of electrolyte solvents [83] [84], while the inner layer is dense and not porous, mostly composed of inorganic products coming from lithium salt decomposition. Lithium diffusion follows Fick’s law through the outer layer, while the mechanism of transport within the inner layer remains uncertain, but theorized to happen through knock off diffusion [18].

The other models presented in the literature adopted different approaches to model mass transport within the SEI. In Yoon *et al.* work [16] the diffusion mechanism was simplified by assuming a linear drop in lithium concentration across the whole SEI thickness, in the case of a bi-ionic conducting SEI; and a zero concentration drop in the case of a single-ionic conducting SEI. The latter was justified by their claim that the typical SEI layer is mostly composed of inorganic compounds [16], which has not major matches in the literature. As described at the beginning of the section, an

accurate model should describe the bi-layer nature of the SEI, thus containing both a part in which the concentration of lithium ions drops (outer organic layer) and a part in which lithium ions concentration is uniform (inner inorganic layer).

On the other hand, Liu and Lu [15] did not consider at all lithium concentration across the SEI layer, despite their work was based on the model of Lin *et al.* [83], which considered an organic component (lithium ethylene dicarbonate) as the main component of the newly formed SEI. As explained in section 1.2.5, lithium transport phenomena in the organic components of the SEI follows the Fick's law, thus, lithium concentration drop has to be considered in order to be consistent with the physical phenomenon.

Since the presented model was based as well on the assumption of Lin *et al.* [83] and to be consistent with the differential EIS experiments (presented in chapter 2 and performed in chapter 5), which found a single average value of diffusion coefficient in the SEI, a linear drop in lithium ion concentration across the SEI was assumed in this thesis work, according to the following equation:

$$c_{e,s} = c_e - \frac{1 - t_+}{FD_{SEI}} h_{SEI} i_{tot} \quad (3.13)$$

where $c_{e,s}$ [mol.m⁻³] is the lithium concentration at the SEI/lithium metal interface, c_e [mol.m⁻³] the salt concentration at the electrolyte/SEI interface and D_{SEI} [m².s⁻¹] the lithium diffusion coefficient inside the organic SEI.

Eq. 3.13 was derived from the following Fick's second law:

$$\frac{\partial c_{e,SEI}}{\partial t} = D_{SEI} \frac{\partial^2 c_{e,SEI}}{\partial n_x^2} \quad (3.14)$$

where $c_{e,SEI}$ [mol.m⁻³] is the lithium concentration within the SEI and n_x is the direction that is normal to the lithium surface.

By assuming that the SEI thickness was thin, thus the lithium concentration within it was constant, the previous equation could be solved analytically (first equation of 3.15), under the assumptions that the gradient of the concentration was proportional to the total current density (second equation of 3.15); and at $n_x = 0$, thus at the electrolyte/SEI interface, the concentration in the SEI was equal to the concentration

in the electrolyte (third equation of 3.15).

$$\begin{cases} c_{e,SEI} = A_1 n_x + A_2 & 0 \leq n_x \leq h_{SEI} \\ D_{SEI} \frac{\partial c_{e,SEI}}{\partial n_x} = -\frac{1-t_+}{F} i_{tot} & 0 \leq n_x \leq h_{SEI} \\ c_{e,SEI} = c_e & n_x = 0 \end{cases} \quad (3.15)$$

where A_2 and A_1 are the constants of integration, and are respectively equal to c_e and $-(1-t_+)i_{tot}/(FD_{SEI})$. Thus, by substituting the constants of integration the following equation was obtained:

$$c_{e,SEI} = c_e - \frac{1-t_+}{FD_{SEI}} n_x i_{tot} \quad (3.16)$$

Lastly, by solving the previous equation at the SEI/lithium interface, thus at $n_x = h_{SEI}$, Eq. 3.13 was obtained. Fig. 3.5 summarizes and shows the different concentration-related definitions used in this section.

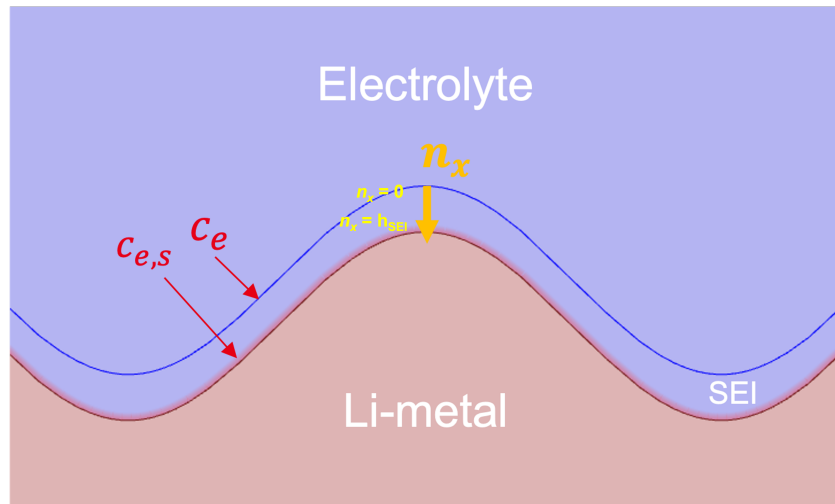


Figure 3.5: Graphical representation of the different concentration-related definitions used in this section.

3.2.4 SEI Mechanics

As pointed out in the experimental literature [11], the mechanics of the SEI influences dendrite nucleation and growth, in particular in the case of whiskers. Despite this, the continuum multi-domain models that incorporated the SEI component [16] [15], did not take into account the mechanics of the SEI.

In our study, the displacement of the SEI was joint with the displacement of the underneath lithium metal electrode. Therefore, the deposition of lithium on the solid electrode, and the consequent change in morphology of the surface, induced a displacement of the SEI, thus, a deformation. The SEI deformation caused mechanical stress within the SEI, which by hypothesis was initially stress-free. Therefore, the stressed SEI applied a pressure on the lithium metal surface, which led to elastic and eventually plastic deformation in the lithium metal.

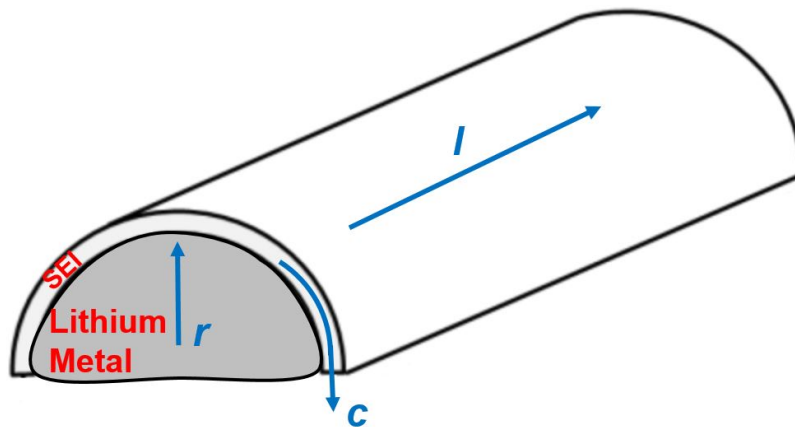


Figure 3.6: Cylindrical thin-walled SEI covering lithium metal electrode. Radial, circumferential and longitudinal directions are highlighted.

In this work, we seeked 2D simulations of the lithium deposition and stripping. Therefore, the mechanics of the SEI was modeled according to the thin-walled cylinder theory, since the wall thickness, in this case the SEI thickness, was much smaller than the characteristic radius of the defect. Fig. 3.6 shows a 3D cylindrical geometry of the SEI, covering the lithium metal electrode. In the figure three main coordinates can be distinguished: radial, circumferential and longitudinal (axial).

Under the hypotheses that the SEI behaved like an isotropic material and that the aforementioned main coordinates were the three principal directions, the principal stress and the principal strains were related by the Hooke's law, according to the

following system of equations:

$$\begin{cases} \epsilon_l = \frac{\sigma_l}{E_{SEI}} - \frac{\nu_{SEI}}{E_{SEI}} (\sigma_c + \sigma_r) \\ \epsilon_c = \frac{\sigma_c}{E_{SEI}} - \frac{\nu_{SEI}}{E_{SEI}} (\sigma_l + \sigma_r) \\ \epsilon_r = \frac{\sigma_r}{E_{SEI}} - \frac{\nu_{SEI}}{E_{SEI}} (\sigma_l + \sigma_c) \end{cases} \quad (3.17)$$

where the subscript l refers to the tangential direction, the subscript c refers to the circumferential direction and the subscript r refers to the radial direction; while E_{SEI} [Pa] and ν_{SEI} [-] are respectively the Young's modulus and the Poisson's ratio of the SEI.

In the thinned-walled theory, the radial stress, σ_r [Pa], is the minimum principal stress and it varies in magnitude from the internal pressure, p , at the inner surface to zero at the outer surface. Therefore, the radial stress was negligible compared to the other two stresses. Moreover, since the geometry considered in this work was 2D, deformations in the longitudinal direction were not allowed, thus $\epsilon_l = 0$. Therefore, both σ_r and ϵ_l were taken equal to zero, and the previous system of the equation, Eq. 3.17, was reduced to the following system:

$$\begin{cases} \sigma_l = \nu_{SEI} \sigma_c \\ \epsilon_c = \frac{1 - \nu_{SEI}^2}{E_{SEI}} \sigma_c \\ \epsilon_r = -\frac{\nu_{SEI}}{E_{SEI}} (\nu_{SEI} + 1) \sigma_c \end{cases} \quad (3.18)$$

The displacement of the SEI normal to the lithium surface, δ_r [m], was the input of the SEI mechanics subunit of the model, but it can also be computed as follows:

$$\delta_r = r_c \epsilon_c = \frac{1 - \nu_{SEI}^2}{E_{SEI}} r_c \sigma_c \quad (3.19)$$

where r_c [m] is the radius of curvature of the electrode surface, thus, the radius of curvature of SEI.

Starting from a balance of forces across the interface between the internal pressure

and the thin-wall stress, for the thin-walled assumption, the circumferential stress (or hoop stress) was computed with the following equation:

$$\sigma_c = \frac{pr_c}{h_{SEI}} \quad (3.20)$$

It is worth to notice that in the classic thin-walled theory applied to pressure vessels, the cylindrical or spherical object is subjected to an internal pressure, which can lead to a deformation or expansion of the vessel itself. Thus, in the classic theory, the pressure is used as an input. On the contrary, in this model the pressure was unknown, while the deformation of the vessel (SEI) was known. Under the hypothesis that the pressure the SEI applied on the lithium surface, p_{SEI} , was equal and opposite in sign to the internal pressure, Eq. 3.20 can be rewritten as follows:

$$\sigma_c = -\frac{p_{SEI}r_c}{h_{SEI}} \quad (3.21)$$

The circumferential stress computed in Eq. 3.21 can be substituted in Eq. 3.19, leading to the following formula to compute the SEI pressure:

$$p_{SEI} = -\frac{E_{SEI}}{1 - \nu_{SEI}^2} \frac{\epsilon_c}{r_c} h_{SEI} \quad (3.22)$$

Therefore, the applied pressure was a function of the mechanical properties of the SEI, E_{SEI} , ν_{SEI} , the change in morphology of the surface, ϵ_c , r_c , and the thickness of the SEI, h_{SEI} .

Following the experimental results of Yoon *et al.* [73], presented in chapter 2 in Fig. 2.26, it was decided to assume the SEI to have an elastic–perfectly plastic behavior. Therefore, an elastic limits, $\sigma_{y,SEI}$ [Pa], was defined, above which the SEI shows perfectly plastic behavior. Thus, depending on the magnitude of the stress, the circumferential stress was computed as follows:

$$\begin{cases} \sigma_c = \frac{E_{SEI}\epsilon_c}{1 - \nu_{SEI}^2} & \text{if } \sigma_c < \sigma_{y,SEI} \\ \sigma_c = \sigma_{y,SEI} & \text{if } \sigma_c \geq \sigma_{y,SEI} \end{cases} \quad (3.23)$$

Finally, taking into account the possible elastic limit and the plastic behavior of the SEI, the applied pressure depends on the circumferential stress, defined in Eq. 3.23,

and it was computed as follows:

$$p_{SEI} = -\frac{\sigma_c h_{SEI}}{r_c} \quad (3.24)$$

3.2.5 Lithium Electrode Mechanics

In this work, lithium electrode mechanics was modeled following the assumptions made by Ferrese *et al.* [51]. Lithium was considered to be an isotropic crystalline material, thus, the new layers of deposited lithium had the same stress state of the previous adjacent one. Lithium behaved as a ductile metal, therefore, it was governed by the following Hooke's law:

$$\bar{\sigma}_{Li} = \frac{E_{Li}}{1 + \nu_{Li}} \bar{\epsilon}_{Li} + \frac{E_{Li} \nu_{Li}}{(1 + \nu_{Li})(1 - 2\nu_{Li})} tr(\bar{\epsilon}_{Li}) \bar{I} \quad (3.25)$$

where $\bar{\sigma}_{Li}$ is the stress tensor within the lithium metal electrode and $\bar{\epsilon}_{Li}$ the deformation (strain) tensor, while $tr(\bar{\epsilon}_{Li})$ is the trace of the deformation tensor and \bar{I} the identity tensor. E_{Li} and ν_{Li} are respectively the Young's modulus and the Poisson's ratio of lithium metal.

The deformation tensor, used in the previous equation, was correlated to the displacement vector, \bar{u} , through the following relationship:

$$\bar{\epsilon}_{Li} = \frac{1}{2} \left(\nabla \bar{u} + (\nabla \bar{u})^T \right) \quad (3.26)$$

Eq. 3.25 is valid only if the materials behave elastically. As in the previous section about the mechanics of the SEI, a threshold between the elastic and the plastic behavior had to be set. In this thesis work, the von Mises yield criterion was used, following the work of Ferrese *et al.* [51]. It states that yielding of a ductile material begins when the Von Mises stress, σ_v reaches a critical value known as yield strength, $\sigma_{y,Li}$, which is a property of the material. The Von Mises stress was computed as follows:

$$\sigma_v^2 = \frac{1}{2} \left[(\sigma_{xx} - \sigma_{yy})^2 + (\sigma_{yy} - \sigma_{zz})^2 + (\sigma_{zz} - \sigma_{xx})^2 + (\sigma_{yz}^2 + \sigma_{zx}^2 + \sigma_{xy}^2) \right] \quad (3.27)$$

where σ_{ij} are the components of the stress tensor, $\bar{\sigma}_{Li}$.

Consistently with the experimental results from Tariq *et al.* work [68], reported in Fig. 3.7; above the yield strength, the stress was computed with the Ludwik isotropic strain hardening law:

$$\sigma_{Li} = \sigma_{y,Li} + K \epsilon_{pl}^n \quad (3.28)$$

where ϵ_{pl} [-] is the plastic parts of the total deformation, K [MPa] the hardening modulus and n [-] the hardening exponent.

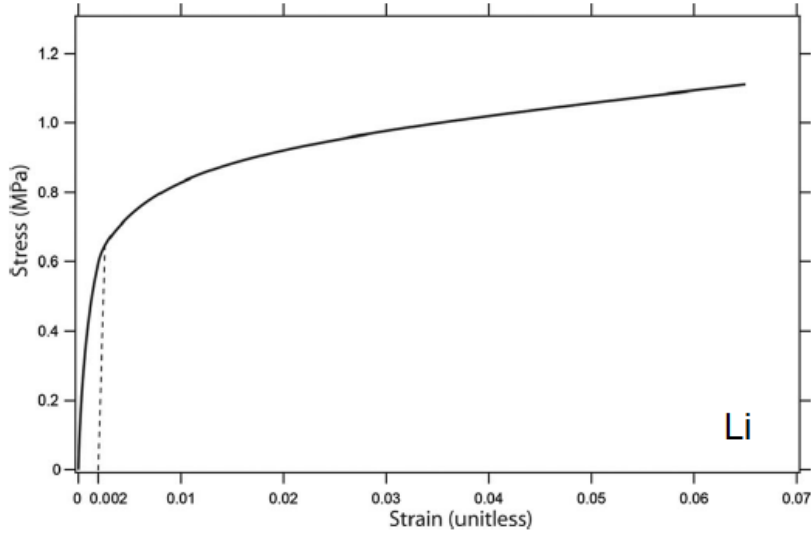


Figure 3.7: Tensile stress-strain curve of a lithium metal specimen from Tariq *et al.* work [68].

Later, in 2019, Masias *et al.* [86] and LePage *et al.* [87] pointed out that besides elastic and plastic deformation lithium metal experiences also creep deformation. This deformation mechanism occurs below the yield strength when the material is closed to its melting point and leads to permanent deformation. Given the low melting temperature of lithium (453 K), lithium metal can experience creep deformation also at ambient temperature [86] [87]. The creep mechanism of deformation is dependent on the strain rate, defined as the temporal derivative of the strain (or deformation) tensor. Thus the deformation is time dependent. Nevertheless, since the proposed model is isothermal, creep deformation was neglected and following the work of Ferrese *et al.* in [51], the time independent plasticity assumption was made. This assumption states that if the tensile stress-strain curves measured at room temperature are changed by only a few percent when the strain rate is changed by an order of magnitude or more, then the stress-strain curve does not depend on

the strain rate. Time independent plasticity was supported by the tensile stress-strain curves performed on a lithium specimen by Tariq *et al.* in their work [68].

The Cauchy momentum equation (called "equation of motion" in [51]) was used to compute the stress tensor within the lithium metal and it was defined as follows:

$$\frac{D\bar{v}}{Dt} = \frac{1}{\rho_{Li}} \frac{\partial \bar{\sigma}_{Li}}{\partial x} + \bar{f} \quad (3.29)$$

where D/Dt is the material derivative, \bar{v} [m.s⁻¹] the flow velocity vector field, ρ_{Li} [kg.m⁻³] the density of lithium metal and \bar{f} a vector containing all of the accelerations caused by body forces (*e.g.* the gravitational term). For the time independent plasticity hypothesis, the mechanical model could be assumed to be in static equilibrium at each time of the electrochemical model, thus the inertial term of the previous equations could be neglected. Moreover body forces were neglected as well, simplifying Eq. 3.29 in the following equation:

$$\frac{\partial \bar{\sigma}_{Li}}{\partial x} = 0 \quad (3.30)$$

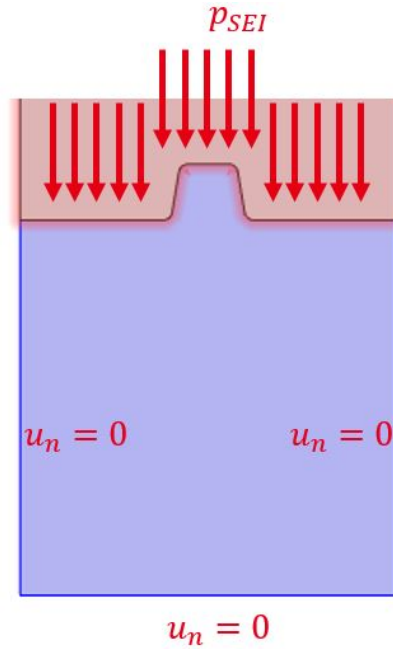


Figure 3.8: Lithium domain from the geometry used in the model in blue, with the boundary conditions of Eq. 3.30.

The previous equation was solved within the 2D lithium metal domain, represented in blue in Fig. 3.8, where its boundary conditions regarding the SEI applied pressure and normal displacement, u_n , are highlighted as well. Like in the work of Ferrese *et al.* in [51], the stresses in the direction perpendicular to the domain were neglected, plus, it was assumed that the lithium did not squeeze out the sides if under compression and it was supported along the bottom. Thus, the normal displacement along the bottom, left and right boundaries was set equal to zero. Differently from Ferrese *et al.* in [51], the opposition to lithium deformation at the top boundary (lithium/electrolyte interface) was not provided by a solid separator but by the SEI. Therefore, the pressure computed in Eq. 3.24 was used as boundary condition for Eq. 3.30.

As reported at the beginning of this chapter, lithium metal was considered to be stress-free at the beginning of the simulation, therefore this was used as initial condition of Eq. 3.30.

3.2.6 Modified Butler-Volmer

In all the multi-domain continuum models presented in chapter 2, lithium deposition and stripping were modeled with a Butler-Volmer kinetics. As presented in chapter 2, Monroe and Newman [46] extended the kinetic model to include the effect of mechanical forces, resulting in a modified Butler-Volmer. This section presents the theory behind the Butler-Volmer relationship used in this work, which includes the electrochemical and mechanical effects of the SEI.

Since lithium metal electrodes experience a huge variation in volume during lithium deposition a distinction between the undeformed state and the deformed state had to be made. Fig. 3.9 is taken from the original work of Monroe and Newman [46] and it defines the different thermodynamics phases used in this theory.

For the purpose of this work, the following phases had to be defined. Phase α' and β' are respectively the undeformed electrode and the electrolyte. On the other hand, α and β represent the deformed electrode and the electrolyte close to the deformed electrode.

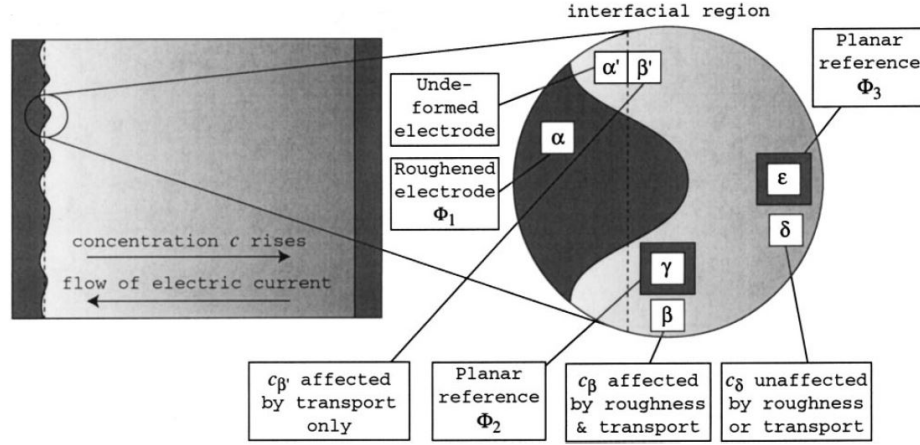


Figure 3.9: Graphical representation of the different phases used by Monroe and Newman in their theory [46].

The electrochemical equilibrium across the surfaces was defined by the following equation:

$$\mu_{Li} = \mu_{Li^+} + \mu_{e^-} \quad (3.31)$$

where μ [$\text{J}\cdot\text{mol}^{-1}$] is the electrochemical potential, the subscript Li refers to the lithium in the metal phase, α , the subscript Li^+ represents to the lithium ion in the electrolyte phase, β , and e^- is the electron. Since the valence of the lithium cation is one, the valence term did not show in the equation.

The next step was to define the electrochemical potential of the lithium metal and the lithium ion. It was assumed that the electrochemical potential depends on the temperature, T , and the pressure, p , of the system, and the concentrations of the elements present in the system, c_i . Thus, the total differential of electrochemical potential in the lithium metal could be defined as follows:

$$d\mu_{Li} = \left. \frac{\partial \mu_{Li}}{\partial p} \right|_{T, c_{Li}} dp + \left. \frac{\partial \mu_{Li}}{\partial c_{Li}} \right|_{T, p} dc_{Li} \quad (3.32)$$

While for the electrolyte phase the total differential of electrochemical potential was the following:

$$d\mu_{Li^+} = \left. \frac{\partial \mu_{Li^+}}{\partial p} \right|_{T, c_{Li^+}, c_{a^-}, c_{sol}} dp + \left. \frac{\partial \mu_{Li^+}}{\partial c_{Li^+}} \right|_{T, p, c_{a^-}, c_{sol}} dc_{Li^+} + \left. \frac{\partial \mu_{Li^+}}{\partial c_{a^-}} \right|_{T, p, c_{Li^+}, c_{sol}} dc_{a^-} + \left. \frac{\partial \mu_{Li^+}}{\partial c_{sol}} \right|_{T, p, c_{Li^+}, c_{a^-}} dc_{sol} \quad (3.33)$$

where the subscript a^- refers to anion species present in the electrolyte and sol refers to the electrolyte solvent.

By defining the partial derivative of the electrochemical potential with respect to the pressure as its partial molar volume, \bar{V} , and by making explicit the dependence of the electrochemical potential on the molar activity coefficient, f , Eq. 3.32 could be rewritten as follows:

$$d\mu_{Li} = \bar{V}_{Li} dp + RT \left[1 + \left. \frac{\partial \ln f_{Li}}{\partial \ln c_{Li}} \right|_{T, p} \right] d \ln c_{Li} \quad (3.34)$$

To find the change in the electrochemical potential between the deformed and the undeformed state, Eq. 3.34 could be integrated between the phases α and α' :

$$d\mu_{Li}^{\alpha} - d\mu_{Li}^{\alpha'} = \int_{\alpha'}^{\alpha} \bar{V}_{Li} dp + RT \int_{\alpha'}^{\alpha} \left[1 + \left. \frac{\partial \ln f_{Li}}{\partial \ln c_{Li}} \right|_{T, p} \right] d \ln c_{Li} \quad (3.35)$$

Under the hypothesis that concentration changes due to volume strain were negligible, the second term on the right-side of the previous equation could be neglected. Moreover, under the assumption that molar volumes were unaffected by small deformations, Eq. 3.35 could be simplified as follows:

$$\mu_{Li}^{\alpha} - \mu_{Li}^{\alpha'} = \bar{V}_{Li} \Delta p^{\alpha, \alpha'} \quad (3.36)$$

where $\Delta p^{\alpha, \alpha'}$ is the change in pressure in the metal phase between the deformed and the undeformed state.

Eq. 3.34 and Eq. 3.35 could be written also for the electrolyte phase, following the same assumption, but for sake of simplicity, they are not reported in this work. Anyhow, they led to the following equation:

$$\mu_{Li^+}^{\beta} - \mu_{Li^+}^{\beta'} = \bar{V}_{Li^+} \Delta p^{\beta, \beta'} \quad (3.37)$$

where $\Delta p^{\beta, \beta'}$ is the change in pressure in the electrolyte phase between the deformed and the undeformed state.

Therefore, it was possible to define, at the equilibrium, the difference in electrochemical potential of electrons in the deformed and undeformed states as follows:

$$\Delta \mu_{e^-}^{\alpha', \alpha} = \bar{V}_{Li} \Delta p^{\alpha, \alpha'} - \bar{V}_{Li^+} \Delta p^{\beta, \beta'} \quad (3.38)$$

By balancing the forces on the phases α and β on the interface the following equation could be written:

$$\bar{n} \cdot (\bar{\sigma}^{\alpha} - \bar{\sigma}^{\beta}) - \gamma \kappa_c = 0 \quad (3.39)$$

where γ [J.m⁻²] is the surface energy and κ_c [m⁻¹] the surface curvature of the lithium metal surface.

The stress tensor, $\bar{\sigma}$ could be decomposed in its deviatoric component, $\bar{\tau}$ and hydrostatic part, p . Thus, Eq. 3.39 could be rewritten in the following manner:

$$(p^{\alpha} - p^{\beta}) + \bar{n} \cdot [\bar{n} \cdot (\bar{\tau}^{\alpha} - \bar{\tau}^{\beta})] - \gamma \kappa_c = 0 \quad (3.40)$$

Therefore, by substituting Eq. 3.40 into Eq. 3.38, the change in electrochemical potential due to the mechanical stress and surface curvature effects, $\Delta \mu_{e^-}^{\alpha', \alpha}$, could be computed as follows:

$$\Delta \mu_{e^-} = -\frac{\bar{V}_{Li} + \bar{V}_{Li^+}}{2} [\bar{n} \cdot [\bar{n} \cdot (\bar{\tau}^{\alpha} - \bar{\tau}^{\beta})] - \gamma \kappa_c] + \frac{\bar{V}_{Li} - \bar{V}_{Li^+}}{2} (\Delta p^{\alpha} + \Delta p^{\beta}) \quad (3.41)$$

In the previous equation, for sake of simplicity and clarity, the superscript (α', α) was dropped. Thus from now on, the change in electrochemical potential due to mechanics will simply be called $\Delta \mu_{e^-}$. In order to make the demonstration more fluent, few steps to arrive at Eq. 3.41 were skipped. The full and detailed demonstration is available in Monroe and Newman work [46].

This approach to account the mechanical effects on the kinetics of reaction, detailed by Monroe and Newman [46], was used by Monroe and Newman themselves

[47] and by Barai *et al.* [80] [82] [88] to model the effect of a solid electrolyte (PEO-based). On the other hand, Ferrese and Newman [51] used the same approach to model the effect of a stiff separator.

Differently from the above mentioned models, the proposed model used a liquid electrolyte and neglected the effects of the separator, but it added the SEI component. Therefore, the phase β , shown in Fig. 3.9, did not refer to the electrolyte but to the SEI, while α always referred to the lithium metal electrode. Thus, Eq. 3.41 became the following equation:

$$\Delta\mu_{e^-} = -\frac{\bar{V}_{Li} + \bar{V}_{Li^+}}{2} [\bar{n} \cdot [\bar{n} \cdot (\bar{\tau}_{Li} - \bar{\tau}_{SEI})] - \gamma\kappa_c] + \frac{\bar{V}_{Li} - \bar{V}_{Li^+}}{2} (\Delta p_{Li} + \Delta p_{SEI}) \quad (3.42)$$

Eq. 3.43 is the equation that was used in our model, and it is a simplified version of Eq. 3.41, with the assumption that the contribution of the deviatoric stress was an order of magnitude lower than the contribution of the pressure, as pointed out by Fu *et al.* [89]. This assumption resulted in a small error on the numerical results but not on the numerical trends, since the contribution of the deviatoric stress is always destabilizing [89]. As well, the simplified expression did not include the contribution of the interfacial surface, since, as pointed out by Newman and Monroe [47] and by Liu and Lu [15], its contribution at this length scale is negligible.

$$\Delta\mu_{e^-} = \frac{\bar{V}_{Li} - \bar{V}_{Li^+}}{2} (\Delta p_{Li} + \Delta p_{SEI}) \quad (3.43)$$

A problem rising from the previous equation was finding the partial molar volume of cations, \bar{V}_{Li^+} , which cannot be obtained by direct measurements [46]. Under the assumption that the sum of the cation and anion transport numbers equals 1, in this work, the following relationship, proposed by Newman and Chapman [90], was used:

$$\bar{V}_{Li^+} = (1 - t_+) \bar{V}_{SEI} \quad (3.44)$$

The hydrostatic stresses in Eq. 3.43 were computed from the first invariant (trace) of the stress tensor. The hydrostatic stress of lithium metal, Δp_{Li} , was computed as follows, from the solution of the simplified Cauchy momentum equation in the domain (Eq. 3.30).

$$\Delta p_{Li} = -\frac{tr(\bar{\sigma}_{Li}^-)}{3} \quad (3.45)$$

On the other hand, the hydrostatic stress of SEI was obtained by averaging the sum of tangential, circumferential and radial stress, defined in Eq. 3.18 and 3.20, resulting in the following relation:

$$\Delta p_{Li} = -\frac{p_{SEI} r_c}{3h_{SEI}} (1 + \nu_{SEI}) \quad (3.46)$$

Once the change in electrochemical potential due to the mechanical stress was defined in Eq. 3.43, its impact on the kinetics of the reaction had to be expressed. Usually, the lithium reaction current density is modeled with the following Butler-Volmer equation:

$$i_{BV} = i_0 \left[\exp\left(\frac{\alpha_a F \Phi}{RT}\right) - \exp\left(-\frac{\alpha_c F \Phi}{RT}\right) \right] \quad (3.47)$$

where i_0 [A.m⁻²] is the exchange current density, α_a and α_c [-] are, respectively, the anodic and cathodic transfer coefficients; Φ [V] is the surface overpotential. Both i_0 and Φ were modified to take into account the electrochemical and mechanical effects of the SEI.

Fig. 3.10 shows the energy landscape of the lithium redox reaction, and it can be followed in both directions, from left to right in case of an anodic reaction (stripping), and from right to left in case of a cathodic reaction (deposition). Following Eyring theory [91], each reaction could be written as follows:

$$r = \frac{k_b T}{h_p} \exp\left(-\frac{E_a}{RT}\right) \quad (3.48)$$

where k_b [J.K⁻¹] is the Boltzmann constant, h_p [J.s] is the Planck constant and E_a [J.mol⁻¹] the energy of activation, which is the energy barrier that has to be overcome in order to make the reaction happen.

As reported in Fig. 3.10, the mechanics modifies the energy diagram along the lithium redox reaction path (difference between the continuous line and the dotted one), thus affecting i_0 and Φ . Associated with the rate of reaction, r , a reaction current density could be defined as follows:

$$i = i_{00} \exp\left(-\frac{E_a}{RT}\right) \quad (3.49)$$

where i_{00} [$\text{A}\cdot\text{m}^{-2}$] is the reference exchange current density, which is the exchange current density at an undeformed interface and at reference concentration.

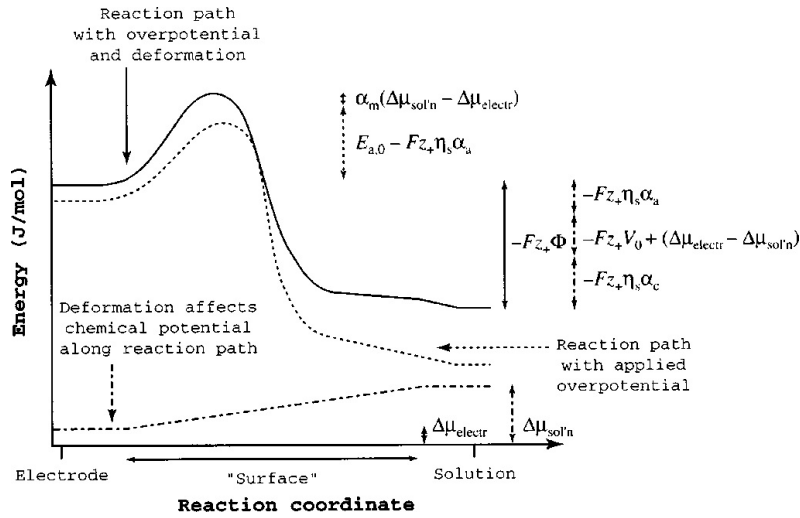


Figure 3.10: Energy landscape during lithium redox reactions. The dotted line represents the profile affected only by the applied overpotential, while the continuous line takes into account the effects of interfacial deformation [46].

The activation energy is different depending on the direction in which the energy landscape of Fig. 3.10 is followed. In both cases it can be seen as the sum of different contributions. In this work, the following ones were highlighted:

- A reference value defined at standard pressure and at a reference value of concentration, $E_{a,ref}$.
- The contribution of the configurational entropy, $E_{a,conf}$, which takes into account when the values of concentrations differ from the reference ones.
- The mechanical contribution, $\Delta\mu_{e^-}$.
- The contribution of the electric potential, $F\Phi$.

Thus, the anodic, i_a , and cathodic, i_c , currents densities could be written as follows:

$$i_a = i_{00} \exp\left(-\frac{E_{a,ref} + E_{a,conf} + \Delta\mu_{e^-}}{RT}\right) \exp\left(\frac{\alpha_a F \Phi}{RT}\right) \quad (3.50)$$

$$i_c = i_{00} \exp\left(-\frac{E_{a,ref} + E_{a,conf} + \Delta\mu_{e^-}}{RT}\right) \exp\left(-\frac{\alpha_c F \Phi}{RT}\right) \quad (3.51)$$

In order to obtain the Butler-Volmer from equation 3.47, Eq. 3.51 had to be

subtracted to equation 3.50. Thus, under the hypothesis that α_a was equal to α and α_c was equal to $(1 - \alpha)$, and by taking into account the mass transport in the SEI, which modified the surface concentration, the exchange current density from Eq. 3.47 could be defined as follows:

$$i_0 = i_{00} \left(\frac{c_{e,s}}{c_{e,0}} \right)^\alpha \exp \left(\frac{(1 - \alpha) \Delta\mu_{e^-}}{RT} \right) \quad (3.52)$$

where i_{00} took into account the reference conditions; the ratio between the two concentrations accounted for the contribution of the configurational entropy; and the exponential for the mechanical contribution.

As well, the overpotential, Φ , used in Eq.3.47, was modified by the mechanics and by the voltage drop across the SEI. Therefore, it was computed with the following equation:

$$\Phi = \phi_s - \phi_e + \frac{\Delta\mu_{e^-}}{F} - r_{SEI} h_{SEI} (i_{BV} + i_{SEI}) \quad (3.53)$$

where r_{SEI} [$\Omega.m$] is the SEI resistivity.

To summarize this section, Eq. 3.54 shows the explicit modified Butler-Volmer equation that was used in the presented model to compute the lithium reaction current density at the lithium interface:

$$i_{BV} = i_{00} \left(\frac{c_{e,s}}{c_{e,0}} \right)^\alpha \exp \left(\frac{(1 - \alpha) \Delta\mu_{e^-}}{RT} \right) \left[\exp \left(\frac{\alpha F \left(\eta + \frac{\Delta\mu_{e^-}}{F} - r_{SEI} h_{SEI} i_{tot} \right)}{RT} \right) - \exp \left(- \frac{(1 - \alpha) F \left(\eta + \frac{\Delta\mu_{e^-}}{F} - r_{SEI} h_{SEI} i_{tot} \right)}{RT} \right) \right] \quad (3.54)$$

where η [V] was defined as $\phi_s - \phi_e$.

3.2.7 Moving geometry

Electrodeposition was modelled by prescribing a normal velocity of deposition, v_{dep} [$m.s^{-1}$], to the electrode/electrolyte interface, which was proportional to the

Butler-Volmer current density defined in Eq. 3.54. The velocity was computed as follows:

$$v_{dep} = \frac{i_{BV} \bar{V}_{Li}}{F} \quad (3.55)$$

The velocity of deposition was not the only factor that modifies the electrode/electrolyte interface. Indeed, as it was shown in section 3.2.5, the lithium metal electrode could mechanically deform. Therefore, from the quasi static momentum balance (Eq. 3.30), the displacement, \bar{u} [m], of the lithium metal, due to the mechanical effect of the SEI, was computed. Thus, the normal component to the lithium surface of the rate of displacement, \dot{u}_n [m.s⁻¹], was added to the velocity of deposition to compute the velocity of the boundary deformation, v_n [m.s⁻¹]:

$$v_n = v_{dep} + \dot{u}_n \quad (3.56)$$

The previous velocity was used as input to compute SEI deformation in the SEI mechanics subunit (Sec. 3.2.4) as show in Fig. 3.2.

3.3 Overview of the Model and Comsol[®] Environment

The model was designed to study the evolution of a surface defect at different current densities by including several interface phenomena. Tab. 3.1 displays a comparison between the proposed model and a selection of the most influential models in the literature of continuum two-domain models. The model proposed in this thesis work is 2D as most of the models in the literature and transient. It has the addition of an active SEI layer, which is not always present in the literature. Moreover, the inclusion of the mechanics of the SEI makes it cutting-edge with respect to other models.

The proposed model was implemented in Comsol[®] Multiphysics, which is a simulation software able to solve numerically partial differential equations with the finite element method. Mass and charge phenomena in the electrolyte were simulated by using tailored equations in the General Form PDEs interface, available in the Mathematics package. As well, interface phenomena, such as current densities computation, SEI thickness evolution and mass transport in the SEI were computed with tailored equations from the same package. On the other hand, the moving geometry was simulated by using the Deformed Geometry interface. According to

the Comsol® Multiphysics manual, the Deformed Geometry interface can be used in cases where the original geometry model shrinks or grows by removal or addition of material, which was the case of lithium deposition or stripping. Finally, lithium electrode mechanics was modeled by using the Solid Mechanics interface with the addition of the Plasticity module.

	Monroe <i>et al.</i> [47]	Yoon <i>et al.</i> [16]	Ferrese <i>et al.</i> [51]	Liu <i>et al.</i> [15]	Proposed Full Model
Geometry	2D	2D	2D	2D	2D
Type of Study	Stationary	Transient	Transient	Transient	Transient
Butler-Volmer Kinetics	Modified	Classic	Modified	Classic	Modified
Surface Overpotential, Φ	$\eta + \frac{\Delta\mu}{F}$	η	$\eta + \frac{\Delta\mu}{F}$	$\eta - rhi$	$\eta + \frac{\Delta\mu}{F} - rhi$
SEI Thickness Variation	No SEI	No	No SEI	Yes	Yes
SEI Mass Transport	No	Yes	No	No	Yes
SEI Mechanics	No	No	No	No	Yes

Table 3.1: Comparison between the proposed model and models in the literature.

Time dependent simulations were solved by using backward differentiation formula (BDF) methods, while the selected linear system solver was MUMPS (multifrontal massively parallel sparse direct solver). which uses direct LU decomposition. All the phenomena equations were solved in parallel. The mesh was composed of free-triangular cells. During the simulation, it was remeshed every time the mesh quality went below 0.4, because of the degradation of the initial mesh quality due to the moving geometry. The choices regarding the numerical simulation of the phenomena were made in order to improve its stability and to be able to simulate an adequate amount of deposited lithium, which enables the distinction between different regimes and structures.

In the next chapter, the results obtained with the proposed model are presented and, by analyzing the results, additional conclusion and remarks on the model are made.

Model Results

In this chapter, three sets of results are presented in order to show the effect of each phenomenon on the lithium defect evolution during electrodeposition. The three models of increasing complexity from which the results are obtained are the following and their differences are summarized in table 4.1:

- I A basic model that considers only transport phenomena in the electrode and the electrolyte, while neglecting the SEI.
- II An improved model that adds the transport phenomena inside the active SEI, which changes its thickness during the simulation.
- III The full model (presented in the previous chapter), which adds the effects of the SEI mechanics to the improved model.

Later, additional results are presented, regarding lithium stripping and porosity creation.

	Basic model	Improved model	Full model
Electrolyte Transport Phenomena	Yes	Yes	Yes
Electrode Transport Phenomena	Yes	Yes	Yes
Butler-Volmer Kinetics	Classic	Classic	Modified
Surface Overpotential, Φ	η	$\eta - rhi$	$\eta + \frac{\Delta\mu}{F} - rhi$
SEI Thickness Variation	No SEI	Yes	Yes
SEI Mass Transport	No SEI	Yes	Yes
SEI and Lithium Mechanics	No	No	Yes
Surface change due to	Deposition	Deposition	Deposition and deformation

Table 4.1: Comparison between the phenomena taken into account in the three different models presented in this chapter.

Universal gas constant, R	8.314 [J.(mol.K) ⁻¹]
Temperature, T	288.15 [K]
Faraday constant, F	96485 [C.mol ⁻¹]
Initial salt concentration, $c_{e,0}$	1000 [mol.m ⁻³]
Electrolyte diffusion coefficient, D_e	7.5 x 10 ⁻¹¹ [m ² .s ⁻¹] [51]
Electrolyte conductivity, κ	1.3 [S.m ⁻¹] [51]
Electrode conductivity, σ_s	1.1 x 10 ⁷ [S.m ⁻¹] [51]
Lithium metal specific molar volume, \bar{V}_{Li}	1.300 x 10 ⁻⁵ [m ³ .mol ⁻¹] [40]
Lithium Young's modulus, E_{Li}	4.3 [GPa] [51]
Lithium Poisson's ratio, ν_{Li}	0.33 [-] [51]
Yield strength of lithium, $\sigma_{y,Li}$	0.655 [MPa] [68]
Hardening modulus of lithium, K	1.9 [MPa] [88]
Hardening exponent of lithium, n	0.4 [-] [88]
Reference exchange current density, i_{00}	20 [A.m ⁻²] [51]
Anodic and cathodic transfer coefficients, α	0.5 [-]
SEI transfer coefficients, α_{SEI}	0.5 [-]
SEI reaction scale factor, λ	1.2 x 10 ⁷ [m ⁻¹] [15]
SEI reaction rate coefficient, k_{SEI}	6 x 10 ⁻¹⁰ [m.s ⁻¹] [15]
Transference number, t_+	0.3 [-]
Solvent concentration, c_{sol}	4541 [mol.m ⁻³] [15]
SEI specific molar volume, \bar{V}_{SEI}	9.586 x 10 ⁻⁵ [m ³ .mol ⁻¹] [15]
SEI resistivity, r_{SEI}	2 x 10 ⁵ [Ω .m] [15]
Initial SEI thickness, $h_{SEI,0}$	10 [nm] [15]
SEI diffusion coefficient, D_{SEI}	$D_e/100$ [m ² .s ⁻¹] [16]
SEI Young's modulus, E_{SEI}	245 [MPa] [73]
Lithium Poisson's ratio, ν_{Li}	0.3 [-] [73]
Yield strength of SEI, $\sigma_{y,SEI}$	8 [MPa] [73]

Table 4.2: List of the parameters and properties used in this work.

Since the chapter shows the significant influence of the SEI film on dendrites formation and growth, a sensitivity analysis on SEI properties was performed and is presented.

Tab. 4.2 lists the parameters that were used to obtain the results presented in this chapter. The electrolyte was a carbonates-based liquid electrolyte (1M LiFP₆/EC:DEC), used by Ferrese and Newman in their work [50] and by Liu and Lu [15]. The electrochemical properties of the SEI are taken from Liu and Lu model [15], while the mechanical properties of the SEI were experimentally obtained by Yoon *et al.* in their work [73]. On the other hand, the values for the mechanical properties of lithium metal were extracted from the work of Barai *et al.* [80].

4.1 Basic Model: no SEI

In this first section, the model is a simplification of the model presented in the previous chapter and it considers only two components; the lithium metal electrode and the electrolyte. Like in most of the models in the literature, the SEI was not considered. The electrolyte was liquid, thus its mechanical effect to contrast electrode volume expansion during lithium deposition was negligible.

Tab. 4.3 shows the phenomena that were considered in this first section. Mass and charge transports were modeled accordingly with section 3.2.1. Lithium deposition was described with Butler-Volmer kinetics, in which the exchange current density took into account the deviation of lithium concentration on the electrode surface with respect to the reference concentration (initial bulk concentration), and the surface overpotential was computed as the difference between the potential of the metal electrode and the one of the electrolyte. The electrode surface deformed solely due to lithium deposition which was proportional to the Butler-Volmer current density. In order to respect the principle of electroneutrality, only current densities lower than the limiting current density were used.

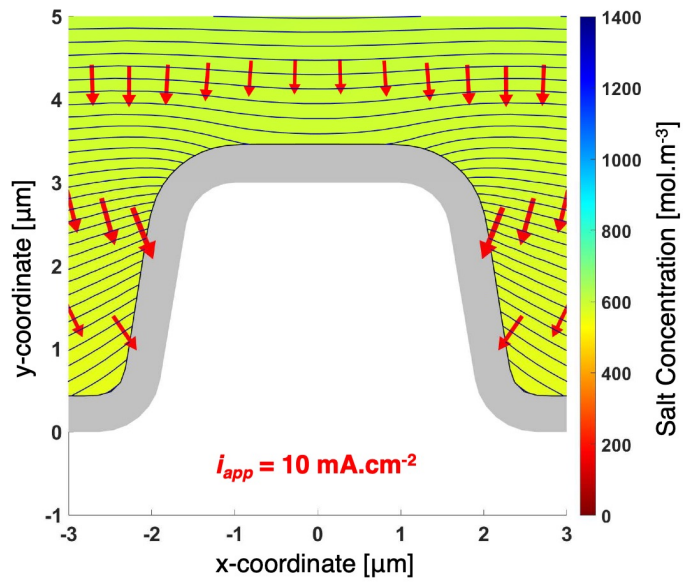
In this first set of simulations, two current densities, 10 mA.cm⁻² and 1 mA.cm⁻², were applied to the top boundary of the geometry in order to simulate the defect evolution due to lithium deposition. By assuming that the electrode capacities for lithium metal are in the range of 3 to 5 mAh.cm⁻², the current densities that were used in the simulation were in the range of C-rates between 3 and 1/3, thus, globally recognized like high-medium rates.

Mass Transport in Electrolyte	$\frac{\partial c_e}{\partial t} = D_e \frac{\partial^2 c_e}{\partial x^2}$
Charge Transport in Electrolyte	$\frac{\partial}{\partial x} \left(\kappa \frac{\partial \phi_e}{\partial x} + \frac{2RT\kappa(1-t_+)}{F} \frac{\partial \ln(c_e)}{\partial x} \right) = 0$
Charge Transport in Electrode	$\sigma_s \frac{\partial^2 \phi_s}{\partial x^2} = 0$
Butler-Volmer Current Density	$i_{BV} = i_0 \left[\exp\left(\frac{\alpha_a F \Phi}{RT}\right) - \exp\left(-\frac{\alpha_c F \Phi}{RT}\right) \right]$
Exchange Current Density	$i_0 = i_{00} \left(\frac{c_e}{c_{e,0}}\right)^\alpha$
Surface Overpotential	$\Phi = \phi_s - \phi_e$
Surface Deformation	$v_n = v_{dep}$

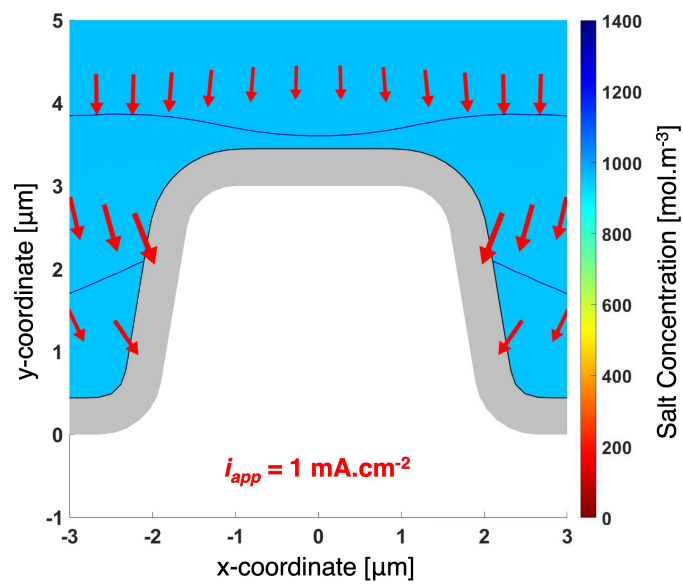
Table 4.3: Set of equations used in the basic model.

The results at the end of the simulations without the effect of the SEI are presented in Fig. 4.1. Using the 40 μm thick electrolyte shown in Fig. 3.1, the salt concentration drops to 500 $\text{mol}\cdot\text{m}^{-3}$ at the electrode surface with 10 $\text{mA}\cdot\text{cm}^{-2}$ applied current density; while it remains around the initial value of 1000 $\text{mol}\cdot\text{m}^{-3}$ with the lower current density, as shown in Fig. 4.2. The isolines of Fig. 4.1 represents a change of 1 mV in the potential of the electrolyte.

The simulations started from the same electrode surface geometry, represented in white in Fig. 4.1, while the deposited lithium is shown in gray. In order to allow a consistent comparison between the different final geometries, the simulations were ended after the same total amount of lithium is deposited (e.g. longer time for smaller current, to obtain an equivalent deposited capacity of 0.111 $\text{mAh}\cdot\text{cm}^{-2}$).



(a)



(b)

Figure 4.1: Salt concentration in the electrolyte at the end of simulation in color [mol.m⁻³]. Red arrows represent the lithium flux in the electrolyte, while black lines are the electrolyte potential isolines, separated from each other by 1 mV. Lithium deposited during the simulation in gray. a) Simulation after 40 s with an applied current of 10 mA.cm⁻². b) Simulation after 400 s with an applied current of 1 mA.cm⁻².

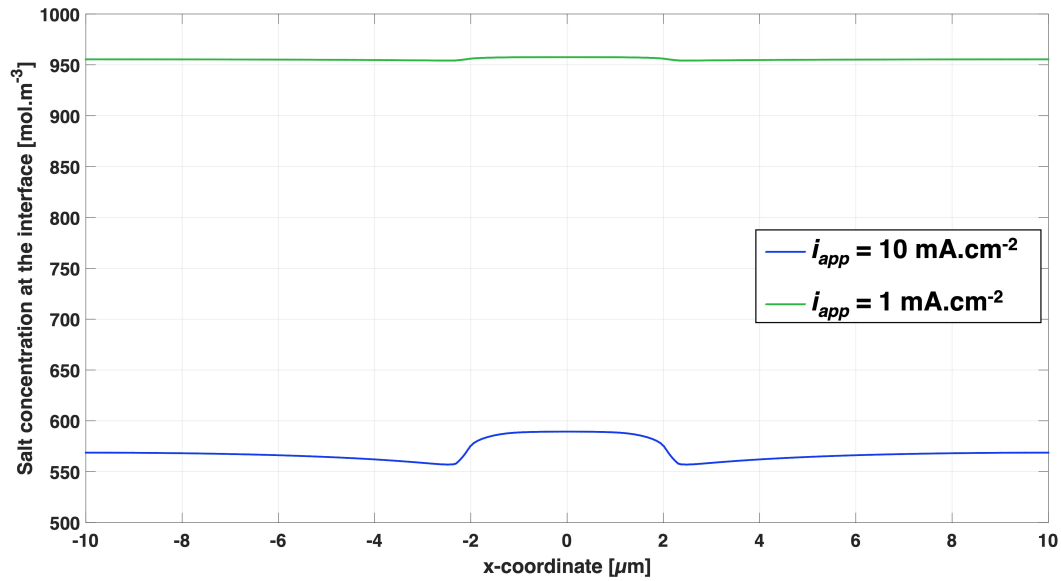


Figure 4.2: Salt concentration profiles at the lithium-electrolyte interface at the end of the simulations presented in Fig. 4.1.

Fig. 4.3 compares the final morphology of the two simulations and the initial one. The profiles show that lithium tends to deposit slightly more on the tip of the defect at higher current density magnitude, favoring the defect growth, due to the higher potential and concentration gradients in that region. On the other hand, it tends to deposit more homogeneously at lower current density, since above mentioned gradients are more uniform at lower current densities. This is consistent with the stability analysis reported in the literature [47] [88].

Both Fig. 4.4 and Fig. 4.5 corroborate the above mentioned thesis. Fig. 4.4 shows the surface overpotential at the end of the simulation. The value obtained with an applied current density of 0.1 mA.cm^{-2} is added for reference. The overpotential with higher applied current density is not only higher in magnitude but also less uniform, with a peak in magnitude in correspondence with the tip of the defect. The same variation in magnitude at high current density applied can be seen as well in the gradient of salt concentration, which is shown in Fig. 4.5. Indeed, the gradients of voltage and concentration are connected through the charge transport equation presented in Tab. 4.3.

The Butler-Volmer current density, which depends on the surface overpotential, is shown in Fig. 4.6. It is scaled with respect to the applied current to better compare the profiles with the three applied current densities. Differently from Fig. 4.3, which compared the final surface morphology, here the difference between the profiles is more prominent, with a 7% difference between the minimum and maximum Butler-

Volmer current densities on the interface at the end of the 10 mA.cm⁻² simulation, while just around 2% for lower current densities.

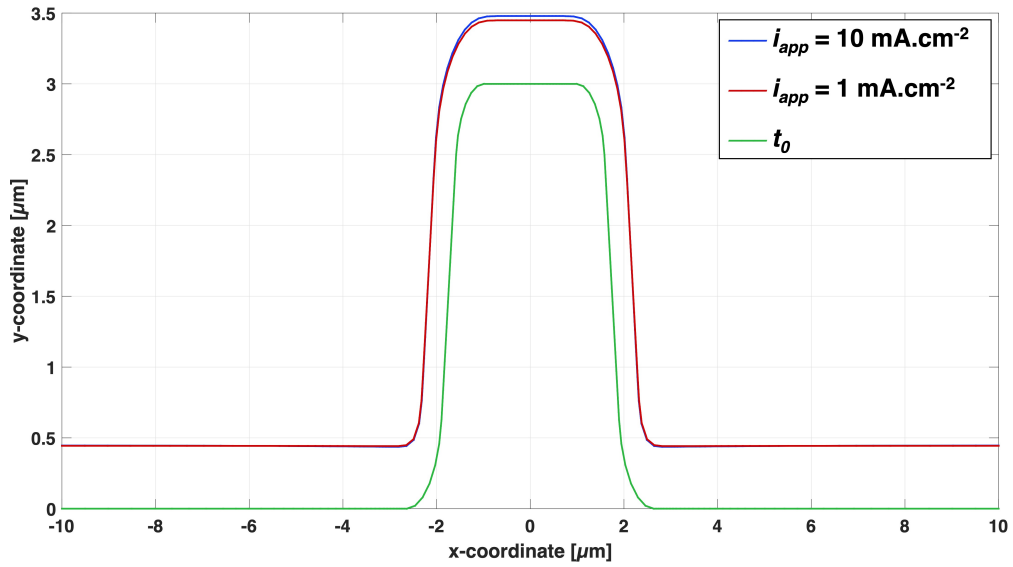


Figure 4.3: Surface profiles at the end of the simulations presented in Fig. 4.1 compared to the initial geometry.

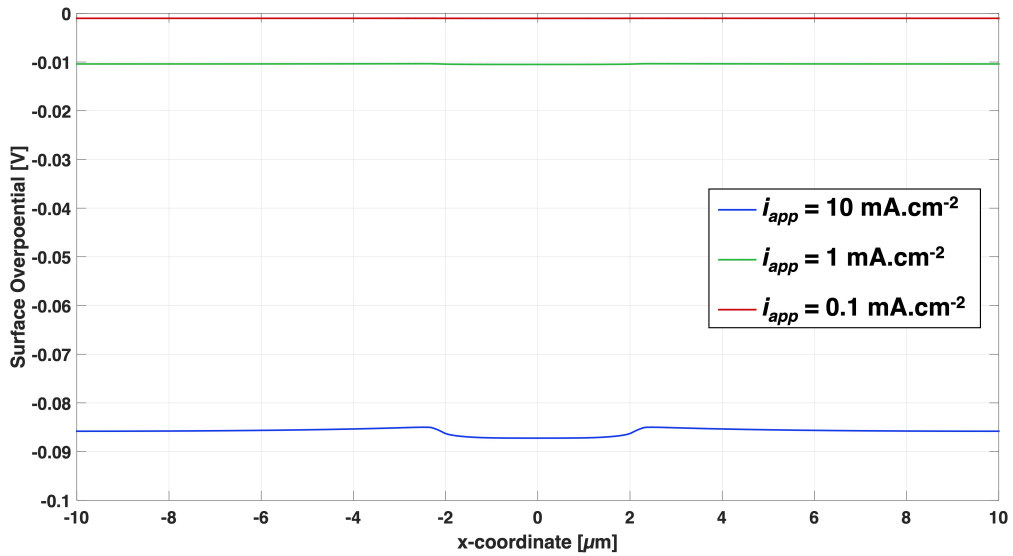


Figure 4.4: Surface overpotential profiles at the end of the simulations presented in Fig. 4.1. A new simulation with an applied current 0.1 mA.cm⁻² is added for reference.

In conclusion, no dendritic behavior was observed with these operating conditions, where the applied current density is lower than the limiting current density theorized by Chazalviel [43]. As already mentioned in the literature review chapter, experimental literature demonstrates the presence of dendrites, also at this current regime, confirming the existence of a missing piece in the basic model [48].

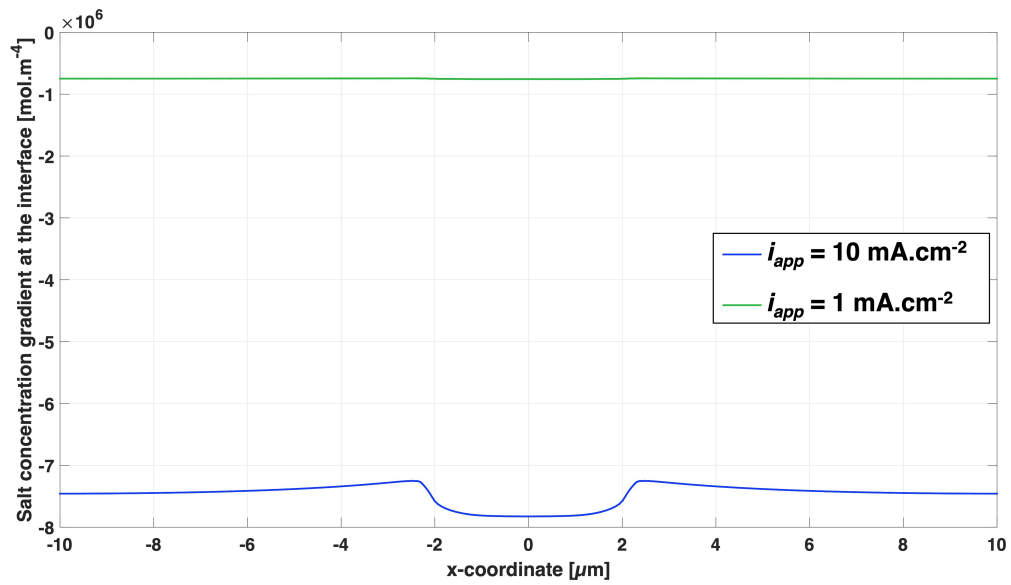


Figure 4.5: Salt concentration gradient profiles at the lithium-electrolyte interface at the end of the simulations presented in Fig. 4.1.

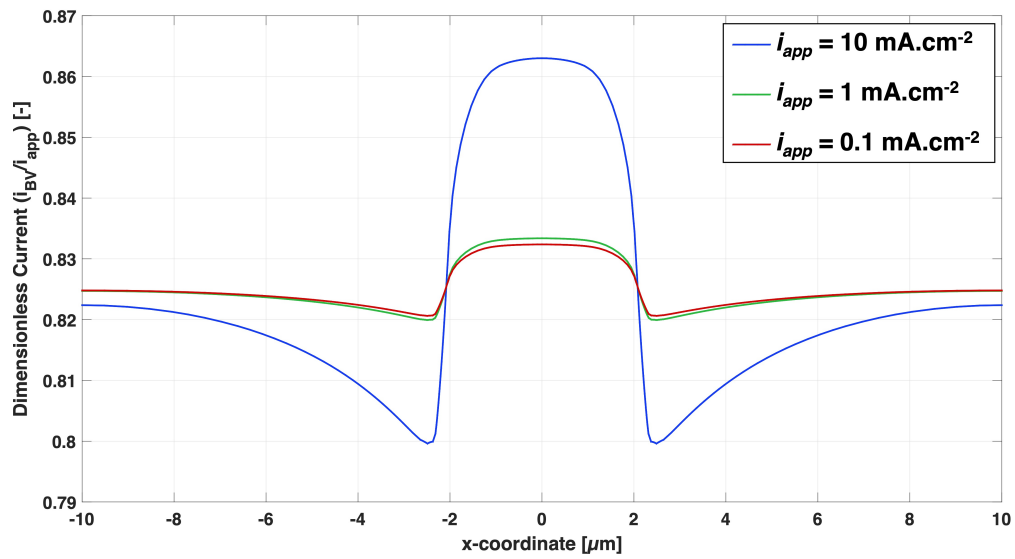


Figure 4.6: Butler-Volmer current density profiles at the end of the simulations presented in Fig. 4.1, weighted on the applied current density. A new simulation with an applied current 0.1 mA.cm^{-2} is added for reference.

4.2 Improved Model: SEI Addition, no Mechanics

Consequently, simulations with the addition of the SEI were made. In this set of simulations the effects of SEI mechanical properties were neglected. As in the previous section, equations that were used for this section are reported in a table, Tab. 4.4. Differently from the previous section, there was the addition of the SEI growth equation and consequently of the SEI formation current density. The surface overpotential was modified to add the drop in potential due to SEI resistivity. The surface concentration used in the exchange current density was modified to take into account the mass transport in the SEI, presented in Sec. 3.2.3.

Mass Transport in Electrolyte	$\frac{\partial c_e}{\partial t} = D_e \frac{\partial^2 c_e}{\partial x^2}$
Charge Transport in Electrolyte	$\frac{\partial}{\partial x} \left(\kappa \frac{\partial \phi_e}{\partial x} + \frac{2RT\kappa(1-t_+)}{F} \frac{\partial \ln(c_e)}{\partial x} \right) = 0$
Charge Transport in Electrode	$\sigma_s \frac{\partial^2 \phi_s}{\partial x^2} = 0$
Mass Transport in SEI	$c_{e,s} = c_e - \frac{1-t_+}{FD_{SEI}} h_{SEI} i_{tot}$
Butler-Volmer Current Density	$i_{BV} = i_0 \left[\exp\left(\frac{\alpha_a F \Phi}{RT}\right) - \exp\left(-\frac{\alpha_c F \Phi}{RT}\right) \right]$
Exchange Current Density	$i_0 = i_{00} \left(\frac{c_{e,s}}{c_{e,0}} \right)^\alpha$
Surface Overpotential	$\Phi = \phi_s - \phi_e - r_{SEI} h_{SEI} (i_{BV} + i_{SEI})$
SEI Growth Equation	$\frac{\partial h_{SEI}}{\partial t} = -\frac{\bar{V}_{SEI}}{2F} i_{SEI} - v_n \kappa_c h_{SEI}$
SEI Formation Current Density	$i_{SEI} = -e^{-\lambda h_{SEI}} F k_{SEI} c_{sol} \exp\left(\frac{\alpha_{SEI} F \Phi}{RT}\right)$
Surface Deformation	$v_n = v_{dep}$

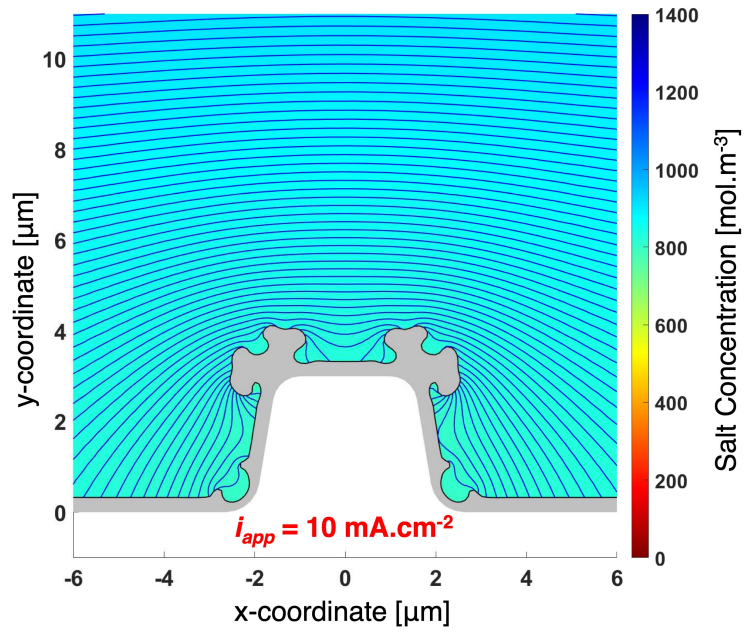
Table 4.4: Set of equations used in the improved model.

Like in the previous simulation, current densities of 10 mA.cm^{-2} and 1 mA.cm^{-2} were applied to the top boundary of the geometry, and the simulation was stopped after the same lithium plating capacity ($0.111 \text{ mAh.cm}^{-2}$). The results of the simulations are presented in Fig 4.7. Differently from the previous simulation, it is possible to spot distinct directions of growth, due to the inhomogeneous deposition of the lithium on the electrode surface. The higher the current density is, the more the directions of growth are present, resulting in the branched shape of the dendrites, as evidenced in Fig. 4.7a. At lower current density (1 mA.cm^{-2}), directions of growth are still present, but the more homogenous deposition results in a more globular growth of the dendrites (Fig. 4.7b), leading to shapes that are closer to the mossy dendrites described in the literature [11].

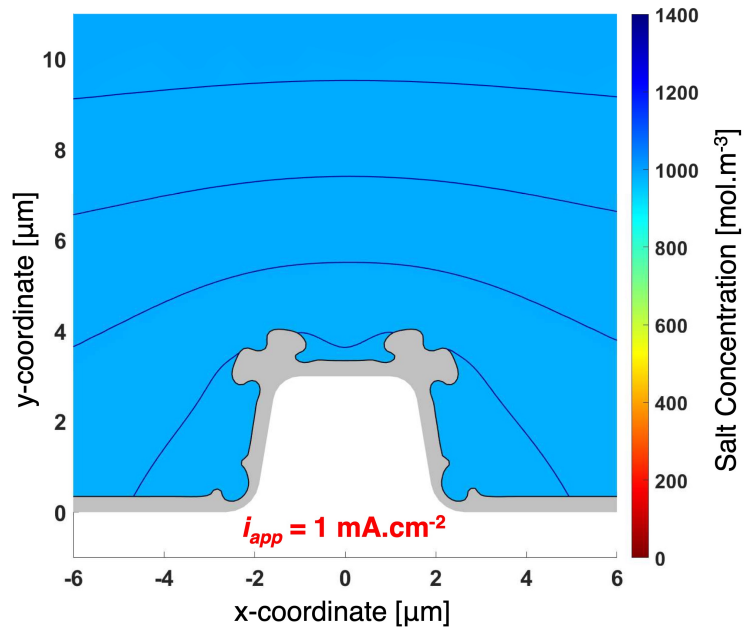
Simulations at lower current densities than 1 mA.cm^{-2} were done in order to find the conditions where the lithium deposition allows for a reabsorption of the initial defect. Through a series of simulations, for this electrolyte and this specific geometry, the current density was found to be around 0.02 mA.cm^{-2} . The results of the simulations at 0.1 and 0.01 mA.cm^{-2} current densities are presented in Fig 4.8. Fig. 4.8a shows filiform dendrites that are produced at 0.1 mA.cm^{-2} , while at 0.01 mA.cm^{-2} no dendritic behavior is present (Fig. 4.8b).

Fig. 4.7 and 4.8 shows the final morphologies of the defect compared to the initial one; and the deposited lithium layer is shown in gray. The colorbar represents the salt concentration in the electrolyte, while the isolines are equipotential lines and they are separated by 1 mV of potential drop in Fig. 4.7 and 0.1 mV in Fig. 4.8. Salt concentration drop across the electrolyte is bigger at higher current density applied, around 400 mol.m^{-3} in Fig. 4.7a, while it is negligible at lower applied current densities (Fig. 4.8). Nevertheless, also at higher current densities no lithium depletion on the electrode surface is reached.

By looking both at the salt concentration and the potential profiles across the electrolyte, it can be concluded that, in this range of applied current densities, the different dendrites morphologies are correlated to interfacial phenomena and properties rather than electrolyte properties and gradients.

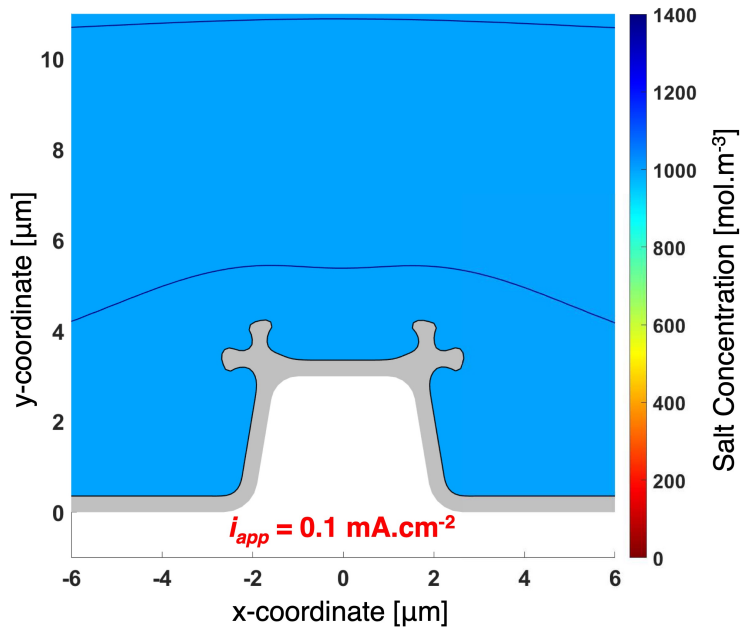


(a)

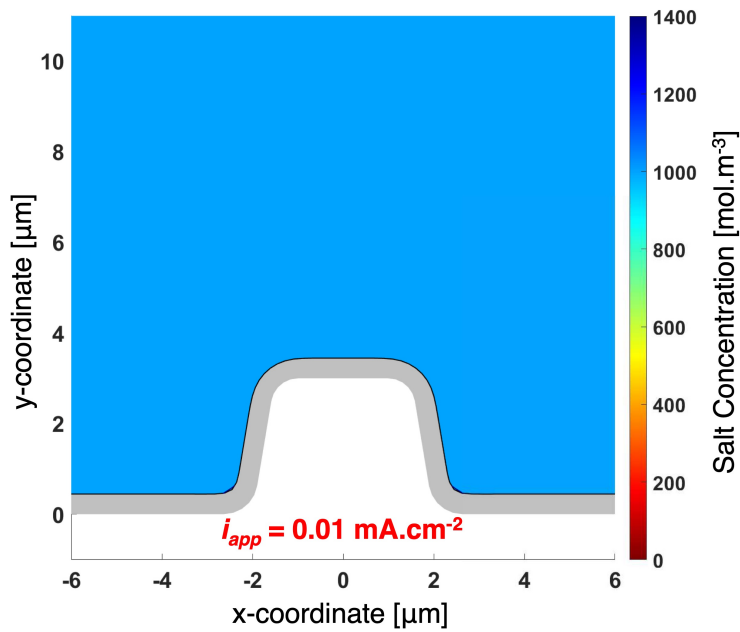


(b)

Figure 4.7: Salt concentration in the electrolyte at the end of simulation in color [mol.m⁻³]. Black lines are electrolyte potential isolines, separated from each other by 1 mV. Lithium deposited during the simulation in gray. a) Simulation after 40 s with an applied current of 10 mA.cm⁻². b) Simulation after 400 s with an applied current of 1 mA.cm⁻².



(a)



(b)

Figure 4.8: Salt concentration in the electrolyte at the end of simulation in color [mol.m⁻³]. Black lines are electrolyte potential isolines, separated from each other by 1 mV. Lithium deposited during the simulation in gray. a) Simulation after 4000 s with an applied current of 0.1 mA.cm⁻². b) Simulation after 40000 s with an applied current of 0.01 mA.cm⁻².

Fig. 4.9, 4.10, 4.11 and 4.12 show the same final morphologies of Fig. 4.7 and 4.8, but in this case the focus is on the final SEI thickness. The four simulations start with the same uniform initial SEI thickness of 10 nm, but the thickness evolution is significantly different depending on the applied current density.

Both Fig. 4.9 and 4.10 show a predominately thin SEI at the end of the simulation (in blue), due to the shorter simulations, respectively 40 and 400 s, and the faster surface deformation, which did not allow time for SEI to form a thick layer. Thicker zones of SEI are found at the base of the defect where the concavity of the initial geometry foster its growth according to Eq. 3.9. A more detailed analysis on the SEI evolution in Fig. 4.9 is presented in Fig. 4.15.

On the other hand, Fig. 4.11 and 4.12 show a thicker SEI thickness at the end of simulation, as red is the most dominant color in the images. In Fig. 4.11, despite the lack of SEI mechanics, filiform dendrites (similar to whiskers) are visible, due to the SEI, which has the necessary time to form a thick layer everywhere on the defect, but its upper corners; while in Fig. 4.10, the deposited lithium layer (in gray) is thicker on the base of the defect than on its tip and no SEI thinning is present.

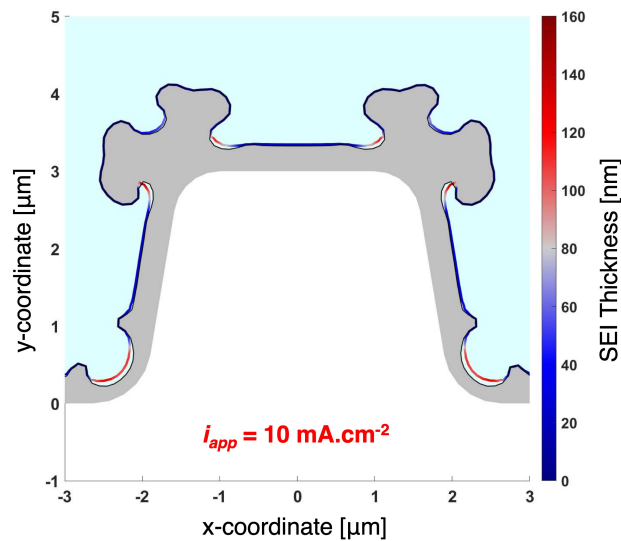


Figure 4.9: SEI thickness at the end of simulation in color [nm]. Lithium deposited during the simulation in gray. Simulation after 40 s with an applied current density of 10 mA.cm^{-2} .

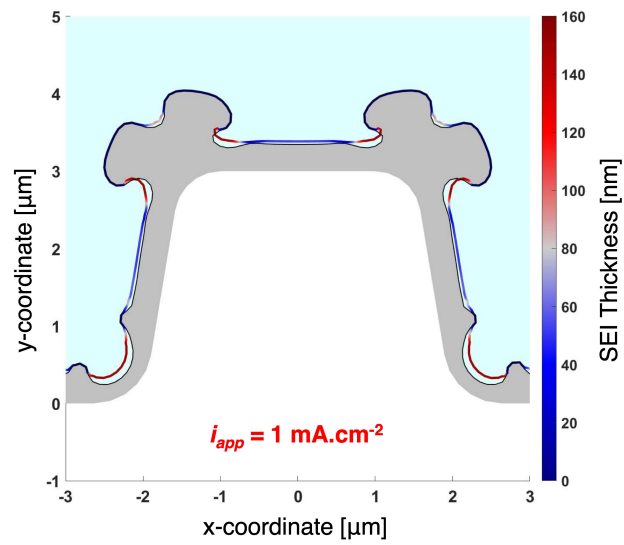


Figure 4.10: SEI thickness at the end of simulation in color [nm]. Lithium deposited during the simulation in gray. Simulation after 400 s with an applied current density of 1 mA.cm^{-2} .

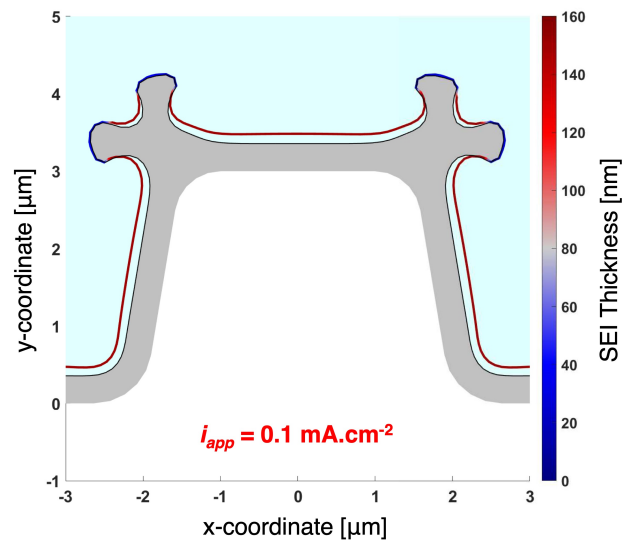


Figure 4.11: SEI thickness at the end of simulation in color [nm]. Lithium deposited during the simulation in gray. Simulation after 4000 s with an applied current density of 0.1 mA.cm^{-2} .

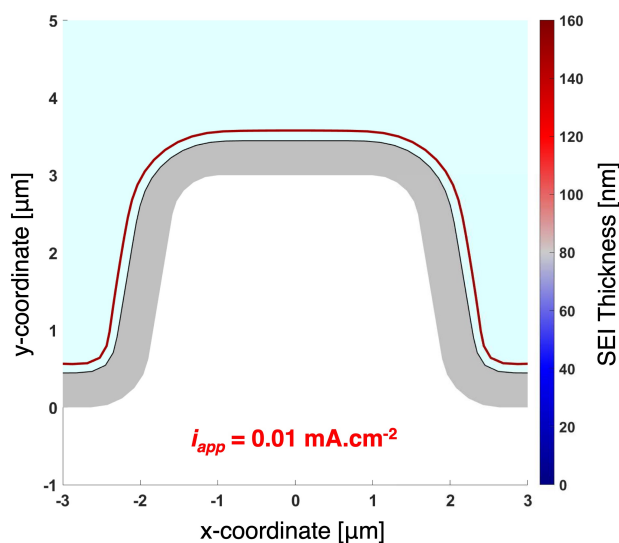


Figure 4.12: SEI thickness at the end of simulation in color [nm]. Lithium deposited during the simulation in gray. Simulation after 40000 s with an applied current density of 0.01 mA.cm^{-2} .

The previous four images confirmed that the SEI is a fundamental component to simulate lithium deposition on the lithium metal surface, and eventually assess its stability. The SEI layer acts like a barrier for lithium deposition, and the thicker the layer is, the higher resistance the lithium will encounter during electrodeposition, resulting in a lower deposition rate in areas covered by a thicker SEI. This can be inferred from Fig. 4.13, while it is evident in Fig. 4.14.

Fig. 4.13 displays Butler-Volmer current densities profiles on the electrode surface at the end of the simulations, scaled to the respective applied current density. A huge variation in the profiles can be observed in the central region ($-3, 3 \mu\text{m}$) where the initial defect is present and where the higher variation in SEI thickness was found in the previous images. The profiles at 10 mA.cm^{-2} (in blue) and 1 mA.cm^{-2} (in green) are similar, with peaks in current density situated in different points, in agreement with the final geometries presented in Fig. 4.7. The lowest values of current density are found around $-2.5, 2.5 \mu\text{m}$, which are the areas with a thick SEI at the base of the defect; and around $-1.8, -1, 1, -1.8 \mu\text{m}$, which are the areas in the top corners where the SEI is thicker (shown in red in Fig. 4.9). The ratio between the maximum and minimum values of current density is 56 for 10 mA.cm^{-2} and 24 for 1 mA.cm^{-2} , while the ratio between the maximum values and a point far from the defect is 12 for 10 mA.cm^{-2} and 10 for 1 mA.cm^{-2} .

The profile at $0.1 \text{ mA}\cdot\text{cm}^{-2}$ is presented in red and it is the one with the highest peaks. This agrees with the filiform nature of the dendrites shown in Fig. 4.11. Differently from the previous two cases, there are no lowest points since the SEI thickness is uniform anywhere else but in the two upper corners of the initial defect. Thus, the ratio between the maximum value and a point far from the defect is 15, which is the maximum ratio, showing that against common sense, a lower current density does not necessarily imply a more uniform behavior, since thin dendrites can grow faster under these conditions. Finally, the profile for $0.01 \text{ mA}\cdot\text{cm}^{-2}$ (in blue) is constant and smaller in module than 1, since the boundary of the electrode surface, given the initial defect, is bigger than the top boundary of the model geometry, where the current density is applied (Fig. 3.1).

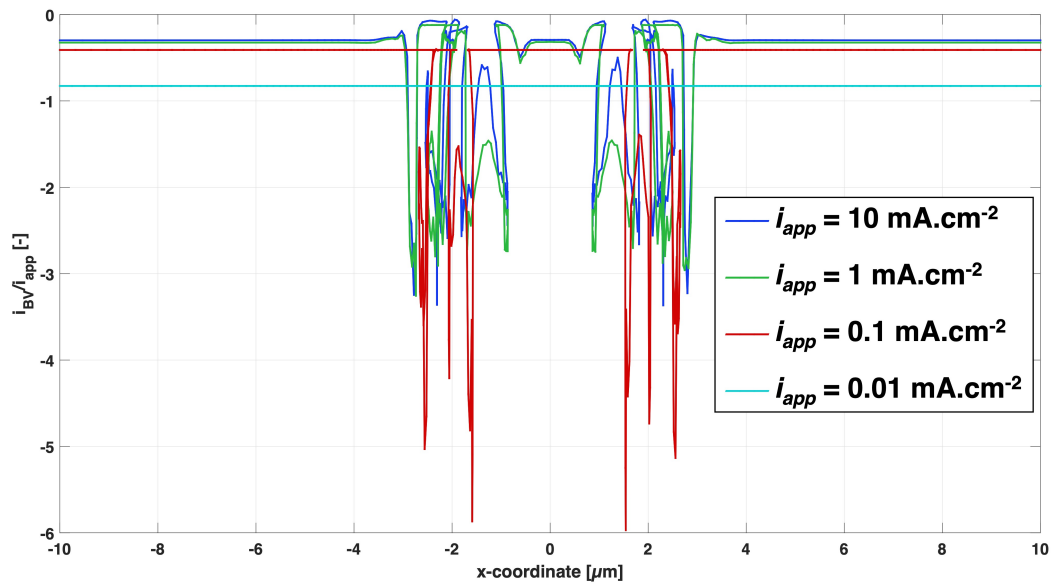


Figure 4.13: Butler-Volmer current density profiles at the end of the simulations presented in Fig. 4.7 and Fig. 4.8, weighted on the applied current density.

Fig. 4.14 strengthens the correlation between the current density and the SEI thickness. Indeed, the ratios from the previous figure are plotted vs the SEI thickness, for the simulations carried out at 10, 1, $0.1 \text{ mA}\cdot\text{cm}^{-2}$ applied current densities. The profile for the simulation with $0.01 \text{ mA}\cdot\text{cm}^{-2}$ is not present, since the thickness of the SEI is uniform in this simulation, and the consequent uniform Butler-Volmer current makes the profile collapse in few, not visible points. All the three profiles have a hyperbolic trend, but there is no perfect correlation between current and thickness, suggesting that the position of the point and its neighbors influence the current magnitude.

The red profile is more scattered around the elbow, because, as shown in Fig. 4.13, for the $0.1 \text{ mA}\cdot\text{cm}^{-2}$ simulation most of the points have a current ratio, in module, below 1. Differently from 4.13, in this figure, it is possible to observe that the ratio for the $0.1 \text{ mA}\cdot\text{cm}^{-2}$ simulation is higher despite the SEI at the end of the simulation is never as thin as the other two simulations. The green profile ($1 \text{ mA}\cdot\text{cm}^{-2}$) has a smoother transition than the blue profile ($10 \text{ mA}\cdot\text{cm}^{-2}$), which results in a more globular (mossy) dendrite evolution.

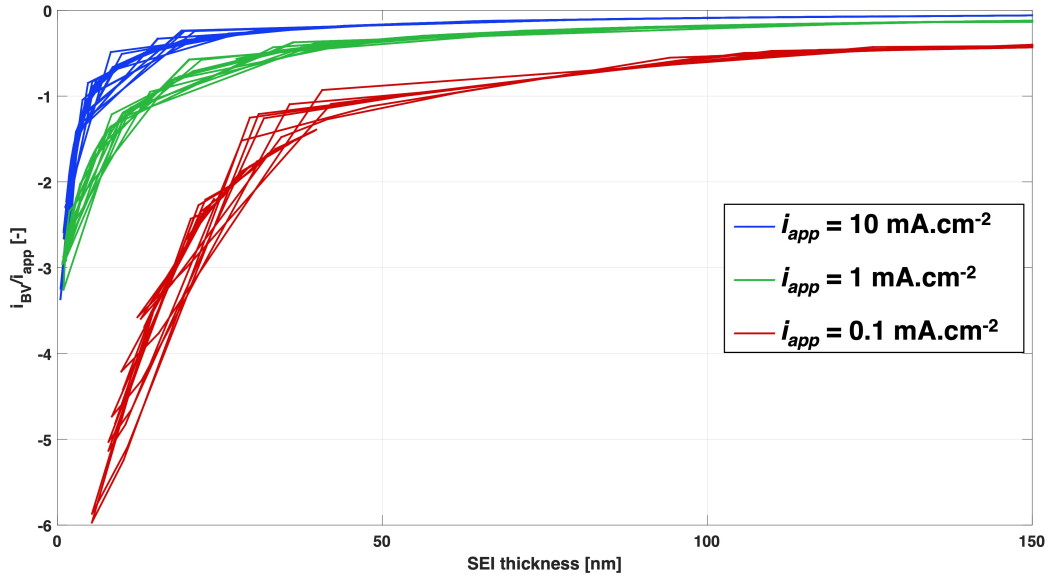


Figure 4.14: Butler-Volmer current densities at the end of the simulations presented in Fig. 4.7 and Fig. 4.8, plotted versus the related SEI thickness.

In order to study deeper the effect of the SEI and the strict correlation between the SEI thickness and the type of evolution of the defect, SEI growth equation from Tab. 4.4 has to be analyzed. The thickness of the SEI is governed by two terms: the rate of SEI formation and the rate of deformation of the SEI. The first term always contributes to increase the SEI thickness and it is proportional to the surface overpotential and to the kinetic coefficient of the reaction. The effect of the second term, on the other hand, depends on the sign of the surface curvature: if the surface is convex, it contributes to reducing the SEI coverage thickness, and the opposite in the case of concave surface. The first term depends on the applied current density indirectly, through its exponential dependence on the overpotential, while the second term is linearly proportional to the applied current density.

Therefore, the evolution of the SEI thickness is not directly proportional to the applied current density. Indeed, at lower current density the rate of deformation

of the electrode surface is slow, giving enough time to the SEI reaction to form a thick and homogenous SEI, which leads to a more homogenous deposition or, in particular case when the deposition is heterogeneous enough to form concave structures on the metal surface below the SEI, to whisker dendrites. On the contrary, at high applied current densities, the deformation of the electrode surface is fast, and therefore, there is not enough time for the new SEI to form. This leads to an important reduction of the SEI thickness in the zones where the surface is convex and the curvature is high. The SEI thickness can be seen as a resistance to the lithium deposition path, therefore, the lithium tends to deposit where the SEI is thinner, creating favorable directions of growth and dendritic structures.

The evolution of the SEI thickness, together with the evolution of the surface is presented in Fig. 4.15. The images refer to zooms on the upper left corner of the surface defect during the high current density simulation at $10 \text{ mA}\cdot\text{cm}^{-2}$ (Fig. 4.9). To better show the inhomogeneous thickness, a multiplier factor of 10 was applied to the SEI thickness in Fig. 4.15a-4.15d, and a multiplier of 5 was applied in Fig. 4.15e-4.15g. At the beginning of the simulation 4.15a, the SEI thickness is uniform and equal to 10 nm. As explained before, due to its convex nature and the relatively high curvature, the thickness decreases in the top corners of the geometrical defect 4.15b, promoting a higher lithium deposition in those zones 4.15c, where a dendrite in its initial stage (a proto-dendrite) is formed. While the proto-dendrite is growing, it reaches a point where the curvature is low enough to promote SEI formation. The formation is not uniform since the surface curvature is not, therefore the lithium finds new favorite directions of deposition. In Fig. 4.15d, the SEI starts to form in the middle zone of the proto-dendrite, decreasing the flux of the lithium deposition in that area, which leads to a concave zone. Thus, the lithium deposition is redirected to the corners of the proto-dendrite, creating two new branches from the original proto-dendrite 4.15e. In the last two figures, this process repeats again. Therefore, this simulation demonstrates that inhomogeneous SEI thickness is a plausible cause of the tree-like nature of dendrites.

Therefore, this section has demonstrated that the SEI is a fundamental component to simulate lithium deposition on the lithium metal surface, and eventually assess its stability. Before adding the mechanical behavior of the SEI, a sensitivity analysis on SEI electrochemical properties was made with this model, and it is presented in the following sections.

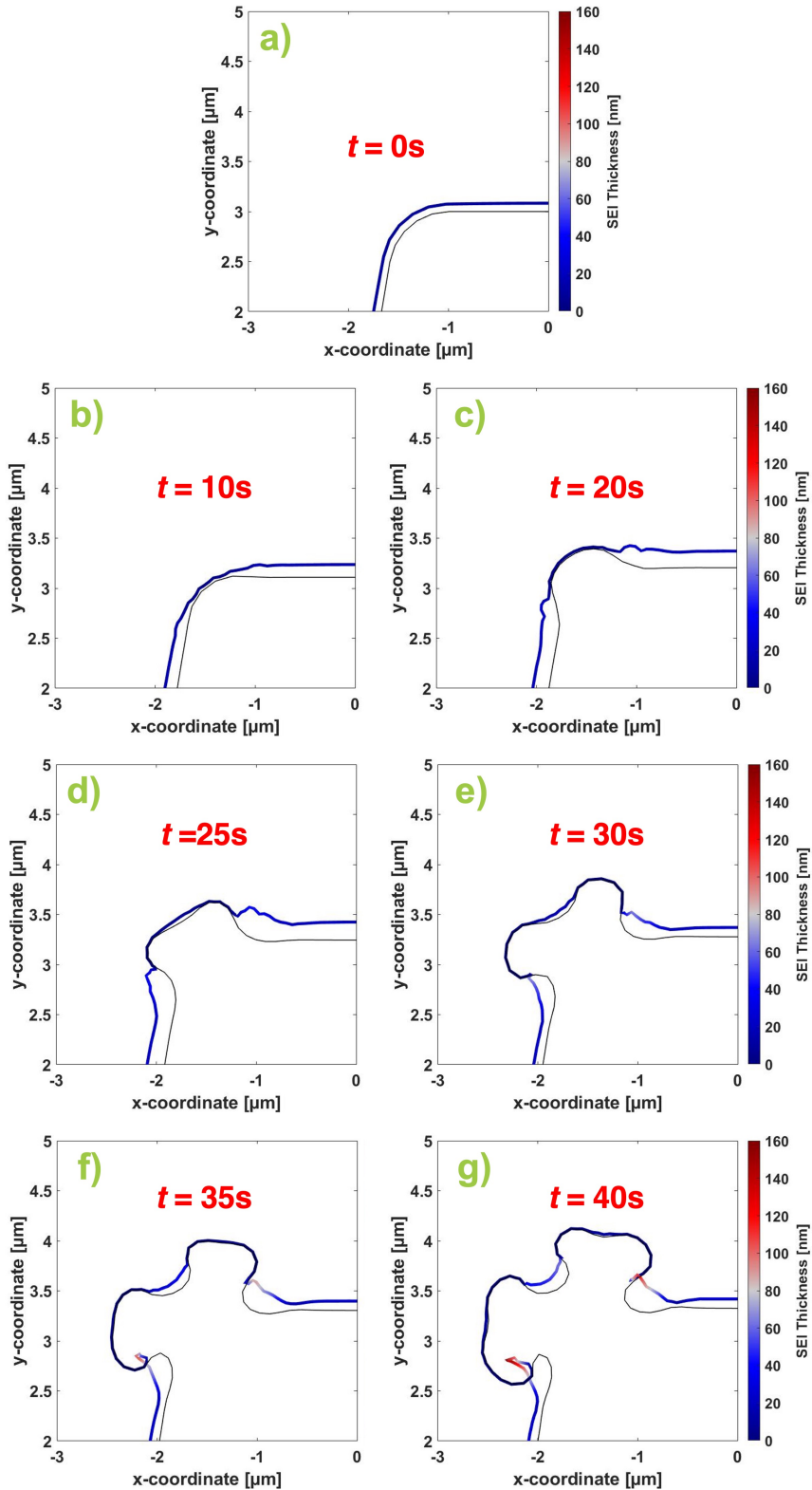


Figure 4.15: SEI thickness in color [nm] during the $10 \text{ mA}\cdot\text{cm}^{-2}$ applied current density simulation presented in Fig. 4.9. SEI thickness was multiplied by a factor of 10 in Fig. a-d, and by a factor of 5 in Fig. e-g. a) $t = 0 \text{ s}$. b) $t = 10 \text{ s}$. c) $t = 20 \text{ s}$. d) $t = 25 \text{ s}$. e) $t = 30 \text{ s}$. f) $t = 35 \text{ s}$. g) $t = 40 \text{ s}$.

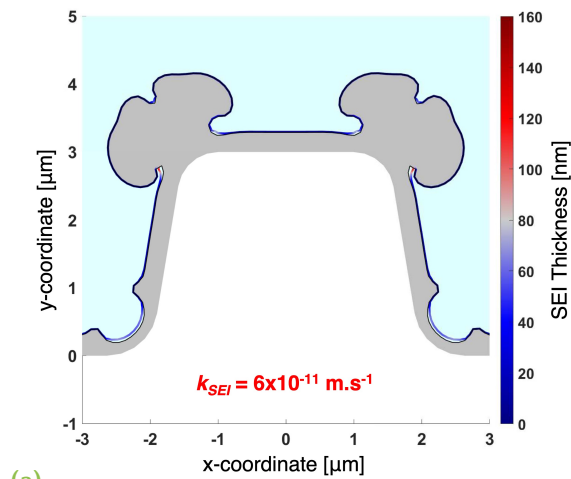
4.2.1 Effect of SEI Formation Kinetics

In this section, the effect of the SEI formation kinetics on the defect evolution is presented. More specifically, the effect of the SEI reaction rate coefficient, k_{SEI} [$\text{m}\cdot\text{s}^{-1}$], is investigated. Since the SEI formation current is directly proportional to it, as shown in Tab. 4.4, it influences the SEI thickness and ultimately the electrode surface morphology. The value that was used in the previous simulation was $6 \times 10^{-10} \text{ m}\cdot\text{s}^{-1}$, and it was taken from the work of Liu and Lu [15]. For the simulation presented in this section, the value of SEI reaction rate coefficient was multiplied and divided by ten, and the new obtained morphologies are compared with the literature case.

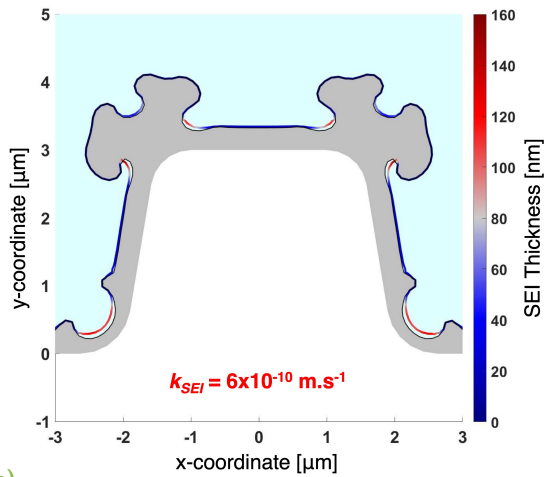
Fig. 4.16 shows how k_{SEI} impacts the simulation where the applied current density is $10 \text{ mA}\cdot\text{m}^{-2}$. The central figure, Fig. 4.16b, is obtained with parameters from literature, thus it is the same morphology shown in Fig. 4.9, while in the other two figures, all the parameters stay the same, except for k_{SEI} . In Fig. 4.16a, k_{SEI} is ten times lower than the value from literature, while in Fig. 4.16c it is ten times higher.

With a slow formation of the SEI (low reaction rate, Fig. 4.16a), a more globular growth of the dendrites happens. This is due to the fact that once the SEI is “broken” at the corner, and the proto-dendrite shown in Fig. 4.15c is formed, the SEI formation is slow and the SEI formation in the middle zone of the proto-dendrite never happens. Thus, the exposed fresh lithium grows quasi-homogeneously, like the simulation in which the SEI was not considered, producing a globular growth. When the reaction rate is high (Fig. 4.16c), fast formation of the SEI happens. Therefore, the SEI thickness is still not uniform through the simulation but the fast SEI formation reduces the zones of thin SEI, as demonstrated by the diffuse red thick SEI in the figure. Thus, a lower difference of lithium flux between the corners of the defect and the other zones is observed, resulting in a less developed dendrite with respect to the base case, while at the same time conditions closer to the filiform dendrites formed in Fig. 4.11 are created.

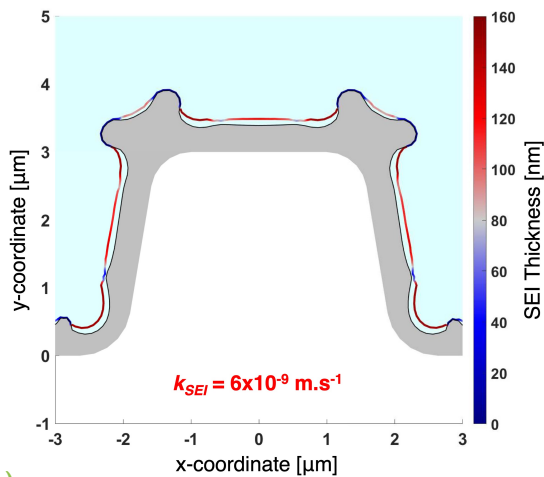
Fig. 4.17 repeats the same procedure of Fig. 4.16 but with the lower applied current density of $0.1 \text{ mA}\cdot\text{m}^{-2}$, thus, the geometry presented in Fig. 4.17b is the same as Fig. 4.11. The slower SEI formation in Fig. 4.16a does not give the opportunity to form a thick uniform SEI, therefore more mossy-like dendrites are formed. On the opposite side, the fast SEI formation of Fig. 4.16c creates a uniform SEI layer which brings the simulation close to the condition of Fig. 4.12, with a quasi-homogeneous deposition.



(a)



(b)



(c)

Figure 4.16: SEI thickness at the end of simulation in color [nm]. Lithium deposited during the simulation in grey. Simulation after 40 s with an applied current density of $10 \text{ mA}\cdot\text{cm}^{-2}$. a) SEI reaction rate coefficient 10 times lower than the value from the literature. b) SEI reaction rate coefficient value from the literature. c) SEI reaction rate coefficient 10 times higher than the value from the literature.

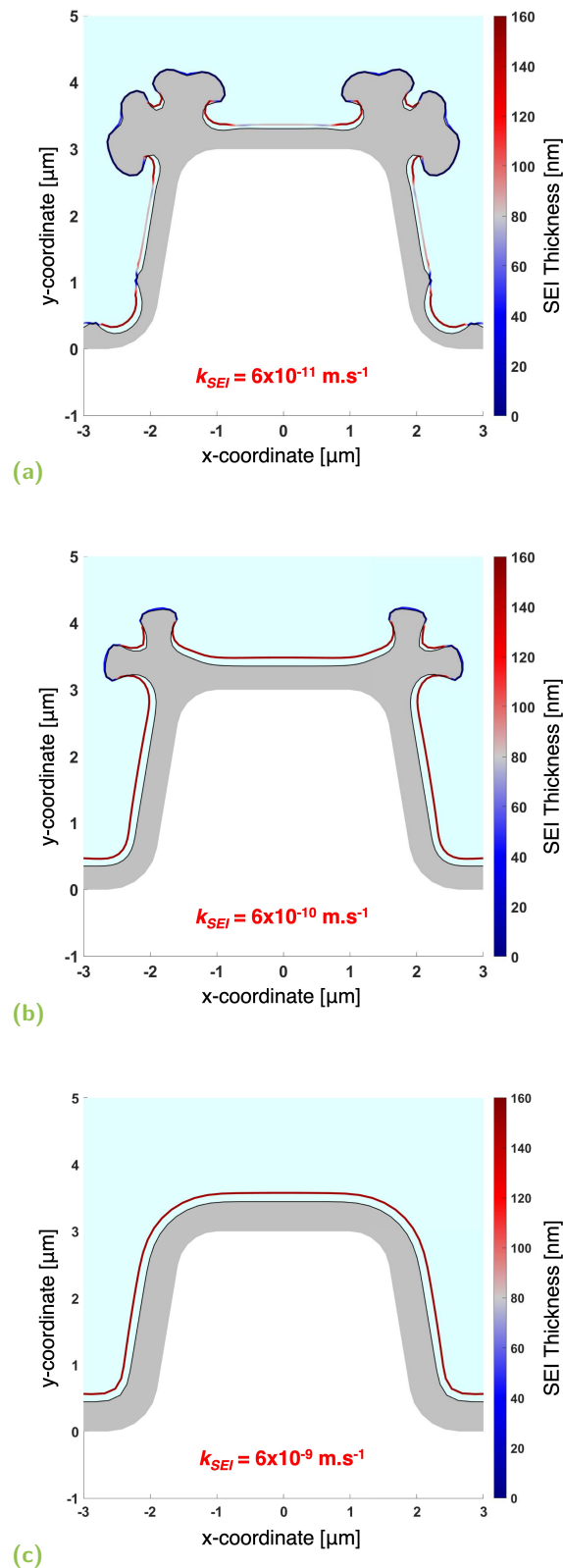


Figure 4.17: SEI thickness at the end of simulation in color [nm]. Lithium deposited during the simulation in grey. Simulation after 4000 s with an applied current density of 0.1 mA.cm^{-2} . a) SEI reaction rate coefficient 10 times lower than the value from the literature. b) SEI reaction rate coefficient value from the literature. c) SEI reaction rate coefficient 10 times higher than the value from the literature.

Therefore, it has been demonstrated that the kinetics of SEI formation can shift the current range in which certain types of dendrites are present, and it influences the electrodeposition of lithium and the morphology of the deposited layer.

4.2.2 Effect of SEI Resistivity

In this section the effect of the SEI resistivity, r_{SEI} [$\Omega.m$], is taken into account. The resistivity of the SEI modifies the overpotential on the electrode interface, as presented in Tab. 4.4. The structure of this section is the same as the previous one. Thus, the value from the literature [15] of SEI resistivity is used as a comparison for the simulations with 10 mA.cm^{-2} and 0.1 mA.cm^{-2} of applied current density, and r_{SEI} is multiplied and divided by a factor of 10 to see its effect on the defect evolution.

Fig. 4.18 shows the effect of changing the value of r_{SEI} with an applied current of 10 mA.cm^{-2} , while all the other parameters are taken from Tab. 4.2. Fig. 4.18a, 4.18b, 4.18c show the geometries at the end of the simulation by using respectively a value of r_{SEI} of 2×10^4 , 2×10^5 (value from literature [15]) and $2 \times 10^6 \Omega.m$. The lower the SEI resistivity is, the lower the effect of the SEI on the lithium deposition is too. If the drop of the concentration of the lithium across the SEI is negligible, a zero-resistivity SEI would lead to the same results of the simulation without any SEI layer (Fig. 4.1). Consequently, as it could be expected, the simulation with a low SEI resistivity (Fig. 4.18a) leads to a more homogenous deposition of lithium. On the other hand, a high resistivity SEI magnifies the difference in lithium deposition between the zones where the SEI is thinner and the zones where it is thicker, with maximum current density being 3 times higher in the case of high SEI resistivity (Fig. 4.18c) compared to the low SEI resistivity case, leading to a more developed dendrite at the end of the simulation.

The same conclusions can be made for Fig. 4.19, where the previous three values of SEI resistance are used in the simulation with an applied current of 0.1 mA.cm^{-2} . In this case the effect of the SEI resistance is higher, since already in the base scenario (Fig. 4.19b) the SEI has the time to grow thicker. Due to the lower resistance, Fig. 4.18a shows a similar final geometry of Fig. 4.17a, despite the SEI being on average seven times thicker than the previous case. In Fig. 4.19c, the difference in flux between the thick SEI regions and the thin ones is enhanced by the high SEI resistance, leading to sharper, thinner and longer whiskers.

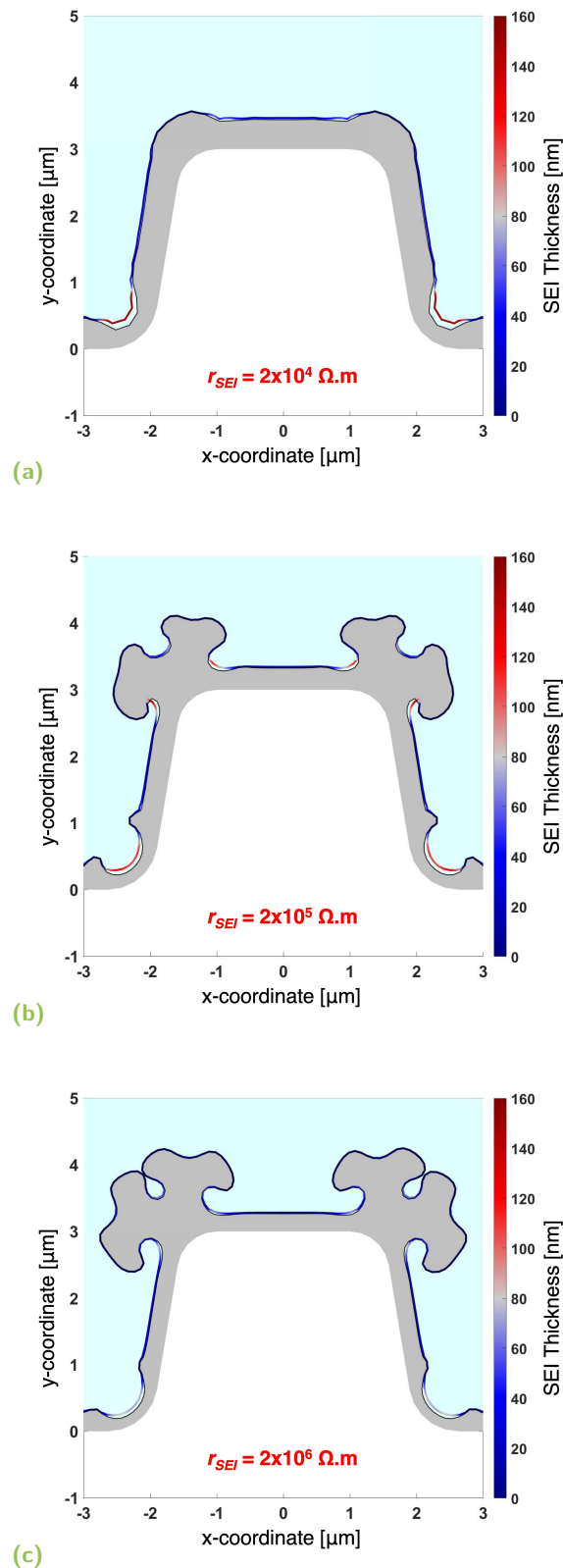


Figure 4.18: SEI thickness at the end of simulation in color [nm]. Lithium deposited during the simulation in grey. Simulation after 40 s with an applied current density of $10 \text{ mA} \cdot \text{cm}^{-2}$. a) SEI resistivity 10 times lower than the value from the literature. b) SEI resistivity value from the literature. c) SEI resistivity 10 times higher than the value from the literature.

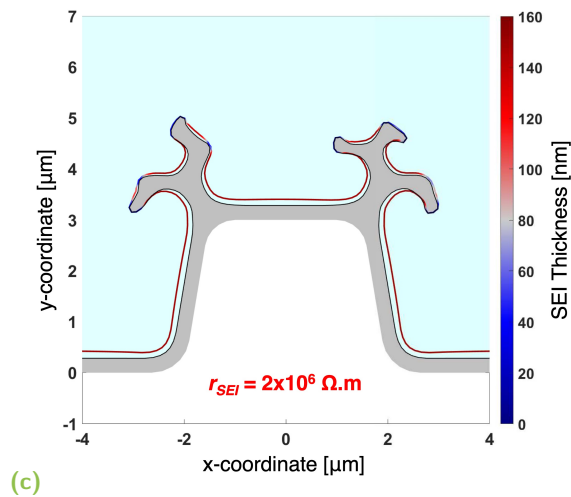
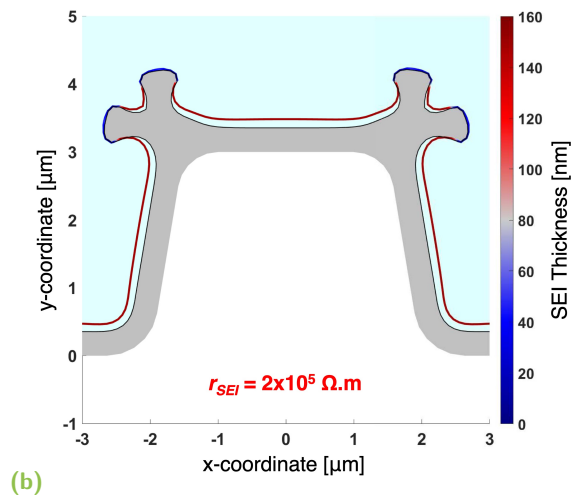
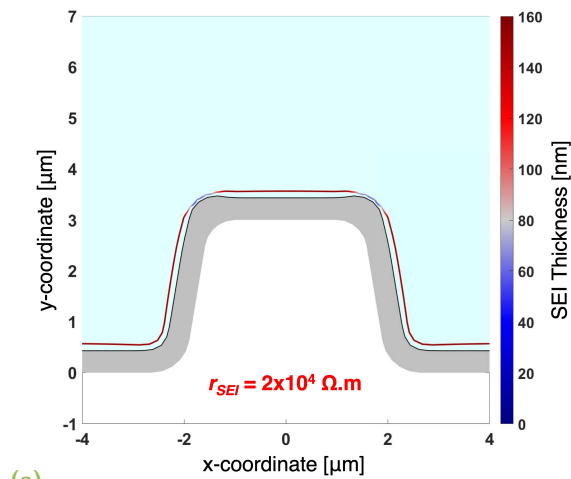


Figure 4.19: SEI thickness at the end of simulation in color [nm]. Lithium deposited during the simulation in grey. Simulation after 4000 s with an applied current density of $0.1 \text{ mA} \cdot \text{cm}^{-2}$. a) SEI resistivity 10 times lower than the value from the literature. b) SEI resistivity value from the literature. c) SEI resistivity 10 times higher than the value from the literature.

The asymmetry in the evolution between the two corners in this last figure is due to the poor remeshing, with the software that has difficulties to follow the sharp difference in lithium flux at the interface.

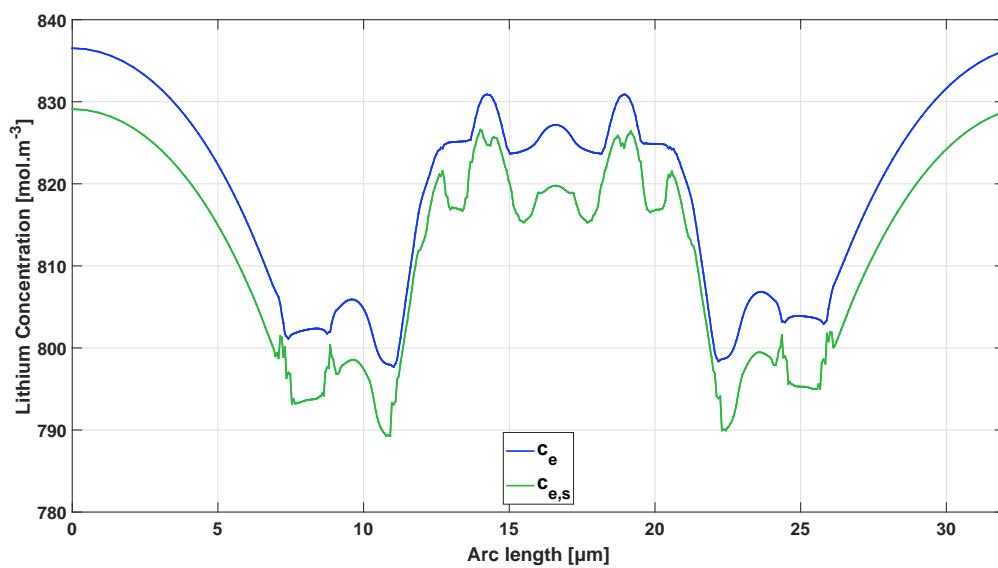
To conclude, a SEI with low resistivity is advisable to prevent dendrites growth, since it can reduce the inhomogeneity in lithium deposition due to the natural variable thickness of the SEI.

4.2.3 Effect of SEI Diffusion Coefficient

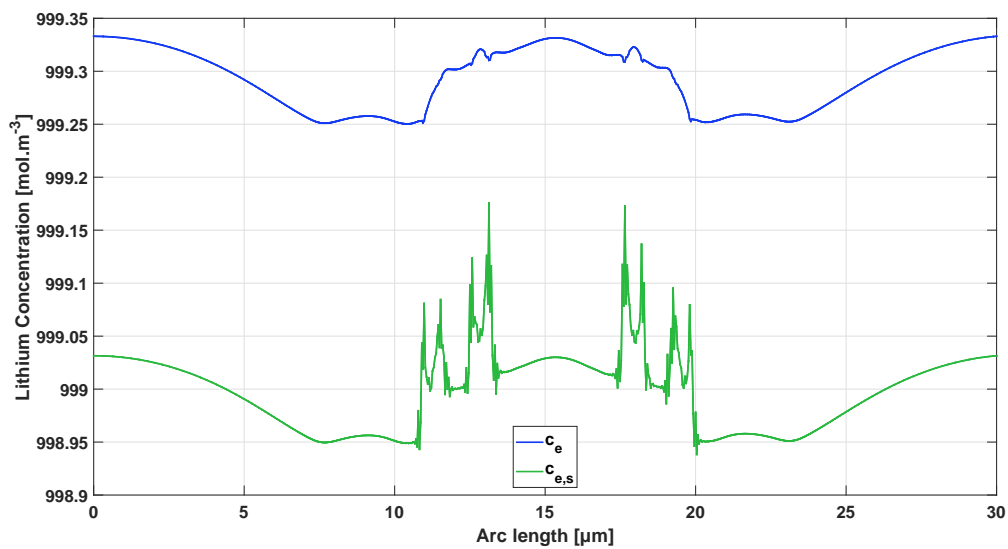
In this section, the results obtained by modifying the SEI diffusion coefficient are shown, following the same logic of the previous two sections. Among the SEI parameters that are studied, the lithium diffusion coefficient in the SEI is the one that influences less the geometry, in the range of current densities studied in this work. Its effect on the defect evolution can be traced back to Eq. 3.54 where $c_{e,s}$ depends on the concentration drop across the SEI layer. As shown in Eq. 3.13, the gradient of concentration does not only depend on the diffusion coefficient but it is also proportional to the applied current density.

Fig. 4.20 shows the profiles of lithium concentration at the electrolyte-SEI interface, c_e (in blue) and at the SEI-electrode interface, $c_{e,s}$ (in green), at the end of the simulations with an applied current density of $10 \text{ mA}\cdot\text{cm}^{-2}$ (Fig. 4.20a) and $0.1 \text{ mA}\cdot\text{cm}^{-2}$ (Fig. 4.20b). In these simulations, parameters from Tab. 4.2 are used, including a value of diffusion coefficient in the SEI of $7.5 \times 10^{-13} \text{ m}^2\cdot\text{s}^{-1}$. In Fig. 4.20a the maximum concentration drop across the SEI is around $10 \text{ mol}\cdot\text{m}^{-3}$ and it depends on the SEI thickness, with a bigger concentration drop for a thicker the SEI. On the other hand in Fig. 4.20b the concentration drop is negligible due to the low applied current density.

Therefore, the high current density case was chosen to study the effect of the SEI diffusion coefficient on the defect evolution. Fig. 4.21a shows the case in which the diffusion coefficient is ten times lower than the value from literature, while 4.21c represents the case in which the diffusion coefficient is ten times higher than the value from literature; and Fig. 4.21b was obtained by using values from literature. As anticipated, the differences between the three images are tiny due to the low concentration drop across the SEI. A bigger impact would be expected at higher applied current densities that lead to lithium depletion at the electrode surface (above the limiting current density).



(a)



(b)

Figure 4.20: Lithium concentration profiles at the electrolyte-SEI interface, c_e and at the SEI-electrode interface, $c_{e,s}$. a) Simulation after 40 s with an applied current density of $10 \text{ mA}\cdot\text{cm}^{-2}$. b) Simulation after 4000 s with an applied current density of $0.1 \text{ mA}\cdot\text{cm}^{-2}$.

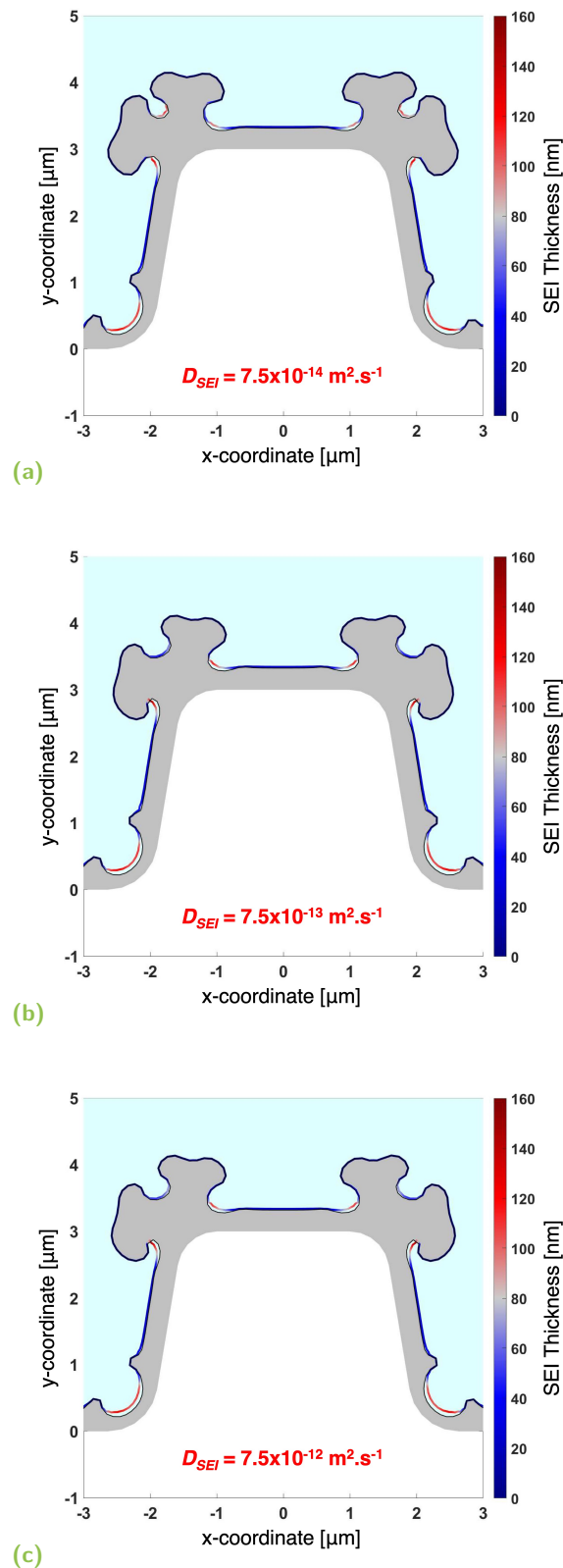


Figure 4.21: SEI thickness at the end of simulation in color [nm]. Lithium deposited during the simulation in grey. Simulation after 40 s with an applied current density of $10 \text{ mA} \cdot \text{cm}^{-2}$. a) SEI diffusion coefficient 10 times lower than the value from the literature. b) SEI diffusion coefficient value from the literature. c) SEI diffusion coefficient 10 times higher than the value from the literature.

Nevertheless, the effect of the diffusion coefficient in the SEI can be understood also with the presented simulation. Indeed, Fig. 4.22 shows a zoom of the defect upper-left corner at the middle (Fig. 4.22a) and at the end (Fig. 4.23c) of the simulation with varying SEI diffusion coefficient. In Fig. 4.22a, the flux on the corner is around 20% higher in the case of low SEI diffusion coefficient ($7.5 \times 10^{-14} \text{ m}^2 \cdot \text{s}^{-1}$) with respect to the other two cases, resulting in a more pronounced dendrite both at the middle and at the end of the simulation (blue line). Indeed, Eq. 3.54 linked the Butler-Volmer current density, thus the lithium deposition, to the surface concentration. Therefore, the lower the surface concentration is, the lower the current density is too. Since, as discussed before, the SEI thickness at the corner of the defect is the lowest (10 times lower than the average thickness in Fig. 4.22a), the lithium deposition is higher in the defect corners than in the zones when the SEI is thick, and this trend is magnified with a low SEI diffusion coefficient, which reduces further the lithium concentration at the surface.

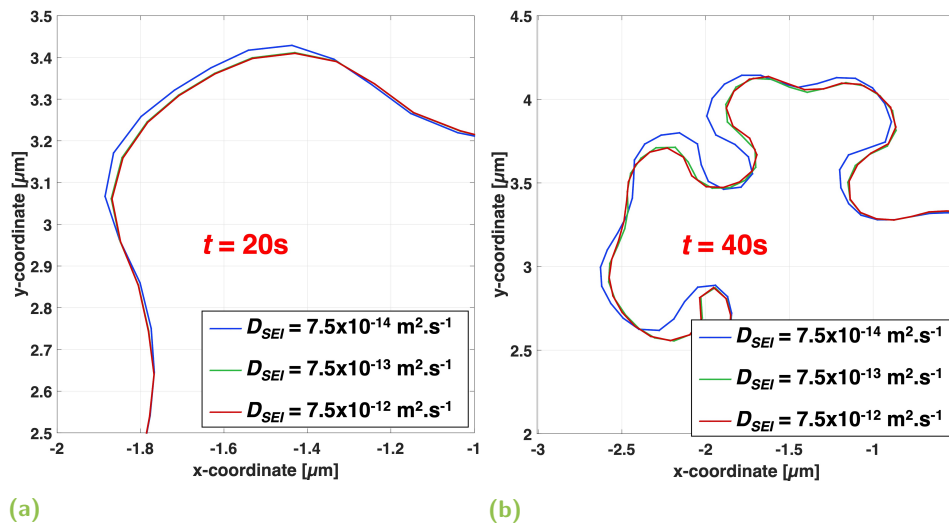


Figure 4.22: Zoom on the upper-left corner during the simulation presented in Fig.6a (green), Fig. 6b (blue) and Fig. 6c (red). a) Simulation after 20 s with an applied current density of $10 \text{ mA} \cdot \text{cm}^{-2}$. b) Simulation after 40 s with an applied current density of $10 \text{ mA} \cdot \text{cm}^{-2}$.

4.2.4 Effect of the Geometry of the Defect

The last parameter used for the sensitivity analysis is not a property of the SEI but of the geometry of the defect, more specifically the radius of curvature of the corners of the defect. This parameter influences the thickness evolution of the SEI, as shown in Eq. 3.9 and 3.11, where the surface curvature, κ_c , which is the inverse of the radius of curvature, was used.

Fig. 4.23 presents the results at the end of the high applied current density simulation ($10 \text{ mA}\cdot\text{cm}^{-2}$) by changing the radius of curvature. Fig. 4.23c is the base case, already presented in the previous section, where the radius of curvature was arbitrarily chosen to be $0.6 \mu\text{m}$. On the other hand, in Fig. 4.23a the radius of curvature is $0.5 \mu\text{m}$ and in 4.23b is $0.7 \mu\text{m}$. The higher the radius of curvature is, the more gentle the curvature is; with a flat surface having an infinite radius of curvature.

From Fig. 4.23 it can be noticed that more gentle curvatures lead to less developed dendrites. This can be explained with the fact that a higher surface curvature, thus lower radius of curvature, amplifies the second term of equation 3.9; which in the case of the upper convex corners, leads to a bigger reduction of the SEI thickness. Therefore, in the case of low radius of curvature (Fig. 4.23c), the ratio in SEI thickness between the flat parts and the corners is higher, so is the difference in flux between the corners and the flat parts. This leads to higher lithium flux at the corners, and ultimately to more developed dendrites. The opposite can be said for the case in which the radius of curvature is higher (Fig. 4.23a).

Therefore, as expected, an electrode surface with zero or, at least, more gentle irregularities is an advisable characteristic to prevent dendrites growth.

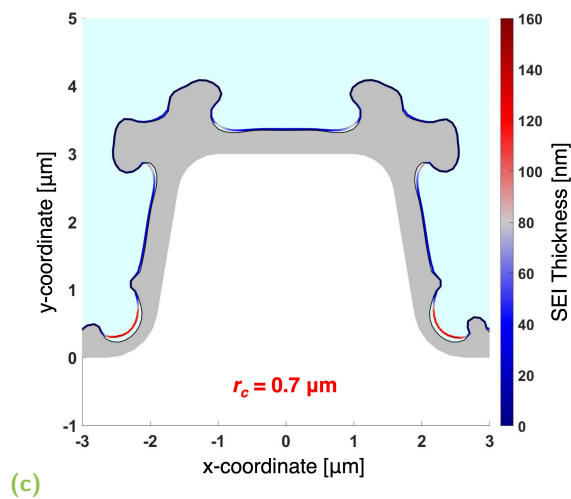
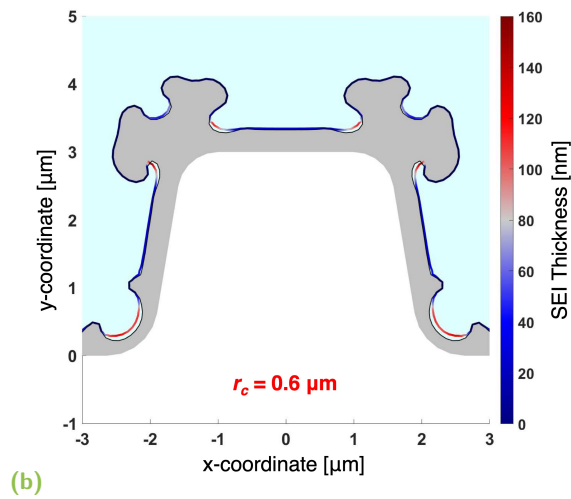
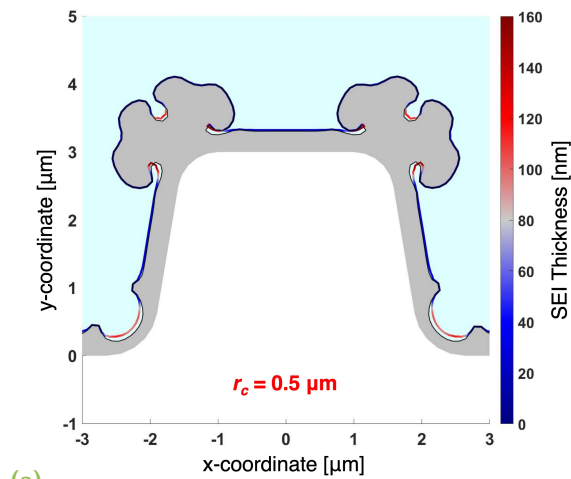


Figure 4.23: SEI thickness at the end of simulation in color [nm]. Lithium deposited during the simulation in grey. Simulation after 40 s with an applied current density of $10 \text{ mA}\cdot\text{cm}^{-2}$. a) $r_c = 0.5 \mu\text{m}$. b) $r_c = 0.6 \mu\text{m}$. c) $r_c = 0.7 \mu\text{m}$.

4.3 Full Model

The third set of results are obtained from the full model, which also considered the mechanical effect of the SEI on the defect evolution. The equations that were used in this section are listed in Tab. 4.5. Differently from the previous section, there was the addition of the change in electrochemical potential due to the pressure that the SEI applies on the lithium interface, $\Delta\mu_{e^-}$, which influences the surface overpotential and the exchange current density. The framework to compute Δp_{Li} and Δp_{SEI} was illustrated in detail in Sec. 3.2.4 and 3.2.5.

As noted from Bai, Bazant *et al.* [11], there is a dendrite growth mechanism which manifests mostly at low current densities. This phenomenon is called root-growth or bottom-induced growth, because like human hairs, lithium grows primarily from the root to form whiskers. As pointed out in the work of Bai *et al.* [11], the root-growing whiskers cannot be predicted by existing mathematical models. Despite this, the SEI has been theorized to have an important role in this phenomenon.

By using the full model, for the first time, a root growth was demonstrated through a model simulation. In order to maintain the numerical accuracy, the domains were remeshed throughout the whole simulation, especially in the case of high applied current density, where the resulting electrode morphology was more complex. The simulation encountered severe nonlinearity involved by the onset of plasticity, which was active in the zones where the Von Mises Stress of the lithium metal is higher than 0.655 MPa. This led to instabilities in the simulations, which become critical in the case of remeshing. Thus, the high current density simulation was stopped before the first remeshing occurs (after 22 s).

Lithium metal mechanical properties were the same of the one used in the model of Ferrese and Newman [51], while the mechanical proprieties of the SEI were experimentally measured by Yoon *et al.* in their work [73]. Therefore, in the model, the SEI had a elastic-perfectly plastic behavior, illustrated in Fig. 2.26. Thus, the SEI Young's modulus used in the model was 245 MPa, its elastic limit was 8 MPa and the maximum hoop strain was 0.06.

Mass Transport in Electrolyte	$\frac{\partial c_e}{\partial t} = D_e \frac{\partial^2 c_e}{\partial x^2}$
Charge Transport in Electrolyte	$\frac{\partial}{\partial x} \left(\kappa \frac{\partial \phi_e}{\partial x} + \frac{2RT\kappa(1-t_+)}{F} \frac{\partial \ln(c_e)}{\partial x} \right) = 0$
Charge Transport in Electrode	$\sigma_s \frac{\partial^2 \phi_s}{\partial x^2} = 0$
Mass Transport in SEI	$c_{e,s} = c_e - \frac{1-t_+}{FD_{SEI}} h_{SEI} i_{tot}$
Butler-Volmer Current Density	$i_{BV} = i_0 \left[\exp\left(\frac{\alpha_a F \Phi}{RT}\right) - \exp\left(-\frac{\alpha_c F \Phi}{RT}\right) \right]$
Exchange Current Density	$i_0 = i_{00} \left(\frac{c_{e,s}}{c_{e,0}} \right)^\alpha \exp\left(\frac{(1-\alpha) \Delta \mu_{e^-}}{RT}\right)$
Surface Overpotential	$\Phi = \phi_s - \phi_e + \frac{\Delta \mu_{e^-}}{F} - r_{SEI} h_{SEI} (i_{BV} + i_{SEI})$
SEI Growth Equation	$\frac{\partial h_{SEI}}{\partial t} = -\frac{\bar{V}_{SEI}}{2F} i_{SEI} - v_n \kappa_c h_{SEI}$
Change in El.ch. Potential	$\Delta \mu_{e^-} = \frac{\bar{V}_{Li} - (1-t_+) \bar{V}_{SEI}}{2} (\Delta p_{Li} + \Delta p_{SEI})$
SEI Formation Current Density	$i_{SEI} = -e^{\lambda h_{SEI}} F k_{SEI} c_{sol} \exp\left(\frac{\alpha_{SEI} F \Phi}{RT}\right)$
Surface Deformation	$v_n = v_{dep} + \dot{u}_n$

Table 4.5: Set of equations used in the full model.

Fig. 4.24, 4.25, 4.26 show the final geometries obtained by applying, respectively, current densities of 10 mA.cm⁻², 1 mA.cm⁻² and 0.1 mA.cm⁻², and after 0.056 mAh.cm⁻²) of lithium capacity was deposited. The white thick line represents the initial surface of the electrode, while the blue one represents the final surface in the case when the effect of the mechanics is not considered. The colored surface with the values of Von Mises Stress, on the contrary, is the electrode morphology that is obtained at the end of the simulation if both deposition and deformation due to mechanics are considered.

At high current density (Fig. 4.24), the evolution of the defect was mainly due to deposition, indeed the difference between the thick blue line (no mechanics considered) and the Von Mises Stress colored surface is negligible on the tip of the defect, while there is a small compression at the base due to the thick SEI in that area. On the other hand, at low current density (Fig. 4.26a), both the mechanics and

the deposition contributed significantly to the evolution of the dendrite morphology. These last results show that the difference in height between the initial defect and its final morphology is not only due to deposition like at high current densities (tip-growth) but also due to a push from the base of the defect (root-growth), in accordance with the experimental results of Bai *et al.* [11].

It has to be remarked that not all the difference is due to the lithium deformation. As a matter of fact, the change in surface overpotential, previously referred as $\Delta\mu_{e^-}$, accounts at maximum for the 10% of the overall surface overpotential, in the low current simulation. Its maximum effect is in the corners at the base of the defect, where the SEI is thicker. Without taking it into account, the difference between the final geometries in Fig. 4.24 (blue line and black thin line) is lower.

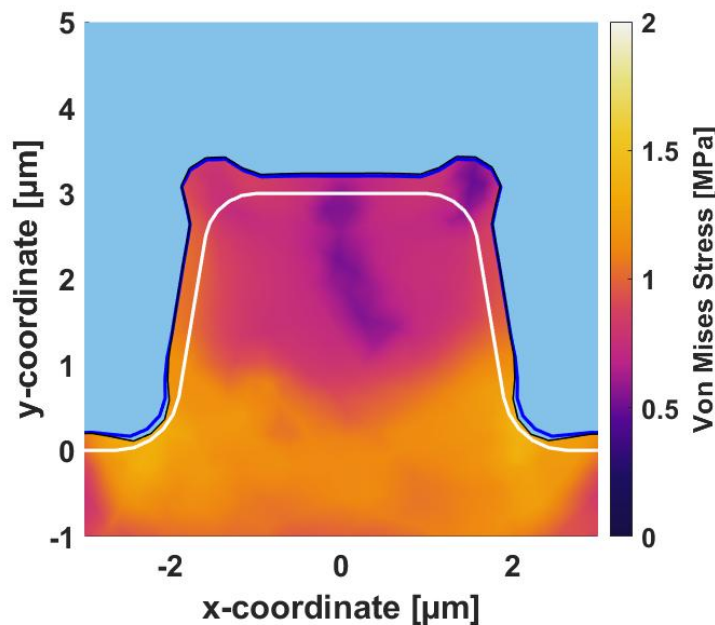


Figure 4.24: Von Mises Stress in color [MPa]. White line: initial surface geometry of the lithium defect. Blue line: final surface geometry without considering the mechanics. Black thin line: final surface geometry taking into account the mechanics. Simulation after 20 s with an applied current density of 10 mA.cm⁻².

The magnitude of the SEI applied pressure depends on the SEI thickness and on the radius of curvature of the surface, as shown in Eq. 3.22. Therefore, a thicker SEI produced a higher pressure. In the low applied current density simulation, the SEI had time to form a thick layer, as previously shown in Fig. 4.11, which justifies the

bigger contribution of lithium deformation with respect to the other two simulation with higher applied current densities.

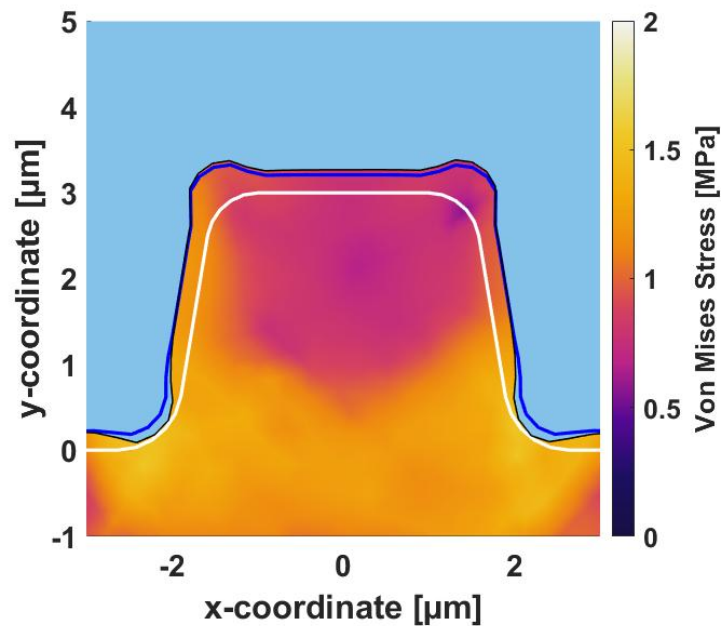
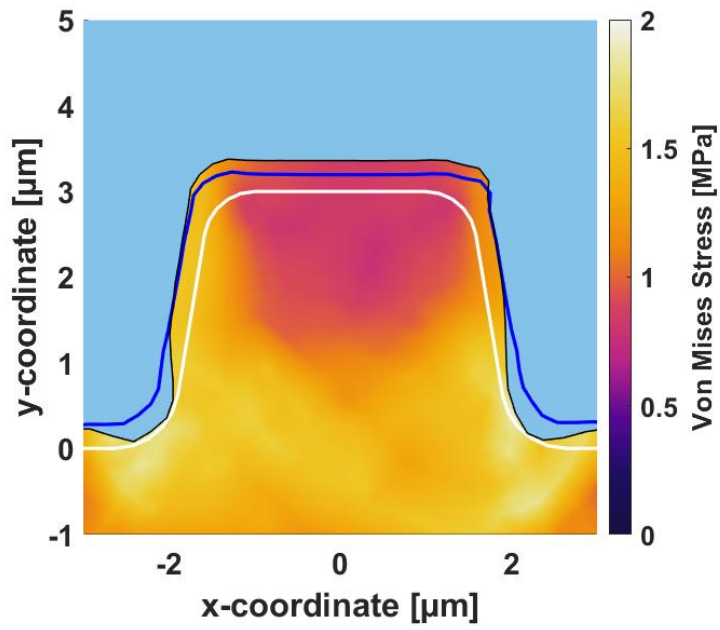
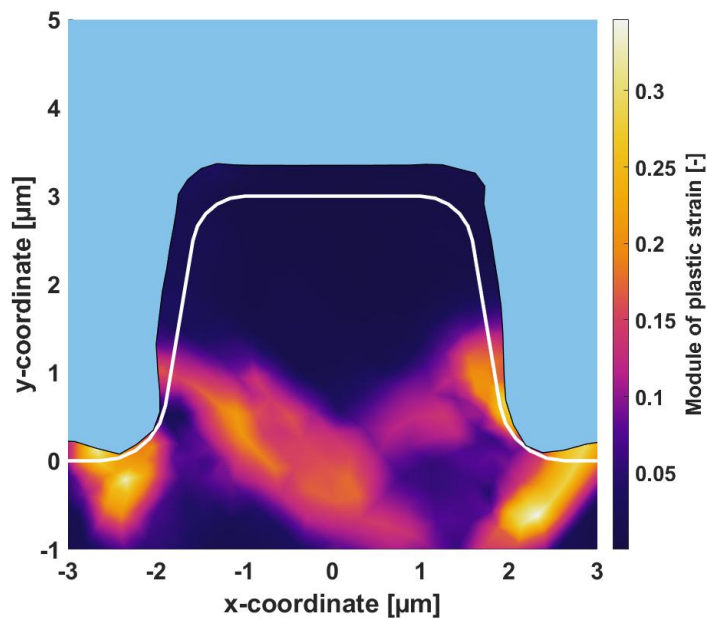


Figure 4.25: Von Mises Stress in color [MPa]. White line: initial surface geometry of the lithium defect. Blue line: final surface geometry without considering the mechanics. Black thin line: final surface geometry taking into account the mechanics. Simulation after 200 s with an applied current density of 1 mA.cm^{-2} .

Since the SEI pressure depends on the curvature of the surface, pressure at the corners is higher than pressure in the flat areas. At the end of the simulation shown in Fig. 4.26, the ratio between the SEI thickness at the bottom corners of the defect and its top corners is between 7 and 30. On the other hand, the pressure in the bottom corners should be just around 3 times higher than the one at the top, due to the higher curvature in the top corners. Nevertheless, the hoop strain at the end of the simulation in the top corners is around 1.8, while everywhere else on the surface it is lower than the maximum assumed hoop strain of 0.06. Therefore, it can be assumed that at the end of the simulation the top corners do not impose any mechanical constraints on the lithium surface, thus the pressure applied by the SEI is negligible there. For this reason, there is a push from the base of the defect (root-growth), due to the higher applied pressure (20 MPa) by the SEI with respect to the tip of the defect, which produced plastic deformation at the base of the defect, as shown in Fig. 4.26b.



(a)



(b)

Figure 4.26: White line: initial surface geometry of the lithium defect. Blue line: final surface geometry without considering the mechanics. Black thin line: final surface geometry taking into account the mechanics. Simulation after 2000 s with an applied current density of $0.1 \text{ mA}\cdot\text{cm}^{-2}$. a) Von Mises Stress in color [MPa]. b) Module of plastic strain in color [-].

On the other hand, Fig. 4.27 represents a simulation in which the top-right corner has no maximum assumed hoop strain, thus it maintains its plastic properties. In this simulation the top-right corner experiences a compression like the bottom corners due the high pressure caused by the high curvature of the surface. Therefore, in order to reduce dendrites, it is important to have a stiff SEI, which at the same time is able to accommodate the morphology change of the underlying electrode without breaking.

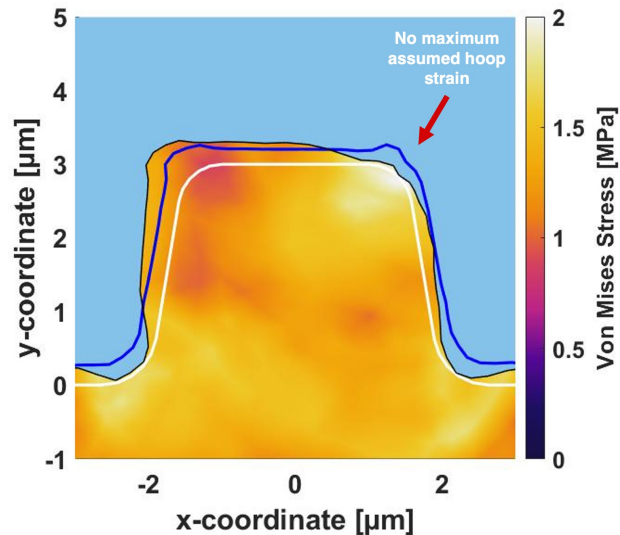


Figure 4.27: Von Mises Stress in color [MPa]. White line: initial surface geometry. Blue line: final surface geometry without considering the mechanics. Black thin line: final surface geometry taking into account the mechanics. Simulation after 2000 s with an applied current density of $0.1 \text{ mA}\cdot\text{cm}^{-2}$. Top-right corner of the defect has no maximum assumed hoop strain.

The previous concept is remarked by Fig. 4.28, where the final morphology of Fig. 4.26 (in blue) is compared with a similar simulation that uses the SEI formed by adding FEC in the electrolyte (in blue), from the work of Yoon *et al.* [73]. Thus, the new SEI has a Young's modulus of 440 MPa and its elastic limit is 10 MPa, while its maximum hoop strain is assumed to stay the same. This stiffer SEI performs better, ensuring a bigger compression, in the top-right corner, where no maximum hoop strain is assumed. On the contrary, the defect grows slightly more in the case of the stiffer SEI, in the top-left corner.

To conclude, the full model confirmed the importance of considering both the electrochemical and the mechanical effects of the SEI, while the mechanical resistance of the SEI was found to be a double-edge sword because high resistance

can limit the uncontrolled expansion of the lithium electrode but it can also boost root-growth in case of fractures.

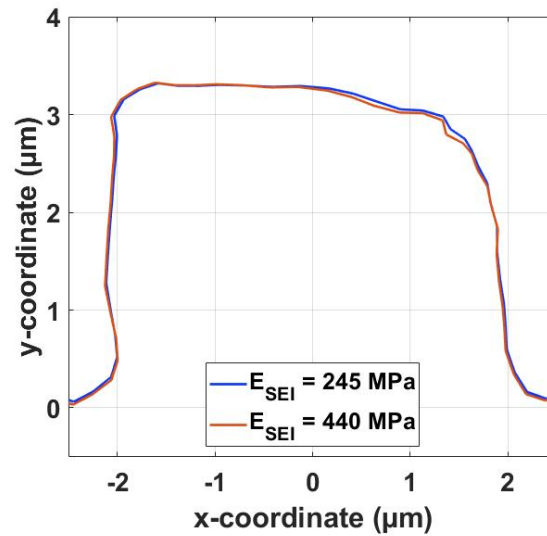


Figure 4.28: Final surface morphology of Fig. 4.27, compared with the surface morphology by performing the same simulation with an SEI with Young's modulus of 440 MPa and elastic limit of 10 MPa.

4.4 Lithium Stripping and Pores Creation

So far all the presented results were related to lithium deposition, but lithium stripping and cell cycling are equally important to be discussed, since they are fundamental to increase the life of lithium metal batteries. Nevertheless, the limits of the multi-domain continuum models prevented the proposed model to study these phenomena in detail. In spite of, in this section additional results regarding lithium stripping and pore creation are presented. The set of equation used is the one described in Sec. 4.2 and listed in Tab. 4.4, given, at the moment, its superior ability to simulate complex geometry with respect to the full model.

4.4.1 Lithium Stripping

As illustrated at the beginning of this work (Fig. 1.2), one of the problems related to dendrites, and more in general to lithium inhomogeneous deposition, is the creation of the so-called "dead lithium".

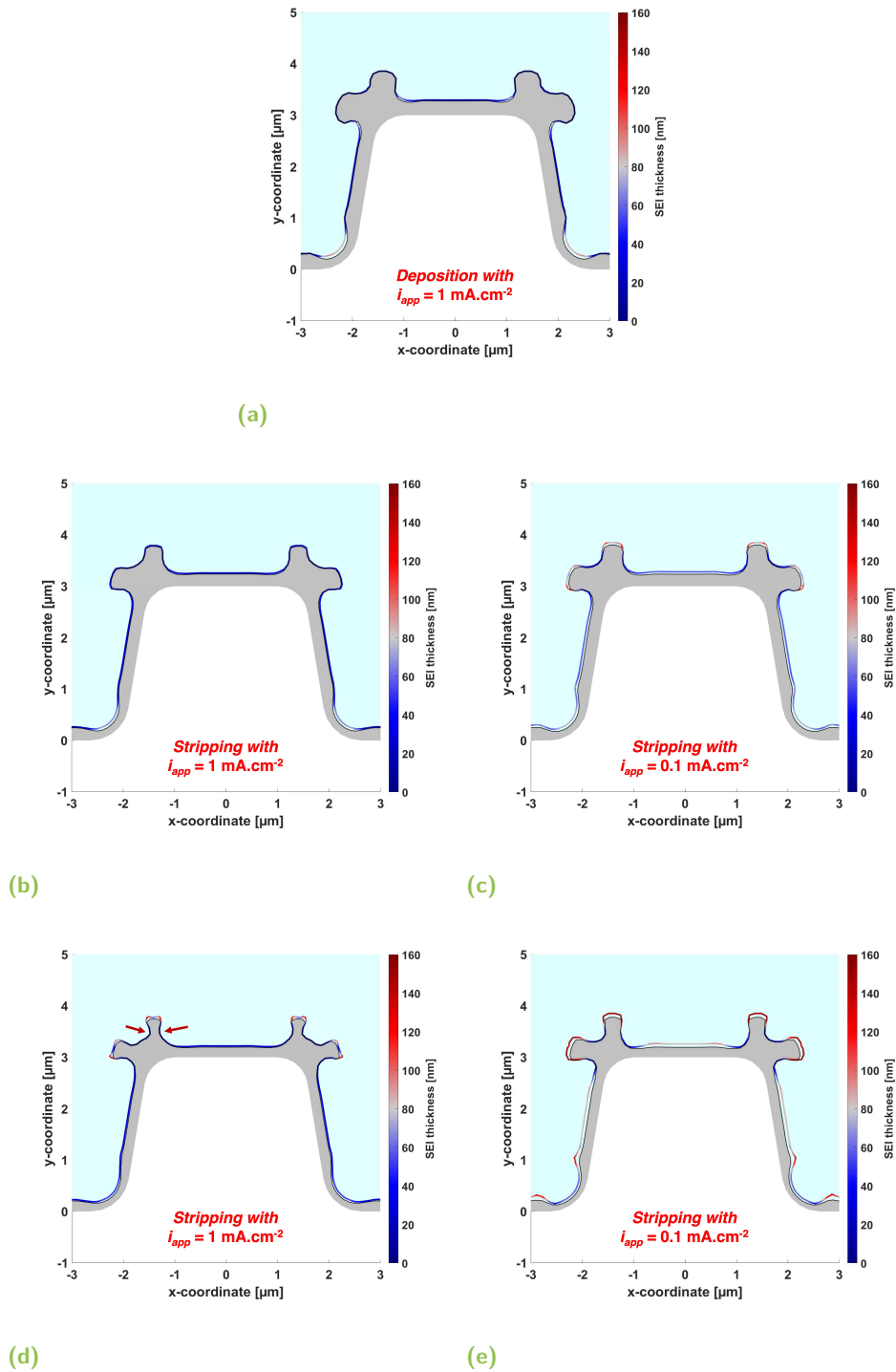


Figure 4.29: SEI thickness at the end of simulation in color [nm]. Lithium deposited during the simulation in gray. a) Deposition simulation after 300 s with an applied current density of $1 \text{ mA}\cdot\text{m}^{-2}$. b) Stripping simulation after 40 s with an applied current density of $1 \text{ mA}\cdot\text{m}^{-2}$. c) Stripping simulation after 400 s with an applied current density of $0.1 \text{ mA}\cdot\text{m}^{-2}$. d) Stripping simulation after 80 s with an applied current density of $1 \text{ mA}\cdot\text{m}^{-2}$. e) Stripping simulation after 800 s with an applied current density of $0.1 \text{ mA}\cdot\text{m}^{-2}$.

During lithium stripping, pieces of branched lithium remain physically or electrically isolated from the bulk electrode, causing a loss in capacity in the cell. Fig. 2.11 showed an example of lithium stripping in the two-domain continuum model developed by Yoon *et al.* [16]. Due to the nature of the model it was not possible to simulate isolated lithium in the electrolyte during lithium stripping, due to the problems discussed in section 2.1.4. Nevertheless, Yoon *et al.* were able to predict that thinning of necking regions, leading to dead lithium, were more likely to happen during a slow stripping.

The model presented in this work was used to reproduce Yoon *et al.* [16] stripping results, with the addition of the SEI component. Fig. 4.29 shows the results of this simulation. First, lithium was deposited for 300 s with an applied current density of $1 \text{ mA}\cdot\text{cm}^{-2}$ (Fig. 4.29a), then the same quantity of lithium was stripped with two different currents, $1 \text{ mA}\cdot\text{cm}^{-2}$ in Fig. 4.29b and 4.29d and $0.1 \text{ mA}\cdot\text{cm}^{-2}$ in Fig. 4.29c and 4.29e. Differently from Yoon *et al.*, in this simulation the fast stripping was more critical for dead lithium formation, given the more severe thinning of necking regions in Fig.4.29d, in the dendrites produced at the corners of the initial defect (highlighted in the figure by red arrows).

The different conclusions between this work and the work of Yoon *et al.* [16] can be traced back to the addition of the SEI. With both the applied current density, the SEI is thicker on the tip of the dendrite during lithium stripping. Therefore, the lower thickness at the sides of the dendrites leads to higher stripping current density in those regions, thus, to the thinning of necking regions, and ultimately to pieces of lithium remaining isolated from the bulk. The difference between the high current density and the low current simulations is that, in the former, the ratio of the SEI thickness between the tip and the sides of the dendrite is around 38, compared to 8 in the case of lower current. This SEI thickness ratio explains why the thinning is more severe in the case of high current density applied during the stripping.

4.4.2 Pores Creation

As expressed in section 2.1.4, one of the weaknesses of the multi-domain model approach is not being able to simulate pores creation, due to topological problems, where cells inside the mesh collapse and reach singularity. This section represents an attempt to bypass this problem. Comsol® Multiphysics offers the opportunity of importing a geometry and variable profiles and gradients from an external file. In Fig. 4.30, the first two images refer to a classic simulation, starting from a surface defect

with homogeneous properties in the electrolyte and SEI and a constant applied current density.

The simulation arrived at singularity due to the collision of the two nearby dendrites, and Fig. 4.30b shows the last useful step before the singularity. From Fig. 4.30b the geometry and quantities (*i.e.* lithium concentration, potential, SEI thickness) were exported and imported in a new simulation (Fig. 4.30c), where the dendrites are manually merged and new boundary conditions can be defined consistently. Thus, the simulation could restart until new pores are on the verge to be generated (Fig. 4.30d).

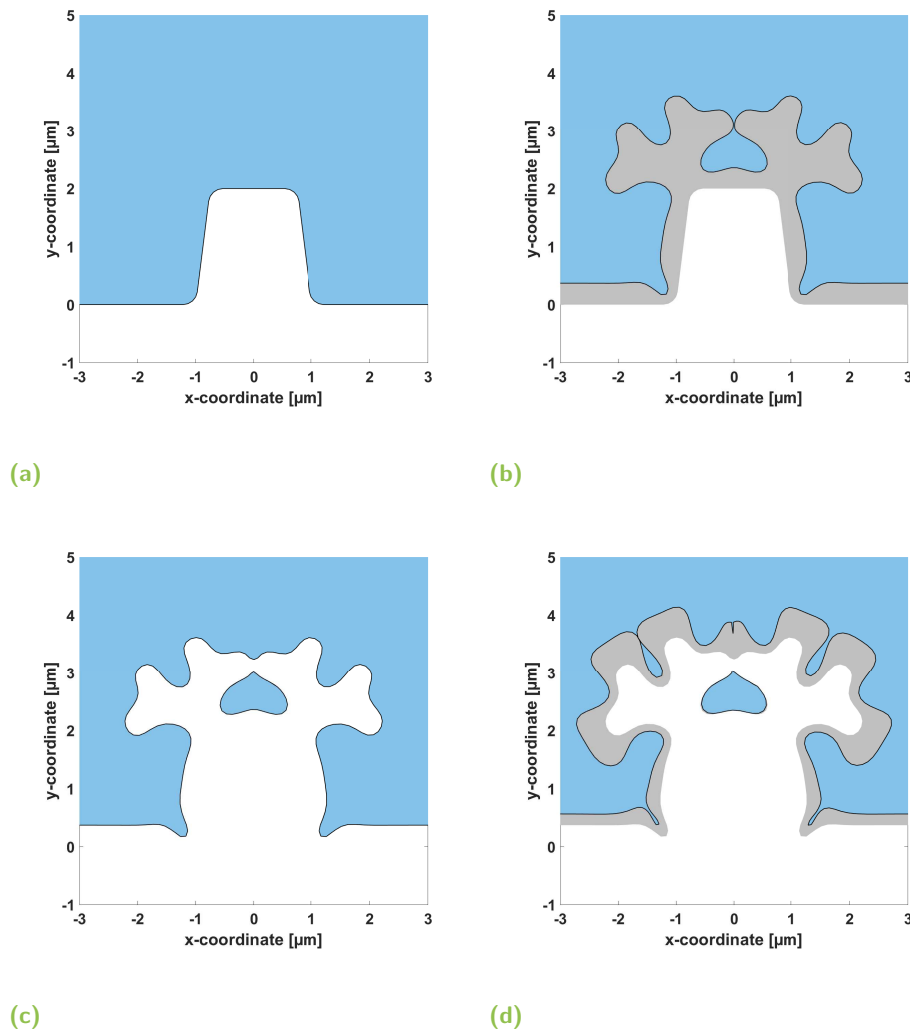


Figure 4.30: Lithium deposited during the simulation in grey. a) Initial geometry of the first simulation. b) Final step of the first simulation before singularity is reached c) Initial redesigned geometry of the second simulation. d) Final step of the second simulation.

This process is long and tedious if done manually, plus it involves small numerical errors due to the manual change of geometry. Nevertheless, if it can be automated, it can unlock new and more complex simulations involving porous creations and lithium isolation.

4.5 Conclusion on Model Results

The presented simulations confirmed that being below the limiting current density is not a sufficient condition to avoid dendrites, moreover low current densities can be more detrimental than higher current densities due to the creation of taller filiform dendrites. By comparing simulations with and without the presence of SEI on electrode surface, the SEI was confirmed to be fundamental to assess dendrites formation and growth, and a strong correlation between SEI thickness and directions of growth was found.

Thanks to the introduction of the SEI into the model, different electrode surface morphologies have been produced by the simulations at different applied current densities, starting from the same initial geometric defect on the lithium surface. The defect was fundamental to produce different geometries because all the properties of the electrolyte, SEI and electrode were considered uniform, which is a strong assumption with respect to reality. The current densities that were used were lower than the limiting current density (thus no lithium depletion at the lithium/electrolyte interface). At this current range, mossy-like dendrites are expected. Nevertheless, using parameters from literature, at $10 \text{ mA}\cdot\text{cm}^{-2}$ the morphology had a more branched nature, while at $1 \text{ mA}\cdot\text{cm}^{-2}$ the growth was more globular. This is consistent with the trend reported in the literature [11]; which describes tree-like dendrites above the limiting current density and more globular structures as the applied current density decreases. An analysis on the behavior of the SEI thickness evolution in the model explained that the difference in morphology is due to the different rate of deformation of the lithium metal surface and consequently to the time available for the SEI to form.

Even without the modeling of the SEI mechanics, the addition of the active SEI was able to produce filiform structures, similar to whiskers, at low applied current densities ($0.1 \text{ mA}\cdot\text{cm}^{-2}$). This was due to the fact that, under these conditions, SEI had more time to grow and get thicker everywhere on the lithium surface, except on the convex upper corners of the defect. Thus, lithium deposition was limited by

the widespread presence of a thick SEI layer, while the filiform dendrites could grow in the few points with a thin SEI. In the literature [11], whiskers are described as filiform structures, but their main other characteristic is that they grow from the root. On the contrary, the model was able to reproduce filiform structures with tip-induced growth, questioning the most widespread knowledge that whiskers are solely due to bottom-induced growth. Therefore, it is important to investigate if all the whisker structures that are found in the literature are effectively growing from their root, or if the root-induced whiskers are a subset of the filiform dendrites.

At even lower current densities (lower than $0.02 \text{ mA}\cdot\text{cm}^{-2}$), the model shows a more homogenous lithium deposition, in spite of the initial surface defect. This current is very low for practical applications, thus limiting the applied current density is not a feasible strategy to prevent dendrites formation.

The choice of a transient model gave the advantage with respect to a stationary study to be able to reproduce different morphologies that could not be detected by a sensitivity analysis on the initial interface. Nevertheless, accuracy regarding the behavior of the SEI had to be sacrificed to allow the model to simulate a reasonable amount of deposited lithium ($0.111 \text{ mAh}\cdot\text{cm}^{-2}$). SEI is known to be a bi-layer structure formed by a porous organic outer layer and a compact inorganic inner layer, while in this model it was considered a homogeneous medium.

Thanks to this last assumption, it was easier to perform a sensitivity analysis on the electrochemical properties of the SEI. It can be concluded that a SEI with low resistivity, high diffusion coefficient or fast reaction rate can reduce dendrite growth. In particular, the SEI formation reaction rate was able to shift the current density ranges in which certain morphologies happened, while a low SEI resistivity was able to reduce dendrites growth at each current density and with each dendrite morphology.

The full model confirmed the importance of considering both the electrochemical and the mechanical effects of the SEI to have a complete description of the different growth mechanisms that have been observed experimentally. Indeed, the addition of the SEI mechanics has made it possible to distinguish between tip- and bottom-induced growths, the latter being present at lower applied current density, in accordance with the literature. Finally, the mechanical resistance of the SEI was found to be a double-edge sword because a high resistance can limit the uncontrolled expansion of the lithium electrode, but it can also boost root-growth in case of fractures.

Additional results on lithium stripping and pores generation were presented, since they are as important as lithium deposition to increase the lifetime of lithium metal batteries. These simulations were constrained by the nature of the chosen model, which was a continuum multi-domain model. Nevertheless, it was found that higher current densities are more detrimental for the formation of dead lithium due to the different ratios in SEI thickness between the tip and the side of the dendrites. Finally, it was demonstrated that improvements in the software could lead to longer and more complex simulations of these phenomena.

Finally, early attempts were made in using in the model the values of the parameters identified with the performed experiments. Nevertheless, the model was found to perform better with parameters from the literature, and the reasons behind this are extensively explained in the next chapter.

Experiments

The goal of the experimental part was to develop a framework of experiments able to provide parameters to the model and to validate its trends. Since the results of the simulations, made with Comsol[®] Multiphysics, showed the importance of the SEI on dendrite evolution, the experimental work carried out during the thesis was focused on finding the electrochemical and mechanical properties of the SEI.

This chapter can be divided in three main parts:

- A summary of the parameters that are used in the model presented in the previous two chapters.
- Explanation and discussion on the EIS experiments that were made to find the electrochemical properties of the SEI, and presentation of the *post-mortem* experiments used to find the mechanical properties of the SEI (AFM) and its chemical components (XPS).
- Validation of the trends predicted by the model with a novel cell configuration suitable for an *operando* optical microscopy.

5.1 Model Parameters

The parameters that are used in the model can be divided in three main categories, the parameters relative to the electrolyte, the ones relative to the lithium electrode, and the ones relative to the SEI. Tab. 5.1 reports the parameters used in the model, listing them according to the above-mentioned division.

There are well-established techniques to study the electrochemical properties of the electrolyte, thus investigating the electrolyte was not part of this study. Among the different techniques, the electrolyte diffusion coefficient used by Ferrese *et al.* [50] and consequently in the model presented in this work, was found by Stewart and Newman [92] by using UV/vis absorption spectroscopy to monitor the relaxation of the concentration gradient in the electrolyte.

Electrolyte Parameters	
Salt initial concentration	$c_{e,0}$ [mol.m ⁻³]
Solvent concentration	c_{sol} [mol.m ⁻³]
Transference number	t_+ [-]
Electrolyte diffusion coefficient	D_e [m ² .s ⁻¹]
Electrolyte conductivity	κ [S.m ⁻¹]
Lithium Parameters	
Lithium metal specific molar volume	\bar{V}_{Li} [m ³ .mol ⁻¹]
Electrode conductivity	σ_s [S.m ⁻¹]
Lithium Young's modulus	E_{Li} [MPa]
Lithium Poisson's ratio	ν_{Li} [-]
Yield strength of lithium	$\sigma_{y,Li}$ [MPa]
Hardening modulus of lithium	K [MPa]
Hardening exponent of lithium	n [-]
Reference exchange current density	i_{00} [A.m ⁻²]
SEI Parameters	
SEI reaction scale factor	λ [m ⁻¹]
SEI reaction rate coefficient	k_{SEI} [m.s ⁻¹]
SEI specific molar volume	\bar{V}_{SEI} [m ³ .mol ⁻¹]
SEI resistivity	r_{SEI} [Ω .m]
Initial SEI thickness	$h_{SEI,0}$ [nm]
SEI diffusion coefficient	D_{SEI} [m ² .s ⁻¹]
SEI Young's modulus	E_{SEI} [MPa]
Lithium Poisson's ratio	ν_{Li} [-]
Yield strength of SEI	$\sigma_{y,SEI}$ [MPa]

Table 5.1: Parameters used in the model simulations divided by group.

Alternatively, EIS can be used for measuring the electrolyte diffusion coefficient, like in the work of Mullin *et al.* [93], and transference number, like in the work of Evans *et al.* [94]. Transference number and diffusion coefficient can also be measured via NMR, like in the work of Zugmann *et al.* [95]. Electrical measurements are used to find electronic and ionic conductivity of the electrolyte, as used by Wu *et al.* in their work [96].

The model can be extended to incorporate the mechanical effect of a solid electrolyte or of the separator, thus their mechanical properties can be added to the list, and they are usually derived from tensile stress-strain curves measurements, like in the work of Geng *et al.* on PEO [97]. Lithium metal mechanical properties can be measured with AFM, as presented in chapter 2, or with stress-strain curves, like in the work of Tariq *et al.* [68] and of Masias *et al.* [86].

Differently from the electrolyte, the literature to investigate the properties of the SEI is less established, with a wider range of techniques and designs that are used, and with doubts on the explanation of the results due to the intrinsic complexity of the SEI itself. For this reason and for the importance of the SEI in the model, we decided to focus on experimentally finding the properties of the SEI, while relying more on the literature for the electrolyte and the lithium metal properties.

5.2 Time-Difference Impedance Spectroscopy

Time-Difference Impedance Spectroscopy was performed following the theory of Vorotyntsev [74]. Like in the work of Morales-Ugarte *et al.* [76] [77], EIS was performed on symmetric lithium/lithium coin cells.

5.2.1 Experimental Methodology

The symmetric lithium/lithium coin cells were assembled in an argon-filled glove box using a CR2032-type case (2.6 mm of spacing) and two lithium (Albemarle[®]) disks as electrodes with a thickness of 135 μm and a diameter of 16 mm. As separators, one disk of Viledon[®] (thickness around 250 μm) and two foils of Celgard[®] 2400 (thickness of 25 μm each) were used for symmetry purpose at the lithium/electrolyte interface (each facing a Celgard[®] membrane). 150 μL of the electrolyte were inserted between the electrodes and soaked within the polymeric separators, while two 0.5 mm thick stainless steel disks were used as current collectors. Finally, a stainless

steel wave spring (1.2 mm non-compressed thickness) was added to maintain the electrodes/electrolyte stack under pressure.

The potentiostatic electrochemical impedance spectroscopy (PEIS) measurements were performed at OCV (Open Circuit Voltage) and at ambient temperature with a multichannel potentiostat (Bio-Logic Science Instruments). Spectra were recorded each hour during the first 24 hours, and each 3 hours in the following two days. An electric signal of 10 mV of amplitude was applied to the cell, in the frequency range between 1 MHz and 5 Hz. This frequency range was chosen to be able to track the impedance response of the SEI layer, without extending too much the duration of the EIS, which can lead to disturbance of the system and SEI artificial evolution. Time for data acquisition was approximately 2 minutes. Between the spectra recording, the cell was left in open circuit voltage condition.

Different liquid electrolytes were used during the experiments, with the goal of studying different SEI properties. Thus, the main two families of liquid electrolytes, presented in section 1.2.6, were investigated: an ethers-based electrolyte composition, which is widely used in lithium-sulfur cells and carbonates-based electrolytes, which are the standard for lithium ion batteries. For the first category, 1M lithium bis(trifluoromethane) sulfonylimide salt (LiTFSI) was dissolved in a mixture of tetraethylene glycol dimethyl ether (TEGDME) and 1,3-dioxolane (DIOX) in a 1:1 volume ratio.

For the second category, several compositions were considered in this study, among them 1M lithium hexafluorophosphate (LiPF_6) dissolved in a mixture of ethylene carbonate (EC), propylene carbonate (PC) and dimethyl carbonate (DMC) (1:1:3); and 1M LiPF_6 /EC:DMC:EMC. The methodology proposed by Vorotyntsev could not be applied by using the above mentioned compositions, due to the fact that the semicircles resulting from the time difference spectra were not regular, thus, not identifiable with a simple equivalent circuit. This led to the conclusion that the SEI formed with these compositions had a very heterogeneous and unstable growth even after a few days. Since vinylene carbonate (VC) and fluoroethylene carbonate (FEC) additives are well-known to promote the formation of a stable SEI on lithium metal [20] [21], which is more compact and stable, an additional composition was investigated based on the use of 1M LiFP6 in a mixture of ethylene carbonate (EC) and diethyl carbonate (DEC) with a 1:1 volume ratio, and with the addition of 2% VC and 10% FEC in mass. This alternative composition allowed the methodology of time difference EIS to be applied. It is worth mentioning that the electrolyte composition was not optimized for the purpose of this study

but selected among the electrolyte reference compositions available in the laboratory.

Fig. 5.1 shows the spectra, obtained at different times during the first day after cell assembly, of one of the lithium/lithium symmetric coin cells containing the ethers-based electrolyte. The observed spectra represent the first semicircle reported in Fig. 2.28 from the work of Bouchet *et al.* [75], and attributed to the SEI passive layer present on the electrode surface. The first measurement was performed around 5 minutes after the coin cell assembly, named as t_0 . Between two PEIS measurements, the cell was turned to OCV conditions, thus, no noticeable lithium deposition or stripping happened. Therefore, due to the short duration of the PEIS acquisition, the difference between spectra should mostly be justified by the evolution of the SEI with time. After 24 hours (measurements not shown here), no significant evolution of the EIS spectra was observed.

The general trend for EIS spectra in the Nyquist representation is presented in Fig. 5.1. At high frequency, the intersection of the spectra with the real axis was attributed to the ohmic resistance associated to the electrolyte conductivity, R_{el} , that stays constant over time. At medium frequencies, a large, depressed semicircle is observed, which may integrate two semicircles contributions, one being relatively stable over time (at high frequency) and the second one evolving significantly over time. As in the work of Bouchet *et al.* [75], this contribution was attributed to the electrochemical response of the SEI layer. Looking at the evolution with time of this predominant semicircle, the evolution of the EIS spectra suggests a change in the composition of the SEI layer and an increase in its thickness.

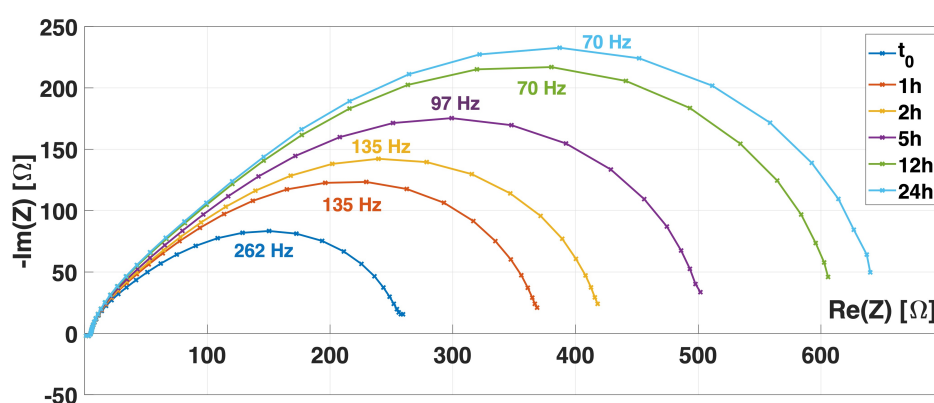


Figure 5.1: Spectra recorded for an ethers-based electrolyte Li/Li cell at different times, in the Nyquist representation.

Fig. 5.2, where the imaginary part of the spectra are plotted vs the logarithm of the frequency, shows that the peaks of the curves, which represents the characteristic frequency of the semicircles, shift towards lower frequencies, in particular between the first 5 hours measurements. This signals a change in the SEI composition, as pointed out in the work of Martinet [98]. The characteristic frequency converges toward a stable value at the end of the experiments (12h, 24h), meaning that the newly formed SEI film is homogeneous with respect to the previous one.

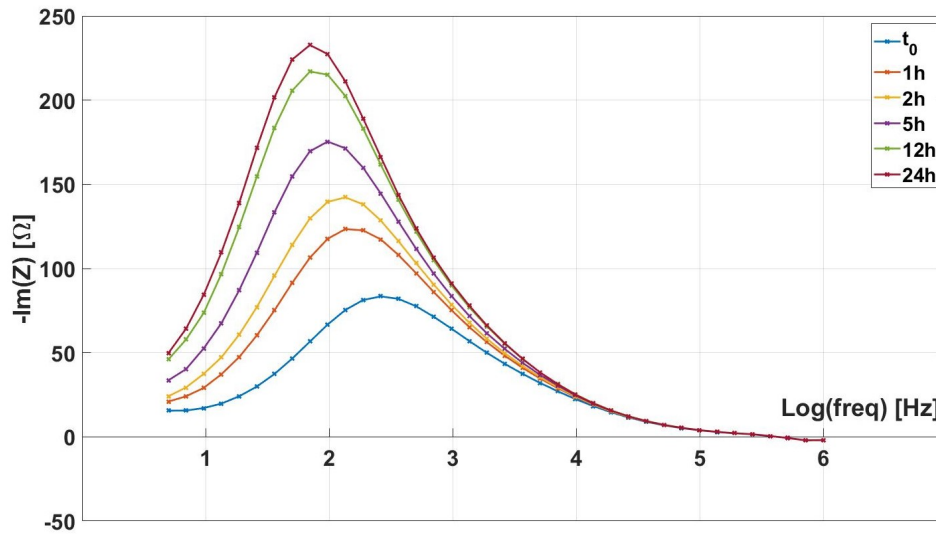


Figure 5.2: Spectra recorded for an ethers-based electrolyte Li/Li cell at different times, imaginary part vs frequency in logarithmic scale.

5.2.2 Data Analysis Methodology

With the help of the software EC-lab, the differences between the spectra were computed and they are shown in Fig. 5.3. Following the work of Morales-Ugarte *et al.* [77], the spectrum obtained at the initial time was subtracted from the following ones.

The resulting differences show regular semicircles expected for the evolution of the SEI thickness, which can be fitted with a simple equivalent circuit, shown in Fig. 5.4, which consists of a resistance in series with the parallel combination of a constant phase element and another resistance. ΔR_{el} and ΔR_{int} are respectively the time difference of the electrolyte and interphase (SEI) resistances, while ΔCPE is the

difference in the constant phase element associated with the interphase capacitance.

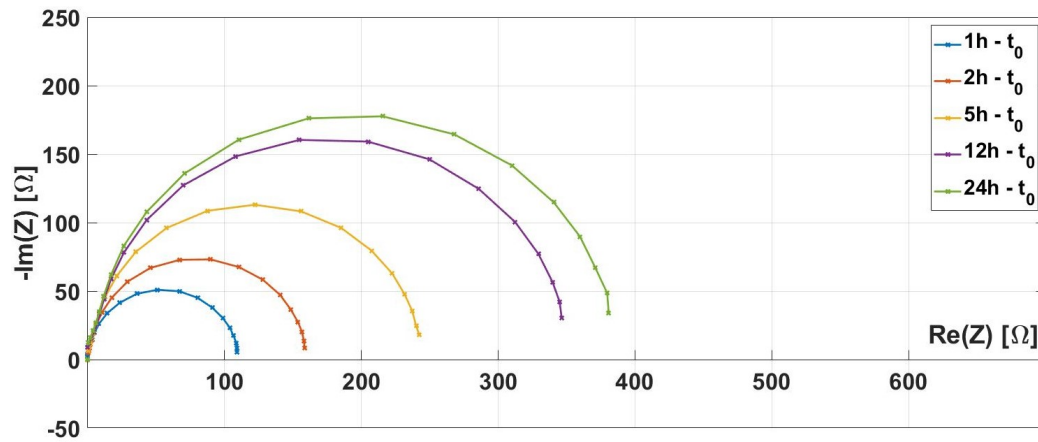


Figure 5.3: Spectra differences from Fig. 5.1.

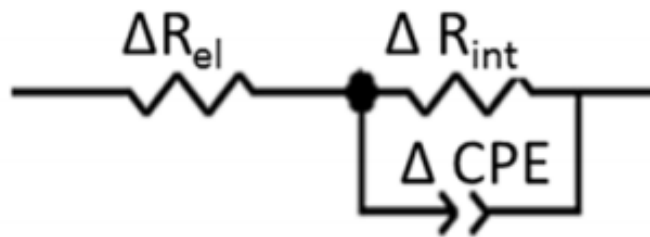


Figure 5.4: Equivalent circuit used to fit spectra differences.

Experimental spectra differences together with the associated fits are shown in Fig. 5.5, while Tab. 5.2 reports the values of the parameters of the equivalent circuits. Tab. 5.2 also shows the parameters of the equivalent circuit used to fit the initial spectrum (t_0), which was used to have an approximate estimation of the SEI thickness at the beginning of the experiments. Like in the work of Bouchet *et al.* [56], the initial spectrum was fitted using an equivalent electric circuit with a single R//CPE component, with a_C being the exponent of the CPE, a parametric value that is equal to 1 in the case of an ideal capacitor.

From the parameters listed in Tab. 5.2, it is possible to compute an estimation of the mean SEI parameters, like lithium diffusion coefficient, conductivity and thickness of the SEI film.

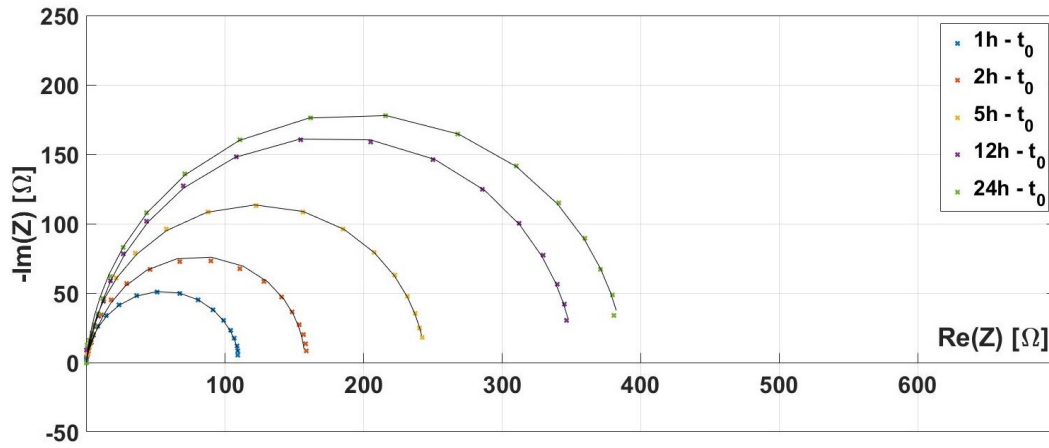


Figure 5.5: Computed spectra differences from Fig. 5.3 (markers) and fitting curves obtained by using the equivalent circuit presented in Fig. 5.4 (black lines).

Spectrum	t_0	1h- t_0	2h- t_0	5h- t_0	12h- t_0	24h- t_0
ΔR_{el} [Ω]	4.20	0.050	0.073	0.076	0.077	-0.078
ΔR_{int} [Ω]	264.9	110.3	160.1	245.0	354.4	389.1
ΔCPE [$F.s^{(a_c-1)}$]	1.68e-5	2.28e-5	1.73e-5	1.31e-5	1.11e-5	1.01e-5
a_C [-]	0.704	0.946	0.945	0.946	0.933	0.941

Table 5.2: Equivalent circuit parameters for the ethers-based electrolyte lithium/lithium cell.

Once defined the characteristic angular frequency of the parallel circuit $\Delta R_{int} // \Delta CPE$ as ω_C [s^{-1}], it is possible to define its electrical impedance, ΔZ_{CPE} [Ω] as follows:

$$\Delta Z_{CPE} = \frac{1}{\Delta CPE (j\omega_C)^{a_C}} \quad (5.1)$$

In a classic R//C circuit, the time constant τ_C [s] is the product of the resistance and the capacitance of the circuit, as well as the inverse of the characteristic angular frequency. Thus, the following equation is valid:

$$\omega_C RC = 1 \quad (5.2)$$

The generalization of the previous equation for an R/CPE parallel circuit is the following:

$$\omega_C R (CPE)^{a_C} = 1 \quad (5.3)$$

Thus, by combining Eq. 5.2 and 5.3 it is possible to define the equivalent capacitance of the circuit, as follows:

$$\Delta C_{int} = \Delta R_{int}^{(1-a_C)/a_C} \Delta CPE^{1/a_C} \quad (5.4)$$

The capacitance of a parallel-plate capacitor is defined as the ratio between the cross-sectional area (in this case equal to the area of the electrode) and the distance between the two plates, multiplied by the permittivity of the medium. Therefore, by assuming the SEI as medium, the distance between the two plates corresponds to the SEI thickness, and the equivalent capacitance of the circuit can be computed as follows:

$$\Delta C_{int} = \frac{\epsilon_0 \epsilon_r A_e}{\Delta h_{SEI}} \quad (5.5)$$

where ϵ_0 [F.m⁻¹] is the vacuum permittivity and ϵ_r [-] is the relative permittivity, which is assumed to be 10 following the work of Bouchet *et al.* [75]. In their paper they stated that the ionic solid conductors varies from 5 to 20, and it is 9.8 for Li₂O and 5 for Li₂CO₃, which are among the main components that form the SEI [75]. A_e [m²] is the area of the electrode, which is not assumed to be porous, thus given its diameter of 16 mm, it is assumed to be around 2 cm². Δh_{SEI} is the change in thickness of the SEI between two spectra.

In the same manner, given the definition of resistance, which defined as the ratio between the length of the medium and the cross-sectional area, divided by its conductivity, it is possible to compute the time difference interface resistance in the following way:

$$\Delta R_{int} = \frac{\Delta h_{SEI}}{A_e \sigma_{SEI}} \quad (5.6)$$

Thus, since ΔC_{int} and ΔR_{int} are the results of the fitting process, from 5.5 it is possible to estimate the mean SEI thickness, h_{SEI} , and from 5.6 the SEI conductivity, σ_{SEI} .

Finally, under the hypothesis that the diffusion of lithium in the SEI follows the Fick's second law (as modeled in chapter 3, the diffusion length, L , is the following:

$$L = 2\sqrt{Dt} \quad (5.7)$$

Since there are two SEI formed in the cell on the respectively lithium electrodes, the semi-diffusion length has to be taken into account, thus, the change in SEI thickness is proportional to the square root of time times the diffusion coefficient, as follows:

$$\Delta h_{SEI} = \sqrt{D_{SEI}t} \quad (5.8)$$

5.2.3 Results with Ethers-based Cells

Tab. 5.3 shows the parameters used in the computation and the resulting evolution of the SEI thickness in one of the ethers-based cells. For reproducibility purposes, two cells were assembled with the same components and the parameters of the SEI were determined and compared. No noticeable differences were found in the SEI diffusion coefficient and conductivity among the cell, while the SEI thickness evolution is presented in Fig. 5.6.

The initial SEI thickness was computed by using Eq.5.5 with the parameters from the equivalent circuit, fitted on the initial spectrum. Both cells, presented in Fig. 5.6, have a similar SEI thickness computed at the initial time, around 10.5 nm, and the same thickness evolution, which leads to a final SEI thickness after 24 h around 13 nm.

The initial thickness and rapid evolution over the first 5 hours is due to the fast side reactions between the lithium metal and the electrolyte as soon as the cell is assembled, and due to the carbonate layer that is already present on the laminated pristine lithium, as shown later on in this chapter, when XPS is discussed.

Spectrum	t_0	1h- t_0	2h- t_0	5h- t_0	12h- t_0	24h- t_0
ΔR_{el} [Ω]	4.20	0.050	0.073	0.076	0.077	-0.078
ΔR_{int} [Ω]	264.9	110.3	160.1	245.0	354.4	389.1
ΔCPE [$F.s^{(a_c-1)}$]	1.68e-5	2.28e-5	1.73e-5	1.31e-5	1.11e-5	1.01e-5
a_C [-]	0.704	0.946	0.945	0.946	0.933	0.941
ΔC_{int} [F]	1.72e-6	1.62e-5	1.24e-5	9.38e-6	7.48e-6	7.14e-6
A_e [cm^2]	2	2	2	2	2	2
ϵ_0 [F.m ⁻¹]	9e-12	9e-12	9e-12	9e-12	9e-12	9e-12
ϵ_r [-]	10	10	10	10	10	10
t [s]	0	3600	7200	18000	43200	86400
Δh_{SEI} [nm]	0	1.11	1.45	1.92	2.41	2.52
h_{SEI} [nm]	10.44	11.56	11.89	12.36	12.85	12.96
σ_{SEI} [S.m ⁻¹]		5.0e-8	4.5e-8	3.9e-8	3.4e-8	3.2e-8
D_{SEI} [m ² .s ⁻¹]		3.4e-22	2.9e-22	2.1e-22	1.3e-22	7.4e-23

Table 5.3: Equivalent circuit parameters, cell assumptions (A_e , ϵ_0 , ϵ_r) and computed SEI parameters relative to the experiment presented in Fig. 5.1.

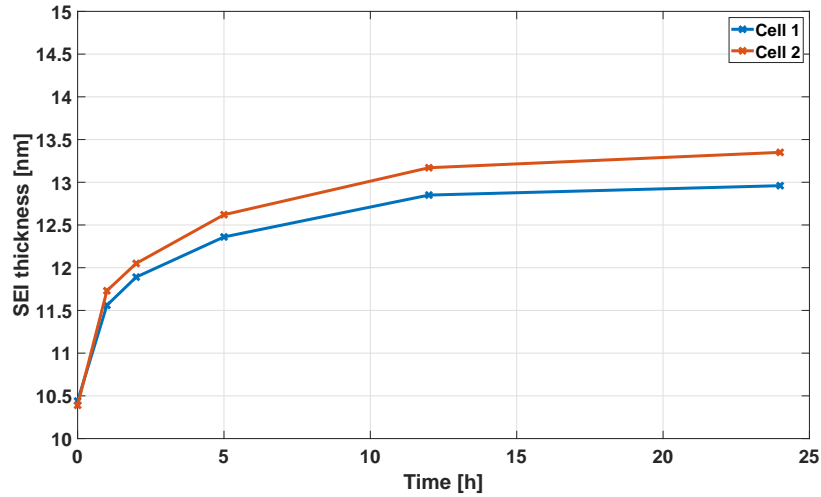


Figure 5.6: SEI thickness evolution determined for two cells with the ethers-based electrolyte, where cell 1 refers to the cell presented in Fig. 5.1.

Complementary to literature [74] [75] [77], a new method to find SEI kinetics parameters from the spectra evolution was developed. Eq. 3.9 was used in the model to compute the SEI thickness evolution. Under the assumption of flat electrode surface and OCV, and combining Eq. 3.10 and Eq. 3.12, Eq. 3.9 can be rewritten as follows:

$$\frac{\partial h_{SEI}}{\partial t} = \frac{\bar{V}_{SEI} k_{SEI} c_{sol}}{2} e^{-\lambda h_{SEI}} \quad (5.9)$$

The pre-exponential term, $\bar{V}_{SEI} k_{SEI} c_{sol}/2$, is a constant and from the literature used for the model [15], it is approximately equal to 2.4×10^{-10} [m.s⁻¹], while λ is equal to 1.2×10^7 [m⁻¹] as estimated by Lin *et al.* in their work [83].

Fig. 5.7 shows the velocity of growth of the SEI, computed at different times for the ethers-based lithium/lithium cell, and an exponential fitting curve, which has the same form as Eq. 5.9. The fitting curve has an R-square of 0.8683, therefore it can be concluded that the evolution of the SEI is more complex than its simplification with an exponential function, especially in the first part where the initial formation of the SEI happens very rapidly. From the fitting curve, the value of the pre-exponential term was found to be around 10^{-9} [m.s⁻¹], thus around 10 times lower than the value from literature. Anyhow, without any additional inputs, it is impossible to evaluate if this is due to a difference in the kinetics of the SEI formation, its specific volume or the concentration of solvent in the electrolyte.

On the other hand, λ was found to be around 4×10^{-5} [m.s⁻¹], which is several orders of magnitude different from the literature value. The reason behind this difference is due to the different methods used to estimate λ . The value of 1.2×10^7 [m⁻¹] was estimated by Lin *et al.* [83], by computing the capacity fade of a lithium ion cell after cycling. In this case, the SEI forms a thick organic outer layer, which is assumed to be composed mainly of lithium ethylene dicarbonate (CH₂OCO₂Li)₂. On the contrary, given the thickness the SEI studied in this work through EIS, it can be estimated that it is mainly composed of inorganic components (assumption confirmed by the *post-mortem* analysis presented in the next section). Therefore, it can be concluded that the two λ identify two different growth mechanisms.

Regarding the values of conductivity and diffusion coefficient of the SEI, presented in Tab. 5.3, both the conductivity and the diffusion coefficient decrease over time.

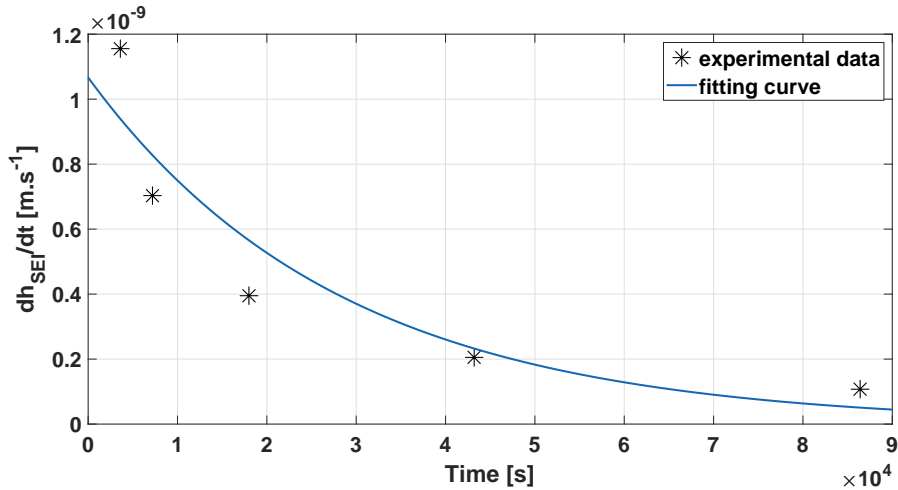


Figure 5.7: SEI experimental velocity of growth (markers), computed from the equivalent circuit parameters, and exponential fitting curve (blue line).

In order to estimate their mean values, the slopes of the curves ΔR_{int} vs \sqrt{t} and $1/\Delta C_{int}$ vs \sqrt{t} , which are shown in Fig. 5.8, were calculated. An estimation of their slopes can only be obtained in the first 12 h of aging time (16 h for the work of Morales-Ugarte *et al.* [77]). Therefore, the weighted mean value computed over the first 12 hours are 3.76×10^{-10} [$S.m^{-1}$] for the SEI conductivity and 1.83×10^{-22} [$m^2.s^{-1}$] for the SEI diffusion coefficient, which are values in the same order of magnitude of the values in Morales-Ugarte's thesis [77], which is the latest iteration of the methodology proposed by Bouchet *et al.* in 2003 [75].

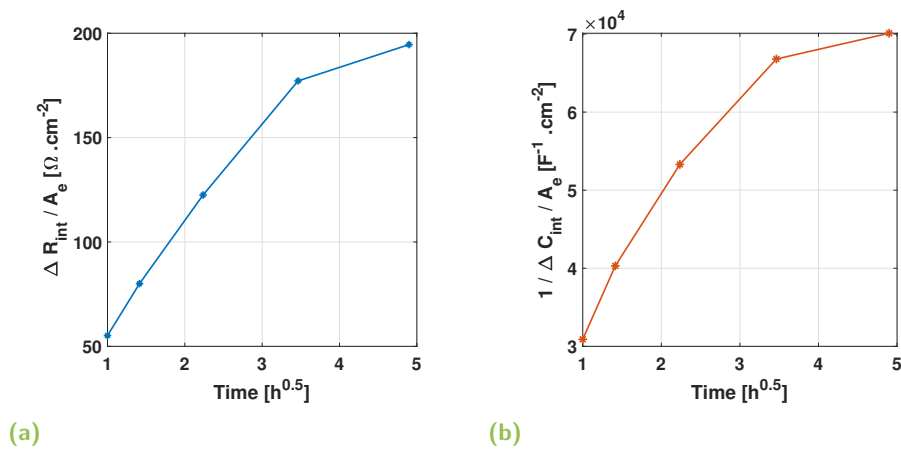


Figure 5.8: ΔR_{int} vs \sqrt{t} and $1/\Delta C_{int}$ vs \sqrt{t} for the cell presented in Fig. 5.1.

Nevertheless, the values are lower than the ones found in the literature for a theorized chemical composition of the SEI, which are in the order of magnitude of 10^{-8} - 10^{-9} [$S.m^{-1}$] for the SEI conductivity [85] [99] and 10^{-18} - 10^{-20} [$m^2.s^{-1}$] for the

SEI diffusion coefficient in the inner inorganic layer [99], while much higher values, closer to the electrolyte are found for the outer organic layer [99].

5.2.4 Results with Comparison with Alternative Methods

To determine these parameters with another approach, the method of Bouchet *et al.* [75] was tried with the ethers-based lithium/lithium cells. As reported in chapter 2, this method consisted of fitting the semicircles at different times with two R//CPE components in series. The first one ($R_1//CPE_1$) computed by fitting the initial spectrum, and the second one ($R_i//CPE_i$) is changing over time. The results of the fitting process are presented in Fig. 5.9, while the parameters of the equivalent circuits are listed in Tab. 5.4. The relative differences between the parameters in Tab. 5.2 and

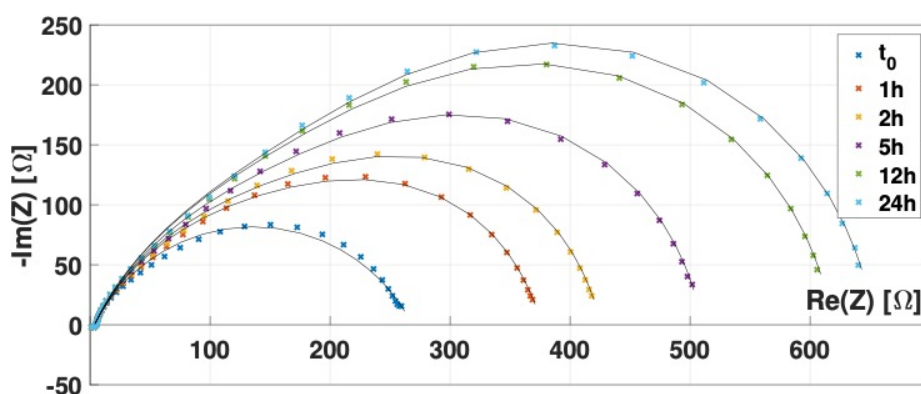


Figure 5.9: Spectra recorded in Fig. 5.1 (markers) with fitting curves (black lines).

Component	R_1CPE_1	$R_{1h}CPE_{1h}$	$R_{2h}CPE_{2h}$	$R_{5h}CPE_{5h}$	$R_{12h}CPE_{12h}$	$R_{24h}CPE_{24h}$
R_{int} [Ω]	264.9	109.1	158.5	242.9	352.4	386
CPE [$F \cdot s^{(a_c-1)}$]	1.68e-5	1.56e-5	1.73e-5	1.04e-5	9.47e-6	8.56e-6
a_C [-]	0.704	1.000	0.990	0.979	0.957	0.966

Table 5.4: Equivalent circuit parameters obtained by following Bouchet's method [75].

Tab. 5.4, are around 1% for R_{int} and 10% for CPE. These differences are likely to be due to the different local minima found by the fitting software, indicating the substantial exchangeability between Morales-Ugarte's method and Bouchet's.

Thus, the underestimation of the conductivity and diffusion coefficient values is independent from the chosen EIS method. The difference could be due to the inhomogeneity in the real SEI evolution which is distant from the homogenous growth hypothesis of this method. Therefore, this method can be useful to identify a qualitative difference between the SEI developed by using different electrolyte compositions but it needs to be combined with other experiments to validate its findings, like EIS at different levels of degradation of the cell.

5.2.5 Results with Carbonates-based Cells

In order to compare with the ethers-based electrolyte, Fig. 5.10 shows the EIS spectra recorded at different times for a Li/Li coin cell using the carbonates-based electrolyte described at the beginning of the section (LiPF_6)/EC:DEC + 2%VC + 10% FEC). Differently from the spectra obtained from the ethers-based electrolyte Li/Li cell, the semicircle is further from intersecting the real-axis at low frequency.

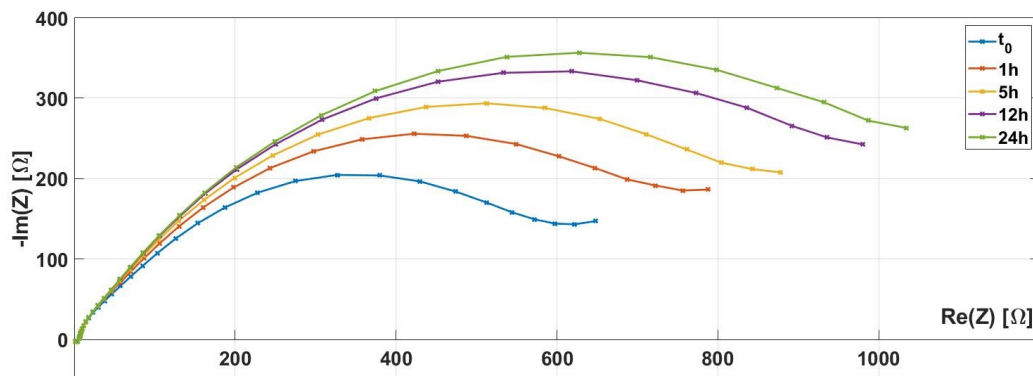


Figure 5.10: Spectra recorded for a carbonates-based electrolyte Li/Li cell at different times, in the Nyquist representation.

Nevertheless, the difference between the following spectra and the initial one, shown in Fig. 5.11 (markers), are still suitable to be fit with the above-mentioned equivalent circuit (Morales-Ugarte's method), though, the lower values of a_C , presented in Tab. 5.5, could flag a lower fitting accuracy with respect to the ethers-based electrolyte.

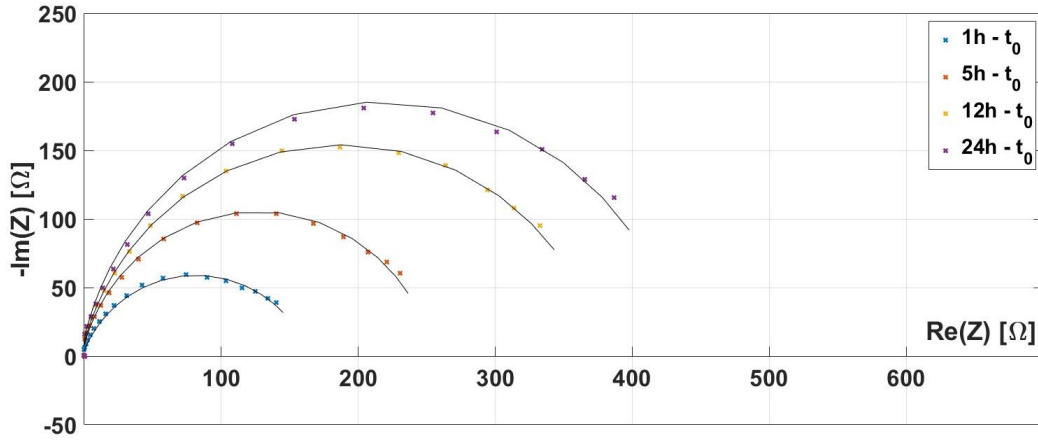


Figure 5.11: Computed spectra difference point from Fig. 5.10 (markers) and fitting curves obtained by using the equivalent circuit presented in Fig. 5.4 (black lines).

Spectrum	t_0	1h- t_0	5h- t_0	12h- t_0	24h- t_0
ΔR_{el} [Ω]	-1.60	-0.20	-0.02	-2.08	-2.35
ΔR_{int} [Ω]	798.1	171.7	268.8.1	408.2	537.1
ΔCPE [$F.s^{(a_c-1)}$]	2.66e-5	7.53e-5	4.15e-5	3.74e-5	2.97e-5
a_C [-]	0.631	0.837	0.8733	0.845	0.850
ΔC_{int} [F]	2.79e-6	3.23e-5	2.16e-5	1.74e-5	1.43e-5
A_e [cm^2]	2	2	2	2	2
ϵ_0 [$F.m^{-1}$]	9e-12	9e-12	9e-12	9e-12	9e-12
ϵ_r [-]	10	10	10	10	10
t [s]	0	3600	18000	43200	86400
Δh_{SEI} [nm]	0	0.56	0.83	1.04	1.26
h_{SEI} [nm]	6.46	7.02	7.29	7.49	7.71
σ_{SEI} [$S.m^{-1}$]		1.6e-8	1.6e-8	1.3e-8	1.2e-8
D_{SEI} [$m^2.s^{-1}$]		8.6e-23	3.9e-23	2.5e-23	1.8e-23

Table 5.5: Equivalent circuit parameters, cell assumptions and computed SEI parameters relative to the experiment presented in Fig. 5.10.

The values listed in Tab. 5.5 indicate a lower diffusion coefficient by a factor of 10 (2.5×10^{-23} vs 1.3×10^{-22} [$\text{m}^2 \cdot \text{s}^{-1}$]) with respect to the ethers-based case, while the conductivity is in the same order of magnitude. The carbonates-based electrolyte leads to the formation of a thinner SEI thickness, as shown in Fig. 5.12, with a smaller initial value and a slower velocity of growth. These different results may be explained by the presence of VC and FEC additives, which are likely to allow rapid and efficient passivation of the lithium metal electrode compared to the ethers composition.

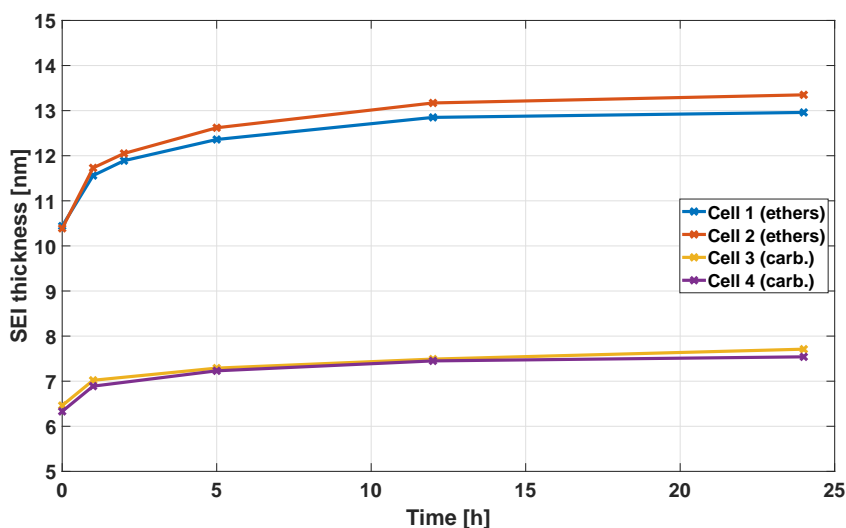


Figure 5.12: SEI thickness evolution comparison between ethers-based cells (Cell 1 and Cell 2) and carbonates-based (Cell 3 and Cell 4).

To conclude, EIS enabled to estimate mean values of the morphological (thickness) and electrochemical (diffusion coefficient and conductivity) properties of the SEI. Mechanical properties were then determined by AFM measurements, which are described in the next section. Moreover, the XPS reveals the composition of the SEI layers that are under study.

5.3 *Post-mortem* Analysis: XPS and AFM

Lithium metal electrodes, aged with the same electrolyte used in the EIS experiments, were analyzed *post-mortem* with AFM and XPS, with the goal of finding Young's modulus values for the formed SEI and identifying its chemical composition.

Measurements on the electrodes surface were performed *post-mortem* and *ex-situ*,

after the coin cells were disassembled in an argon-filled glove box. The cells were assembled one day prior to the experiment, in order to ensure the stabilization of the SEI formation (confirmed in Fig 5.12).

To avoid the presence of salt on the surface of the samples, the electrodes were washed for 30 seconds in 4000 μL solvents: 1,3-dioxolane (DIOX) for the ethers-based electrolyte cell and dimethyl carbonate (DMC) for the carbonates-based. Parallel to the cells used for the AFM measurements, two cells were assembled to evaluate the effect of the electrode washing on the SEI properties. All the EIS experiments showed a reduction of the diameter of the semicircle after washing, indicating that a portion of the SEI was washed away with the solvent, mostly the organic outer layer of the SEI.

For instance, Fig. 5.13 shows PEIS spectra before and after the electrodes washing for the ethers-based electrolyte cell (same lithium electrodes reassembled in a coin cell after washing). Before cell disassembly, and as expected from the previous section, the spectrum after one day is larger than the one at the initial time, t_0 . Following the first EIS measurements, the cell was then disassembled, the electrodes were washed and assembled in a new coin cell with the same separators and electrolyte as for the initial one. The spectrum recorded after the reassembly is very close to the initial one, thus, the AFM will measure the properties of an SEI, whose composition and morphology is close to the layer that was present as soon as the electrode was in contact with the electrolyte.

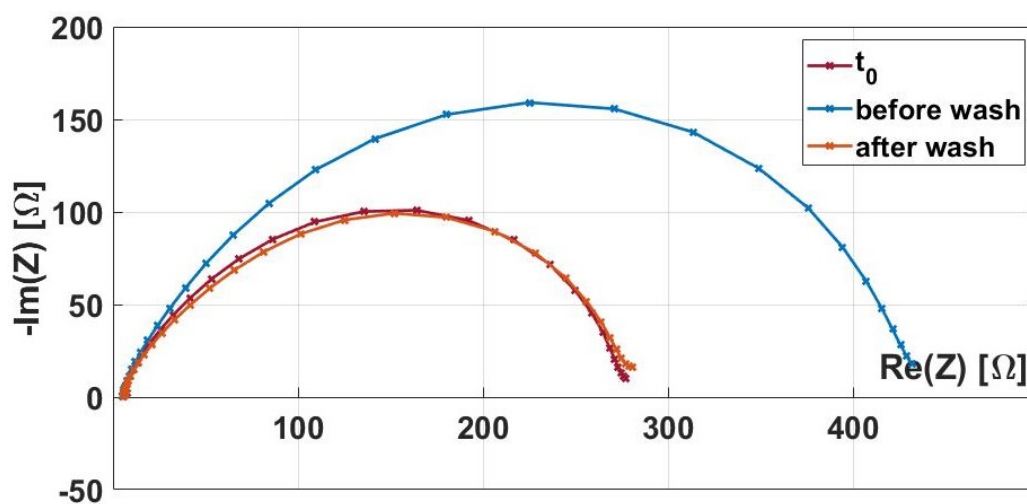


Figure 5.13: EIS spectra for the ethers-based cell, recorded at the initial time, and before and after the electrodes washing with DIOX.

Since the spectra recorded after the reassembly, inevitably, were influenced by the new SEI formed after the reassembly, XPS became fundamental to validate the conclusions regarding the nature of the SEI that was investigated by the AFM.

5.3.1 X-ray Photoelectron Spectroscopy

In order to identify the chemical composition of the SEI, thus validate the results of EIS and AFM, the same samples used for the AFM were analyzed with the XPS. For this work, the XPS spectrometer was an ULVAC-PHI[®] VersaprobeII, with a monochromatic source (AlK α -1486.6 eV) and a beam diameter of 100 μ m, while the penetration depth was estimated to be between 5 and 10 nm. The samples aged with the ethers-based and the carbonates-based electrolytes were compared with the pristine lithium, as shown in Fig. 5.14.

Concerning pristine lithium, C 1s spectrum, relative to the carbon bonds, shows three peaks, which are associated with C-C/C-H (285 eV), -CO (287 eV) and -CO₃ (290 eV) bonding. The C-C/C-H peak usually comes from hydrocarbon contamination, often present on the surface of samples [76], but it can also be explained by the remaining traces of lubricant coming from the process of lithium metal foil preparation. The presence of -CO and -CO₃ groups can be attributed to the formation of lithium alkyl carbonates and lithium carbonate (Li₂CO₃), already on the sample of pristine lithium (no contact with the electrolyte yet). These results are confirmed by the two peaks observed in the O 1s spectrum (oxygen bonds-related), located at 533 and 531.6 eV.

Looking at the lithium electrodes aged in the different electrolytes, the slight shift in the O 1s peak of lithium alkyl carbonates suggests that the alkyl carbonates found in the aged electrodes are not exactly of the same composition as those found on the pristine lithium. The comparison between the pristine and the aged lithium electrodes shows a reduction in the peak of the Li₂CO₃ for the aged lithium samples, which means that the native layer of the pristine foil is covered by an additional layer, mostly composed of organic species (increase in C-C/C-H and alkyl carbonate peaks). Nevertheless, as the initial layer found on the pristine lithium metal foil is still observed after aging, and given the penetration depth of XPS analysis, the thickness of the SEI formed onto the aged lithium electrode is expected to be in the range of 5 nm for ethers (higher intensity of the Li₂CO₃ signal), and in the range of 5 to 10 nm for carbonates (higher attenuation of Li₂CO₃ signal of pristine lithium). It is worth mentioning that the higher attenuation of the pristine lithium signal for

the carbonates could be due to the compact layer of LiF, invalidating the above mentioned SEI thickness comparison with the ethers.

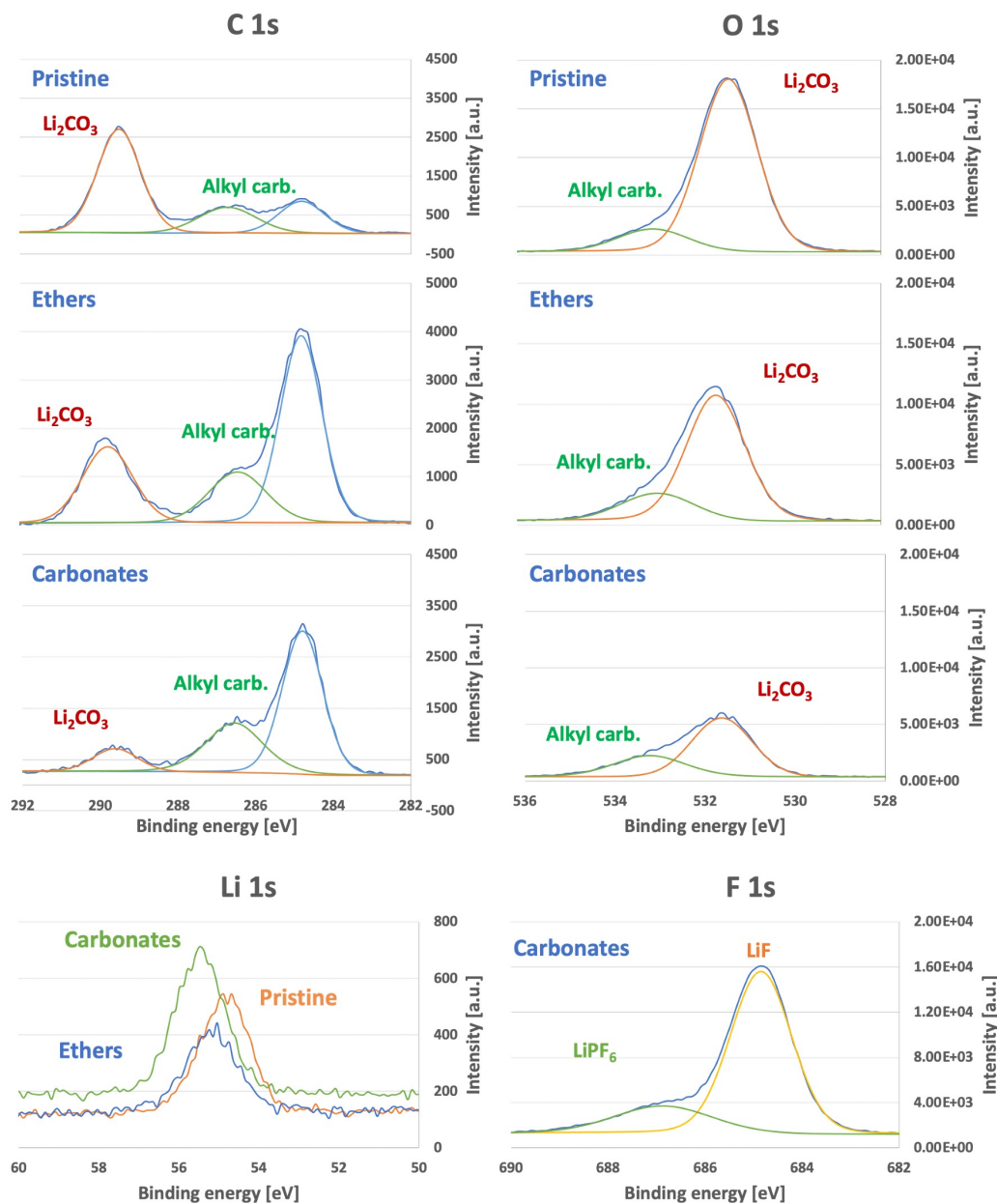


Figure 5.14: C 1s, O 1s, Li 1s, F 1s XPS spectra measured on pristine lithium metal, a lithium metal electrode aged with the ethers-based electrolyte and a lithium metal electrode aged with the carbonates-based electrolyte.

Indeed, concerning the lithium electrode aged in carbonates, F 1s spectrum shows the significant presence of lithium fluoride, LiF, as well as the residual presence of salt, LiPF₆. The significant presence of LiF was also confirmed by the Li 1s spectra of lithium, indicating a shift of the lithium peak towards higher binding energy in the case of aging in carbonates [100]. It is interesting to see that such an intense signal of fluorine was not observed for the ethers-based composition. These results confirm that the use of FEC additive is crucial for lithium metal electrodes, because it influences the passive layer composition by increasing the LiF content within the SEI, which is likely to increase the mechanical properties of the SEI [21]. LiF is denser than organic component [18] and has a lower diffusion coefficient [99]. Therefore, these results about the presence of LiF validate the conclusions from the EIS study that a thinner (or more compact) SEI layer is formed in presence of carbonates-based electrolyte with a lower diffusion coefficient.

To conclude, the native passive layer of the pristine lithium was found to be covered by an additional layer of organic components for the ethers-based electrolyte, and by a layer of organic compounds mixed with LiF for the carbonates-based electrolyte with the addition of FEC.

5.3.2 AFM Methodology

The experiments were performed with an AFM Bruker Dimension ICON[®] equipment, which was placed in an argon-filled glove box. The AFM machine was used in the force spectroscopy mode, in which the cantilever approaches the sample and "pierces" it (nanoindentation), and then withdraws. This measurement was repeated several times across the sample surface, and for each measurement the cantilever deflection vs the piezoelectric element's response was recorded, and then converted in a force vs. tip-sample distance curve (Fig. 5.16, 5.18), often simply referred to as the force-distance curve. Two different forces were applied, 2 and 5 μN , to investigate the impact on the lithium metal mechanical behavior under the tip.

In order to fit force-distance curves obtained with the AFM and to find the Young's moduli, the software AtomicJ[®] was used. Fig. 5.15 shows the interface of the software, where different parameters have to be set to fit the curve and compute the associated Young's modulus. These parameters can be divided in four major categories: fitting options, sample material parameters, tip geometry and calibration. Regarding the fitting options, software default values were used, while the Poisson ratio was taken from literature [51].

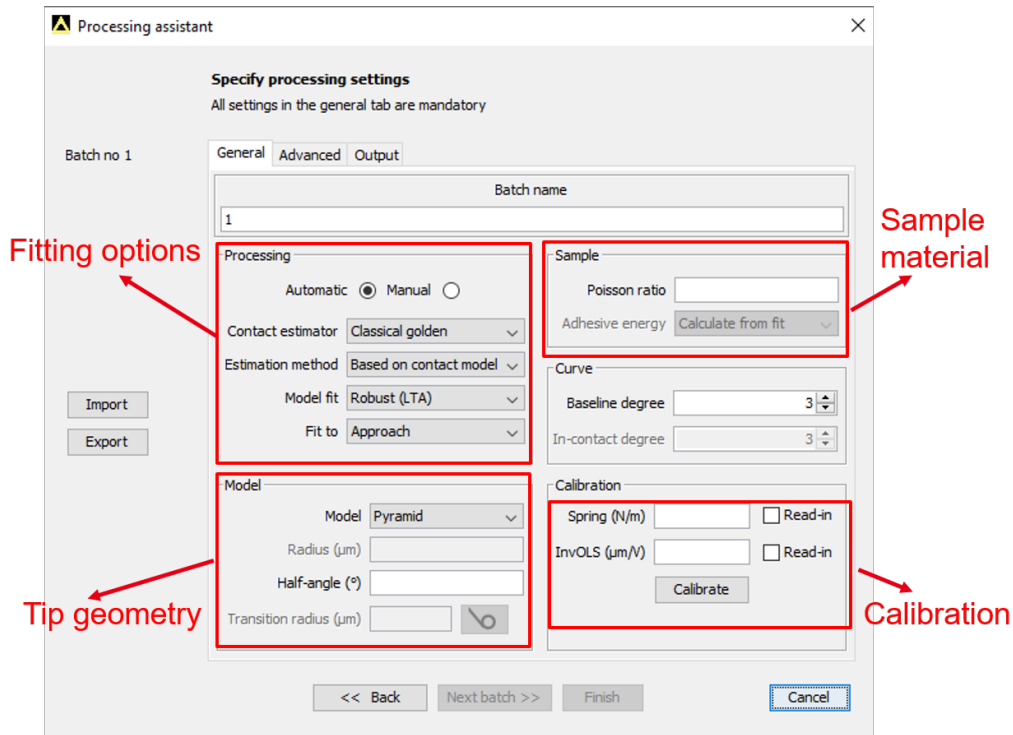


Figure 5.15: AtomicJ[®] interface for finding Young's modulus from a force-distance curve.

Parameters for the tip geometry were taken from the producer data sheet. DNISP-HS probe from Brunker[®] was used. The tip had a pyramidal shape with half-angle of 25°. Therefore, the following geometry-dependent equation to fit force-distance curves was used in AtomicJ[®] (Bilodeau [101]):

$$F = \frac{1.4906E \tan(\theta)}{2(1 - \nu^2)} d^2 \quad (5.10)$$

where F is the force [N], E is the Young's modulus [MPa], Θ the tip half-angle [°], ν is the Poisson's ratio [-] and d the distance.

Regarding the calibration parameters, the spring constant was taken from the probe producer data sheet, while the instrument was calibrated on silicon 111 in order to find InvOLS parameter (sometimes called sensitivity in other versions of the software). InvOLS is used to convert voltage into deflection expressed in microns. It can be calculated based on a force curve recorded on a clean, rigid substrate, and in this case, silicon 111 was chosen for its homogeneous properties and known Young's modulus. In the literature, the silicon Young's modulus is estimated to be between 165 and 188 GPa [102] [103].

Fig. 5.16 shows one of the force-distance curves acquired by performing force spectroscopy on the silicon 111 sample. The slope of both the approach and withdrawal curves is regular, and this facilitates the fitting process for the software.

Different values of InvOLS were used in order to find a feasible value for the Young's modulus for the silicon value. After a trial and error approach, the found value returned the Young's modulus map shown in Fig. 5.17, where Young's moduli for each of the 64 sample points are presented. From the map, the mean value for the silicon Young's modulus was 169 GPa, while the median one was 167 GPa. The value for InvOLS parameter, 0.151, was then used for the experiments with lithium samples.

As shown in Fig. 5.18, force-distance curves are more irregular with lithium samples. Problems arise from the fact that lithium is highly reflective, which disturbs the measurement. This can be noticed in the horizontal part of the force-distance curve, which is not as straight as the one of the silicon sample. Most importantly for the fitting of the curve, the left part of the curve, attributed to the contact point, has not a constant slope and the contact point is often not well defined. This is due to the nature of lithium, which forms different layers of passivation, each layer having its specific Young's modulus. Moreover lithium has a low yield strength, thus, locally, it can deform plastically under the tip force.

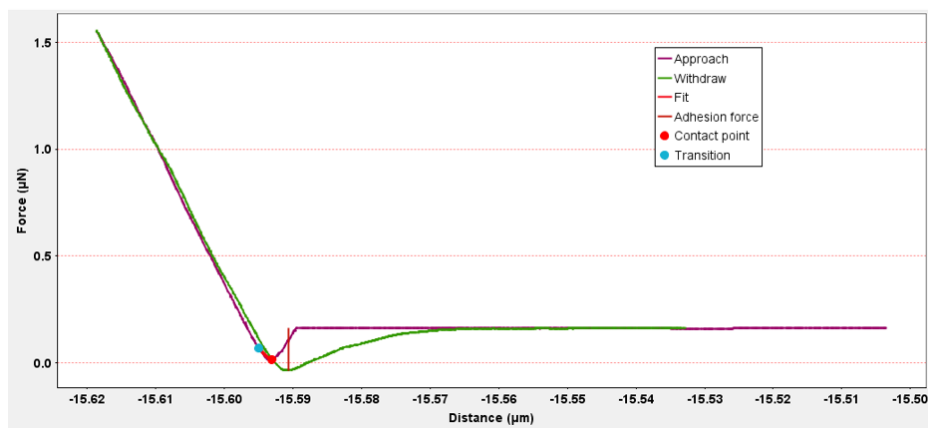


Figure 5.16: Force-distance curve measured from the silicon 111 sample.

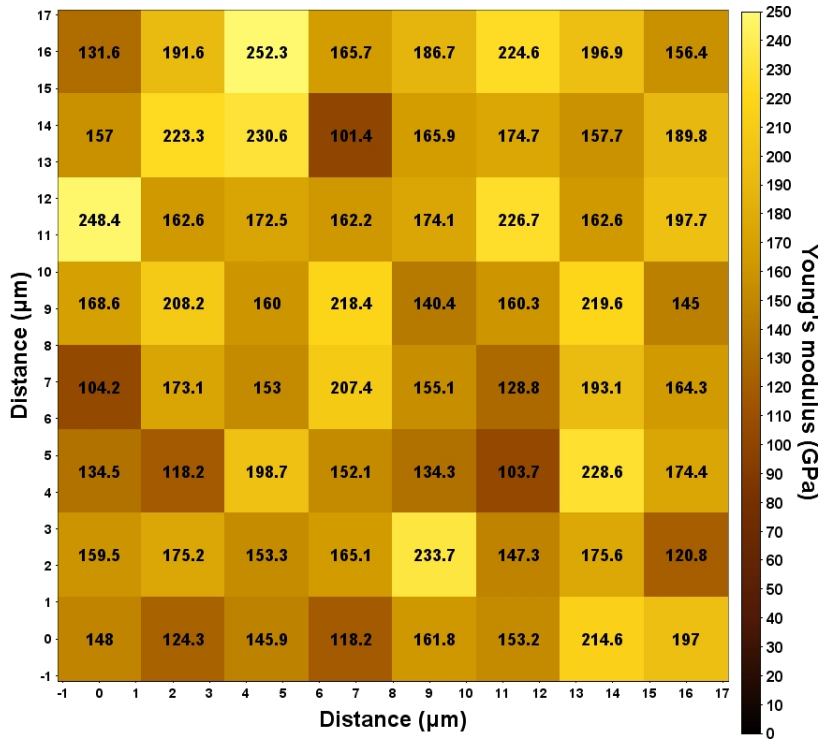


Figure 5.17: Young's moduli map from the silicon 111 sample with 2 μN applied.

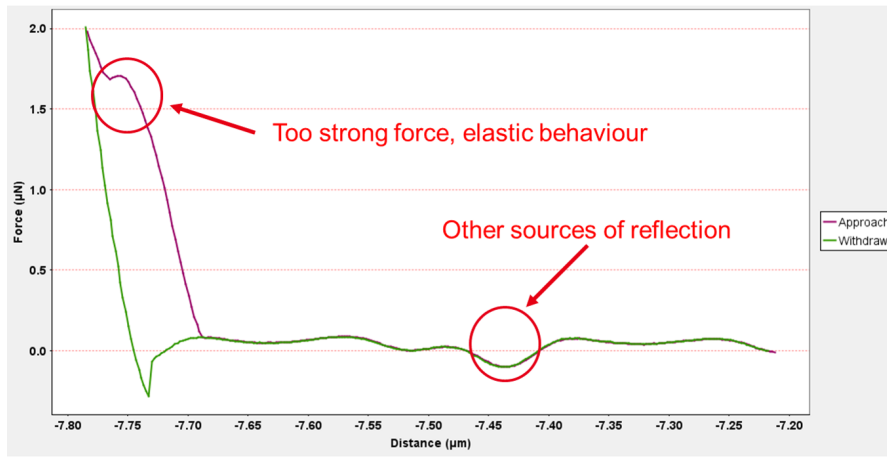


Figure 5.18: Force-distance curve measured from the pristine lithium sample, highlighting the problems associated with lithium metal characterization.

5.3.3 AFM Results

Pristine lithium foil was studied as reference. In order to understand the maximum force to apply with the cantilever, and to prevent major plastic deformation, two different forces were used: $2\ \mu\text{N}$ and $5\ \mu\text{N}$. Young's moduli maps on pristine lithium are shown in Fig. 5.19 for $2\ \mu\text{N}$ and in Fig. 5.20 for $5\ \mu\text{N}$.

In the $2\ \mu\text{N}$ map, the mean value for the Young's modulus was found to be around 36 GPa, while the median was around 31 GPa. This could be due to the presence of Li_2CO_3 , whose presence was confirmed by XPS measurements (Fig. 5.14), and which Young's modulus is reported to be around 35 GPa [71]. On the contrary, the $5\ \mu\text{N}$ map returned a mean value for the Young's modulus around 15 GPa, and a median around 14 GPa. The lower values could be due to plastic response of lithium or due to a lower effect of Li_2CO_3 due to bigger penetration depth associated with the higher force.

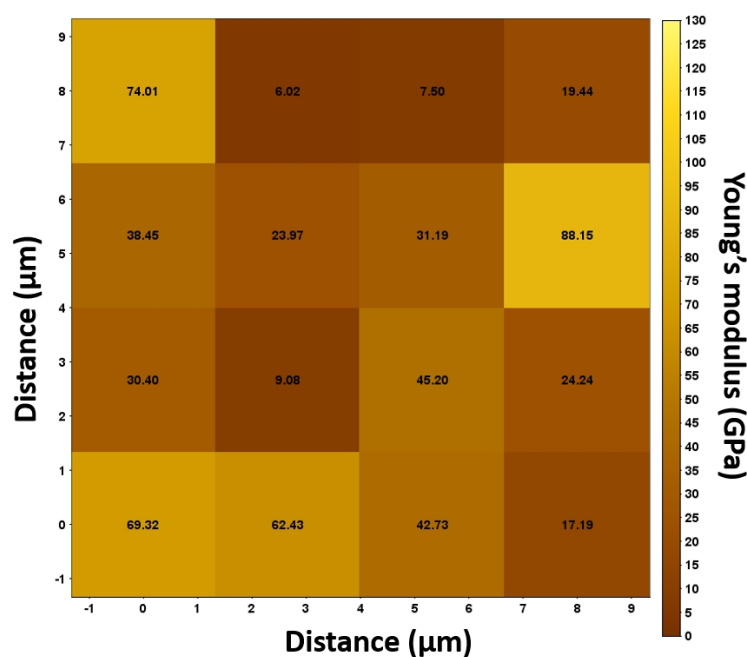


Figure 5.19: Young's moduli map from the pristine lithium sample at $2\ \mu\text{N}$.

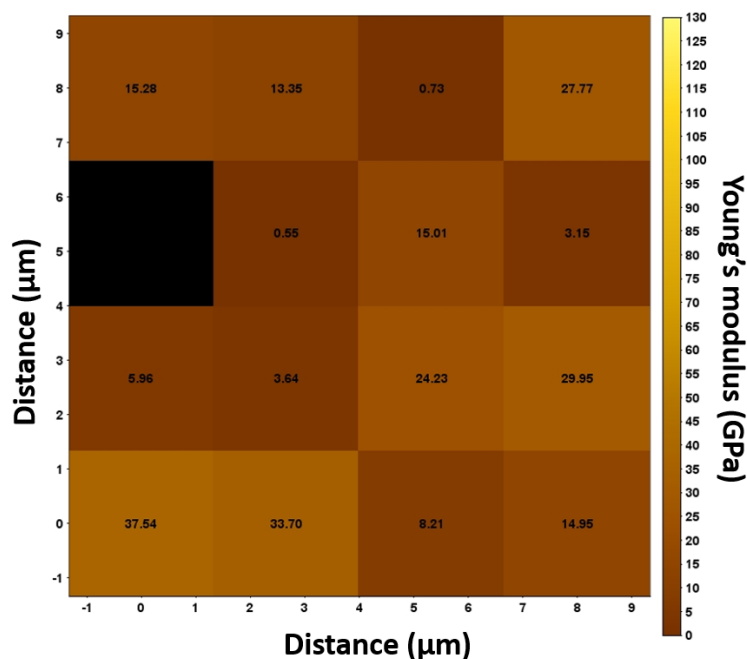


Figure 5.20: Young's moduli map from the pristine lithium sample at 5 μN .

Since the goal of these experiments was to study the mechanical properties of the SEI, and given the results from the pristine lithium, a maximum force of 2 μN was chosen to be applied on the aged electrode samples. Young's moduli maps for the lithium electrode aged in the ethers-based electrolyte and the one aged in the carbonates-based electrolyte are shown respectively in Fig. 5.21 and in Fig. 5.22.

Young's modulus mean value was around 40 GPa for the lithium electrode that was in contact with the ethers-based electrolyte (Fig. 5.21), while the median value was around 32 GPa. The bigger difference between the mean and the median value demonstrates a higher heterogeneity in the sample with respect to pristine lithium. The areas with lower Young's modulus can be associated with the lower concentration of Li_2CO_3 on the surface, which was confirmed by XPS measurements (Fig. 5.14), and the higher concentration of lithium alkyl carbonates (ROLi) species, which have a lower Young's modulus, in the order of hundreds of MPa [71] [73].

On the other hand, the lithium electrode that was in contact with the carbonates-based electrolyte (Fig. 5.22) showed a higher Young's moduli, both in term of median value, 50 GPa, and mean value, 40 GPa, due to the presence of LiF, as confirmed by the XPS data, and in relative good agreement with the Young's modulus of 58 GPa reported in the literature [71].

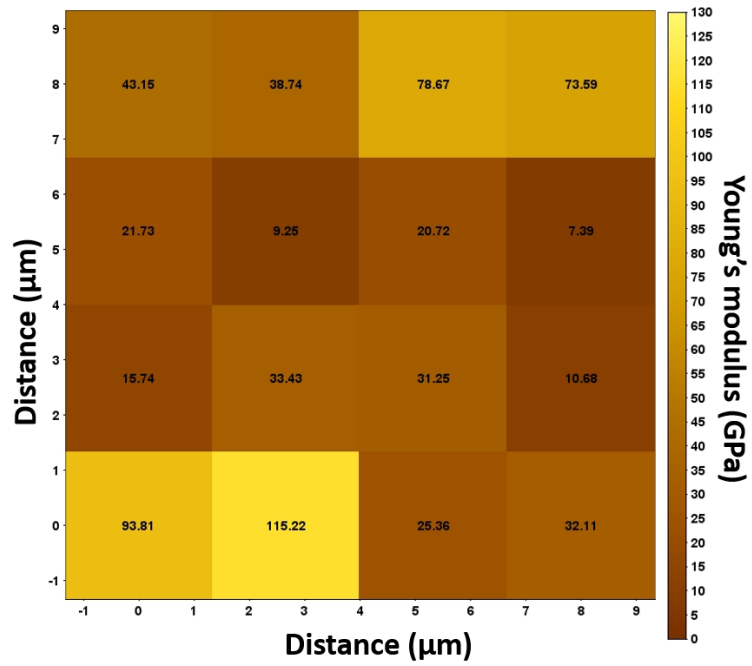


Figure 5.21: Young's moduli map from the lithium sample aged with the ethers-based electrolyte, at 2 μN .

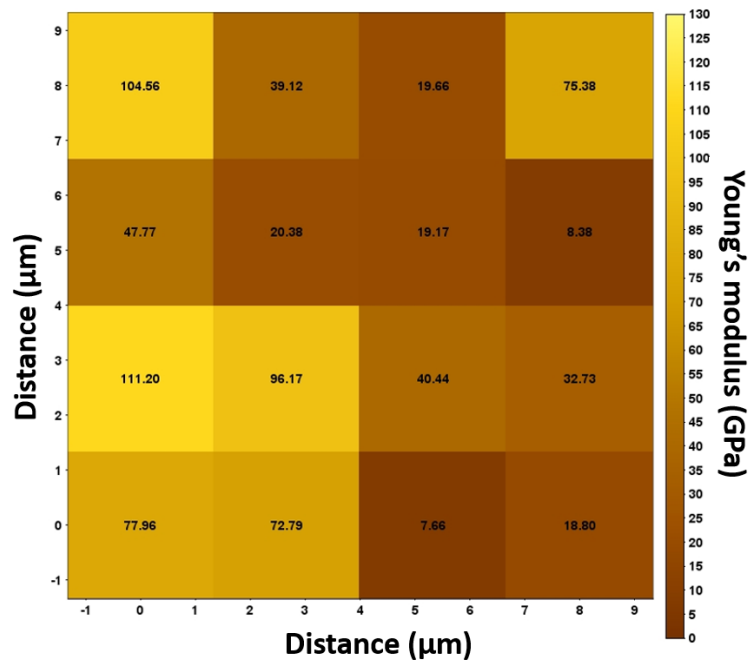


Figure 5.22: Young's moduli map from the lithium sample aged with the carbonates-based electrolyte, at 2 μN .

AFM results are summarized in Tab. 5.6. They were consistent with the findings from EIS and XPS and with the theoretical values from the literature. More specifically, the impact of LiF, which is formed due to the presence of the additive FEC in the carbonates-based electrolyte, was detected by all three experiments. Since, the AFM was performed *post-mortem* after solvent washing, it was not possible to distinguish the contribution of the outer organic layer from the inner inorganic layer, the latter of which was prominent. Therefore, refinements and improvements in the way of performing this technique are necessary to give more meaningful contributions to the model.

Sample	Medium Young's Modulus	Median Young's Modulus	Relevant Features
Li 2 μ N	36 GPa	31 GPa	Presence of Li ₂ CO ₃
Li 5 μ N	15 GPa	14 GPa	Li plastic response
Li + Ethers	40 GPa	32 GPa	
Li + Carbonates	50 GPa	40 GPa	Presence of LiF

Table 5.6: Summary of AFM results.

5.4 *Operando* Optical Microscopy

Differently from the previous sets of experiments (XPS, EIS, AFM), the goal of the optical microscopy was not to find experimental parameters to be used in the model, but to show instead a qualitative comparison between the trends of the model and the experiments, in term of dendrites formation and morphology. Optical microscopy has been chosen because this technique is relatively easier to apply under *operando* conditions, compared to other microscopy techniques (SEM, TEM).

5.4.1 Methodology

In order to perform *operando* optical microscopy, a special lithium symmetric cell had to be designed. Section 2.2.1 already presents the different cell designs reported in the literature to make a suitable cell for *operando* optical microscopy. Nevertheless,

the designs presented in the literature are far from representative cells, whether coin or pouch. Therefore, the goal of this work was to design a cell that was as close as possible to the coin cells used for the EIS. The final design is presented in Fig. 5.23.

The cells were assembled in a dry room (-20°C dew point). First, two disks of lithium metal were cut from the same lithium foil used for the EIS study, with the same dimensions: 16 mm of diameter and 135 μm of thickness. The lithium disks were positioned and pressed on a 10 μm thick copper foil used as the current collector. Later on, a copper-stainless steel welded collector substituted the copper current collector, since the stainless steel ensured a better welding with the plastic case. Each lithium disk was then positioned on a glass plate, as shown in Fig 5.23. The two electrodes were positioned in front of each other and separated at the sides by two pieces of glass plate of 2 mm of thickness. This configuration ensured that lithium ions main direction of flow is perpendicular to the surface of the electrode, like in the real case scenario. The stacked electrodes were then enclosed in a plastic transparent sealed bag. Two sides of the packaging were sealed in the dry room, while one side stayed open. The cell was finally put in an argon-filled glove box, where around 600 μL of electrolyte were introduced to fill the bag and the last side was sealed.

The main differences between the *operando* cell design and a coin cell are the bigger distance between the two electrodes, the lack of a separator in between the two electrodes and the lower internal pressure of the cell, which may have an impact on the dendrites formation of growth. On the other hand, this cell design was comparable to the one used in the model, due to the lack of separator. Overall, the design was successful, as it is shown in the next section, even if some difficulties arose from it. Among them, it was noticed that the plastic bag and the liquid electrolyte could distort the images of the dendrites, especially if these were situated on the lithium disk, on the furthest point from the microscope lens. Moreover, argon bubbles were often created in the electrolyte during filling and sealing, which were sometimes hiding the lithium electrodes growth.

Fig. 5.24 shows the setup of the experiment. Thanks to this cell design, the microscope was able to capture cross-section images of the cell. The microscope used was VHX-500FE, with a magnification of 30x.

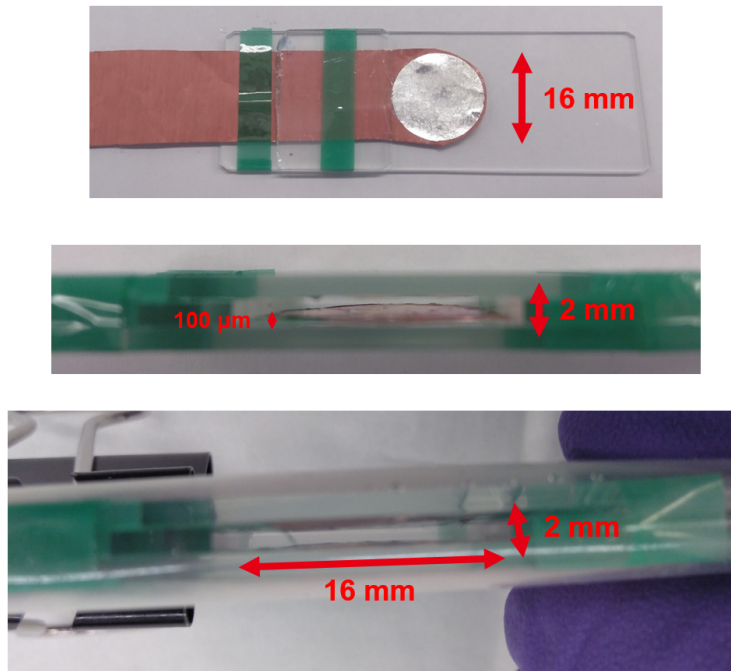


Figure 5.23: Design of the lithium symmetric cell used for *operando* optical microscopy.

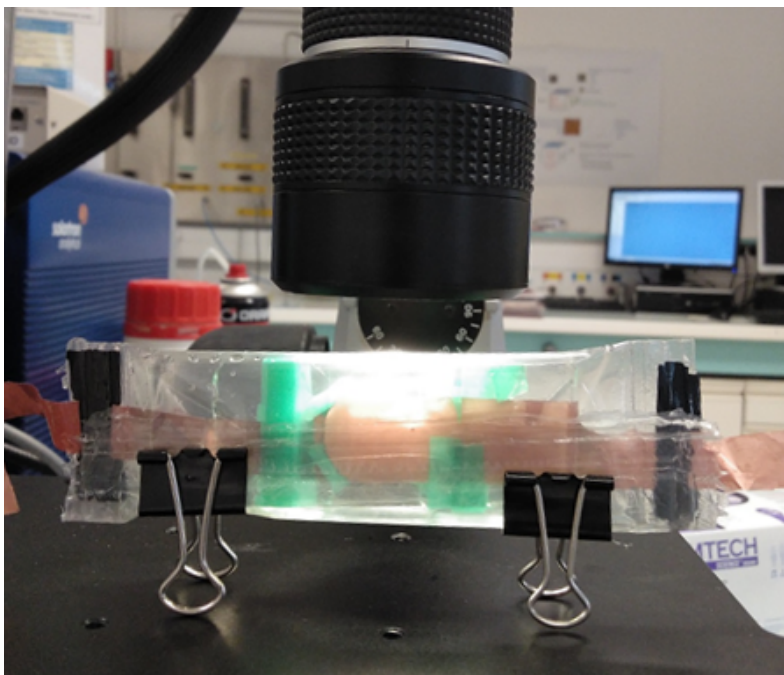


Figure 5.24: Setup of the *operando* optical microscopy measurements.

5.4.2 Results

The same carbonates-based ($\text{LiPF}_6/\text{EC}:\text{DEC}$ with the addition of FEC and VC additives) compositions was used for these *operando* measurements, as well as the same current densities applied in the model, which used $\text{LiPF}_6/\text{EC}:\text{DEC}$ as electrolyte.

From section 4.2, four different applied current densities were used 10, 1, 0.1 and 0.01 $\text{mA}\cdot\text{cm}^{-2}$. Since the surface of the electrodes was 2 cm^{-2} , currents of 20, 2, 0.2 and 0.02 mA were applied to the cells, with a multichannel potentiostat (Bio-Logic Science Instruments). Before starting the experiment, a PEIS measurement was done to detect possible cell failure (like short circuit or too high impedance response). Lithium deposition was arbitrarily stopped after 4 mAh, thus $2\text{ mAh}\cdot\text{cm}^{-2}$, which was around 18 times the capacity deposited during the model simulation. It is important to remember that the length of the simulations was limited by mesh and boundary constraints, thus it is important to detect whether the simulations were able to predict dendritic morphologies in spite of the limited time span.

Applied current density of $10\text{ mA}\cdot\text{cm}^{-2}$

Fig. 5.25 shows the images taken by the microscope during a deposition on the right lithium electrode (top), which lasted 12 minutes with a magnitude of 20 mA, followed by a lithium deposition on the left electrode with the same magnitude and duration (bottom). The images show clear evidence of dendrites, and their morphology can be classified as mossy-like dendrites with evident branched nature. The presence of many thin branched dendrites generates the impression of a lithium foam. In accordance with these data, the model also predicted this morphology of dendrites with this magnitude of applied current density (Fig. 4.9). It is important to notice that during lithium stripping from the right electrode, dendrites were not dissolved meaning that their formation was not reversible, while new dendrites were also formed at the same time on the left electrode.

The dendrites formation can easily be seen as well from the *post-mortem* photos, shown in Fig. 5.26, which were taken after the cell was disassembled in the dry room. Differently from pristine lithium metal foil, the higher surface area of the dendrites gets rapidly oxidized in the dry room environment. Therefore, this is the reason why a dark gray foam was present on both electrodes, in contrast with the shiny gray aspect of the pristine lithium metal foil. The photo on the left represents the lithium electrode visible on the left side of the microscope images

(same correspondence for the electrode in the right figure). The electrode in the right figure, on the other hand, was subjected first to deposition and then to stripping, thus the quantity of lithium dendrites seems to be lower but not null, confirming that the dendrites formation is not reversible.

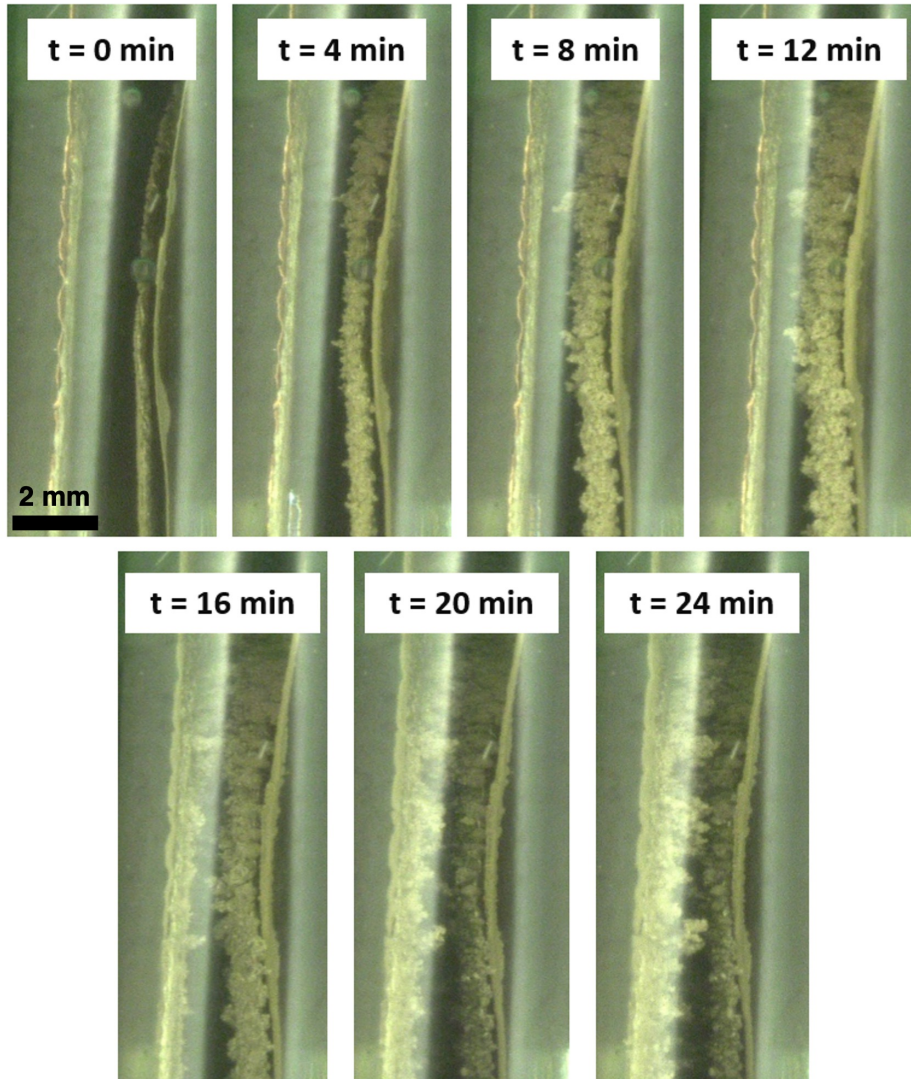


Figure 5.25: Images recorded by optical microscopy during a lithium stripping/plating experiment on a cell with the carbonates-based electrolyte. $10 \text{ mA}\cdot\text{cm}^{-2}$ were applied to the cell for 12 minutes, followed by $-10 \text{ mA}\cdot\text{cm}^{-2}$ for the same amount of time.

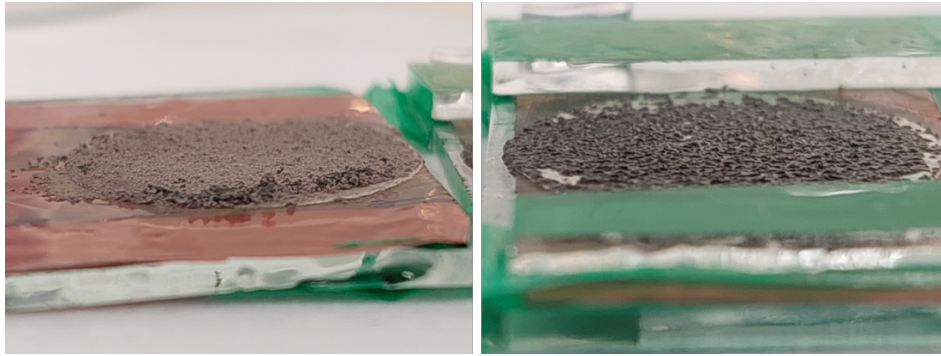


Figure 5.26: *Post-mortem* images from the same cell presented in Fig. 5.25. The electrode on the left corresponds to the electrode on the left in Fig. 5.25 that was subjected to stripping followed by plating of lithium (same correspondence for the electrode on the right).

Applied current density of 1 mA.cm^{-2}

In Fig. 5.27, images taken by the microscope during the 2 mA experiment are presented. Like in the previous experiment, lithium deposition was stopped after 4 mAh of exchanged capacity. Since 2 mA were applied, lithium deposition on the right electrode lasted for 2 hours. Like in the previous case, dendrites were clearly present. Unlike the previous case, their vertical development was less pronounced, therefore the dendrites look more globular, like predicted by the model with this magnitude of applied current density (Fig. 4.10). At the end of the deposition, some areas of the lithium electrode did not show any dendrite formation, while the dendrites forest was covering the totality of the electrode surface in the previous experiment at higher current density.

A detail of a dendrite globule can be seen in Fig. 5.28. The photo is relative to an experiment performed on a cell with the same design and components, with 1 mA.cm^{-2} of applied current density, before a consistent procedure to take the images and compare the different experiments was defined.

Yet, the most important difference between the experiments with 10 mA.cm^{-2} and 1 mA.cm^{-2} of applied current density happens during the deposition on the left electrode, does during the stripping on the right electrode. Indeed, differently from the previous case, dendrites are almost not anymore present on the right electrode at the end of the experiment, which is confirmed by the *post-mortem* photo, Fig. 5.30, where the right electrode (right in both photos) is almost undamaged.

Far from being a definitive conclusion, the more globular shape of these dendrites

with respect to the previous section could ensure a more homogeneous stripping. As well, the simulations showed in section 4.4.1 predicted that lithium stripping causes more dead lithium with higher currents.



Figure 5.27: Images recorded by optical microscopy during a lithium stripping/plating experiment on a cell with the carbonates-based electrolyte. $1 \text{ mA}\cdot\text{cm}^{-2}$ was applied to the cell for 2 hours, followed by $-1 \text{ mA}\cdot\text{cm}^{-2}$ for the same amount of time.

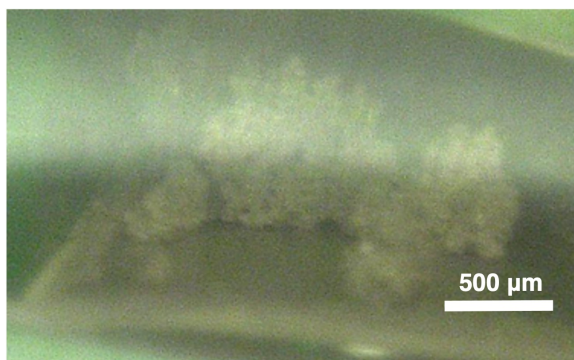


Figure 5.28: Detail of a mossy dendrite, recorded by the optical microscope during an experiment on a cell with the carbonates-based electrolyte and with $1 \text{ mA}\cdot\text{cm}^{-2}$ of applied current density.



Figure 5.29: *Post-mortem* images from the same cell presented in Fig. 5.27. The electrode on the left corresponds to the electrode on the left in Fig. 5.27 (same correspondence for the electrode on the right).

Applied current density of $0.1 \text{ mA}\cdot\text{cm}^{-2}$

Similarly, the experiment at 0.2 mA was performed for 20 hours. Filiform bumps were present on the electrodes but barely noticeable. Still, in the *post-mortem* photo, shown in Fig. 5.30, holes in the left electrode can be seen. It is supposed that these holes were left by the dendritic material that formed the whiskers or filiform dendrites, and which was detached from the electrode during the cell *post-mortem* disassembly.



Figure 5.30: Post-mortem images for the $0.1 \text{ mA}\cdot\text{cm}^{-2}$ experiment.

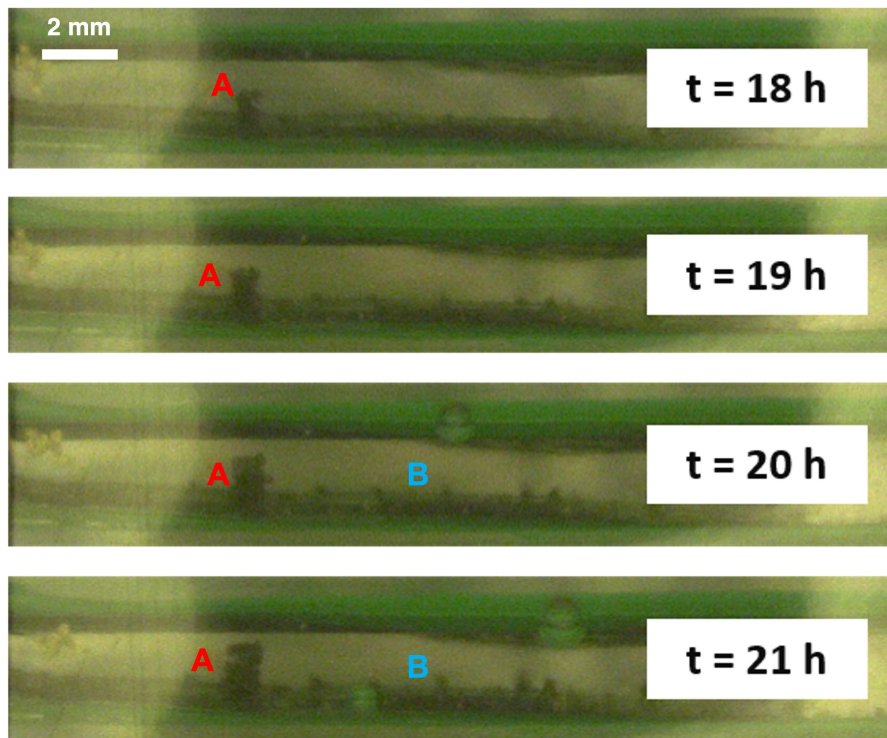


Figure 5.31: Images recorded with the optical microscope during an experiment on a cell with the carbonates-based electrolyte and with $0.1 \text{ mA}\cdot\text{cm}^{-2}$ of current applied density.

Moreover, in a previous experiments conducted at a current density of 0.1 mA.cm^{-2} , two different structures could be seen (Fig. 5.31), a bulkier pillar on the left, marked with a red letter A, and thinner filiform structures on the right (blue B). It is unlikely that the growth of structure A is solely due to root-induced growth, thus cannot be classified as a proper whisker. Nevertheless, the experiments confirmed the results of the model that was able to predict filiform structures forming at this current density range, growing with a tip-induced mechanism (Fig. 4.11). On the contrary, the smaller and thinner B structures could be attributed to the formation of proper whiskers with root-induced growth.

Given the design of the cell, with a lower internal pressure, high distance between the electrodes and the absence of a separator, it can be hypothesized that dendrites initially grow from their root in cracks formed in the thick SEI covering the lithium electrode (structure B). Once these whiskers are well developed they continue to grow due to lithium deposition, forming the filiform pillar noticeable in Fig. 5.31 and predicted by the model.

Applied current density of 0.01 mA.cm^{-2}

Finally, the experiment using an applied current of 0.02 mA was performed. In order to be consistent with the other experiments, the measurements were supposed to last 400 hours (200 hours of deposition and 200 hours of stripping for each electrode). Nevertheless, after approximately 90 hours of deposition, the experiment was stopped due to the lack of evidence of dendritic structures formation, as shown in Fig. 5.32. These results were in agreement with the model output, predicting a quasi-homogeneous deposition at such low current density (Fig. 4.12).

The findings were confirmed by the *post-mortem* analysis and by the voltage profiles recorded during the experiments. Fig. 5.33 shows the voltage profiles vs deposited capacity for the experiments with 1 mA.cm^{-2} and 0.01 mA.cm^{-2} applied current densities. No evidence of dendrites formation is observed on the voltage profile recorded at low current density, while the irregularities of the voltage profile, observed after 5 hours of applied current, are clear evidence of micro-short circuits and beginning of lithium electrode failure, as stated in the work of Barchasz *et al.* [104].

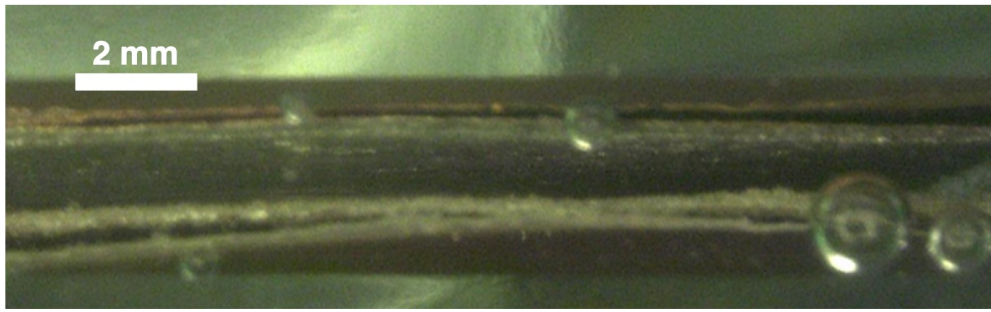


Figure 5.32: Image recorded with the optical microscope after an experiment on a cell with the carbonates-based electrolyte. 0.02 mA were applied to the cell for 90 hours.

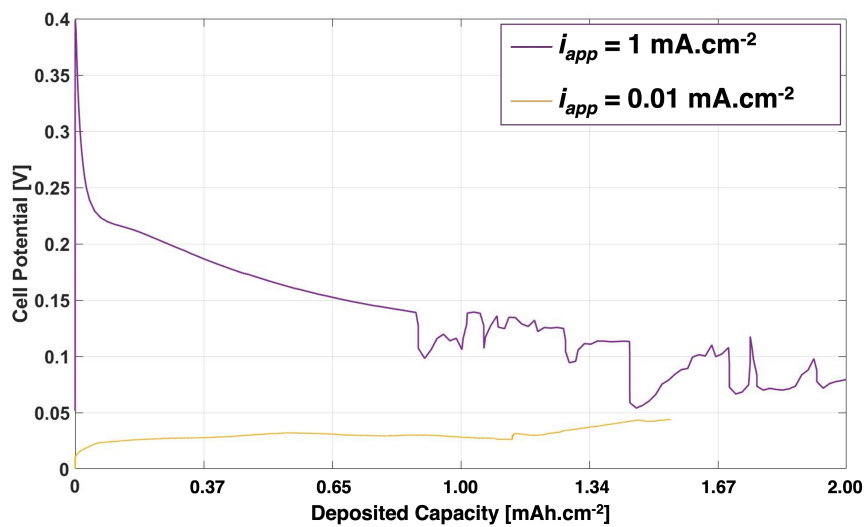


Figure 5.33: Voltage profiles recorded during *operando* optical microscopy.

***Operando* optical microscopy with the presence of a separator**

Finally, a last experiment was made to assess the impact of the separator on the dendrites growth, which impact is hard to be modeled with high fidelity during numerical simulations. Fig. 5.34 shows the cell assembly process. The lithium electrode was positioned on the copper current collector, on a glass plate. A stainless-steel tab was welded to the copper foil. Then, the lithium electrode was covered by a layer of Celgard® 2400 separator, which was the same separator used in the coin cells for the EIS experiments. The process was repeated for the other electrode, while pieces of glass plate were also used as spacers between the two electrodes.

Differently from the coin cell, no pressure was applied on the electrodes/separator

stack, explaining why the separator tends to fold naturally in this cell design (Fig. 5.35). Therefore, the experiment was not perfectly comparable to the real case scenario. Nevertheless, during deposition at 20 mA in the carbonates-based electrolyte cell containing a separator (Fig. 5.35), after 12 minutes, dendrites were prevented from growing like in Fig. 5.25. Indeed, dendrites seemed to push the separator but did not penetrate through it (the only dendrite in Fig. 5.35 that seemed to penetrate (marked with a red arrow) was actually bypassing the separator). In addition, the *post-mortem* observation confirmed the absence of dendrites material above the separators.

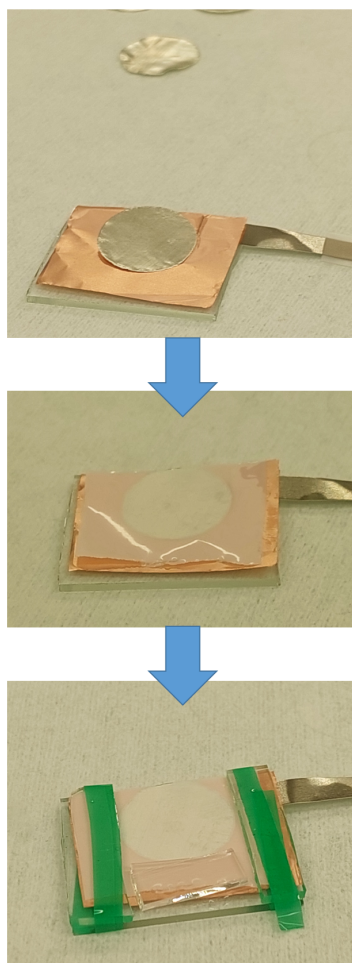


Figure 5.34: Design of the lithium/lithium cell with a separator used for *operando* optical microscopy.

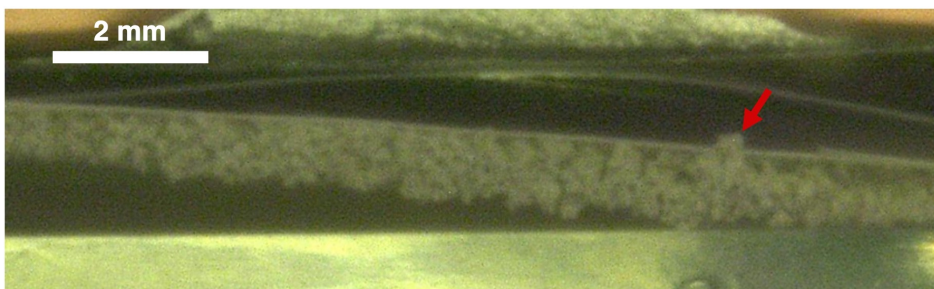


Figure 5.35: Image recorded by optical microscopy after a lithium stripping/plating experiment at 20 mA for 12 minutes on a cell containing the carbonates-based electrolyte and two layers of polymeric separator.

The *operando* optical microscopy was useful to confirm the trends of the model. Both the model and the optical microscopy studied a cell with carbonates-based electrolyte ($\text{LiPF}_6/\text{EC}:\text{DEC}$) and with the same current densities applied.

5.5 Conclusions on the Performed Experiments

The performed experiments aimed to identify the morphological, electrochemical and mechanical properties of the SEI, which were found of great importance in the model. Moreover, the inherent complexity of the SEI makes it hard to identify these properties, therefore it was fundamental to keep improving and refining experimental techniques in a consistent framework of experiments.

The SEI formed on the lithium electrode in contact with two different electrolytes was studied *in-situ* by differential EIS measurements and *post-mortem* by XPS and AFM techniques. Two different electrolytes were studied, belonging to the two main families of liquid electrolytes, a carbonate-based electrolyte with the addition of FEC, and an ether-based electrolyte.

EIS experiments were able to identify mean values for the SEI thickness, diffusivity and resistance, while a new method to find its kinetics properties was proposed. The thickness evolution was in accordance with the SEI formation law proposed in the model (Eq. 3.12), with a decrease in formation velocity as the SEI grows. Despite this, the initial SEI formation (in the first few minutes) was too fast to be modeled with the current known equations. XPS data confirmed that the thickness of the SEI was in the order of 10 nm.

The identified values for SEI diffusion coefficient and conductivity were consistent with the literature that performed the same typology of experiments [77] but lower than the theoretical ones [99]. So far, no clear explanation was found for these results, most probably the hypothesis of homogenous medium that is required for computing them is too strong with respect to the heterogeneous physical nature of the SEI. It would be interesting in the future to compare these results with other characterization methods. For example, the parameters determined by EIS could be compared with the diffusion coefficient determined by means of solid NMR (if possible, to produce a “reference SEI” composition).

AFM, used in the force spectroscopy mode, returned local values of Young’s modulus for the studied samples. The same samples were investigated with XPS to correlate their chemical composition with the mechanical properties determined by AFM. The electrodes aged with the electrolytes showed higher heterogeneities with respect to the pristine lithium, in accordance with the newly formed SEI that was detected by XPS. Also the pristine lithium electrode has a passive layer that covers it, mainly composed of Li_2CO_3 as detected by XPS. Its presence was confirmed by the values of Young’s modulus determined with AFM, which were close to the theoretical values of Li_2CO_3 .

Most notably, the presence of LiF, formed with the carbonate-based electrolyte due to the addition of FEC and detected with XPS, was found to increase the Young’s modulus of SEI layer on the lithium electrode. At the same time, it allowed the formation of a more compact and stabilizing SEI, with respect to the ether-based electrolyte, as confirmed by the EIS measurements over time.

To conclude, the results of the three performed experimental techniques were consistent with each other. Differently from the model, which considered the SEI as a homogenous layer with averaged properties, resulting from the contribution of the inner inorganic SEI layer and the outer organic layer, the three performed experimental techniques were able to study mainly the inner inorganic layer. This is shown from the low thickness of the SEI found through the EIS, and as well from its properties, which are closer to the theoretical ones of the inner inorganic components than the outer organic ones [99]. XPS confirmed these results by showing the observed chemical components (Fig. 5.14). Indeed, the presence of Li_2CO_3 and LiF was stronger than alkyl carbonate components. Finally, the results of AFM confirmed that the SEI remaining after washing was mainly composed of inorganic components, since the experimental Young’s moduli were closer to the ones of the species forming the inner compact layer [18] [73].

Since the identified properties referred mainly to the inner layer of the SEI, the model was found to perform better with the parameters from the literature. Indeed, using for the whole thickness of the SEI the lower values of diffusivity of the inner inorganic components, as well as the higher mechanical resistance, led to an over-estimation of the SEI effect on dendrites growth. Thus, lithium depletion at very low currents due to the very low diffusion coefficient in the SEI, and geometrical defect collapsing under the absurdly high pressure of the SEI, due to its very high mechanical properties.

The trends from the simulations that were carried out with the parameters from the literature (presented in chapter 4) were confirmed by the *operando* optical microscopy, which was made on a tailored designed cell, with the goal to be as close as possible to the real case scenario. In particular, the optical microscopy observations confirmed that even at low current densities ($0.1 \text{ mA}\cdot\text{cm}^{-2}$), dendrites protrusions can grow. Different morphologies were found at different current densities, consistently with the model simulations. Moreover, the presence of a separator was confirmed to effectively mechanically block or reduce dendrites growth. This validates the direction of deploying solid state electrolytes in the next generation of batteries, in order to add a further barrier to dendrites growth.

Final Conclusions and Future Developments

In this work an extensive analysis of dendrites evolution on lithium metal electrodes was presented, both from the modeling side and from the experimental one, motivated by the strong belief that a strict correlation between experiments and model is necessary to understand the formation and the growth of dendrites, in order to make lithium metal batteries safer and commercially widespread. A foundation work was required in order to explore the different modeling alternatives in the literature. The model was designed with the scope of capturing the principal phenomena and components that influence dendrites evolution. On the other hand, the goals of the experimental part were to define a framework of techniques to find reliable parameters to be used in the model, and to validate its trends. EIS was found to be the ideal technique to study SEI evolution and its electrochemical properties, while AFM was used to identify SEI mechanical properties. XPS was performed to validate the findings of EIS and AFM, by identifying the chemical components present on the electrode surface. Finally, *operando* optical microscopy was used as the first attempt to validate the trends of the model.

The presented simulations confirmed that being below the limiting current density is not a sufficient condition to avoid dendrites, moreover low current densities can be as detrimental or even more than higher current densities due to the creation of taller filiform dendrites. By comparing simulations with and without the SEI, the SEI was confirmed to be fundamental to assess dendrites formation and growth, as a strong correlation between SEI thickness and directions of growth was found. Nevertheless, the SEI was assumed to be a homogenous layer with uniform properties, which is a strong assumption (confirmed also by the performed experiments), given its composite structure and inhomogeneous nature. Therefore, as a perspective, this model could be integrated in a multi-scale model framework to be coupled with smaller scale models that are able to simulate in detail SEI evolution and composition.

Thanks to the introduction of the SEI effect in the model, different electrode surface morphologies have been produced by the simulations at different applied current densities, starting from the same initial geometric defect on the lithium surface.

The applied current densities were lower than the limiting current density (thus no lithium depletion at the lithium electrode/electrolyte interface). At this current density range, mossy-like dendrites are expected. Nevertheless, using parameters from literature, distinguishable features could be spotted at $10 \text{ mA}\cdot\text{cm}^{-2}$ and at $1 \text{ mA}\cdot\text{cm}^{-2}$. The morphology at the end of the $10 \text{ mA}\cdot\text{cm}^{-2}$ simulation had a more branched nature, being closer to the limiting current density, where tree-like structures are formed according to the literature [11]. On the other hand, in the geometry at the end of the $1 \text{ mA}\cdot\text{cm}^{-2}$ simulation, the growth was more globular, consistently with the trend expected in the literature [11]. These results were confirmed by the *operando* optical microscopy observations. An analysis on the behavior of the SEI thickness evolution in the model explained that the difference in lithium morphology is due to the different rates of deformation of the lithium metal surface and consequently to the time available for the SEI to form. This important result could justify a pulse charging protocol, which is a technique considered in the literature to reduce dendrites growth [34]. It consists in the application of controlled current pulses into the battery, giving time for the cell to rest and for the SEI to form. Early attempts to simulate pulse charging with the model were made, but without meaningful results. In the future, it would be interesting to analyze if the effect of pulse charging can be produced with the proposed model at smaller geometric scales, as demonstrated by the work of Aryanfar *et al.* [34], which considered dendrites in the scale of tens of nanometers.

Filiform structures were produced by the model at lower applied current densities ($0.1 \text{ mA}\cdot\text{cm}^{-2}$), and they were confirmed by the *operando* optical microscopy observations. They were formed thanks to the SEI that had time to grow thicker everywhere on the lithium surface except few spots where the curvature of the electrode surface prevented it. Thus, lithium deposition was enhanced in the few spots where the SEI was thinner, creating tall filiform dendrites. In the literature [11], whiskers are described as filiform structures, but they are also expected to grow from their roots. On the contrary, the model and the experiments were able to reproduce filiform structures with tip-induced growth, questioning the most widespread knowledge that whiskers are solely due to root-induced growth. Therefore, it is important to investigate if all the whisker structures that are found in the literature are effectively growing from their root, or if the root-induced whiskers are a subset of the filiform dendrites. From the different structures found with the optical microscopy, it was hypothesized that without the presence of a separator, at low current density, dendrites initially grow from their roots in the cracks formed in the thick SEI covering the bulk of the lithium electrode. Once these whiskers are well developed, they continue to grow due to lithium deposition, thus tip-induced

growth, forming more bulky filiform structures.

At even lower current densities (lower than $0.02 \text{ mA}\cdot\text{cm}^{-2}$), the model, as well as the optical microscopy experiments, showed a more homogenous lithium deposition. However, this current is very low for practical applications, thus limiting the applied current density is not a feasible strategy to prevent dendrites formation.

Since the SEI was considered as a homogenous medium, it was easier to perform a sensitivity analysis on the electrochemical properties of the SEI. The effect of the SEI properties on dendrites evolution confirmed that tailoring the composition and the properties of the SEI, or of an artificial coating, to prevent dendrites is a must to advance lithium metal battery technology. Ideally, a perfect SEI would have a low resistivity, a high diffusion coefficient and a fast reaction rate to reduce dendrites growth.

The SEI formation reaction rate was able to shift the current density range in which certain morphologies happened. To avoid high heterogeneities in lithium deposition, the SEI formation kinetics was found to be more important in the regions where the SEI is thinner (few nanometers) rather than the regions where an already thick SEI is present (tens of nanometers). Thus, it is crucial to boost the formation (or re-formation after cracking) of the inner inorganic layer of the SEI. The reaction rate of SEI formation can be tuned by increasing the temperature, or by using electrolyte additives, which promote the formation of specific components in the SEI, or by increasing the electrolyte content of the reagents involved in the SEI formation reactions, *i.e.* electrolyte salt for the inner inorganic layer or solvent ratio for the outer organic layer. The research is going in the direction of employing superconcentrated electrolyte [105] (high concentration of salt), boosting the formation of a thicker dense inorganic layer, which is consistent with the findings of the simulations.

A low SEI ionic resistivity was able to reduce dendrites growth at each current density and with each dendrite morphology. On the opposite of the SEI formation kinetics, resistivity was more crucial for the areas where the SEI was thicker (higher voltage drop in the SEI). From literature [99], no major differences in resistivity were found among the main components of the SEI. Thus, the main way to reduce SEI ionic resistance remains to reduce its thickness, thus preferring a thinner compact SEI layer.

Finally, high SEI diffusion coefficient could be achieved by tailoring the morphology of the SEI. The diffusion coefficient depends on the porosity of the SEI and on

the size of its grains. These parameters could be changed in the phase of initial SEI formation by changing the conditions at which the SEI is formed, for instance temperature or potential.

The mechanical effect of the SEI was well theorized, and through simulations it was confirmed to be the reason behind the root-based growth regime of dendrites. Nevertheless, its applicability to the model was limited by numerical and software constraints. A future objective could be to find ways to pass these limits, in order to simulate the effect of an artificial coating or a solid state electrolyte, or the combined mechanical effects of the SEI and the separator, as well as introducing creep deformation and the effect of the temperature on the mechanical properties of lithium.

The choice of a transient model gave the advantage with respect to a stationary study to be able to reproduce different morphologies that could not be detected by a sensitivity analysis on the initial interface. Nevertheless, encountered limitations were often of numerical nature and sometimes associated with the commercial software that was used in this work. Due to its limitations, it was not possible to simulate more complex structures nor cycles. Nevertheless, the multi-domain continuum model showed an important integration with the proposed experiments, asserting its validity in the modeling literature landscape. Always in a logic of multi-scale model framework, the proposed model can be coupled with discrete models or phase-field models in order to simulate more complex structures, bridging their distance from the experiments. Also, improvements in the software in terms of dealing with geometry variation and remeshing could extend the range of application of the proposed model. For instance, a sensitivity analysis on the effect of the SEI properties on lithium stripping would be very useful for the battery community.

An experimental framework was designed to identify electrochemical and mechanical properties of the SEI. Two different electrolytes were studied, belonging to the two main families of liquid electrolytes, a carbonate-based electrolyte with the addition of FEC, and an ether-based electrolyte. As a perspective, this methodology could be extended to other compositions of electrolytes.

EIS, XPS and AFM techniques showed consistent results among each other, nevertheless the inherent complexity of the SEI makes it hard to identify these properties clearly and unambiguously, concerning the organic outer layer. Therefore, it is fundamental to keep improving and refining experimental techniques in a consistent framework of experiments. A future goal could be to define experiments able to

study and separate the properties of the two layers, which is fundamental to use these properties in the model.

EIS experiments were able to identify mean values for the SEI thickness, diffusivity and resistance, while a new method to find its kinetics properties was proposed. The thickness evolution was in accordance with the SEI formation law proposed in the model, but the initial SEI formation (in the first few minutes) was too fast to be modeled with the current known equations, confirming the complex nature of SEI phenomena. The identified values for SEI diffusion coefficient and conductivity were consistent with the literature that performed the same typology of experiments [77] but lower than the theoretical ones [99]. It would be interesting in the future to compare these results with other characterization methods, for example diffusion coefficient determined by means of solid NMR or the local SEI thickness determined by AFM.

The same typology of samples used in the EIS were investigated *post-mortem* with XPS and AFM techniques, to correlate their chemical compositions with the mechanical properties. The results were in accordance with the literature, most notably, the presence of LiF, formed with the carbonate-based electrolyte due to the addition of FEC and detected with XPS, was found to increase the Young's modulus of SEI layer on the lithium electrode. Both techniques were influenced by the washing of the samples prior to the experiments, which altered the composition and the structure of the SEI. Solutions to bypass this step are required to acquire more meaningful results.

Since the identified properties referred mainly to the inner layer of the SEI, the model was found to perform better with the parameters from the literature. Indeed, using for the whole thickness of the SEI the lower values of diffusivity of the inner inorganic components, as well as the higher mechanical resistance, led to an overestimation of the SEI effect on dendrites growth, remarking the need for experiments that can distinguish the different properties of the two layers.

The trends from the simulation with the parameters from the literature were confirmed by the *operando* optical microscopy observation made on a tailored designed cell, which showed improvements with respect to many designs from the literature. The presence of a separator was confirmed to effectively mechanically block or reduce dendrites growth. This validates the direction of deploying solid state electrolytes in the next generation of batteries, nevertheless, in the optic of replicating this work on a cell with a solid electrolyte, the cell used in this work has to be redesigned. On the other hand, a protected lithium electrode, for instance with

atomic-layer deposition coating, can be studied with this design, and its extended lifetime can be optically verified. *Operando* tomography can also be considered due to its higher resolution, to further reduce the dimensions of the cell, especially the distance between the two electrodes, to be closer to the dimension of the commercial cells.

To conclude, this thesis works laid the foundation for an extensive investigation of dendrites evolution, coupling model and experiments; and different lines of research can start from it.

List of Figures

0.1	Illustration théorique des phénomènes de formation, de croissance et de vieillissement des dendrites dans les batteries au lithium métal. . .	8
0.2	Épaisseur de la SEI en fin de simulation en couleur [nm]. Lithium déposé lors de la simulation en gris. a) Simulation après 40 s avec une densité de courant appliquée de 10 mA.cm ⁻² . b) Simulation après 400 s avec une densité de courant appliquée de 1 mA.cm ⁻² . c) Simulation après 4 000 s avec une densité de courant appliquée de 0,1 mA.cm ⁻² . d) Simulation après 40 000 s avec une densité de courant appliquée de 0,01 mA.cm ⁻²	10
0.3	Images de dendrites obtenues par microscopie optique <i>operando</i> . a) Dendrites arborescentes avec une densité de courant appliquée de 10 mA.cm ⁻² . b) Dendrites moussues avec une densité de courant appliquée de 1 mA.cm ⁻² . c) Whiskers avec une densité de courant appliquée de 0,1 mA.cm ⁻² . d) Dépôt homogène avec une densité de courant appliquée de 0,01 mA.cm ⁻²	11
1.1	Specific energy [Wh.kg ⁻¹] and energy density [Wh.l ⁻¹] of different lithium cell technologies compared to gasoline [7].	20
1.2	Theoretical illustration of dendrites formation, growth and aging phenomena in lithium metal batteries [7].	22
1.3	Illustration of different dendrite morphologies that can growth on a lithium metal electrode [11].	24
1.4	Ion diffusion mechanisms in the SEI [18].	25
2.1	Difference between diffuse and sharp interfaces. On the left: diffuse interface, where properties evolve continuously between their equilibrium values in the neighbor of the interface. On the right: sharp interface, where properties are discontinuous at the interface [28]. . .	30
2.2	Deposition morphologies during charging, obtained through Tewari and Mukherjee's model [29].	31
2.3	Deposition morphologies during discharging, obtained through Tewari and Mukherjee's model [29].	32

2.4	Results of phase-field model: Phase field (first row), lithium ion concentration (second row) and electric potential (third row) [33].	35
2.5	Results of phase-field model: Phase field (first row), lithium ion concentration (second row), electric potential (third row) and hydrostatic stress (fourth row). a) Filament growth. b) Bush-like morphology [33].	36
2.6	2D geometry used by Ferrese and Newman, consisting of a negative current collector, a lithium metal negative electrode, a polymer separator, a composite positive electrode, and an aluminum positive current collector [51].	41
2.7	Movement of lithium along the lithium/separator interface during one cycle at a rate of C/5, with different mechanical phenomena considered [51].	42
2.8	Evolution of lithium deposition at different deposition rates, with lithium concentration in color [M]. Left: slow deposition rate (at 0.4 V). Right: fast deposition rate (at 0.7 V) [16].	43
2.9	Evolution of lithium deposition with the addition of the SEI. Left: single-ionic conducting SEI. Right: bi-ionic conducting SEI [16].	43
2.10	Defect evolution due to lithium deposition at different applied current densities (5 A.m ⁻² top figure and 20 A.m ⁻² bottom), according to Liu and Lu's model [15].	45
2.11	Lithium stripping simulations at fast and slow rates from Yoon's model [16].	46
2.12	Merge of nearby dendrites based on Yoon's model prediction [16].	47
2.13	Dendrites obtained with optical microscopy by applying different current densities: a) Needle-like dendrites. b) Tree-like dendrites c) Bush-like dendrites [44].	49
2.14	Cell design used by Kong <i>et al.</i> for <i>operando</i> optical microscopy [59].	49
2.15	<i>In-situ operando</i> observations of lithium electrodeposition in a glass capillary. a) Design of the cell. (b) Voltage profiles under current. c–g) <i>Operando</i> optical photos of the growth of lithium during the electrodeposition. (h) Theoretical interpretation of the growth mechanisms [60].	50
2.16	Morphology of deposition from optical microscopy at different applied current densities [60].	51
2.17	TEM images of mossy lithium growth on the gold electrode at -4.0 V vs lithium cobalt oxide. The morphology of the surface changed, indicating a tip-induced growth [38].	53

2.18	TEM images of a whisker during lithium deposition at -6.0 V vs lithium cobalt oxide (a) and dissolution at 0.0 V vs LCO (b). The morphology suggests a root-based mechanism [38].	53
2.19	Morphology of deposition found by Zachman <i>et al.</i> using cryo-TEM. a) Structure of the coin cell. b-d) Images of the electrode surface and dendrites cross-sections. e) Reconstruction of dendrite morphologies. f) Occurrence of the different types of dendrites [64].	54
2.20	AFM images of lithium metal surface during electrodeposition. White scale bars indicated a length of 100 nm. a-c) Topographic height. d-f) Adhesion mapping [67].	56
2.21	Theoretical interpretation of protrusion growth and SEI formation during lithium deposition in (a) and open circuit conditions in (b) [67].	57
2.22	a) Setup of the AFM machine with the lithium sample. b-c) TEM images of the AFM cantilever and tip. d) TEM images of whisker growth and collapse [49].	58
2.23	Theoretical Young's modulus value of the most common components of the SEI [71].	59
2.24	a-b) SEI free-standing narrow membrane on a rigid substrate. c) Pressure response to membrane deflection. d) Hoop stress response to hoop strain [73].	60
2.25	Custom cell design that enabled controlled pressure to be applied on the final SEI sample [73].	60
2.26	Pressure-deflection response, and hoop stress vs strain curves measured with AFM during the deformation of the SEI membrane. [73]	61
2.27	Impedance spectra from the work of Vorotyntsev <i>et al.</i> (top-left plot). Impedance spectra differences between the second and the first spectrum (2-1), the fourth and the third (4-3) and the fifth and the fourth (5-4) [74].	63
2.28	Equivalent electric circuit and impedance spectrum relative to a lithium symmetric cell, from the work of Bouchet <i>et al.</i> [75].	65
2.29	Evolution of the impedance response containing (a) C ₁ C ₆ ImTFSI, (b) C ₁ C ₆ ImFSI, (c) C ₁ C ₆ ImTFSI/LiTFSI, and (d) C ₁ C ₆ ImFSI/LiTFSI electrolytes [76].	65
2.30	Evolution of the impedance spectra difference containing (a) C ₁ C ₆ ImTFSI, (b) C ₁ C ₆ ImFSI, (c) C ₁ C ₆ ImTFSI/LiTFSI, and (d) C ₁ C ₆ ImFSI/LiTFSI electrolytes [76].	66

2.31	XPS spectra of carbon C 1s core level (first row) and F 1s core level (second row), with different IL-based electrolytes, registered at the surface of a) neat IL-based electrolyte, b) separator, c) lithium electrode [76].	67
3.1	Geometry of the model, electrolyte (light blue), lithium negative electrode (white).	72
3.2	Framework of the model. Subunits in the orange boxes. Input/output in the blue boxes.	74
3.3	Thickness of the SEI (100 nm - red line) compared to a zoom of the 2D geometry used in our model.	79
3.4	Graphical representation of the different current densities used in the model.	81
3.5	Graphical representation of the different concentration-related definitions used in this section.	83
3.6	Cylindrical thin-walled SEI covering lithium metal electrode. Radial, circumferential and longitudinal directions are highlighted.	84
3.7	Tensile stress-strain curve of a lithium metal specimen from Tariq <i>et al.</i> work [68].	88
3.8	Lithium domain from the geometry used in the model in blue, with the boundary conditions of Eq. 3.30.	89
3.9	Graphical representation of the different phases used by Monroe and Newman in their theory [46].	91
3.10	Energy landscape during lithium redox reactions. The dotted line represents the profile affected only by the applied overpotential, while the continuous line takes into account the effects of interfacial deformation [46].	96
4.1	Salt concentration in the electrolyte at the end of simulation in color [mol.m ⁻³]. Red arrows represent the lithium flux in the electrolyte, while black lines are the electrolyte potential isolines, separated from each other by 1 mV. Lithium deposited during the simulation in gray. a) Simulation after 40 s with an applied current of 10 mA.cm ⁻² . b) Simulation after 400 s with an applied current of 1 mA.cm ⁻²	105
4.2	Salt concentration profiles at the lithium-electrolyte interface at the end of the simulations presented in Fig. 4.1.	106
4.3	Surface profiles at the end of the simulations presented in Fig. 4.1 compared to the initial geometry.	107

4.4	Surface overpotential profiles at the end of the simulations presented in Fig. 4.1. A new simulation with an applied current 0.1 mA.cm^{-2} is added for reference.	107
4.5	Salt concentration gradient profiles at the lithium-electrolyte interface at the end of the simulations presented in Fig. 4.1.	108
4.6	Butler-Volmer current density profiles at the end of the simulations presented in Fig. 4.1, weighted on the applied current density. A new simulation with an applied current 0.1 mA.cm^{-2} is added for reference.	108
4.7	Salt concentration in the electrolyte at the end of simulation in color [mol.m^{-3}]. Black lines are electrolyte potential isolines, separated from each other by 1 mV. Lithium deposited during the simulation in gray. a) Simulation after 40 s with an applied current of 10 mA.cm^{-2} . b) Simulation after 400 s with an applied current of 1 mA.cm^{-2}	111
4.8	Salt concentration in the electrolyte at the end of simulation in color [mol.m^{-3}]. Black lines are electrolyte potential isolines, separated from each other by 1 mV. Lithium deposited during the simulation in gray. a) Simulation after 4000 s with an applied current of 0.1 mA.cm^{-2} . b) Simulation after 40000 s with an applied current of 0.01 mA.cm^{-2}	112
4.9	SEI thickness at the end of simulation in color [nm]. Lithium deposited during the simulation in gray. Simulation after 40 s with an applied current density of 10 mA.cm^{-2}	113
4.10	SEI thickness at the end of simulation in color [nm]. Lithium deposited during the simulation in gray. Simulation after 400 s with an applied current density of 1 mA.cm^{-2}	114
4.11	SEI thickness at the end of simulation in color [nm]. Lithium deposited during the simulation in gray. Simulation after 4000 s with an applied current density of 0.1 mA.cm^{-2}	114
4.12	SEI thickness at the end of simulation in color [nm]. Lithium deposited during the simulation in gray. Simulation after 40000 s with an applied current density of 0.01 mA.cm^{-2}	115
4.13	Butler-Volmer current density profiles at the end of the simulations presented in Fig. 4.7 and Fig. 4.8, weighted on the applied current density.	116
4.14	Butler-Volmer current densities at the end of the simulations presented in Fig. 4.7 and Fig. 4.8, plotted versus the related SEI thickness.	117
4.15	SEI thickness in color [nm] during the 10 mA.cm^{-2} applied current density simulation presented in Fig. 4.9. SEI thickness was multiplied by a factor of 10 in Fig. a-d, and by a factor of 5 in Fig. e-g. a) $t = 0 \text{ s}$. b) $t = 10 \text{ s}$. c) $t = 20 \text{ s}$. d) $t = 25 \text{ s}$. e) $t = 30 \text{ s}$. f) $t = 35 \text{ s}$. g) $t = 40 \text{ s}$	119

4.16	SEI thickness at the end of simulation in color [nm]. Lithium deposited during the simulation in grey. Simulation after 40 s with an applied current density of 10 mA.cm ⁻² . a) SEI reaction rate coefficient 10 times lower than the value from the literature. b) SEI reaction rate coefficient value from the literature. c) SEI reaction rate coefficient 10 times higher than the value from the literature.	121
4.17	SEI thickness at the end of simulation in color [nm]. Lithium deposited during the simulation in grey. Simulation after 4000 s with an applied current density of 0.1 mA.cm ⁻² . a) SEI reaction rate coefficient 10 times lower than the value from the literature. b) SEI reaction rate coefficient value from the literature. c) SEI reaction rate coefficient 10 times higher than the value from the literature.	122
4.18	SEI thickness at the end of simulation in color [nm]. Lithium deposited during the simulation in grey. Simulation after 40 s with an applied current density of 10 mA.cm ⁻² . a) SEI resistivity 10 times lower than the value from the literature. b) SEI resistivity value from the literature. c) SEI resistivity 10 times higher than the value from the literature. . .	124
4.19	SEI thickness at the end of simulation in color [nm]. Lithium deposited during the simulation in grey. Simulation after 4000 s with an applied current density of 0.1 mA.cm ⁻² . a) SEI resistivity 10 times lower than the value from the literature. b) SEI resistivity value from the literature. c) SEI resistivity 10 times higher than the value from the literature. . .	125
4.20	Lithium concentration profiles at the electrolyte-SEI interface, c_e and at the SEI-electrode interface, $c_{e,s}$. a) Simulation after 40 s with an applied current density of 10 mA.cm ⁻² . b) Simulation after 4000 s with an applied current density of 0.1 mA.cm ⁻²	127
4.21	SEI thickness at the end of simulation in color [nm]. Lithium deposited during the simulation in grey. Simulation after 40 s with an applied current density of 10 mA.cm ⁻² . a) SEI diffusion coefficient 10 times lower than the value from the literature. b) SEI diffusion coefficient value from the literature. c) SEI diffusion coefficient 10 times higher than the value from the literature.	128
4.22	Zoom on the upper-left corner during the simulation presented in Fig.6a (green), Fig. 6b (blue) and Fig. 6c (red). a) Simulation after 20 s with an applied current density of 10 mA.cm ⁻² . b) Simulation after 40 s with an applied current density of 10 mA.cm ⁻²	129

4.23	SEI thickness at the end of simulation in color [nm]. Lithium deposited during the simulation in grey. Simulation after 40 s with an applied current density of 10 mA.cm ⁻² . a) $r_c = 0.5 \mu\text{m}$. b) $r_c = 0.6 \mu\text{m}$. c) $r_c = 0.7 \mu\text{m}$	131
4.24	Von Mises Stress in color [MPa]. White line: initial surface geometry of the lithium defect. Blue line: final surface geometry without considering the mechanics. Black thin line: final surface geometry taking into account the mechanics. Simulation after 20 s with an applied current density of 10 mA.cm ⁻²	134
4.25	Von Mises Stress in color [MPa]. White line: initial surface geometry of the lithium defect. Blue line: final surface geometry without considering the mechanics. Black thin line: final surface geometry taking into account the mechanics. Simulation after 200 s with an applied current density of 1 mA.cm ⁻²	135
4.26	White line: initial surface geometry of the lithium defect. Blue line: final surface geometry without considering the mechanics. Black thin line: final surface geometry taking into account the mechanics. Simulation after 2000 s with an applied current density of 0.1 mA.cm ⁻² . a) Von Mises Stress in color [MPa]. b) Module of plastic strain in color [-]. . .	136
4.27	Von Mises Stress in color [MPa]. White line: initial surface geometry. Blue line: final surface geometry without considering the mechanics. Black thin line: final surface geometry taking into account the mechanics. Simulation after 2000 s with an applied current density of 0.1 mA.cm ⁻² . Top-right corner of the defect has no maximum assumed hoop strain.	137
4.28	Final surface morphology of Fig. 4.27, compared with the surface morphology by performing the same simulation with an SEI with Young's modulus of 440 MPa and elastic limit of 10 MPa.	138
4.29	SEI thickness at the end of simulation in color [nm]. Lithium deposited during the simulation in gray. a) Deposition simulation after 300 s with an applied current density of 1 mA.m ⁻² . b) Stripping simulation after 40 s with an applied current density of 1 mA.m ⁻² . c) Stripping simulation after 400 s with an applied current density of 0.1 mA.m ⁻² . d) Stripping simulation after 80 s with an applied current density of 1 mA.m ⁻² . e) Stripping simulation after 800 s with an applied current density of 0.1 mA.m ⁻²	139

4.30	Lithium deposited during the simulation in grey. a) Initial geometry of the first simulation. b) Final step of the first simulation before singularity is reached c) Initial redesigned geometry of the second simulation. d) Final step of the second simulation.	141
5.1	Spectra recorded for an ethers-based electrolyte Li/Li cell at different times, in the Nyquist representation.	149
5.2	Spectra recorded for an ethers-based electrolyte Li/Li cell at different times, imaginary part vs frequency in logarithmic scale.	150
5.3	Spectra differences from Fig. 5.1.	151
5.4	Equivalent circuit used to fit spectra differences.	151
5.5	Computed spectra differences from Fig. 5.3 (markers) and fitting curves obtained by using the equivalent circuit presented in Fig. 5.4 (black lines).	152
5.6	SEI thickness evolution determined for two cells with the ethers-based electrolyte, where cell 1 refers to the cell presented in Fig. 5.1.	155
5.7	SEI experimental velocity of growth (markers), computed from the equivalent circuit parameters, and exponential fitting curve (blue line).	157
5.8	ΔR_{int} vs \sqrt{t} and $1/\Delta C_{int}$ vs \sqrt{t} for the cell presented in Fig. 5.1.	157
5.9	Spectra recorded in Fig. 5.1 (markers) with fitting curves (black lines).	158
5.10	Spectra recorded for a carbonates-based electrolyte Li/Li cell at different times, in the Nyquist representation.	159
5.11	Computed spectra difference point from Fig. 5.10 (markers) and fitting curves obtained by using the equivalent circuit presented in Fig. 5.4 (black lines).	160
5.12	SEI thickness evolution comparison between ethers-based cells (Cell 1 and Cell 2) and carbonates-based (Cell 3 and Cell 4).	161
5.13	EIS spectra for the ethers-based cell, recorded at the initial time, and before and after the electrodes washing with DIOX.	162
5.14	C 1s, O 1s, Li 1s, F 1s XPS spectra measured on pristine lithium metal, a lithium metal electrode aged with the ethers-based electrolyte and a lithium metal electrode aged with the carbonates-based electrolyte.	164
5.15	AtomicJ [®] interface for finding Young's modulus from a force-distance curve.	166
5.16	Force-distance curve measured from the silicon 111 sample.	167
5.17	Young's moduli map from the silicon 111 sample with 2 μ N applied.	168
5.18	Force-distance curve measured from the pristine lithium sample, highlighting the problems associated with lithium metal characterization.	168
5.19	Young's moduli map from the pristine lithium sample at 2 μ N.	169

5.20	Young's moduli map from the pristine lithium sample at 5 μN	170
5.21	Young's moduli map from the lithium sample aged with the ethers-based electrolyte, at 2 μN	171
5.22	Young's moduli map from the lithium sample aged with the carbonates-based electrolyte, at 2 μN	171
5.23	Design of the lithium symmetric cell used for <i>operando</i> optical microscopy.	174
5.24	Setup of the <i>operando</i> optical microscopy measurements.	174
5.25	Images recorded by optical microscopy during a lithium stripping/plating experiment on a cell with the carbonates-based electrolyte. 10 $\text{mA}\cdot\text{cm}^{-2}$ were applied to the cell for 12 minutes, followed by -10 $\text{mA}\cdot\text{cm}^{-2}$ for the same amount of time.	176
5.26	<i>Post-mortem</i> images from the same cell presented in Fig. 5.25. The electrode on the left corresponds to the electrode on the left in Fig. 5.25 that was subjected to stripping followed by plating of lithium (same correspondence for the electrode on the right).	177
5.27	Images recorded by optical microscopy during a lithium stripping/plating experiment on a cell with the carbonates-based electrolyte. 1 $\text{mA}\cdot\text{cm}^{-2}$ was applied to the cell for 2 hours, followed by -1 $\text{mA}\cdot\text{cm}^{-2}$ for the same amount of time.	178
5.28	Detail of a mossy dendrite, recorded by the optical microscope during an experiment on a cell with the carbonates-based electrolyte and with 1 $\text{mA}\cdot\text{cm}^{-2}$ of applied current density.	179
5.29	<i>Post-mortem</i> images from the same cell presented in Fig. 5.27. The electrode on the left corresponds to the electrode on the left in Fig. 5.27 (same correspondence for the electrode on the right).	179
5.30	<i>Post-mortem</i> images for the 0.1 $\text{mA}\cdot\text{cm}^{-2}$ experiment.	180
5.31	Images recorded with the optical microscope during an experiment on a cell with the carbonates-based electrolyte and with 0.1 $\text{mA}\cdot\text{cm}^{-2}$ of current applied density.	180
5.32	Image recorded with the optical microscope after an experiment on a cell with the carbonates-based electrolyte. 0.02 mA were applied to the cell for 90 hours.	182
5.33	Voltage profiles recorded during <i>operando</i> optical microscopy.	182
5.34	Design of the lithium/lithium cell with a separator used for <i>operando</i> optical microscopy.	183
5.35	Image recorded by optical microscopy after a lithium stripping/plating experiment at 20 mA for 12 minutes on a cell containing the carbonates-based electrolyte and two layers of polymeric separator.	184

List of Tables

3.1	Comparison between the proposed model and models in the literature.	99
4.1	Comparison between the phenomena taken into account in the three different models presented in this chapter.	101
4.2	List of the parameters and properties used in this work.	102
4.3	Set of equations used in the basic model.	104
4.4	Set of equations used in the improved model.	109
4.5	Set of equations used in the full model.	133
5.1	Parameters used in the model simulations divided by group.	146
5.2	Equivalent circuit parameters for the ethers-based electrolyte lithium/lithium cell.	152
5.3	Equivalent circuit parameters, cell assumptions (A_e , ϵ_0 , ϵ_r) and computed SEI parameters relative to the experiment presented in Fig. 5.1.	155
5.4	Equivalent circuit parameters obtained by following Bouchet's method [75].	158
5.5	Equivalent circuit parameters, cell assumptions and computed SEI parameters relative to the experiment presented in Fig. 5.10.	160
5.6	Summary of AFM results.	172

List of Acronyms

AFM	Atomic Force Microscopy
BDF	Backward Differentiation Formula
CEA	Commissariat à l'énergie atomique et aux énergies alternatives
CPE	Constant Phase Element
DEC	DiEthyl Carbonate
DEHT	Département Electricité et Hydrogène pour les Transports
DIS	time-Difference Impedance Spectroscopy
DMC	DiMethyl Carbonate
EC	Ethylene Carbonate
EMC	Ethyl Methyl Carbonate
EIS	Electrochemical Impedance Spectroscopy
ETEM	Environmental Transmission Electron Microscopy
FEC	FluoroEthylene Carbonate
FTIR	Fourier-Transform Infrared Spectroscopy
IEA	International Energy Agency
IL	Ionic Liquid
KMC	Kinetic Monte Carlo
LMO	Lithium transition-Metal Oxide
LMP	Lithium Metal Polymer
MRI	Magnetic Resonance Imaging
MUMPS	Multifrontal Massively Parallel Sparse Direct Solver
NMR	Nuclear Magnetic Resonance
PC	Propylene Carbonate
PDE	Partial Differential Equation
PEO	Poly(Ethylene Oxide)
PFT	Peak Force Tapping
SEI	Solid Electrolyte Interphase
SEM	Scanning Electron Microscope
SHE	Standard Hydrogen Electrode
SSE	Solid State Electrolyte
TEM	Transmission Electron Microscopy
VC	Vinylene Carbonate
XPS	X-ray Photoelectron Spectroscopy

List of Main Symbols

Symbols	Unit of Measurement	Description
α_a	[-]	Anodic transfer coefficients
α_c	[-]	Cathodic transfer coefficients
α_{SEI}	[-]	Transfer coefficient of SEI formation reaction
γ	[J.m ⁻²]	Surface energy
δ_r	[m]	Displacement of the SEI
ϵ	[-]	Strain
ϵ_c	[-]	Circumferential strain
ϵ_l	[-]	Longitudinal strain
ϵ_{pl}	[-]	Plastic strain
ϵ_r (Ch.3)	[-]	Radial strain
ϵ_r (Ch.5)	[-]	Relative permittivity
ϵ_0	[F.m ⁻¹]	Vacuum permittivity
$\dot{\epsilon}$	[s ⁻¹]	Strain rate
$\bar{\epsilon}_{Li}$	[-]	Lithium strain tensor
κ	[S.m ⁻¹]	Electrolyte conductivity
κ_c	[m ⁻¹]	Surface curvature
λ	[m ⁻¹]	Scale factor of SEI formation current
μ	[J.mol ⁻¹]	Electrochemical potential
$\Delta\mu_{e^-}$	[J.mol ⁻¹]	Change in electrochemical potential due to mechanics
ν_{Li}	[-]	Lithium Poisson's ratio
ν_{SEI}	[-]	SEI Poisson's ratio
ρ_{Li}	[kg.m ⁻³]	Density of lithium
σ_c	[Pa]	Circumferential stress
σ_l	[Pa]	Longitudinal stress
σ_r	[Pa]	Radial stress
σ_s	[S.m ⁻¹]	Electrode conductivity
σ_{SEI}	[S.m ⁻¹]	SEI conductivity
σ_v	[Pa]	Von Mises stress
$\sigma_{y,Li}$	[Pa]	Yield strength of lithium
$\sigma_{y,SEI}$	[Pa]	Yield strength of SEI
$\bar{\sigma}_{Li}$	[Pa]	Lithium stress tensor
Φ	[V]	Surface overpotential
ϕ_e	[V]	Electrolyte potential
ϕ_s	[V]	Electrode potential

Symbols	Unit of Measurement	Description
A_e	[m ²]	Area of the electrode
a_C	[-]	Exponent of the constant phase element
C_{int}	[F]	Interface capacitance
CPE	[F.s ^(a_c-1)]	CPE capacitance
c_e	[mol.m ⁻³]	Salt concentration
$c_{e,s}$	[mol.m ⁻³]	Lithium concentration at the SEI/lithium metal interface
$c_{e,SEI}$	[mol.m ⁻³]	Lithium concentration in the SEI
c_{sol}	[mol.m ⁻³]	Solvent concentration
D_e	[m ² .s ⁻¹]	Electrolyte diffusion coefficient
D_{SEI}	[m ² .s ⁻¹]	SEI diffusion coefficient
E_{Li}	[Pa]	Lithium Young's modulus
E_{SEI}	[Pa]	SEI Young's modulus
F	[C.mol ⁻¹]	Faraday constant
h_{SEI}	[m]	SEI thickness
i_0	[A.m ⁻²]	Exchange current density
i_{00}	[A.m ⁻²]	Reference exchange current density
i_{app}	[A.m ⁻²]	Applied current density
i_{BV}	[A.m ⁻²]	Butler-Volmer current density
i_{SEI}	[A.m ⁻²]	SEI formation current density
K	[Pa]	Hardening modulus of lithium
k_{SEI}	[m.s ⁻¹]	SEI reaction rate coefficient
n	[-]	Hardening exponent of lithium
p_{Li}	[Pa]	Lithium pressure on the interface
Δp_{Li}	[Pa]	Hydrostatic stress of lithium
p_{SEI}	[Pa]	SEI pressure on the interface
Δp_{SEI}	[Pa]	Hydrostatic stress of SEI
q_{SEI}	[m.s ⁻¹]	Velocity of formation of SEI
R	[J.(mol.K) ⁻¹]	Universal gas constant
R_{el}	[Ω]	Electrolyte resistance
R_{int}	[Ω]	Interface resistance
r_c	[m]	Radius of curvature
r_{SEI}	[Ω.m]	SEI resistivity
T	[K]	Temperature
t	[s]	Time
t_+	[-]	Transference number
\bar{u}	[m]	Displacement vector
\dot{u}_n	[m.s ⁻¹]	Rate of displacement
\bar{V}_{Li}	[m ³ .mol ⁻¹]	Lithium specific molar volume
\bar{V}_{SEI}	[m ³ .mol ⁻¹]	SEI specific molar volume
\bar{v}	[m.s ⁻¹]	Flow velocity vector field
v_{dep}	[m.s ⁻¹]	Velocity of deposition
v_n	[m.s ⁻¹]	Velocity of the boundary deformation
Z_{CPE}	[Ω]	Impedance of the CPE

Bibliography

- [1] IEA, “Energy storage,” *IEA*, <https://www.iea.org/reports/energy-storage> 2021.
- [2] IEA, “Electric vehicles,” *IEA*, <https://www.iea.org/reports/electric-vehicles> 2021.
- [3] M. S. Whittingham, “Chemistry of intercalation compounds: Metal guests in chalcogenide hosts,” *Progress in Solid State Chemistry*, vol. 12, no. 1, pp. 41–99, 1978.
- [4] B. Scrosati, “History of lithium batteries,” *Journal of solid state electrochemistry*, vol. 15, no. 7, pp. 1623–1630, 2011.
- [5] K. Mizushima, P. Jones, P. Wiseman, and J. B. Goodenough, “ LiCoO_2 ($0 < x < 1$): A new cathode material for batteries of high energy density,” *Materials Research Bulletin*, vol. 15, no. 6, pp. 783–789, 1980.
- [6] M. S. Whittingham, “Lithium batteries and cathode materials,” *Chemical reviews*, vol. 104, no. 10, pp. 4271–4302, 2004.
- [7] D. Lin, Y. Liu, and Y. Cui, “Reviving the lithium metal anode for high-energy batteries,” *Nature nanotechnology*, vol. 12, no. 3, pp. 194–206, 2017.
- [8] H. Popp, N. Zhang, M. Jahn, M. Arrinda, S. Ritz, M. Faber, D. U. Sauer, P. Azais, and I. Cendoya, “Ante-mortem analysis, electrical, thermal, and ageing testing of state-of-the-art cylindrical lithium-ion cells,” *e & i Elektrotechnik und Informationstechnik*, vol. 137, no. 4, pp. 169–176, 2020.
- [9] J.-G. Zhang, W. Xu, and W. A. Henderson, *Lithium metal anodes and rechargeable lithium metal batteries*, vol. 249. Springer International Publishing Switzerland, 2017.
- [10] J. Steiger, D. Kramer, and R. Mönig, “Microscopic observations of the formation, growth and shrinkage of lithium moss during electrodeposition and dissolution,” *Electrochimica Acta*, vol. 136, pp. 529–536, 2014.

- [11] P. Bai, J. Guo, M. Wang, A. Kushima, L. Su, J. Li, F. R. Brushett, and M. Z. Bazant, “Interactions between lithium growths and nanoporous ceramic separators,” *Joule*, vol. 2, no. 11, pp. 2434–2449, 2018.
- [12] E. Peled, “The electrochemical behavior of alkali and alkaline earth metals in nonaqueous battery systems—the solid electrolyte interphase model,” *Journal of The Electrochemical Society*, vol. 126, no. 12, p. 2047, 1979.
- [13] P. Verma, P. Maire, and P. Novák, “A review of the features and analyses of the solid electrolyte interphase in li-ion batteries,” *Electrochimica Acta*, vol. 55, no. 22, pp. 6332–6341, 2010.
- [14] A. Wang, S. Kadam, H. Li, S. Shi, and Y. Qi, “Review on modeling of the anode solid electrolyte interphase (sei) for lithium-ion batteries,” *npj Computational Materials*, vol. 4, no. 1, pp. 1–26, 2018.
- [15] G. Liu and W. Lu, “A model of concurrent lithium dendrite growth, sei growth, sei penetration and regrowth,” *Journal of The Electrochemical Society*, vol. 164, no. 9, pp. A1826–A1833, 2017.
- [16] G. Yoon, S. Moon, G. Ceder, and K. Kang, “Deposition and stripping behavior of lithium metal in electrochemical system: continuum mechanics study,” *Chemistry of Materials*, vol. 30, no. 19, pp. 6769–6776, 2018.
- [17] T. Yoshida, M. Takahashi, S. Morikawa, C. Ihara, H. Katsukawa, T. Shiratsuchi, and J.-i. Yamaki, “Degradation mechanism and life prediction of lithium-ion batteries,” *Journal of The Electrochemical Society*, vol. 153, no. 3, p. A576, 2006.
- [18] S. Shi, P. Lu, Z. Liu, Y. Qi, L. G. Hector Jr, H. Li, and S. J. Harris, “Direct calculation of li-ion transport in the solid electrolyte interphase,” *Journal of the American Chemical Society*, vol. 134, no. 37, pp. 15476–15487, 2012.
- [19] K. Xu, “Nonaqueous liquid electrolytes for lithium-based rechargeable batteries,” *Chemical reviews*, vol. 104, no. 10, pp. 4303–4418, 2004.
- [20] H.-H. Lee, Y.-Y. Wang, C.-C. Wan, M.-H. Yang, H.-C. Wu, and D.-T. Shieh, “The function of vinylene carbonate as a thermal additive to electrolyte in lithium batteries,” *Journal of Applied Electrochemistry*, vol. 35, no. 6, pp. 615–623, 2005.
- [21] X.-Q. Zhang, X.-B. Cheng, X. Chen, C. Yan, and Q. Zhang, “Fluoroethylene carbonate additives to render uniform li deposits in lithium metal batteries,” *Advanced Functional Materials*, vol. 27, no. 10, p. 1605989, 2017.

- [22] D. Aurbach, "Review of selected electrode–solution interactions which determine the performance of li and li ion batteries," *Journal of Power Sources*, vol. 89, no. 2, pp. 206–218, 2000.
- [23] R. Knödler, "Thermal properties of sodium-sulphur cells," *Journal of applied electrochemistry*, vol. 14, no. 1, pp. 39–46, 1984.
- [24] A. Manthiram, X. Yu, and S. Wang, "Lithium battery chemistries enabled by solid-state electrolytes," *Nature Reviews Materials*, vol. 2, no. 4, pp. 1–16, 2017.
- [25] D. Fenton, "Complexes of alkali metal ions with poly (ethylene oxide)," *polymer*, vol. 14, p. 589, 1973.
- [26] J. Bates, N. Dudney, G. Gruzalski, R. Zuhr, A. Choudhury, C. Luck, and J. Robertson, "Electrical properties of amorphous lithium electrolyte thin films," *Solid state ionics*, vol. 53, pp. 647–654, 1992.
- [27] A. Varzi, K. Thanner, R. Scipioni, D. Di Lecce, J. Hassoun, S. Dörfler, H. Altheus, S. Kaskel, C. Prehal, and S. A. Freunberger, "Current status and future perspectives of lithium metal batteries," *Journal of Power Sources*, vol. 480, p. 228803, 2020.
- [28] N. Moelans, B. Blanpain, and P. Wollants, "An introduction to phase-field modeling of microstructure evolution," *Calphad*, vol. 32, no. 2, pp. 268–294, 2008.
- [29] D. Tewari and P. P. Mukherjee, "Mechanistic understanding of electrochemical plating and stripping of metal electrodes," *Journal of Materials Chemistry A*, vol. 7, no. 9, pp. 4668–4688, 2019.
- [30] F. Hao, A. Verma, and P. P. Mukherjee, "Electrodeposition stability of metal electrodes," *Energy Storage Materials*, vol. 20, pp. 1–6, 2019.
- [31] P. P. Trigueros, F. Mas, J. Claret, F. Sagués, J. Galceran, and J. Puy, "Monte carlo simulation of diffusion-controlled response functions at 2d experimental rough electrodes," *Journal of Electroanalytical Chemistry*, vol. 348, no. 1-2, pp. 221–246, 1993.
- [32] L. Guo, A. Radisic, and P. C. Searson, "Kinetic monte carlo simulations of nucleation and growth in electrodeposition," *The Journal of Physical Chemistry B*, vol. 109, no. 50, pp. 24008–24015, 2005.

- [33] V. Yurkiv, T. Foroozan, A. Ramasubramanian, R. Shahbazian-Yassar, and F. Mashayek, "Phase-field modeling of solid electrolyte interface (sei) influence on li dendritic behavior," *Electrochimica Acta*, vol. 265, pp. 609–619, 2018.
- [34] A. Aryanfar, D. Brooks, B. V. Merinov, W. A. Goddard III, A. J. Colussi, and M. R. Hoffmann, "Dynamics of lithium dendrite growth and inhibition: Pulse charging experiments and monte carlo calculations," *The journal of physical chemistry letters*, vol. 5, no. 10, pp. 1721–1726, 2014.
- [35] J. E. Guyer, W. J. Boettinger, J. A. Warren, and G. B. McFadden, "Phase field modeling of electrochemistry. i. equilibrium," *Physical Review E*, vol. 69, no. 2, p. 021603, 2004.
- [36] D. R. Ely, A. Jana, and R. E. García, "Phase field kinetics of lithium electrodeposits," *Journal of Power Sources*, vol. 272, pp. 581–594, 2014.
- [37] L. Chen, H. W. Zhang, L. Y. Liang, Z. Liu, Y. Qi, P. Lu, J. Chen, and L.-Q. Chen, "Modulation of dendritic patterns during electrodeposition: A nonlinear phase-field model," *Journal of Power Sources*, vol. 300, pp. 376–385, 2015.
- [38] A. Kushima, K. P. So, C. Su, P. Bai, N. Kuriyama, T. Maebashi, Y. Fujiwara, M. Z. Bazant, and J. Li, "Liquid cell transmission electron microscopy observation of lithium metal growth and dissolution: Root growth, dead lithium and lithium flotsams," *Nano Energy*, vol. 32, pp. 271–279, 2017.
- [39] C. Brissot, M. Rosso, J.-N. Chazalviel, and S. Lascaud, "Dendritic growth mechanisms in lithium/polymer cells," *Journal of power sources*, vol. 81, pp. 925–929, 1999.
- [40] C. Monroe and J. Newman, "Dendrite growth in lithium/polymer systems a propagation model for liquid electrolytes under galvanostatic conditions," *Journal of The Electrochemical Society*, vol. 150, no. 10, pp. A1377–A1384, 2003.
- [41] J. Barton and J. O. Bockris, "The electrolytic growth of dendrites from ionic solutions," *Proceedings of the Royal Society of London. Series A. Mathematical and Physical Sciences*, vol. 268, no. 1335, pp. 485–505, 1962.
- [42] J. Diggle, A. Despic, and J. Bockris, "The mechanism of the dendritic electrocrystallization of zinc," *Journal of The Electrochemical Society*, vol. 116, no. 11, pp. 1503–1514, 1969.

- [43] J.-N. Chazalviel, "Electrochemical aspects of the generation of ramified metallic electrodeposits," *Physical review A*, vol. 42, no. 12, p. 7355, 1990.
- [44] C. Brissot, M. Rosso, J.-N. Chazalviel, P. Baudry, and S. Lascaud, "In situ study of dendritic growth in lithium/peo-salt/lithium cells," *Electrochimica acta*, vol. 43, no. 10-11, pp. 1569–1574, 1998.
- [45] M. Rosso, T. Gobron, C. Brissot, J.-N. Chazalviel, and S. Lascaud, "Onset of dendritic growth in lithium/polymer cells," *Journal of power sources*, vol. 97, pp. 804–806, 2001.
- [46] C. Monroe and J. Newman, "The effect of interfacial deformation on electrodeposition kinetics," *Journal of The Electrochemical Society*, vol. 151, no. 6, pp. A880–A886, 2004.
- [47] C. Monroe and J. Newman, "The impact of elastic deformation on deposition kinetics at lithium/polymer interfaces," *Journal of The Electrochemical Society*, vol. 152, no. 2, pp. A396–A404, 2005.
- [48] T. Foroozan, S. Sharifi-Asl, and R. Shahbazian-Yassar, "Mechanistic understanding of li dendrites growth by in-situ/operando imaging techniques," *Journal of Power Sources*, vol. 461, p. 228135, 2020.
- [49] L. Zhang, T. Yang, C. Du, Q. Liu, Y. Tang, J. Zhao, B. Wang, T. Chen, Y. Sun, P. Jia, *et al.*, "Lithium whisker growth and stress generation in an in situ atomic force microscope–environmental transmission electron microscope set-up," *Nature nanotechnology*, vol. 15, no. 2, pp. 94–98, 2020.
- [50] A. Ferrese, P. Albertus, J. Christensen, and J. Newman, "Lithium redistribution in lithium-metal batteries," *Journal of The Electrochemical Society*, vol. 159, no. 10, p. A1615, 2012.
- [51] A. Ferrese and J. Newman, "Mechanical deformation of a lithium-metal anode due to a very stiff separator," *Journal of The Electrochemical Society*, vol. 161, no. 9, p. A1350, 2014.
- [52] R. Bhattacharyya, B. Key, H. Chen, A. S. Best, A. F. Hollenkamp, and C. P. Grey, "In situ nmr observation of the formation of metallic lithium microstructures in lithium batteries," *Nature materials*, vol. 9, no. 6, pp. 504–510, 2010.
- [53] H. J. Chang, N. M. Trease, A. J. Ilott, D. Zeng, L.-S. Du, A. Jerschow, and C. P. Grey, "Investigating li microstructure formation on li anodes for lithium batteries by in situ 6li/7li nmr and sem," *The Journal of Physical Chemistry C*, vol. 119, no. 29, pp. 16443–16451, 2015.

- [54] H. J. Chang, A. J. Ilott, N. M. Trease, M. Mohammadi, A. Jerschow, and C. P. Grey, "Correlating microstructural lithium metal growth with electrolyte salt depletion in lithium batteries using ^7Li MRI," *Journal of the American Chemical Society*, vol. 137, no. 48, pp. 15209–15216, 2015.
- [55] K. J. Harry, D. T. Hallinan, D. Y. Parkinson, A. A. MacDowell, and N. P. Balsara, "Detection of subsurface structures underneath dendrites formed on cycled lithium metal electrodes," *Nature materials*, vol. 13, no. 1, pp. 69–73, 2014.
- [56] O. O. Taiwo, D. P. Finegan, J. Paz-Garcia, D. S. Eastwood, A. Bodey, C. Rau, S. Hall, D. J. Brett, P. D. Lee, and P. R. Shearing, "Investigating the evolving microstructure of lithium metal electrodes in 3d using x-ray computed tomography," *Physical Chemistry Chemical Physics*, vol. 19, no. 33, pp. 22111–22120, 2017.
- [57] F. Sun, L. Zielke, H. Markotter, A. Hilger, D. Zhou, R. Moroni, R. Zengerle, S. Thiele, J. Banhart, and I. Manke, "Morphological evolution of electrochemically plated/stripped lithium microstructures investigated by synchrotron x-ray phase contrast tomography," *ACS nano*, vol. 10, no. 8, pp. 7990–7997, 2016.
- [58] K.-i. Morigaki and A. Ohta, "Analysis of the surface of lithium in organic electrolyte by atomic force microscopy, fourier transform infrared spectroscopy and scanning auger electron microscopy," *Journal of power sources*, vol. 76, no. 2, pp. 159–166, 1998.
- [59] L. Kong, Y. Xing, and M. G. Pecht, "In-situ observations of lithium dendrite growth," *Ieee Access*, vol. 6, pp. 8387–8393, 2018.
- [60] P. Bai, J. Li, F. R. Brushett, and M. Z. Bazant, "Transition of lithium growth mechanisms in liquid electrolytes," *Energy & Environmental Science*, vol. 9, no. 10, pp. 3221–3229, 2016.
- [61] H. Ghassemi, M. Au, N. Chen, P. A. Heiden, and R. S. Yassar, "Real-time observation of lithium fibers growth inside a nanoscale lithium-ion battery," *Applied Physics Letters*, vol. 99, no. 12, p. 123113, 2011.
- [62] R. L. Sacci, N. J. Dudney, K. L. More, L. R. Parent, I. Arslan, N. D. Browning, and R. R. Unocic, "Direct visualization of initial SEI morphology and growth kinetics during lithium deposition by in situ electrochemical transmission electron microscopy," *Chemical Communications*, vol. 50, no. 17, pp. 2104–2107, 2014.

- [63] B. L. Mehdi, J. Qian, E. Nasybulin, C. Park, D. A. Welch, R. Faller, H. Mehta, W. A. Henderson, W. Xu, C. M. Wang, *et al.*, “Observation and quantification of nanoscale processes in lithium batteries by operando electrochemical (s) tem,” *Nano letters*, vol. 15, no. 3, pp. 2168–2173, 2015.
- [64] M. J. Zachman, Z. Tu, S. Choudhury, L. A. Archer, and L. F. Kourkoutis, “Cryo-stem mapping of solid–liquid interfaces and dendrites in lithium-metal batteries,” *Nature*, vol. 560, no. 7718, pp. 345–349, 2018.
- [65] D. Aurbach and Y. Cohen, “The application of atomic force microscopy for the study of li deposition processes,” *Journal of the Electrochemical Society*, vol. 143, no. 11, p. 3525, 1996.
- [66] Y. S. Cohen, Y. Cohen, and D. Aurbach, “Micromorphological studies of lithium electrodes in alkyl carbonate solutions using in situ atomic force microscopy,” *The Journal of Physical Chemistry B*, vol. 104, no. 51, pp. 12282–12291, 2000.
- [67] M. Kitta and H. Sano, “Real-time observation of li deposition on a li electrode with operand atomic force microscopy and surface mechanical imaging,” *Langmuir*, vol. 33, no. 8, pp. 1861–1866, 2017.
- [68] S. Tariq, K. Ammigan, P. Hurh, R. Schultz, P. Liu, and J. Shang, “Li material testing-fermilab antiproton source lithium collection lens,” in *Proceedings of the 2003 particle accelerator conference*, vol. 3, pp. 1452–1454, IEEE, 2003.
- [69] N. Weadock, N. Varongchayakul, J. Wan, S. Lee, J. Seog, and L. Hu, “Determination of mechanical properties of the sei in sodium ion batteries via colloidal probe microscopy,” *Nano Energy*, vol. 2, no. 5, pp. 713–719, 2013.
- [70] H. Zhang, D. Wang, and C. Shen, “In-situ ec-afm and ex-situ xps characterization to investigate the mechanism of sei formation in highly concentrated aqueous electrolyte for li-ion batteries,” *Applied Surface Science*, vol. 507, p. 145059, 2020.
- [71] H. Shin, J. Park, S. Han, A. M. Sastry, and W. Lu, “Component-/structure-dependent elasticity of solid electrolyte interphase layer in li-ion batteries: experimental and computational studies,” *Journal of Power Sources*, vol. 277, pp. 169–179, 2015.
- [72] T. Kranz, S. Kranz, V. Miß, J. Schepp, and B. Roling, “Interrelation between redox molecule transport and li⁺ ion transport across a model solid electrolyte

interphase grown on a glassy carbon electrode,” *Journal of The Electrochemical Society*, vol. 164, no. 14, p. A3777, 2017.

- [73] I. Yoon, S. Jurng, D. P. Abraham, B. L. Lucht, and P. R. Guduru, “Measurement of mechanical and fracture properties of solid electrolyte interphase on lithium metal anodes in lithium ion batteries,” *Energy Storage Materials*, vol. 25, pp. 296–304, 2020.
- [74] M. A. Vorotyntsev, M. D. Levi, A. Schechter, and D. Aurbach, “Time- difference impedance spectroscopy of growing films containing a single mobile charge carrier, with application to surface films on li electrodes,” *The Journal of Physical Chemistry B*, vol. 105, no. 1, pp. 188–194, 2001.
- [75] R. Bouchet, S. Lascaud, and M. Rosso, “An eis study of the anode li/peo-litfsi of a li polymer battery,” *Journal of the electrochemical society*, vol. 150, no. 10, p. A1385, 2003.
- [76] J. Morales-Ugarte, A. Benayad, C. Santini, and R. Bouchet, “Electrochemical impedance spectroscopy and x-ray photoelectron spectroscopy study of lithium metal surface aging in imidazolium-based ionic liquid electrolytes performed at open-circuit voltage,” *ACS applied materials & interfaces*, vol. 11, no. 24, pp. 21955–21964, 2019.
- [77] J. E. M. Ugarte, *In operando study of lithium batteries by coupling X-ray photoelectron spectroscopy and impedance spectroscopy*. PhD thesis, Université Grenoble Alpes, 2019.
- [78] D. Aurbach, M. Daroux, P. Faguy, and E. Yeager, “Identification of surface films formed on lithium in propylene carbonate solutions,” *Journal of The Electrochemical Society*, vol. 134, no. 7, p. 1611, 1987.
- [79] I. Ismail, A. Noda, A. Nishimoto, and M. Watanabe, “Xps study of lithium surface after contact with lithium-salt doped polymer electrolytes,” *Electrochimica Acta*, vol. 46, no. 10-11, pp. 1595–1603, 2001.
- [80] P. Barai, K. Higa, and V. Srinivasan, “Effect of initial state of lithium on the propensity for dendrite formation: a theoretical study,” *Journal of the Electrochemical Society*, vol. 164, no. 2, p. A180, 2016.
- [81] M. Doyle, T. F. Fuller, and J. Newman, “Modeling of galvanostatic charge and discharge of the lithium/polymer/insertion cell,” *Journal of the Electrochemical society*, vol. 140, no. 6, p. 1526, 1993.

- [82] P. Barai, K. Higa, and V. Srinivasan, "Lithium dendrite growth mechanisms in polymer electrolytes and prevention strategies," *Physical Chemistry Chemical Physics*, vol. 19, no. 31, pp. 20493–20505, 2017.
- [83] X. Lin, J. Park, L. Liu, Y. Lee, A. Sastry, and W. Lu, "A comprehensive capacity fade model and analysis for li-ion batteries," *Journal of The Electrochemical Society*, vol. 160, no. 10, p. A1701, 2013.
- [84] D. Aurbach, Y. Ein-Eli, O. Chusid, Y. Carmeli, M. Babai, and H. Yamin, "The correlation between the surface chemistry and the performance of li-carbon intercalation anodes for rechargeable 'rocking-chair' type batteries," *Journal of The Electrochemical Society*, vol. 141, no. 3, p. 603, 1994.
- [85] M. Safari, M. Morcrette, A. Teysot, and C. Delacourt, "Multimodal physics-based aging model for life prediction of li-ion batteries," *Journal of The Electrochemical Society*, vol. 156, no. 3, p. A145, 2008.
- [86] A. Masias, N. Felten, R. Garcia-Mendez, J. Wolfenstine, and J. Sakamoto, "Elastic, plastic, and creep mechanical properties of lithium metal," *Journal of materials science*, vol. 54, no. 3, pp. 2585–2600, 2019.
- [87] W. S. LePage, Y. Chen, E. Kazyak, K.-H. Chen, A. J. Sanchez, A. Poli, E. M. Arruda, M. Thouless, and N. P. Dasgupta, "Lithium mechanics: roles of strain rate and temperature and implications for lithium metal batteries," *Journal of The Electrochemical Society*, vol. 166, no. 2, p. A89, 2019.
- [88] P. Barai, K. Higa, and V. Srinivasan, "Impact of external pressure and electrolyte transport properties on lithium dendrite growth," *Journal of The Electrochemical Society*, vol. 165, no. 11, pp. A2654–A2666, 2018.
- [89] C. Fu, V. Venturi, J. Kim, Z. Ahmad, A. W. Ells, V. Viswanathan, and B. A. Helms, "Universal chemomechanical design rules for solid-ion conductors to prevent dendrite formation in lithium metal batteries," *Nature materials*, vol. 19, no. 7, pp. 758–766, 2020.
- [90] J. Newman and T. W. Chapman, "Restricted diffusion in binary solutions," *AIChE Journal*, vol. 19, no. 2, pp. 343–348, 1973.
- [91] H. Eyring, "The activated complex in chemical reactions," *The Journal of Chemical Physics*, vol. 3, no. 2, pp. 107–115, 1935.
- [92] S. G. Stewart and J. Newman, "The use of uv/vis absorption to measure diffusion coefficients in lipf6 electrolytic solutions," *Journal of the Electrochemical Society*, vol. 155, no. 1, p. F13, 2007.

- [93] S. A. Mullin, G. M. Stone, A. Panday, and N. P. Balsara, "Salt diffusion coefficients in block copolymer electrolytes," *Journal of the Electrochemical Society*, vol. 158, no. 6, p. A619, 2011.
- [94] J. Evans, C. A. Vincent, and P. G. Bruce, "Electrochemical measurement of transference numbers in polymer electrolytes," *Polymer*, vol. 28, no. 13, pp. 2324–2328, 1987.
- [95] S. Zugmann, M. Fleischmann, M. Amereller, R. M. Gschwind, H. D. Wiemhöfer, and H. J. Gores, "Measurement of transference numbers for lithium ion electrolytes via four different methods, a comparative study," *Electrochimica Acta*, vol. 56, no. 11, pp. 3926–3933, 2011.
- [96] S.-L. Wu, A. E. Javier, D. Devaux, N. P. Balsara, and V. Srinivasan, "Discharge characteristics of lithium battery electrodes with a semiconducting polymer studied by continuum modeling and experiment," *Journal of the Electrochemical Society*, vol. 161, no. 12, p. A1836, 2014.
- [97] H. Geng, R. Rosen, B. Zheng, H. Shimoda, L. Fleming, J. Liu, and O. Zhou, "Fabrication and properties of composites of poly (ethylene oxide) and functionalized carbon nanotubes," *Advanced Materials*, vol. 14, no. 19, pp. 1387–1390, 2002.
- [98] A. Martinent-Beaumont, *Etude physico-chimique des électrolytes d'hexafluorophosphate de lithium pour une application dans la batterie lithium-ion*. PhD thesis, Grenoble INPG, 2037.
- [99] P. Guan, L. Liu, and X. Lin, "Simulation and experiment on solid electrolyte interphase (sei) morphology evolution and lithium-ion diffusion," *Journal of The Electrochemical Society*, vol. 162, no. 9, p. A1798, 2015.
- [100] R. Grissa, V. Fernandez, N. Fairley, J. Hamon, N. Stephant, J. Rolland, R. Bouchet, M. Lecuyer, M. Deschamps, D. Guyomard, *et al.*, "Xps and sem-edx study of electrolyte nature effect on li electrode in lithium metal batteries," *ACS Applied Energy Materials*, vol. 1, no. 10, pp. 5694–5702, 2018.
- [101] G. Bilodeau, "Regular pyramid punch problem," 1992.
- [102] J. Dolbow and M. Gosz, "Effect of out-of-plane properties of a polyimide film on the stress fields in microelectronic structures," *Mechanics of materials*, vol. 23, no. 4, pp. 311–321, 1996.

- [103] M. Zhou, Q.-A. Huang, and M. Qin, "Design and simulation of integrated cmos-compatible capacitive absolute pressure-sensing microsystems," in *MEMS/MOEMS Technologies and Applications*, vol. 4928, pp. 118–126, International Society for Optics and Photonics, 2002.
- [104] C. Barchasz, L. Boutafa, E. Mayousse, and B. Chavillon, "Diagnostic of failure mechanisms in li/s rechargeable batteries using thermal micro-calorimetry technique applied to pouch and cylindrical type cells," *Electrochimica Acta*, vol. 292, pp. 974–981, 2018.
- [105] Y. Yamada and A. Yamada, "Superconcentrated electrolytes for lithium batteries," *Journal of The Electrochemical Society*, vol. 162, no. 14, p. A2406, 2015.

Résumé :

Le lithium métal représente le candidat optimal comme électrode négative dans les batteries au lithium, de par sa capacité théorique élevée. En revanche, l'inconvénient majeur de cette technologie est la formation de dendrites qui peut provoquer des emballements thermiques et des courts-circuits internes et sont responsables de la durée de vie limitée des cellules lithium métal. L'objectif de ce travail est de corrélérer données expérimentales et modèle afin de comprendre la formation et la croissance des dendrites pour le développement de cette technologie.

Le modèle proposé montre que l'interphase électrode/électrolyte ('SEI' pour Solid Electrolyte Interphase) est fondamentale pour évaluer la formation de dendrites et leur croissance, tandis que la définition d'une densité de courant limite n'est pas une condition suffisante pour éviter les dendrites. Cette prise en compte de la SEI dans le modèle permet d'étudier l'influence de ses propriétés mécaniques et électrochimiques, de prédire les conditions qui favorisent la croissance dendritique et de distinguer différentes morphologies de surface. Des dendrites arborescentes (tree-like), moussues (mossy-like) et whiskers sont obtenues selon la densité de courant appliquée. De plus, l'ajout de la mécanique de la SEI permet au modèle de faire la distinction entre la croissance induite par la pointe (tip-induced) et celle induite par la racine (root-induced). Les propriétés électrochimiques et mécaniques de la SEI formée dans un électrolyte liquide sont déterminées par spectroscopie d'impédance électrochimique (SIE) et microscopie à force atomique (AFM) et les composants chimiques sont identifiés par la spectrométrie photoélectronique X (XPS). Enfin, les tendances prédites par le modèle sont validées grâce à la mise au point d'une nouvelle configuration de cellule lithium métal, adaptée à une étude *operando* de l'électrodépôt du lithium métal par microscopie optique.

Ce travail représente une étude complète de la formation et croissance des dendrites dans les accumulateurs au lithium métal. Tandis que seuls les électrolytes liquides sont considérés ici, la méthodologie pourrait tout à fait être étendue aux électrolytes solides et aux revêtements artificiels à la suite de ce travail.

Abstract:

Lithium metal represents the optimal candidate for the negative electrode in lithium batteries, due to its high theoretical capacity. On the other hand, the major drawback of this technology is the formation of dendrites, which can cause thermal runaway and internal short-circuits, and are responsible for the limited lifetime of the cells. The goal of this work is the correlation between experiments and modeling, to understand the formation and the growth of dendrites to improve this technology.

The proposed model shows that the Solid Electrolyte Interphase (SEI) is fundamental to assess dendrites formation and growth, while the definition of a limiting current density is not a sufficient condition to avoid dendrites. Thanks to the introduction of the SEI concept and properties, the proposed model studies the influence of its mechanical and electrochemical properties on the dendritic growth and it is able to predict the conditions that favours dendritic growth and to distinguish different surface morphologies. Tree-like, mossy-like and whisker dendrites are obtained, depending on the applied current density. Moreover, the addition of the mechanics of the SEI allows the model to distinguish between tip-induced growth and root-induced growth. Electrochemical impedance spectroscopy (EIS) and atomic force microscopy (AFM) techniques are used to find electrochemical and mechanical properties of the SEI formed in liquid electrolytes and the chemical components are identified with X-ray photoelectron spectroscopy (XPS). Finally, the trends predicted by the model are validated with a novel cell configuration suitable for an *operando* optical microscopy study of lithium metal stripping/plating.

This work represents a comprehensive study on dendrites formation and growth in lithium metal batteries. While it considers only liquid electrolytes so far, as a perspective, it could easily be expanded to solid electrolytes and artificial coatings.